MICROMECHANICS OF ASPERITY INTERACTION IN WEAR

-A NUMERICAL APPROACH

A Dissertation

Presented to

The Graduate Faculty of the University of Akron

In Partial Fulfillment

of the Requirements for the Degree

Doctor of Philosophy

Sunil Acharya

December, 2005

MICROMECHANICS OF ASPERITY INTERACTION IN WEAR

-A NUMERICAL APPROACH

Sunil Acharya

Dissertation

Approved:	Accepted:
_____	_____
Advisor Dr. Arkadii I. Leonov	Department Chair Dr. Sadhan Jana
_____	_____
Co-Advisor/Committee Member Dr. Joseph P. Padovan	Dean of the College Dr. Frank N. Kelley
_____	_____
Committee Member Dr. Gary R. Hamed	Dean of the Graduate School George R. Newkome, Ph.D
_____	_____
Committee Member Dr. Erol Sancaktar	Date
_____	
Committee Member Dr**.** Rudolph J. Scavuzzo, Jr**.**	

ABSTRACT

In last 50 years, research on elastomer wear has produced qualitative and statistical data regarding wear debris and associated morphologies. However, the exact wear mechanism and the evolution of wear morphologies is not understood to the level where a quantitative prediction or description of wear is possible

In this study a numerical analysis (FEA) has been used to understand mechanical interactions related to pattern wear. A blunt surface crack and it's interaction with a single penetrating asperity has been modeled for varying frictional, material and kinematic conditions. An interacting asperity creates a deformation field in an elastomeric body. This stress field is altered in the presence of a crack. The resulting stress relief is quantitatively estimated for varying geometric, material and friction parameters. Consequently, the energy available for a new crack to propagate in the vicinity of the existing crack decreases leading to a characteristic spacing between successive cracks. Energy release rate data from fracture experiments on thin rubber sheets is used to calculate the spacing between the cracks. The approach sheds some light on crack propagation characteristics in pattern wear.

Other numerical experiments in this study analyze: (1) Elastomer response to dynamic asperity loading (2) Asperity loading at micro-scale where filled rubber has high degree of non-homogeneity (3) Effect of asperity loading at an angle on a rubber flap. As a result, we now better understand the evolution of wear related morphologies.

DEDICATION

To My Parents.

ACKNOWLEDGEMENTS

With this project, my advisors Dr Leonov and Dr Padovan were a tremendous source of insight and practicality. I thank my committee members Dr Sancaktar, Dr Hamed and Dr. Scavuzzo for helpful suggestions and making time from their schedules.

Santosh Bawiskar and Mehdi Kashani were diligent in their role as informal committee members. Their guidance was crucial. Bob Shardy (ECNS) and his crew through the years were extremely helpful in providing me with computational support. A host of friends and well-wishers provided me the distractions from the drudgery of the work while gently reminding me to take care of the less important things in my life. Thanks are in order to Steve Bloomfield, Partha Mukherjee and Howard Haines, PhD to mention a few. Marianne Bahr, Kay and Mike Millush and Paula and Bill Fulmer all were affectionate and patient cheerleaders as members of the parental committee. I am extremely grateful for that. Lastly, Chris Craycroft was wonderful in encouragement and generous with time in getting through the last mile.

TABLE OF CONTENTS

Page

LIST OF TABLES

LIST OF FIGURES

CHAPTER I

INTRODUCTION

Wear is an important event in industry that determines the life of mechanical components. Among elastomeric applications, tire wear is a prime example of this. Wear in general is a complicated process that involves mechanical or chemical degradation of material. In the case of elastomers, the non-linear material properties and friction behavior add a new dimension to the complexity of wear. There have been several experimental and numerical approaches to this problem over the years that have resulted in observations regarding wear at different scales. Here we propose a few different numerical models to extend the understanding of these observations.

Chapter II describes the various aspects of wear as presented in literature over the last 50 years. This includes the existing understanding of elastomeric friction and contact mechanics, the effect of elastomer properties on the tear behavior and fatigue crack propagation. Several experimental observations of wear in elastomers are discussed. These observations reveal the multi-scale nature of the wear process from the macroscopic to the microscopic. The observations raise several questions about the evolution of the cracks from micro-scale to the macro-scale that leads to material removal and wear. Three different problems are proposed that will be analyzed with a set of numerical models that use the FEA techniques. The most basic event in the process of wear is the interaction of an asperity (such as those from a hard surface viz. road) with a

crack. Typically, the asperities are at several scales. Also, they are affected by the highly nonlinear (and possibly viscoelastic) material response of the elastomers. Much of the tire wear involves highly dynamic events. The friction behavior of elastomers is equally complicated because of the strong adhesive forces involved. The proposed models are organized to address the effect of these specific issues on asperity- crack/defect interaction. In the process, a better understanding of wear evolution is expected.

Chapter 3 discusses the single 2D asperity interaction model. A new method is proposed for calculation of energy release rates in Chapter 4. This method allows different estimations of crack spacing on the surface of a material.

Chapter 5 discusses the complications when asperity interaction with inertial dynamics is analyzed. Additional physical phenomena related to elastic waves come into the picture.

Chapter 6 briefly discusses the model for microscales and the three dimensional flap problems. It is seen that although mathematically it is possible to scale results at microscale, the resulting computation may not be realistic due to the inhomogeneous nature of the filled material at that scale. Also, in the case of three-dimensional flap geometry, there are several locations where crack propagation may occur. These correspond well with Gerrard's qualitative observation.

In conclusion, Chapter 7 discusses the usefulness of the numerical exercises described in the previous chapters. A number of experiments are suggested to verify some of the predictions with respect to crack propagation and related wear.

CHAPTER II

LITERATURE SURVEY

Tire wear is a complicated yet important phenomenon with enormous implications related to transportation and environmental concerns. The complications arise due to various physical phenomena involved at various scales and their interaction.

The pneumatic tire is a highly engineered composite structure with non-homogeneity. This includes the tread pattern, elastomeric component with fillers and additives, and the composition of sidewall including the chords. The loading experienced by the tire is equally complicated and depends upon the vehicle's power transmission system, suspension and driver's habits, among other things. The kinematics of tire movement over the pavement is complicated and involves rolling, slipping, twisting, and cornering. Since wear is principally frictional in nature [1], tire wear is also a function of the interacting road surface. Road surface is textured with asperities of different scales. Rain, snow and heat from the sun are constantly changing the nature of the asperities on the road surface. This seasonal variation can lead to a different type of wear depending upon the 'aging' of the road surface.

2.1.1 Wear of Rubber

Rubber (tire) wear is defined as removal of rubber particles from the surface of rubber (tire) and is accompanied by heating of the interacting surfaces and noise generation. The complicated nature of tire motion and the interacting surface results in

complex state of stress and deformation on the tire footprint. To account for this, Veith [2] explained wear in terms of "severity" of tire-force, abrasive surface and weather-temperature. Frictional work involved in tire surface interaction contributes to the process of rubber wear [1]. This work is the source of energy required to break bonds and micro-crack propagation.

Much of the experimental work is by using two different test methods. The first is the test in which a tire mounted on a vehicle follows specific driving profile. The second type of test involves a trailer mounted tire with a known toe – in or slip angle. The trailer is then pulled over a test-track with a prescribed profile. The trailer test thus offers a more controlled environment by fixing the tire orientation. In both the experimental tests, loss of tire weight is measured. Observation of the worn surfaces and measurements on size of detached particles illustrate two distinct types of rubber wear in tires. Typically [3] when abrasion takes place unidirectionally, worn debris is large in size and the corresponding wear rate is high. This type of wear leads to formation of patterns on the tire surface and is called as 'pattern wear'. The second type of wear is multidirectional and is at a smaller geometric scale. This is termed as the intrinsic wear. Theoretical treatment on how rubber particles with certain sizes form, how ridges develop in the pattern wear, and why a wear process alters from the intrinsic wear to the pattern wear where a unidirectional load is applied to the surface is limited.

2.1.2 Types of Wear Processes

The experimental procedures mentioned in the last section, have led to a large data on rubber wear in tires. Wear can be broadly classified as adhesive, abrasive, erosive, corrosive and fatigue, wear. Each of these wear processes is highly non-linear and

depends upon a number of factors such as material properties, interface geometry, kinematics and temperature. Much of the experimental work aimed at studying the wear process is hampered by abrasion debris. Typically, the abrasion debris contaminates the wear interface by forming a coating on the interface, changing the nature of friction and the surface from the perspective of correlation between the rupture strength of rubber and external factors such as loading conditions and environment. Rubber wear has been categorized in the literature into three major processes as abrasive wear, fatigue wear, and corrosive wear.

Adhesive wear and abrasive wear both refer to the dominant nature of friction during certain types of material removal. In adhesive wear, material removal is by transient adhesion of asperities. On the other hand, in abrasive wear the magnitude of applied load to the surface of rubber exceeds the tear strength (T_c) of rubber to initiate rupture. Only a few aspirates are enough to detach rubber particles from the surface in this case. In the abrasion process, rubber shows a rate dependent or plastic response [4]. At high rate of slippage as in braking and cornering, an abrader with sharp asperities immediately leads to a grooved rubber surface characterizing abrasion.

Erosion and fatigue wear correspond to a more long term wear process where the material is removed over a period of time by accumulation of damage. Erosive wear is essentially a gradual abrasion wear. In fatigue wear, cracks undergo mechanical fatigue at tearing energies lower than the critical tearing energy (T_c) obtained from monotonic tear experiments [5]. This leads to crack growth by the process of fatigue crack propagation. Response of rubber in this case is mainly elastic [4]. This type of rubber wear might occur during the rolling of a tire on the pavement with slight slip under low to

moderate friction. If the movement of the abrader with respect to the rubber surface is multidirectional, the resulting intrinsic wear leads to a particle size in the range of 1 to 5 microns. Further breakdown of particles into smaller sizes (less than 1 micron nominal diameter) has not been observed [6]. The exact cause of these wear-characteristics is an unknown, because of the complicated nature of the wear process. When a rubber product slides over a track only in one direction, certain patterns show up on its surface. Similar to the formation of intrinsic particles, pattern wear is also result of fatigue propagation of surface cracks[7]. Topological studies of worn rubber surfaces reveal that with sliding, pattern formation starts with ring- shape micro-tears and progresses to formation of ridges and ruffles. The density, shape, and size of these ridges depend on the rubber mechanical properties, intensity of the friction force, and abrader characteristics [7]. The existing ridges typically are bent back, exposing their underside to the abrasion and protecting the topside from the abrasive. A hierarchical wear pattern may develop when the same process is repeated on the ridge surface. Fatigue crack propagation may also lead the bent ridges to peel and grow through their leading edge. One of the speculations suggests that when a ridge grows, its crest will break as a result of tensile rupture. This type of large scale material removal is characteristic of pattern wear and results in relatively higher rate of wear when compared to the intrinsic wear [9]. The size of the particle debris in this case ranges from 50 to 100 micrometers in nominal diameter. Padovan et al [8] have observed that most of the larger particles are nothing but agglomeration of basic particles. Statistical analysis on the shape, size and distribution of the wear particles, illustrates the evolution of these agglomerates. The study also

illustrates the importance of laboratory tests, which provide control on directionality of tire motion in separating kinematic aspects of tire abrasion.

Corrosive wear, refers to material breakdown by chemical degradation. This may be induced by mechanical effects such as breakage of polymer chains under loading and is often exacerbated by oxidation from environmental oxygen. Rubber as used in tires, comes with a number of chemical additives and plasticizers that get released from the rubber matrix onto the surface. This is part of the aging process, and leads to further hydrocarbon interactions with environment. The chemical degradation of polymer usually reduces the polymer molecular weight leading to decrease in critical tear energy. Pulford and Gent [10] observed the result of this chemical degradation in the form of smeared gum in natural rubber (NR) and styrene butadiene rubber (SBR), and a dry powder in butadiene rubber (BR) vulcanizates. In the first case, permanent reduction of molecular weight is attributed to the reaction of broken chains with oxygen. Smeared gummy rubber produced on the surface of rubber reduces the rate of wear due to reduction of contact between the abrader and rubber. Tackiness of the rubber compound due to this degradation results in "rolling up" of ridges before they detach from the surface. In the case of BR, free radicals of the broken polymer chain promote crosslinking between broken chains and polymer chain surfaces, causing a dry powder substrate.

It should be noted that the different wear processes exist simultaneously in different degrees depending on the wear conditions and influence each other. For example, mechanical degradation may indirectly lead to increased corrosive wear because of high

intensity forces. Also long term abrasive wear may contribute to fatigue wear at a small scale and so on.

2.1.3 Principal Mechanical Phenomena Affecting Wear Process

From the observations related to the wear processes, it is clear that the process of wear is a very complicated interaction between multiple competing mechanisms. The principal phenomena is friction, which affects the macroscopic interaction between asperities and the texture of the rubber (tire) surface. Ultimately, this micromechanical interaction between asperities and the rubber (tire) surface leads to the material removal characterizing the wear process, as observed macroscopically. The material removal process is dominated by crack propagation in the rubber media. With these general observations, it may be safe to say that a comprehensive investigation of the wear process from a mechanical viewpoint, should take into account the phenomena of friction, contact micromechanics between the interacting surfaces and crack propagation. All the other factors contributing to the wear process can be accounted for by treating them as parameters controlling the above three phenomena. For example, the effect of temperature may be accounted through its effect on material properties and friction. Similarly, the chemical effects may be accounted through its effect on adhesion, and resulting changes in the micromechanical interaction. In the following sections, the three dominant phenomena of friction, contact mechanics and the eventual crack propagation are discussed.

2.2.1 Friction

The phenomenon of wear is dissipative in nature and the essential force related to this dissipation is the frictional force between and near the two sliding surfaces. The

external work done by the frictional forces equals the sum of the internal energy increase and the dissipated energy at and around the interface. Internal energy changes are typically manifested through the creation of new surfaces and the residual elastic stress fields. The dissipation is manifested through plastic and viscous deformation, hysteresis loss, dislocation formations etc. Much of the frictional behavior between two sliding surfaces is thus dependent on following three fundamental aspects:

(1) The effect of environment on surface characteristics through physico-chemical interaction.

(2) The force generation and transmission between the contact surfaces.

(3) The material behavior near the surface in response to the external forces acting at the surface contact points.

Most initial theoretical development for friction was related to metal friction. Bowden and Tabor described this phenomenon using the adhesion theory [11,12]. In this theory, the friction force is the force generated at the interface during sliding of metallic contact. The theory assumes that two opposing asperities from the two metallic surfaces come in contact and the load at the tips of the asperity are high enough to cause local plastic deformation of the asperities. The local plastic deformation of asperity tip(s) are assumed to cause strong adhesive junctions. The actual area of contact (A_{rc}) of the two asperities is proportional to the load W and inversely proportional to the yield pressure of the softer material - typically estimated by the indentation hardness (H_s).

$$A_{rc} = \frac{W}{H_s} \qquad 2.1$$

The shear strength of the adhesive junctions between the two surfaces is also the shear strength of the softer material (K_s). Thus the friction force (F) which is to be overcome in order for the relative motion to occur is given by:

$$F = A_{rc} K_s \qquad 2.2$$

This leads to the classic definition of coefficient of friction (μ) as:

$$\mu = \frac{K_s}{H_s} \qquad 2.3$$

The adhesion theory was largely formulated on the observation that sliding surfaces with greater mutual solubility have higher coefficient of friction. It however still failed to predict the high friction coefficient observed experimentally. Also, the frictional behavior of metals with little solubility has a very large variation in coefficient of friction. This is not explained by the adhesion theory [13].

The adhesion theory was largely replaced by a more 'mechanistic' model proposed by Suh and Sin [14]. The theory attributes the genesis of frictional force to the phenomena of plowing, adhesion and asperity deformation. This theory takes into account the time of variation of frictional behavior during sliding and explains the variation of coefficient of friction during static and sliding conditions. Figure 2.1 shows the variation of friction coefficient with the sliding distance [14, 15]. The variation in friction coefficient can be roughly divided into 6 regions, largely due to varying dynamics between the three competing mechanisms of plowing, adhesion and asperity deformation.

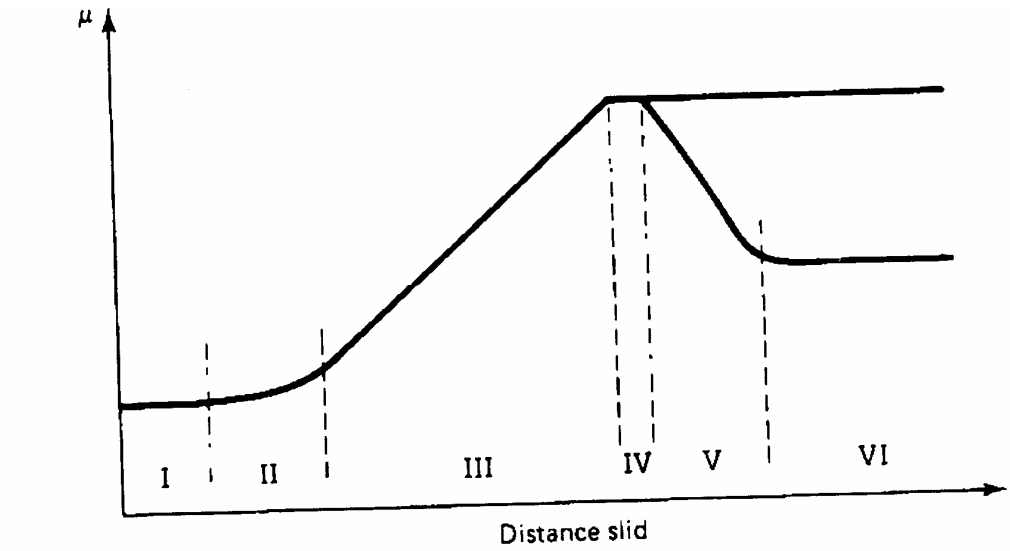

FIGURE 2.1: Stages of friction. From Suh [62]

The first stage of friction is largely free of adhesion as the two surfaces are contaminated. There is a predominant plowing action on the surfaces by asperities and some deformation of asperities. The second stage (stage II) is when the adhesion between surfaces rises steadily and the friction coefficient rises as a result. This stage maybe absent in the case of highly lubricated surfaces and maybe severe in case the wear particles generated by the deformation and fracture process aid the plowing of the surfaces. The second stage is the transitional phase between the first and third stage. The third stage is characterized by steep increase in friction as the wear particle entrapment and resulting plowing action increases further. Much of the wear particle generation is a result of subsurface deformation, crack nucleation and crack propagation [15].

Stage IV of the friction behavior is reached when the number of wear particles generated, reaches saturation. This occurs when the wear particle generation and wear particle removal rates reach equilibrium. In this case, the adhesion mechanism of friction has reached a stable value. This is the steady state coefficient of friction. In some cases the creation of extremely smooth surfaces on the harder material from asperity wear results in a decrease in friction force (Stage V). The softer surface may also acquire 'smoother' surface characteristics at a later stage in sliding, resulting in further decrease in friction force (Stage VI).

2.2.2 Friction in Elastomers

The basic mechanism contributing to friction in metals, plowing, adhesion and asperity deformation is present in polymeric materials as well. However the situation is more complicated because of the visco-elastoplasticity of the material. Johnson et al [16] showed that the area of contact between a rigid sphere and the flat and smooth surface of

a rubber like material is greater than the value which can be deduced from the classical elasticity theory. Around the same time, Schallamach [1] observed that in certain circumstances, when a blunt rigid asperity moves over a rubber surface, the true sliding friction does not occur. Instead, waves of detachment propagate across the interface from the leading edge to the trailing one of the contact area. The velocity at which these waves of detachment progress is greater than the imposed speed. This creates the relative motion between the two surfaces. In addition to the visco-elastoplasticity of the elastomers, their comparatively low modulus and softening temperatures, leads to a frictional behavior that is much more sensitive to the applied load, temperature and the sliding velocity. Typically, an increase in temperature is equivalent to a decrease in sliding speed and vice versa. The time temperature superposition principle valid for polymers in general is active in the frictional phenomena for the elastomers. Fig (2.2) from Grosch [17] shows the dependence of coefficient of friction on temperature and velocity. Using the William Landau Ferry (WLF) equation, a so-called master curve can be obtained to describe the variation of friction based on temperature and velocity. In reality, it should be noted that the velocity and temperature at the contacting asperities have a strong inter-relationship. The work done during sliding raises the surface temperature and is affected by interface geometry, applied load and physical properties as well as sliding velocity.

Attempts to model the friction phenomena in rubbers have been numerous. The particular nature of 'detachment wave' propagation leads to a stick-slip type of friction. This is detected experimentally even at low sliding speeds (Figure (2.3)). Barquins et al [18] tried to relate the various regimes of a friction coefficient vs. velocity curve to the

changes in experimental tangential force recordings (Figure (2.4)). As sliding force increases and detachment folds appear in an elastomer, there is a discontinuity in the friction curve, indicating a physical instability. The propagation of waves relaxes stresses in the contact area, decreasing the tangential forces slightly. There is a transient region generated by this effect. This instability disappears at higher speeds where the propagation becomes regular. Once again, the friction force increases in a fashion similar to the increase in peeling force with the crack propagation speed. The studies on the formation of a detachment fold are experiments that use the interference methods. This method allows one to determine both the profile of the rubber surface in the contact zone vicinity and the shape of the detachment folds [68]. At slow sliding speeds, there is a viscoelastic bulge that propagates at the same velocity. At a critical speed, the slider overtakes the 'bulge' and sticks to it (Figure 2.5). The contact point is shown by the letter M and the previous contact limit is indicated by M_0. Beyond this speed, the fold acts as a 'channel' which is open at its extremities and the detachment wave propagates across the contact area (figure2.6). This analogy is used in literature as rubber first 'peels' from the surface of the rigid slider and 'sticks' again, in a continuous fashion. So it was concluded that the 'peeling force' in front of the wave is related closely to the tangential force recordings. For a contact area of diameter 2a, if n is the number of waves present, that move with a mean speed of 'v', the tangential force (T) should satisfy the energy balance:

$$VT = nFv \qquad 2.4$$

Where V is the imposed slider velocity and F is the local 'peeling' force ahead of the detachment fold. The strain energy release rate G is proportional to F/l for the peeling test with l= 2a and is power function of the detachment wave velocity as :

$$G = v^n \qquad 2.5$$

This rather simplistic model has been verified experimentally by plotting the quantities VT/nl with the wave speed (figure 2.7). In spite of several laboratory experiments since 1971 [18], the regime in which the detachment waves exist has been found to be difficult to obtain. However it is known that the detachment waves appear at a critical sliding speed determined by the adhesive properties of the interface, the geometrical characteristics of the contact, and on the viscoelasticity of the rubber like material. It is found that the critical speed required for the detachment waves to occur, decreases as the applied normal load decreases. A decrease in temperature and or increase in the radius of the slider also have a similar effect. An increase in size of the slider also increases the friction linearly. The variation in friction coefficient with the slider velocity also has a similar effect.

A number of researchers have pointed out that the negative slope of the friction velocity curve is not the prerequisite for stick-slip oscillation. These alternative explanations use the Ludema and Tabor [19] model to explain the phenomenon. In this model, the peak in the friction-velocity curve occurs because of the competing effects of strain rate dependence of the shear strength and the reduced area due to viscoelastic stiffening of the elastomer Figure 2.3. Supporting this argument, Rorrer et al [20] report that stick-slip phenomenon is typically accompanied by deposition of transfer film on the sliding interface.

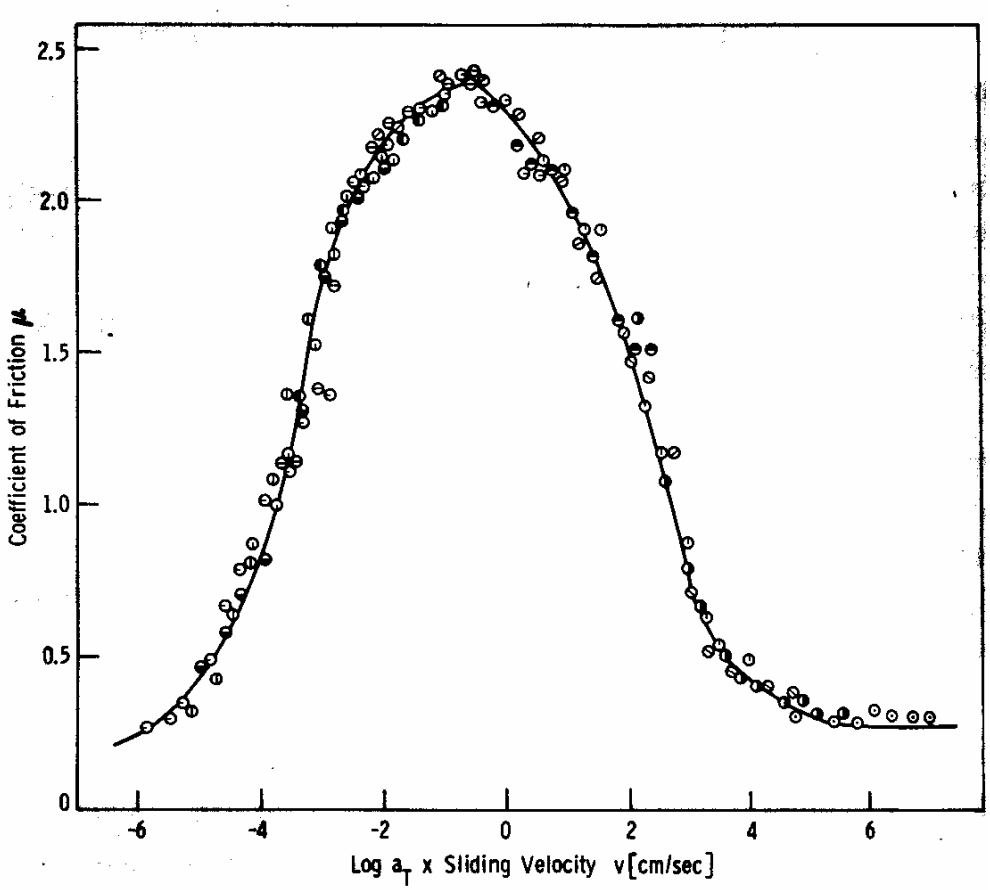

FIGURE 2.2: Master curve for friction coefficient of acrylonitrile butadiene rubber at 20 C From Grosch [17]

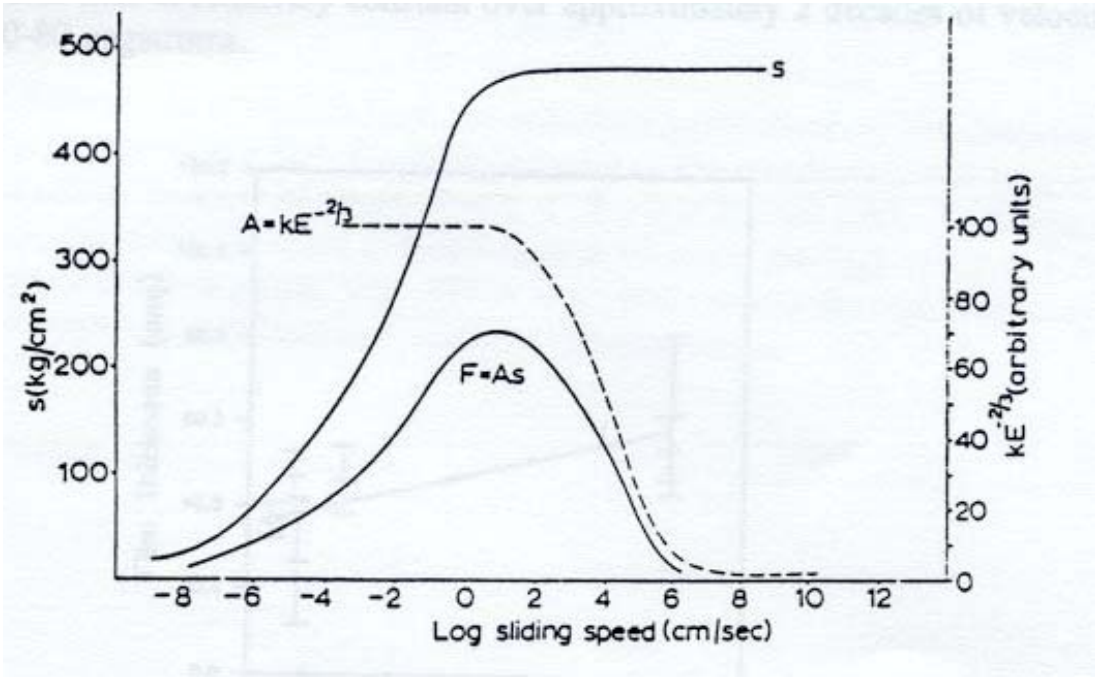

FIGURE 2.3: Ludema and Tabor model for friction in elastomers [20]

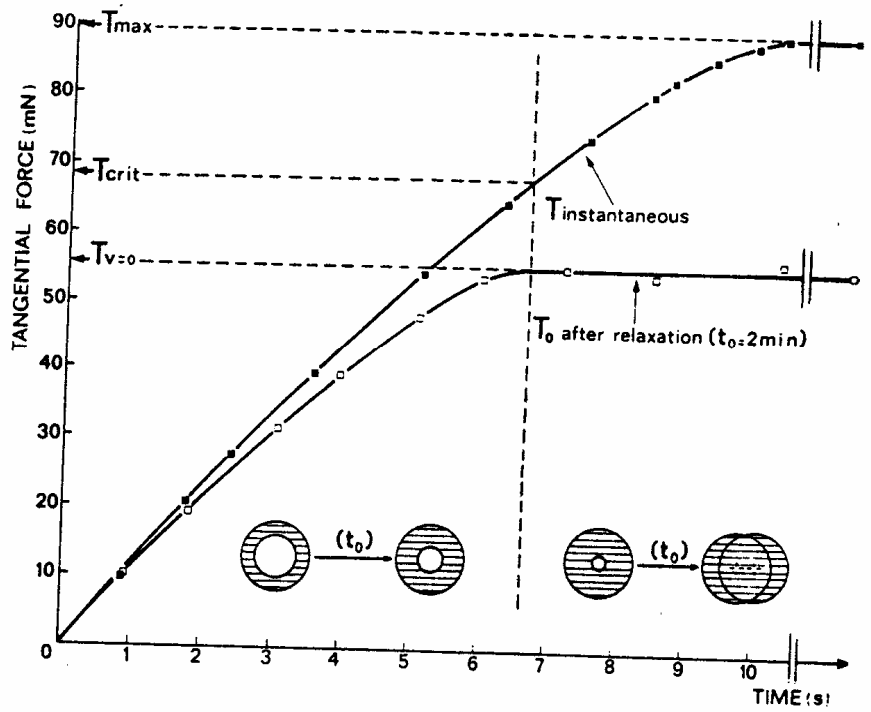

FIGURE 2.4: Time variation of tangential forces during the preliminary phase of the rubber friction for a glass sphere under fixed normal load. ■ represents the instantaneous response and ◘ represents the relaxation response after 2 minutes. From Barquins [68]

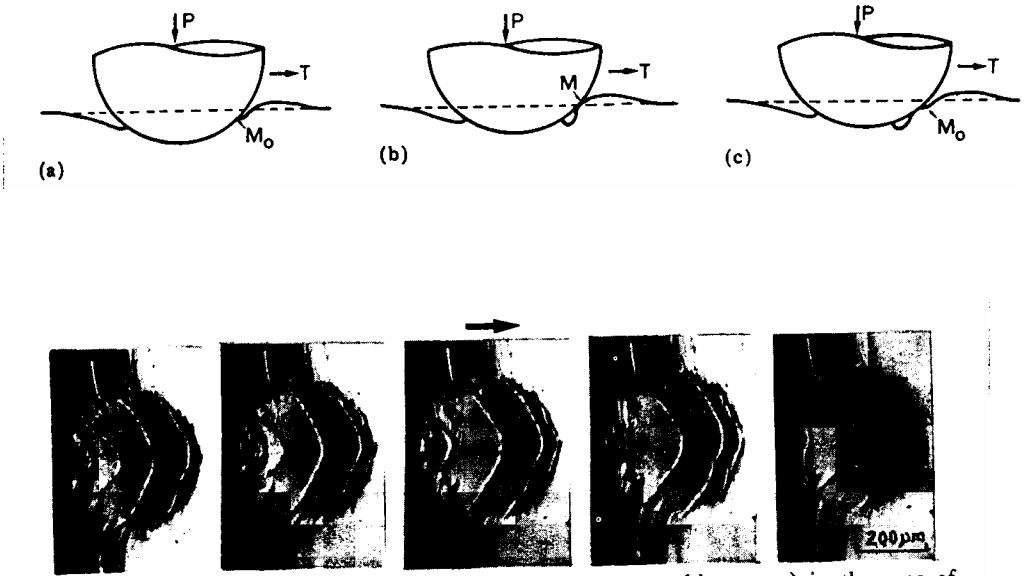

FIGURE 2.5: Propagation of detachment folds in the contact area of a rigid asperity moving on a smooth rubber surface. Top: Schematic cross section : Top view. From Barquins[68]

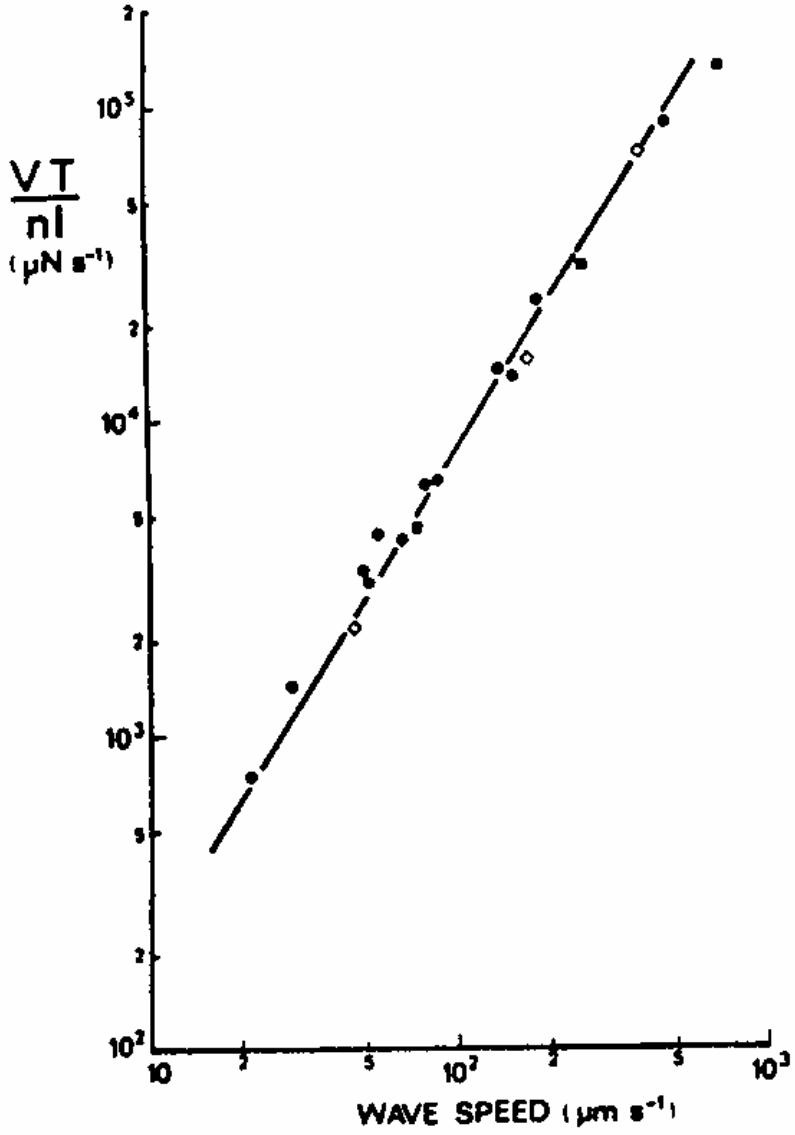

FIGURE 2.6: The parameter VT/nl vs the wavespeed v for various normal loads and imposed sliding speeds V. From Barquins [68]

Much of these experiments were conducted with glass with or without chromium oxide coating as a slider and different elastomers. The transfer film is treated as an elastomeric sheet which undergoes shearing. Greensmith and Thomas [21, 22] have obtained results for the tearing of elastomeric sheets without any negative slope to the curves. Under a tensile state of stress at the crack tip, experiments show the reappearance of steady tearing in regions of positive slope below and above the stick slip regions. However, under shearing state at the crack tip, the same material had a non-vanishing stick-slip behavior at the higher tear rates or lower temperatures.

Because of the complexity of physics involved in elastomeric frictions, a number of friction models have been attempted. The most comprehensive theoretical effort in this regard has been by Leonov and Chernyak [23]. Their approach treats the adhesion between elastomer and the sliding surface as a statistical Markov-chain process with viscoelasticity of the polymer. The model successfully describes an 'S'-shaped dependence of sliding force on sliding velocity. The S-shaped curve may or may not have a negative sloping branch depending on a parameter related to the time scale of Brownian motion of the polymer chains. On the other hand, Ettles et al [24], suggest an experimental curve-fit model that describes tire-friction on specific heat, asperity size, hardness and asperity density. The model describes coefficient of friction as a power-law function of the above mentioned variables as:

$$\mu = \frac{2.06}{S^{0.1}} \frac{T_d}{P} \left(\frac{k\rho c}{BV} \right)^{0.5} \qquad 2.6$$

where, S = non dimensional sliding distance,

T_d = decomposition temperature with respect to the ambient

P = Mean interface contact pressure

V = sliding velocity

B = Contact length or diameter of a local contact

k= thermal conductivity

ρ = density

c = heat capacity.

2.3.1 Types of Contacts

As discussed in previous sections, the nature of friction and wear in general is strongly dependant on the contact mechanics between the asperities on the road surface and the tire surface itself. The nature of the road surface varies with season and the surface characteristics can change tremendously from winter to summer (figures 2.8 and 2.9). Surface variation can be characterized by treating the variation in heights of the surface asperities as a Gaussian distribution with a given mean and standard deviation. Surface models based on this statistical concept are presented in Appendix A.

The simplest geometrical idealization of two surfaces in contact, are the so-called 'conformal contacts'. A contact is said to be conforming if the potential contact surfaces of two bodies 'fit' exactly in an unloaded state. In such conditions, the apparent area of contact is independent of the load. For this reason, the load history for this type of contact problems is not important. In the situation where, the potential contact areas of the two bodies have different profiles, the problem typically is known as nonconforming contact. Here, the size of the initial contact area changes once the bodies are subjected to an external load. This class of contact problems is dependent on initial profiles,

properties of materials, rate of applied load, direction of load, contact characteristics, and methods of support etc. These interacting factors make this type of contact behavior complicated. Thus a successful theory would predict the evolution of contact area with increasing or decreasing load, and the magnitude and distribution of surface tractions, normal as well as tangential, transmitted across the interface. Finally it should have mechanism to incorporate a transition from the contact behavior to global deformation field. The early contact-mechanical research further simplified the models by neglecting the friction involved.

2.3.1.1 Frictionless Contact

Few real life situations such as well-lubricated, smooth and continuous machine parts may be modeled as frictionless contact. In a frictionless situation, contacting bodies possess the ability to slide over each other without any resistance along the tangential direction (parallel to the contact interface). Under the application of external load, only normal compressive stress is developed at the interface. Transfer of the normal compressive stress through the contact interface, in this case maintains the system equilibrium. At the same time, the strain energy is balanced by deformation process undergone everywhere on the bodies without incurring any geometric incompatibility. Thus, bodies can separate but any interpenetration is forbidden. In the absence of friction, traction continuity is trivially preserved within the contact region. Such a contact problem is therefore linear and independent of loading history.

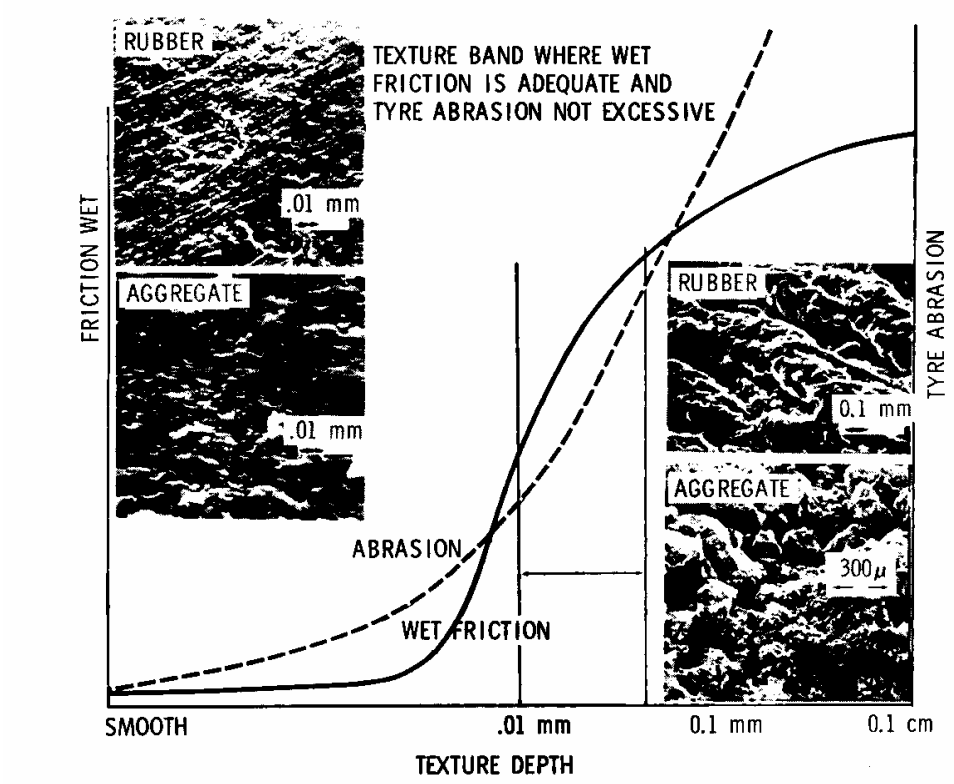

FIGURE 2.7: The increase in wet friction and tire abrasion with increase in road surface microstructure. From Bond [69]

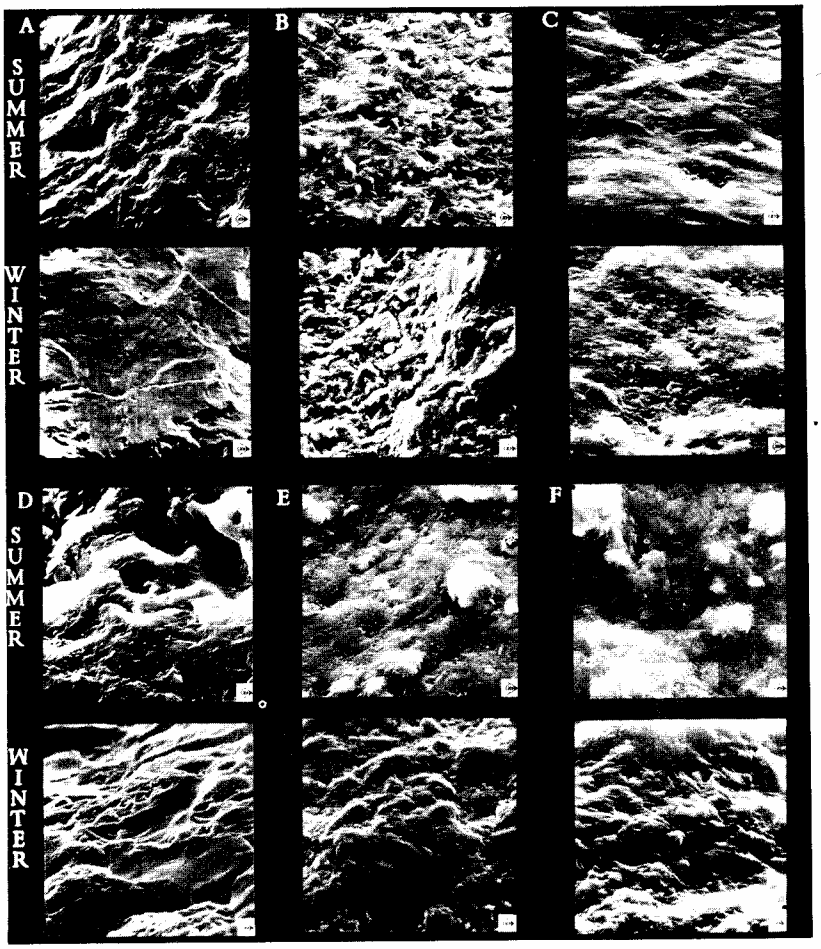

FIGURE 2.8: The annual evolution of road surface microtexture morphologies from tire wear test circuit. From Bond [69]

The problem of frictionless indentation of an elastic half-space by a rigid axisymmetric frictionless punch (see Figure 2.10), has mixed boundary conditions (includes both stresses and displacements) as follows:

$$u_z(\rho,0) = \delta - f(\rho), \quad 0 \le \rho \le 1, \tag{2.6}$$

$$\sigma_z(\rho,0) = 0, \quad \rho > 1, \tag{2.7}$$

$$\tau_{rz}(\rho,0) = 0, \tag{2.8}$$

where δ is the penetration depth of the punch, a is the radius of contact, $\rho = r/a$, *and* $z = f(\rho)$ is its shape function (with $f(0) = 0$), which must conform with the surface of the half-space inside the contact area. Furthermore, all stresses must approach zero at infinity. Note that the function of f depends on a for a given shape of punch.

The first solution of such a problem is due to Hertz [26], for the case of contact of a sphere on a plane. Hertz assumed a hemispherical pressure distribution in the contact area, and showed that it provides a complete solution to the problem. Boussinesq [27] pointed out that, except for the case of a flat punch, the radius of contact a is generally unknown beforehand, and that is calculation needs the introduction of a supplementary hypotheses: that the normal stress falls to zero at the edge of the contact. This condition leads to tangential contact between the punch and the elastic half-space, and determines the penetration c of the punch. Boussinesq pointed out further that a difference in the penetration depth corresponds to the superposition of a rigid-body displacement $\delta_0 - \delta$ of the punch, which gives rise to the singular stresses and to the discontinuities of displacements characteristic of a flat punch. Compressive singular stresses must be ruled out, for they lead to negative discontinuities of displacements and thus to an

interpenetration of the solids. On the other hand, the tensile singular stresses seemed also to be impossible, unless the solids are capable of adhesion. So, the necessity of cancellation of stresses on the edge of a rounded punch seemed well established for about a century.

Hertz's theory can be explained by considering two non-conforming surfaces with radius R1 and R2 and brought into contact over an infinitesimal contact area. Under the application of normal load P (per unit length), the contact pressure developed over a half-width a << R1, R2; is given as a distribution t(x), where:

$$t(x) = \frac{2P}{\pi a}\left(1 - \frac{x^2}{a^2}\right)^{\frac{1}{2}} \qquad 2.9$$

The radius a is related to the applied load by the relationship:

$$a = \left(\frac{4PR^*}{\pi E^*}\right)^{\frac{1}{2}} \qquad 2.10$$

This distribution has a maximum given by:

$$t_{\max} = \left(\frac{PE^*}{\pi R^*}\right)^{\frac{1}{2}} \qquad 2.11$$

Where the constants E* and R* are defined as follows where 1 and 2 denote the individual contacting cylinders, n is the Poisson's ratio and R is the radius of the two contacting cylinders.

$$\frac{1}{E^*} = \frac{1-\nu_1^2}{E_1} + \frac{1-\nu_2^2}{E_2} \qquad 2.12$$

$$\frac{1}{R^*} = \frac{1}{R_1} + \frac{1}{R_2} \qquad 2.13$$

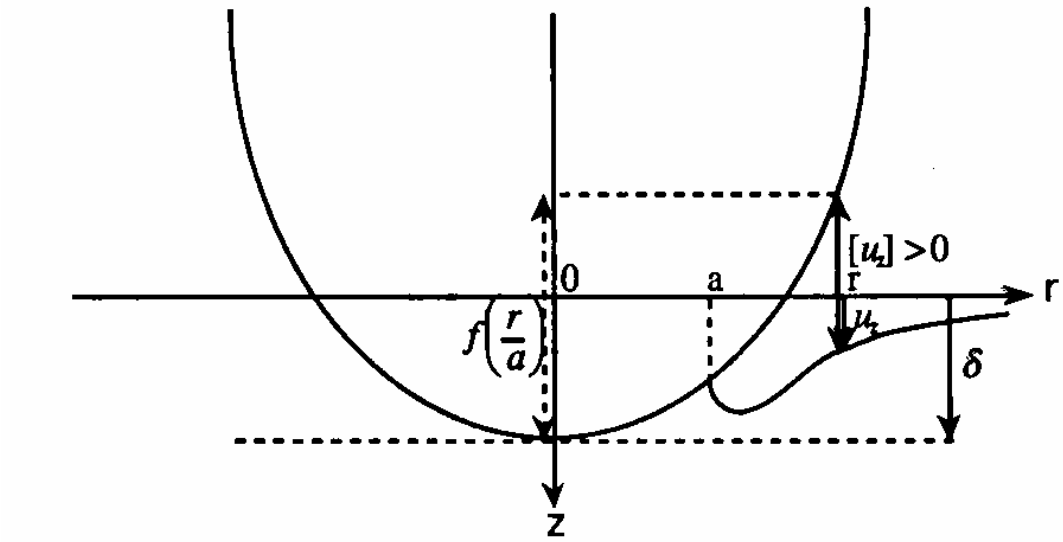

FIGURE 2.9: Displacement field under the indentation of an elliptical punch. From Maguis [63]

It is evident that this theory is only applicable when the contacting surfaces are smooth i.e., frictionless and continuous, the bodies are homogeneous, isotropic and obey linear elastic theory. Also, it is assumed that the dimensions of the contact area must be small compared with the dimensions of each body i.e., a<< R1, R2. Another significant assumption in this analysis is that the contact stress and strain fields can be predicted by elastic Boussinesq half-space theory [27].

Investigations in 1960s first indicated the existence of adherence force. Bradley [28] and Deryagin [29] showed that the adherence force between a rigid sphere and a rigid plane should be equal to $2\pi wR$. It became particularly evident that, for soft elastic solids such as rubber, the area of contact could be larger than in the Hertz theory and that an adherence force could be measured. By a balance of elastic, potential and surface energies, Johnson, Kendall and Roberts [30, 31], in the JKR theory, resolved the paradox. In the presence of surface energy, the area of contact is larger than in the Hertz theory, sustains infinite stresses on its periphery, and remains finite under negative loads until a critical traction force $F=(3/2)\pi wR$ is reached at which the surfaces separate abruptly; furthermore, the connection to the surface is normal rather than tangential. Kendall [32,.33] applied the same method to the adherence of a flat punch, and showed that the geometry was similar to that of a solid with a deep external circular crack. The reason why rough surfaces may have negligible adherence, although individual spheres adhere, was explained by Johnson [34] and, Fuller and Tabor [35]. Figure 2.11 shows the comparison between a Hertzian contact (w=0) and a JKR contact ($w\neq0$) under the same applied load P. During contact, while some asperities (the highest) are compressed, while others are stretched. Assuming the same radius of curvature *R* for all asperities and

a Gaussian distribution of heights with a standard deviation σ, Fuller and Tabor introduced an adhesion index θ, which is the ratio of the adherence of a sphere to the force needed to push this sphere at a depth σ into the solid. For rough solids of high modulus, adherence can disappear.

Maugis et al. [36], showed that the JKR theory was consistent with linear elastic fracture mechanics if the edge of the contact area is treated as a crack in mode I that recedes or advances as the area of contact *A* increases or decreases. In this case the equilibrium point defined by $G = w$ and its stability by $(\partial G/\partial A) > 0$. The adherence force is the limit of stability of the system and depends on the stiffness of the measuring apparatus. Its value is $F= (3/2)\pi wR$ at fixed load, but $F=(5/6)\pi wR$ at fixed displacement with a smaller area of contact. (Later they showed that the kinetics of crack propagation was in complete agreement with the expression of *G* deduced from the JKR theory.) The equilibrium condition $G = w$ corresponds to the supplementary hypothesis discussed by Boussinesq, and enables determination of the punch displacement (∂). For $w = 0$, the JKR theory reduces to that of Hertz. However, this adherence force, being independent of Young's modulus, was incompatible with the adherence force $2\pi wR$ computed by Bradley and Derjaguin for a rigid sphere on a rigid plane. In 1975, Derjaguin, Muller and Toporov [37] presented a completely different theory, the DMT theory, in which molecular forces act in a ring-shaped zone around the contact but are assumed unable to change their profile, which remains Hertzian (Young's modulus not too small). By a "thermodynamic approach" they found that the attractive force is $2\pi wR$ at the point of contact but decreases rapidly to πwR when the approach increases. In this theory there is

no stress singularity at the edge, the air gap closes smoothly, and separation occurs when the contact is reduced to a point (thus without stability) under an adherence force $F = 2\pi wR$. Muller et al. [39] improved upon this theory in a self-consistent numerical calculation using a Lennard-Jones potential. This allowed the inclusion of the effect of adhesion forces on Hertzian process. The result was a continuous transition from the DMT to the JKR theory when a single parameter μ, proportional to the parameter introduced earlier by Tabor, increases. The DMT theory applies for $\mu << 1$ (hard solids, small radius of curvature and low energy of adhesion), and that of JKR for $\mu >> 1$ (soft solids, large radius, large energy of adhesion). As shown later [40], these two extreme theories do not depend on the exact form of the interaction potential between surfaces.

Barquins and Maugis [41], using the Sneddon [42] theory of the contact of axisymmetric punches in which an arbitrary rigid-body displacement $_X(1)$ is cancelled such as to have zero stress at the edge of the contact, showed that if $_X(1) \neq 0$ the stress singularities and discontinuity of displacement that appear are those of fracture mechanics, with a stress intensity factor K_1 proportional to $_X(1)$. Using the LEFM relation between G and K_1^2, the JKR results are immediately obtained. However, this relationship is valid only for linear fracture mechanics when the interaction zone, characterized by the radius of contact is small. By applying a Dugdale model, where interaction forces are assumed constant on an annulus of width *d* around the contact [43], the JKR-DMT transition is accomplished.

It should be noted that much of these theoretical developments are from frictionless elastic contact with adhesion. Although adhesion plays important role in friction itself, a truly generalized frictional elastic contact is not yet analytically resolved at the level of

asperity. The relationship between the tangential and normal components of forces imposes the nonlinear behavior between the sliding movement of the forces imposes the nonlinear behavior between the sliding movement of the contact surfaces and the external load. In a frictional condition the contact conditions are either stick (no relative tangential displacement) or slip (i.e. sliding against resistance in the tangential direction). Figure 2.12 shows the change in area of contact between a glass sphere and a smooth surface of natural rubber under the same normal load during the preliminary phase of motion as well the static initial contact area. The diagram clearly identifies the adhesion and the slip zone. Figure 2.11 shows the corresponding changes in tangential force with time and indicates slip zone as part of the contact area.

As expected, the tangential force is significantly affected by the time relaxation. The complex interaction between the contact mechanical and frictional behavior is further illustrated from discussion in section 2.2.

2.4.1 Tear Behavior in Elastomers: Initiation

Gent [6] proposed a crack initiation mechanism in rubber in which initiation of surface cracks is attributed to the unbounded elastic expansion of microscopic precursor voids until they burst open as cracks on the surface under the internal pressure or triaxial tension in the rubber sample. Non-homogeneity resulting from non-uniform cure conditions at the molecular level or from the random nature of vulcanization and polymerization reactions may be the source of flaw generation. This heterogeneity can be considered as a region in the specimen with a lower modulus than surrounding material. When the specimen is subjected to a tensile stress, an ellipsoidal crack may be generated in the soft region due to the hydrostatic tensile component of the stress.

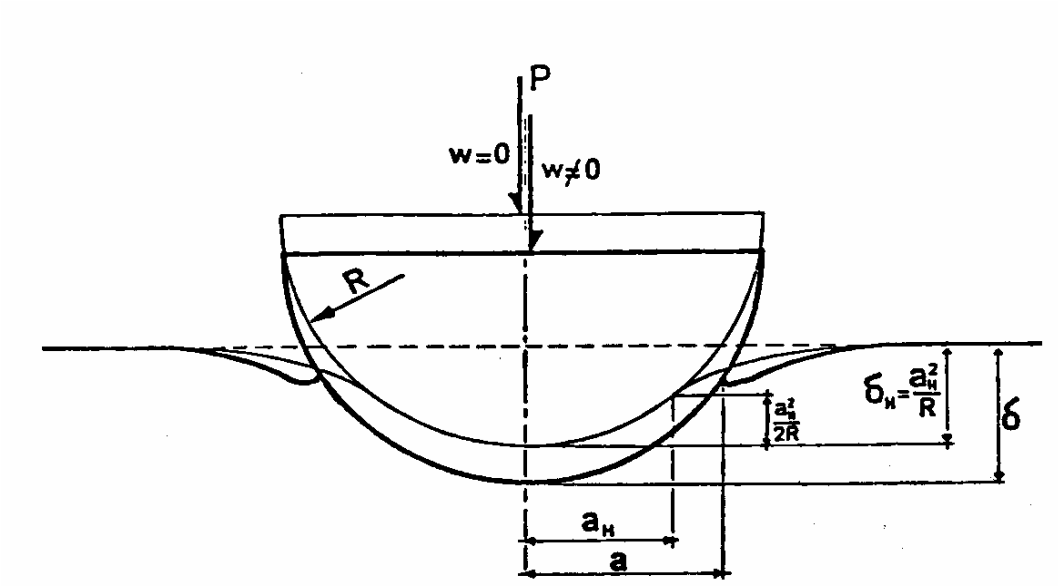

FIGURE 2.10: Hertzian (w=0) and JKR contact (w≠0) under identical normal load P. From Maguis [63].

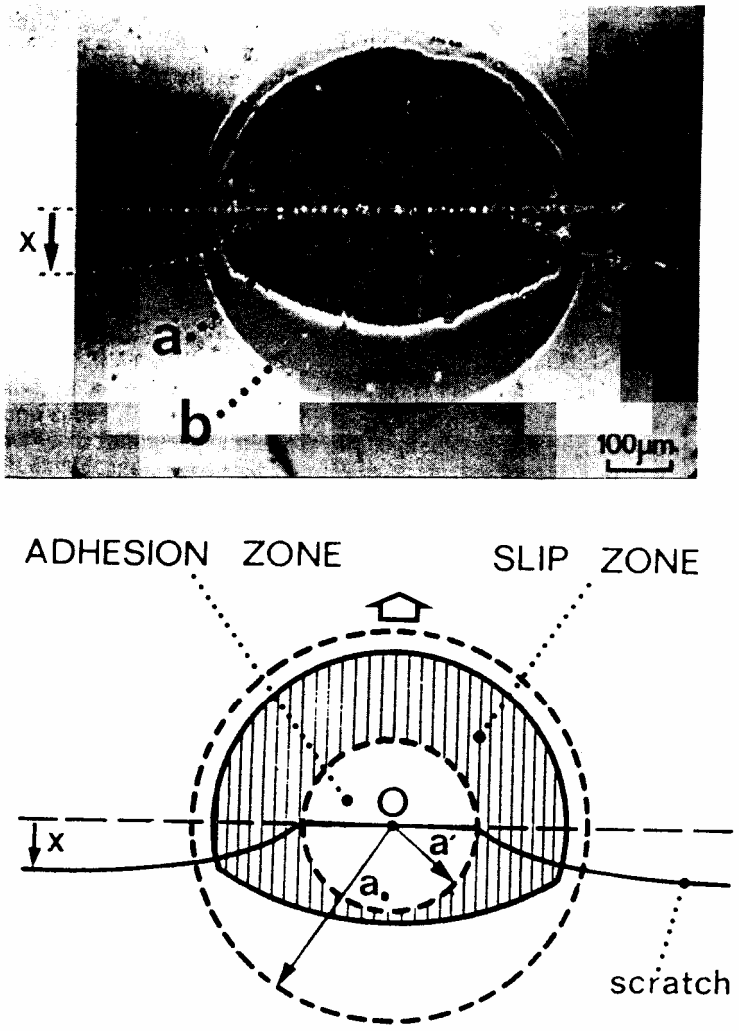

FIGURE 2.11: Contact area between a glass sphere and a smooth surface of natural rubber under the same normal load. Top: superimposed views of (a) During preliminary phase of friction (b) static initial contact area. Bottom: Schematic showing the adhesion and micro-slip zone . From Barquins [68]

Schallamach [1] attributed the initiation of some lateral micro-cracks, perpendicular to the direction of sliding, to the tensile tearing of rubber surfaces. This tearing process results from stress concentrations at the rear of contact area between moving asperities and the surface. He related this tear mechanism to both tensile strength and stiffness of rubber at very high strains.

Therefore, crack initiation can be considered as an important mechanism accounting for the rate of rubber wear. However, close examination of virgin rubber surfaces reveals existence of some flaws on the surface prior to any loading. Presence of these cracks can promote the process of rubber wear by eliminating part of the initiation step. Elastomers have ability to undergo large deformations which changes the nature of stress distribution around the crack as compared to the brittle materials. Viscous dissipation and other viscoelastic phenomena also are exhibited in rubber. Similarly, cavitation has been observed ahead of the crack leading to reduction in stored energy in this region [6, 44]. All these effects render the classical Griffith theory used for brittle materials inapplicable. The energy release rate during crack propagation in elastomers is linked to the change in total stored elastic energy and represents the fracture toughness of the material. The tear energy of the elastomer is thus defined as [50]:

$$T = -\frac{dU}{dA} \qquad 2.14$$

where "U" is the total elastic strain energy stored in the sample, and "A" is the area of one crack surface in an unstrained condition. "T" includes not only the surface energy (as in Griffith's theory) but also the viscous dissipation. Tear energy, by its dependency on viscoelasticity of elastomers, is also a function of temperature and the rate of tearing [3].

The standard experimental tests for the measurement of tear energy include the trouser test, the pure shear test and the simple tension test. The expressions for tear energy for each of the tests with standard specimen geometry are as follows [9] :

Trouser Test: $$T = \frac{2F}{t} \quad (2.15)$$

Pure Shear Test: $$T = Wh \quad (2.16)$$

Simple Tension Test: $$T = 2kWC \quad (2.17)$$

where "F" is the applied force, "t" is thickness of the sample, "W" is the strain energy density, "h" is height of the sample in the pure shear test, "k" is a constant, and "C" is the crack length. The strain energy density is typically measured as the area under the stress-strain curve for a certain strain level. The variation in sample geometry or loading corresponding to the type of the test measuring tear energy is not found to have significant effect on the value of the tear energy obtained. This is found particularly true for completely crosslinked elastomers. Thus the tearing energy is considered as a material property. Experimentally, it is found that the radius of curvature of the crack-tip influences the tearing energy [46].

Higher temperatures and lower tearing rates are associated with less internal dissipation and reduce the magnitude of tear energy for crack propagation. Figure 2.13 [48] shows the dependency of tear energy on the tearing rate for three elastomers. Since the crack propagation is a strong function of the elastomer viscoelasticity, the temperature dependence of tearing energy of at different temperatures is related through the famous time temperature superposition applicable to the viscoelastic materials. This is expressed through the Williams-Landel-Ferry (WLF) equation [47] as:

$$\log a_T = \frac{-C_1 (T - T_g)}{(C_2 + T - T_g)} \qquad 2.18$$

where "a_T" is a temperature function showing dependency of the mobility of polymeric segments on temperature, and T_g is the glass transition temperature of each elastomer. The universal values of C_1 and C_2 are 17.4 and 51.6 respectively. Different elastomers have the same tear energy if these constants are scaled by the molecular segmental mobility for that temperature [3]. A so-called master-curve [48] for four common elastomers at $T_s = T_g$+20 °C as shown in Figure 2.13. Studies of the morphology of the ruptured surfaces in elastomers clearly show that the process is dependant on the velocity. At higher crack velocities or strain rates, torn surfaces exhibit increasing smoothness. This has been attributed to the glassy fracture of elastomers and corresponds to the discontinuity in the T-r curve in Figure 2.14 On the other hand, at lower strain rates the surface roughness has been related to tensile rupture of fiber tips [46]. Cavitation in the 'rubbery' zone ahead of crack at lower strain rates has also been cited as a cause of the roughness of the fractured surface [49].

2.4.2 Effect of Material Properties

The subject of strength and extensibility of rubber vulcanizates has been studied by Smith [46]. Viscoelastic characteristics of rubber become important under high strain rate and temperature conditions in the vicinity of the crack tip. These local conditions are usually different from the macroscopic conditions applied to the specimen in an experimental setup.

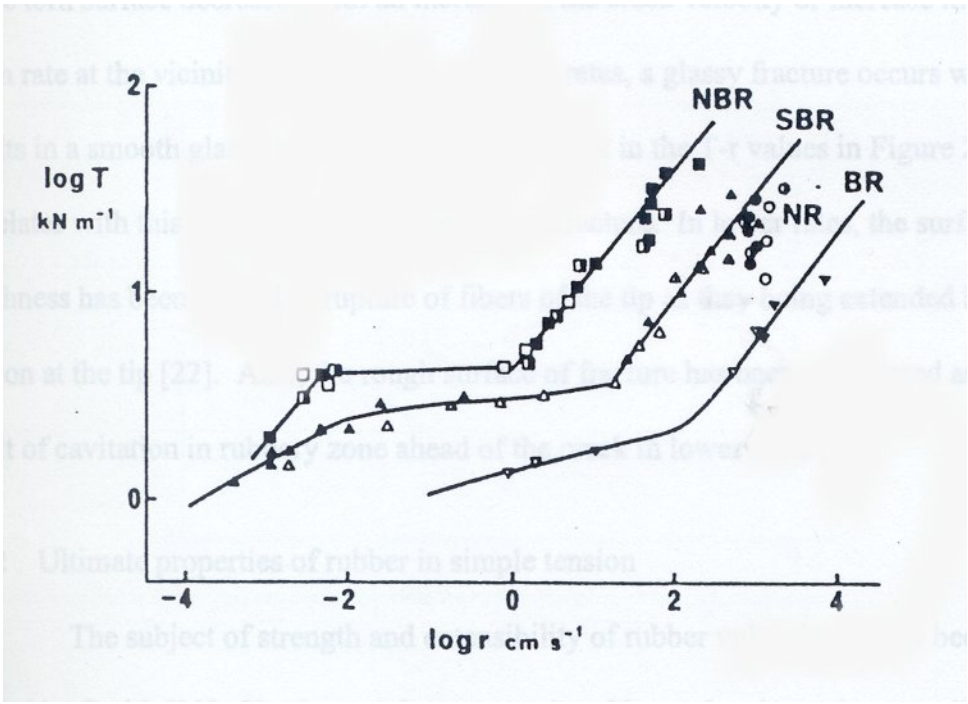

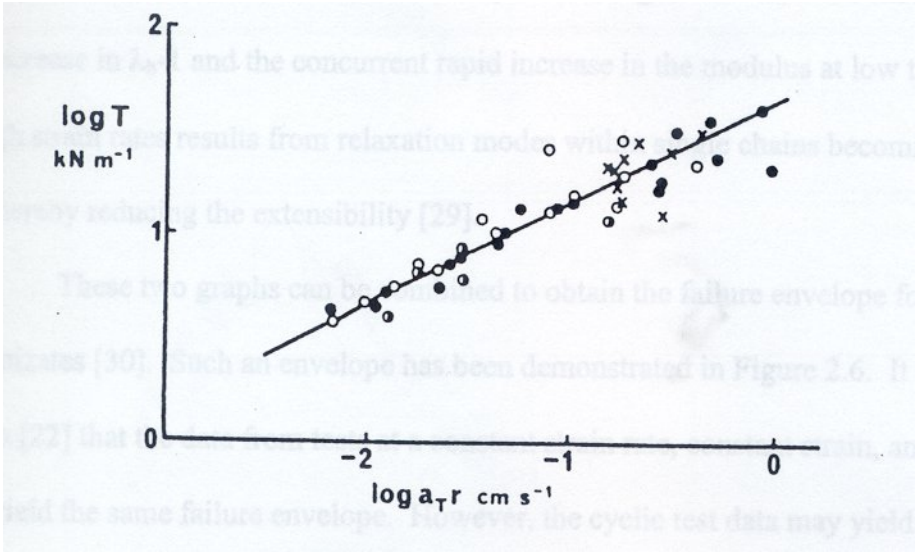

FIGURE 2.12: Tear energy NBR ■, SBR ▲, NR ●, and BR▼. TOP as function of rate of crack growth, BOTTOM Mastercurve . From Kadir [48]

Therefore, the process that controls the rupture occurs on a time scale different from that for the macroscopic viscoelastic response. Smith measured the ultimate failure properties (stress at break, σ_b, and elongation at break, λ_b) for unfilled SBR vulcanizates [49]. Figure 2.14 shows the dependencies of these properties on the strain rate at reference temperature of Ts=263 °K. The WLF relation has been applied for time-temperature reduction in these graphs. The curves show $\sigma_b 263/T$ and λ_b-1 as a function of the reduced strain rate $\dot{\varepsilon} a_T$. In the composite graphs of Figure 2.14, when the experimental time scale is less than the longest relaxation time of single network chains, the extensibility of network is reduced because the chains can not attain a highly extended configuration prior to specimen rupture, owing to their reduced mobility. Thus the decrease in λ_b-1 and the concurrent rapid increase in the modulus at low temperatures or high strain rates are a result of reduced extensibility. This is because the relaxation modes within single chain become effective at low temperatures [51].

These two graphs can be combined to obtain the failure envelope for SBR vulcanizates [52]. It has been shown [46] that the data from tests at a constant strain rate, constant strain, and constant load yield the same failure envelope. However, changing the loading conditions to a cyclic test may yield an envelope, which is different from the envelope of less complex loading conditions. The extremum point on the envelope defines the maximum observable extension ratio $(\lambda_b)_{max}$. Observations of stress distribution around a crack tip also show some interesting effects attributed to the peculiar nature of rubber. Optical methods used by Andrews [53] showed that the maximum tensile stress along the crack axis follows the classical elasticity solution. Knauss [54] measured deformations around the tip of an edge crack in rubber under

tension by means of imprinted grids. His measurements of stress distribution around a crack-tip show a principal stress along the crack axis that is approximately equivalent to the stress near a hyperbolically notched plate under tension. The classical elastic theory has solution of the form:

$$\sigma_y(x) = \frac{f_1(\varepsilon_\infty)\sigma_\infty}{\left[x/b + (\xi/2)\right]^{1/2}} \qquad 2.19$$

where "x" is the distance along the crack axis, "σ_∞"is the far-field tensile stress, "b" is half width of the test specimen. (ξ/2) is "quasi-radius of curvature" and a strain dependent quantity ($f_2(\varepsilon_\infty)$). As seen, the radius of curvature or the extent of crack tip opening determines the size of crack tip principal stress, which is responsible for growth of the crack. In a load-controlled experiment, this factor depends on the stretchability of elastomer and its elastic properties.

2.4.3 Fatigue Crack Propagation (F.C.P)

Once crack propagation is initiated from an existing flaw or defect, it is propagated by stretching the rubber sample. Experimental observations attribute a large part of rubber wear to fatigue crack propagation of cracks on the surface [55]. For instance, wear of a rubber sample in a wheel test may be as a result of cumulative growth of cracks by tearing under repetitive loading, as in mechanical fatigue processes [3]. Critical tear energy, "T_c", has been defined for rubber under monotonic extension after which the crack will propagate catastrophically. In the monotonic loading, the crack will not propagate before reaching this energy limit. However, if the rubber is exposed to a cyclic loading condition, the crack is able to propagate even by tear energies less than "T_c"[56]. Rate of crack propagation is a function of the tear energy:

$$\frac{dc}{dn} = f(T) \qquad \text{..2.20}$$

where "c" is the initial crack length and “n” is the number of cycles.

In the case of cyclic loading, if the tear energy is less than the threshold tear energy 'T_o", rate of crack propagation ceases to be a function of "T", and is related to the chemical degradation of rubber by ozone attack [57]. In Figure 2.16, propagation rate or dc/dn is plotted against tear energy, "T", on a logarithmic scale. Four distinguished zones in these plots are as following [58]:

$$\frac{dc}{dn} = r_o \qquad T \le T_o \qquad 2.21$$

$$\frac{dc}{dn} = A(T - T_o) + r_o \qquad T_o \le T \le T_t \qquad 2.22$$

$$\frac{dc}{dn} = BT^m \qquad T_t \le T \le T_c \qquad 2.23$$

$$\frac{dc}{dn} = \infty \qquad T = T_c \qquad 2.24$$

where "r_o", "A", "B", and “m” are constants, depending on type of rubber, and "T_t" is the tear energy before which the plot is linear. The value of m is generally 2 for most of natural rubber compounds and 4 for non-crystallizing elastomer compounds. There exists a strain limit "e_o" correlated to "T_o" below which mechanical crack propagation will not occur, although propagation due to chemical effects may occur [58]. This strain limit is called mechanical fatigue limit. Young [59] has investigated effects of temperature, strain level, strain rate, and oxidation on fatigue curves for some rubber compounds.

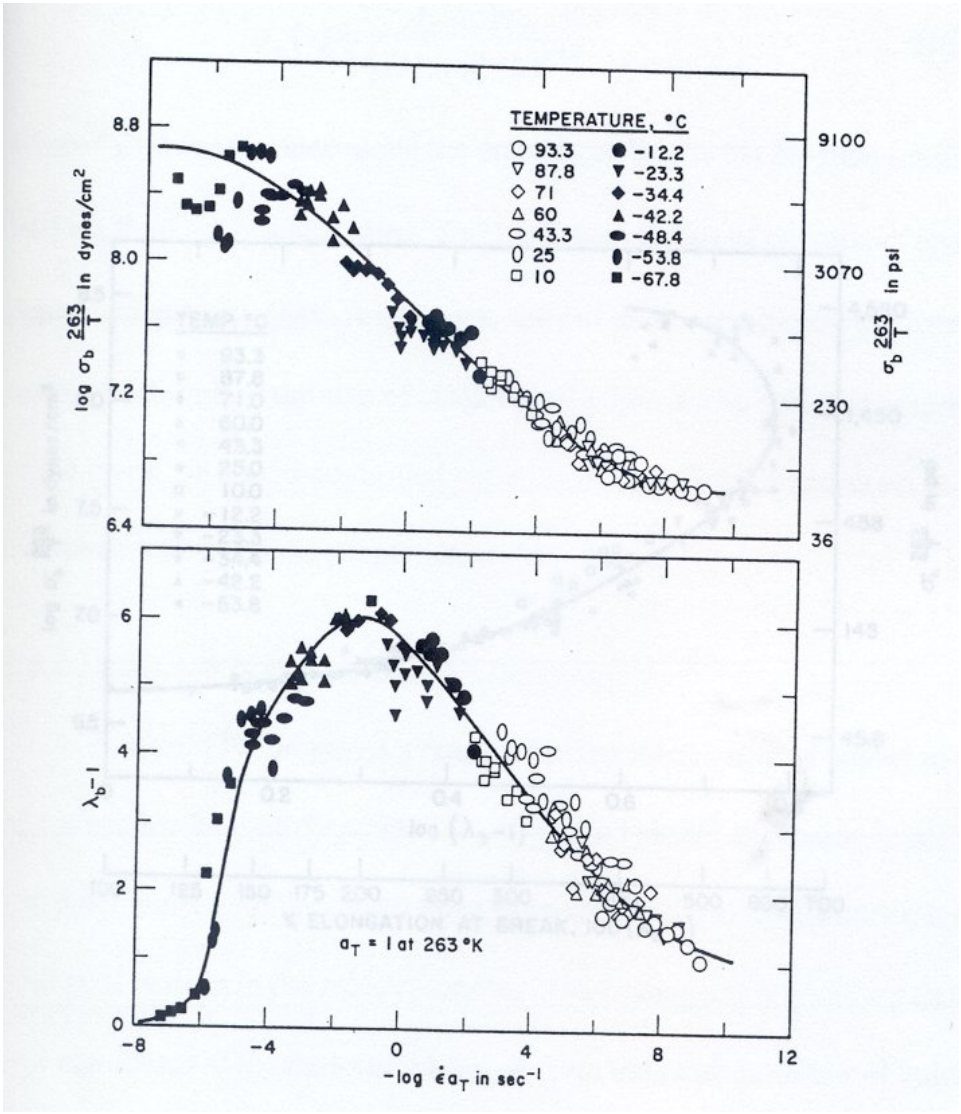

FIGURE 2.13: Composite curved formed by superposition of ultimate properties for SBR Top: Stress at break, Bottom: Stretch at break. From Smith [49].

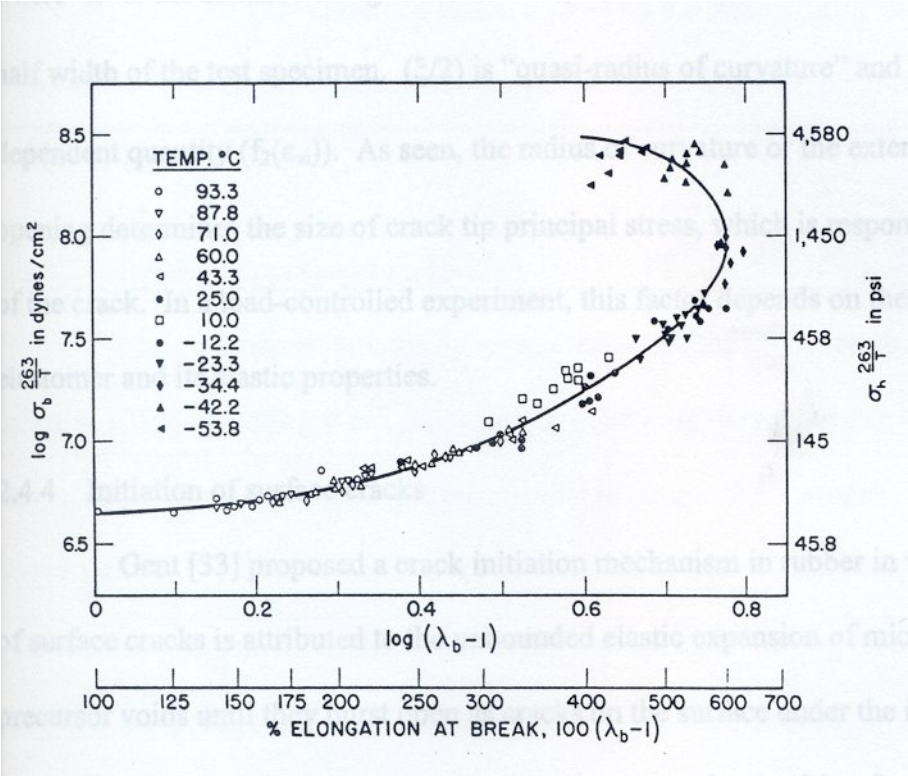

FIGURE 2.14: Failure envelope for SBR. From Smith [49]

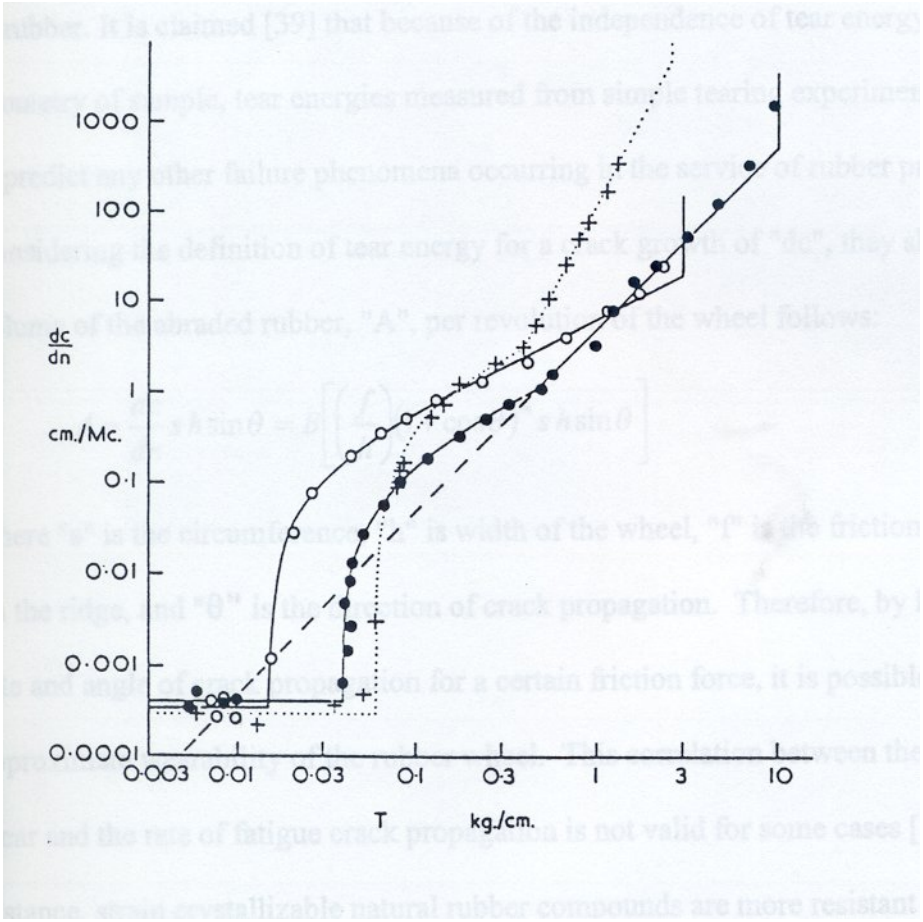

FIGURE 2.15: Rate of fatigue crack propagation versus tear energy for typical rubber vulcanizates From Lake[58].

2.4.4 Step-wise Crack Propagation in Pattern Wear

As it will be explained in the next section, a ridge pattern develops on the surface of rubber, which has been worn uni-directionally, for instance by a blade abrader. In a model proposed by Southern and Thomas [3] for fatigue crack propagation of a ridge, an idealized wear ridge is considered as shown in Figure 2.17. This pattern is assumed to be uniform on a rubber surface. It is claimed [60] that because of the independence of tear energy to the geometry of sample, tear energies measured from simple tearing experiments can be used to predict any other failure phenomena occurring in the service of rubber products.

Considering the definition of tear energy for a crack growth of "dc", they showed that volume of the abraded rubber, "A", per revolution of the wheel follows:

$$A = \frac{dc}{dn} s\,h \sin\theta = B\left[\left(\frac{f}{h}\right)(1+\cos\theta)^m s\,h \sin\theta\right] \qquad 2.25$$

where "s" is the circumference, "h" is width of the wheel, "f" is the friction force applied on the ridge, and "θ" is the direction of crack propagation. Therefore, by knowing the rate and angle of crack propagation for a certain friction force, it is possible to predict the approximate wearability of the rubber wheel. This correlation between the rate of rubber wear and the rate of fatigue crack propagation is not valid for some cases [61]. For instance, strain crystallizable natural rubber compounds are more resistant to fatigue crack propagation than other rubber compounds at high strains, but wear resistance of these compounds is not superior to others at the same conditions. Besides, application of carbon black enhances the wear resistance of filled rubber compounds, whereas these compounds are not much more resistant to crack propagation under intermittent stressing.

Another disagreement appears by changing the test temperature. While fatigue crack propagation is very sensitive to the variation of temperature, the rate of wear does not show much dependency to this variable.

The literature survey outlined in the previous chapter illustrates that wear occurs through rubber particle removal. Both intrinsic and pattern wear happens as particles of various sizes are removed in a stepwise process. This particle removal is a direct result of interaction of the abrasive asperities and rubber morphology at differing scales. A number of experiments in the University of Akron, Tire Lab, have exposed characteristics of the wear process. Section 3.1 describes the experiments. A number of questions related to the wear process are raised from these observations. A proposal to investigate these questions using numerical technique is presented in section 3.2.

2.5.1 Wheel Abrasion Tests

In order to study the evolution of pattern wear at a micro-scale, Gerrard [65] and Pathasarathy [67] used a rubber tire/wheel abrader setup with a concrete surface in a controlled (laboratory) environment. A schematic of a wear machine setup is shown in Figure 2.17. Figure 2.18(A) and (B) show 3x magnification of a rubber surface wear through a period of travel on the concrete surface. Initially, the abrasion is characterized by a uniform, nearly continuous distribution of surface damage (cracks). As the specimen is revolved further on, some of the cracks or surface defects become more pronounced where as the population of cracks at comparatively smaller scales decreases. Thus, the initial, nearly homogeneous distribution of cracks is replaced by more uniformly spaced defects. This is the genesis of pattern wear, and is described by a number of experimental researchers [1,3,9].

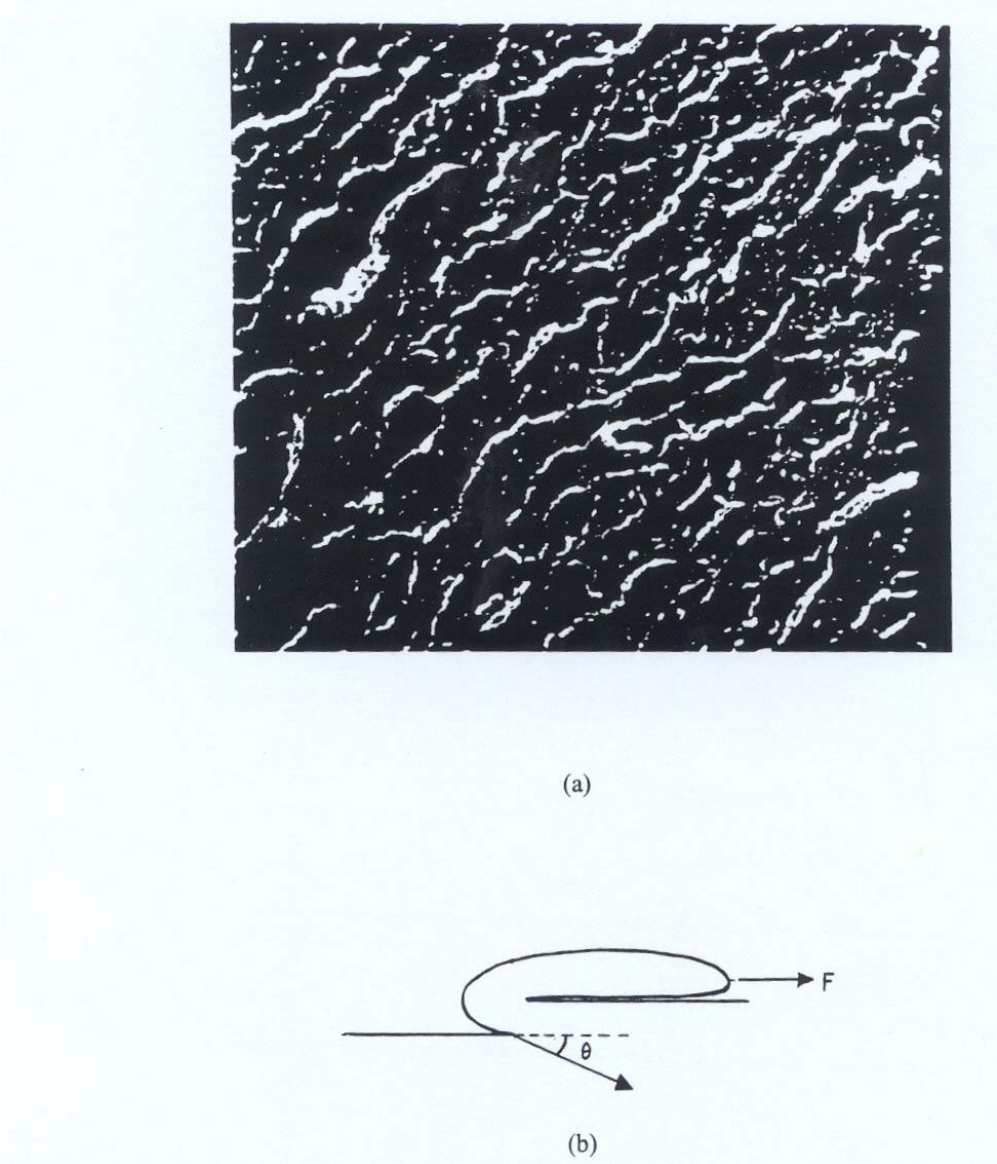

FIGURE 2.16: Pattern wear generated in a laboratory experiment. (a) Magnified view. (b) Schematic profile of a ridge.

Figure 2.19 illustrates this type of progressive wear schematically. This type of wear is characterized by a 'virgin surface' created between any two successive defects. This implies that the particles with effective size up to the largest crack or defect size are removed. In the same time, a few uniformly spaced cracks or defects 'grow' in the plane perpendicular to the direction of travel. The profile of the defects in the plane of contact can be roughly considered to be elliptical. As the length of the travel increases, the number of 'living' cracks per unit length decreases. Schallamach [71] has proposed a linear relationship between the spacing and the wear.

Ultimately, the profile of these few large defects tends to resemble a rubber flap. It should be noted that during the travel, material is constantly removed as the older surface defects disappear. This removal is more of the 'intrinsic wear' in nature (Re: cross section view, Figure 2.19). This process can be viewed as 'succession of defects' at different scales. In this succession it is not known why certain cracks tend to 'grow' whereas some other cracks may cease to grow and eventually disappear due to intrinsic wear. Gerrard [65] speculates a possible mechanism for this kind of pattern wear formation. He proposes that the characteristic spacing between the flaws (cracks) in the direction of the asperity travel may be influenced by the relaxation induced by a crack in the 'wake' of the tensile zone behind a traveling asperity. The leading edge of asperity has a large compressive stress distribution followed by a trailing edge that is a dominantly high shear and tensile stress. This zone is relatively narrow. However, the peculiar tensile stress and shear distribution created in the wake of the traveling asperity may affect an initiator flaw in the region. This mechanism is similar to the transverse ply cracks observed in composite laminates under tension (Fig 2.20).

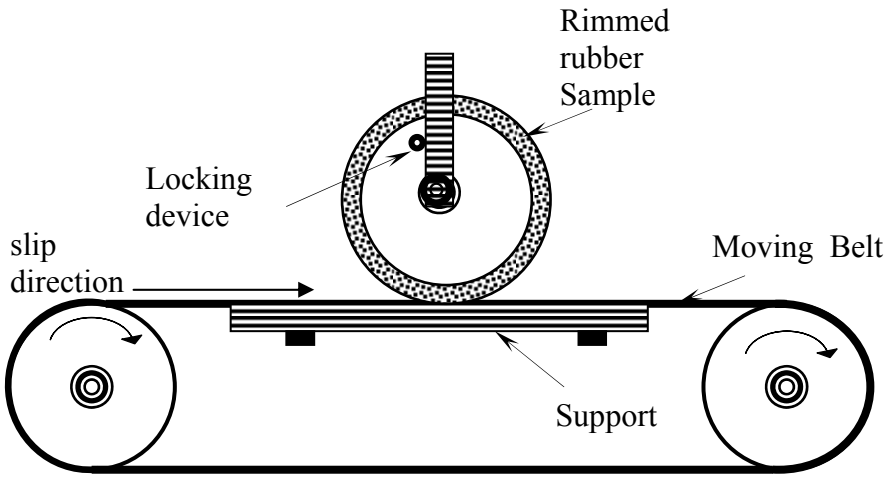

FIGURE 2.17: Gerrard's Wear machine setup. From Quereshi [66].

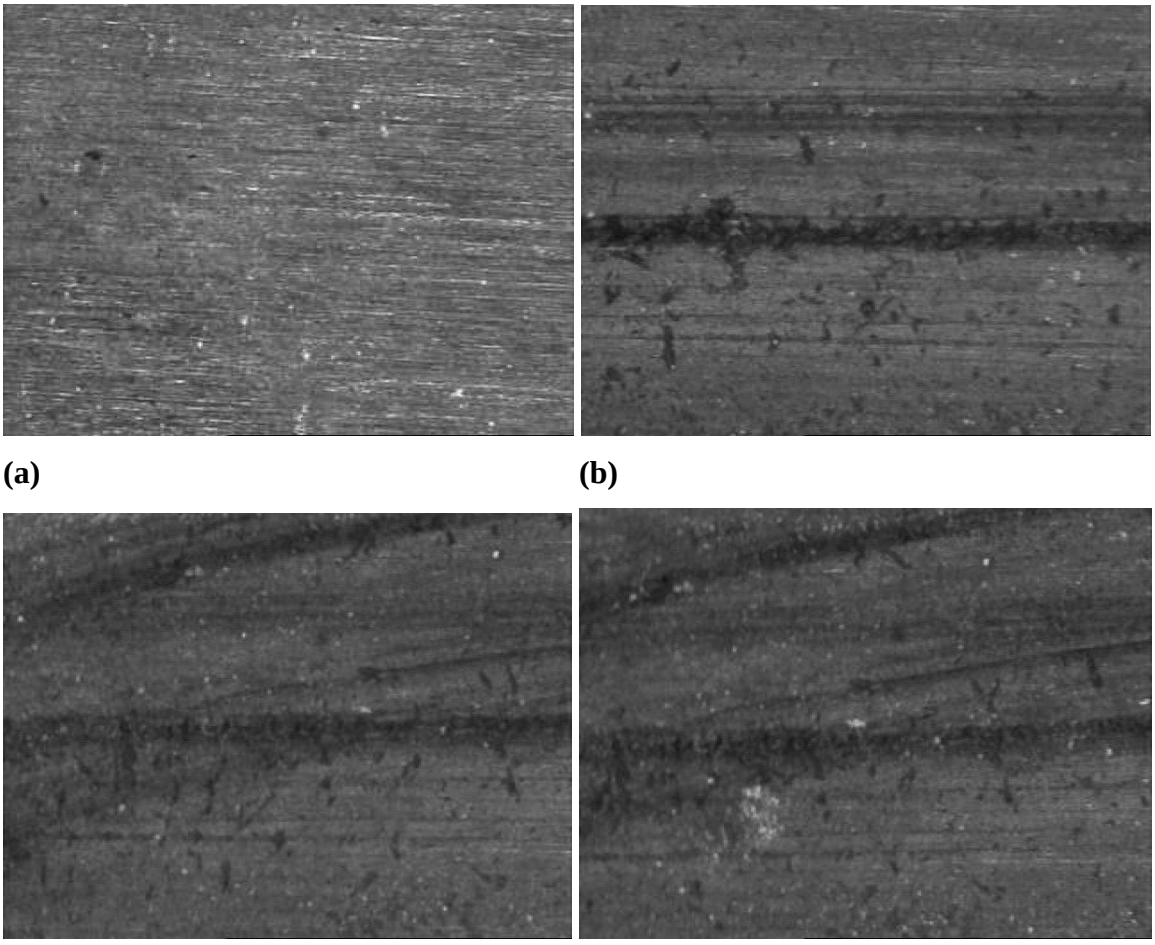

(a) **(b)**

(c) **(d)**

FIGURE 2.18 **:** Progression of pattern wear in experiments.
(a): Virgin Surface **(b):** 10 in **(c):** 15 in **(d):** 20 in
From Parthasarthy [67]

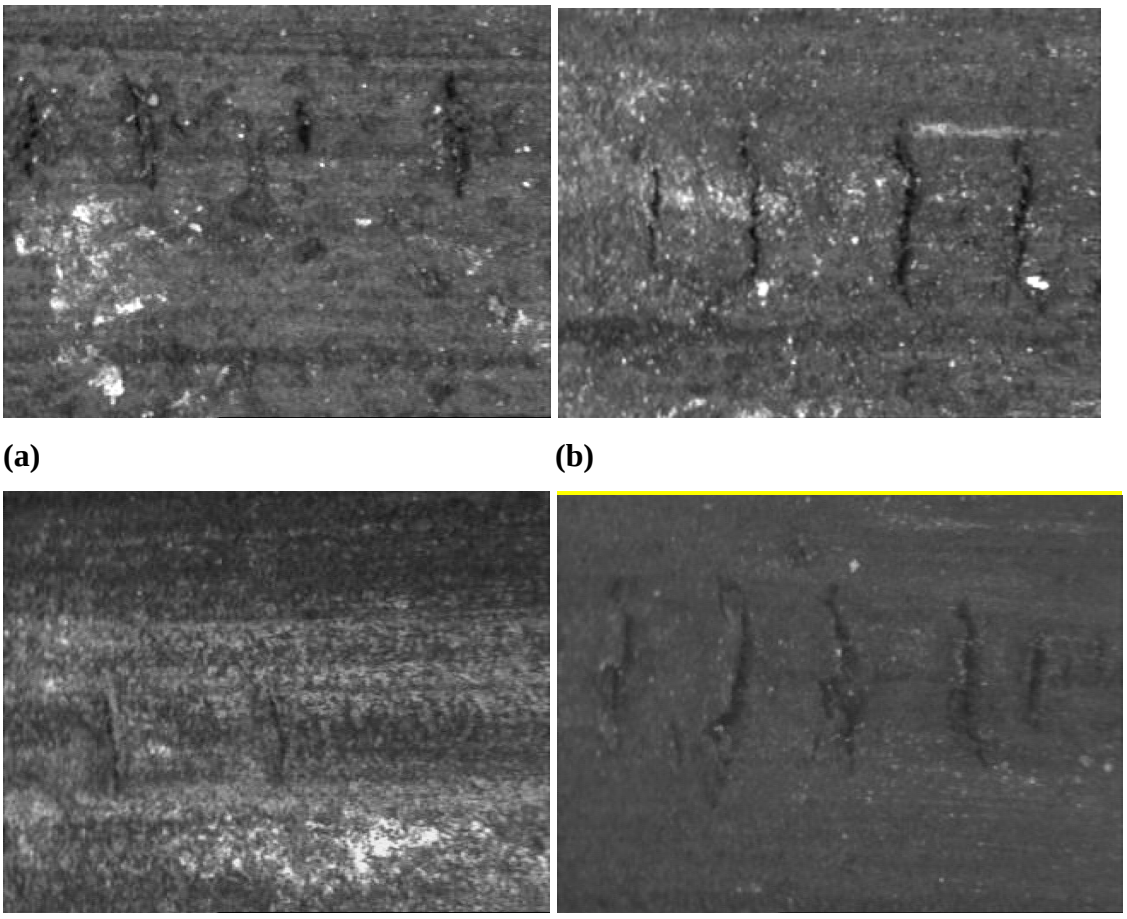

(a) **(b)**

(c) **(d)**

FIGURE 2.18 (B): Progression of pattern wear in experiments.
(a): 25 in **(b):** 30 in **(c):** 35 in **(d):** 40 in
From Parthasarthy [67]

2.5.1.2 Rubber Flap Growth and Wear

Another set of experiments conducted by Gerrard [65] show the mechanism by which an individual rubber flap may evolve during a typical surface abrasion process. This is when a rubber 'flap' is formed at a specific defect site. Typically, the flap formation is on a larger geometric scale (size) and occurs in less frequency than the smaller but more numerous cracks.

The flap may roll up under certain contact situations with the asperity. Excessive roll up may lead to further initiation of a crack at the bifurcation point of the flap. This crack initiation increases the size of the flap which in turn may lead to further roll up. In the contact situations where the further roll up creates strain on the flap-tip, the cycle perpetuates creating a larger flap. This type of damage is long term and relates to significant amount of material removal. Figure 2.21 shows the stages in evolution of the flap when a moving asperity comes in contact with it [65].

The above experimental observations were made under a wide variety of slip conditions. Also, hierarchical wear morphologies are observed along the entire flap length. These morphologies are in the form of smaller cracks and may result in particle removal at smaller scale.

These scale-up experiments are also relevant in detail to the deformation of a rubber 'nodule'. Shiratori et al [70] report FEA analysis of a cylinder with an elliptical crack, where loading change from parallel to the crack front to the transverse. Also, Schallamach [71], has observed a decrease in the wear rate with changing slip directions, experimentally.

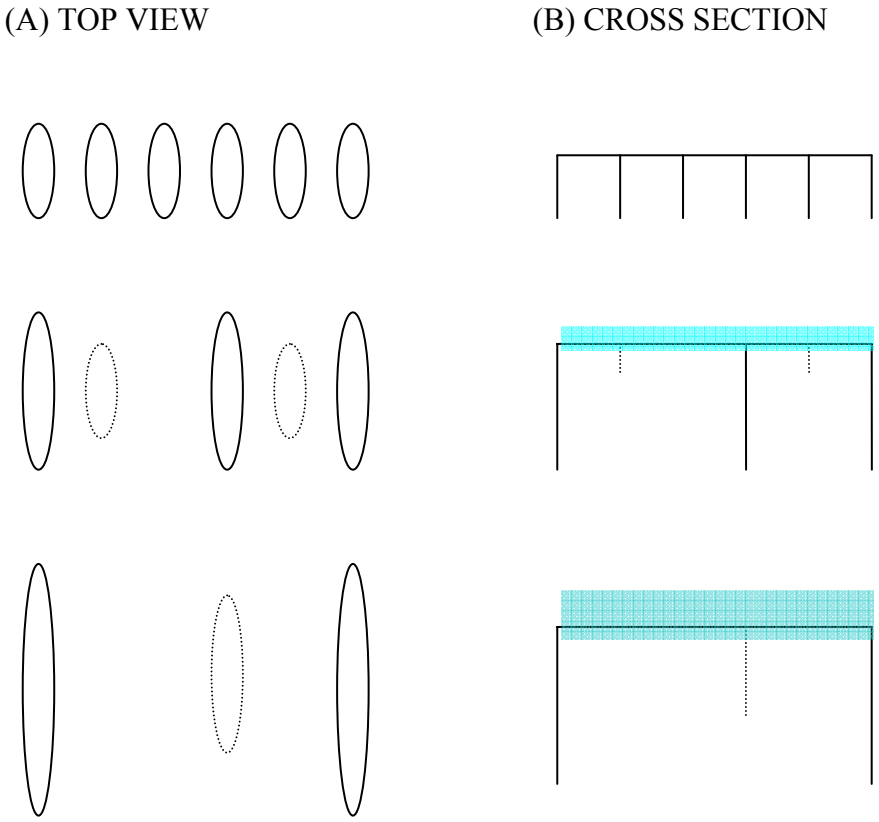

FIGURE 2.19: Defect (crack) population (A) Top view and (B) Cross sectional view. Dotted lines indicate 'dying' cracks whereas solid lines indicate 'living' cracks. The shaded area in cross sectional view indicates material removed by intrinsic wear.

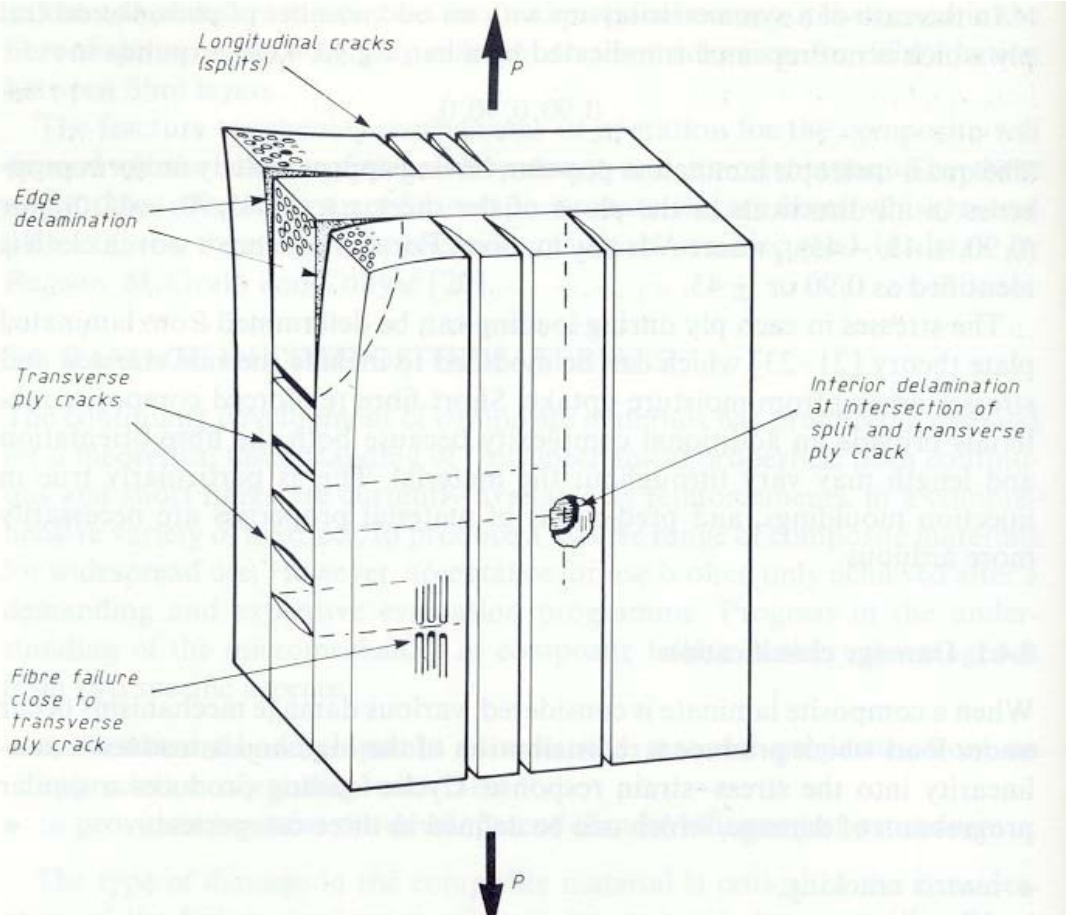

FIGURE 2.20: Longitudinal and transverse cracks in a fiber composite under tensile loading.

2.5.1.3 Morphological Studies and Particle Size

The wear studies in previous two sections are at macroscopic scale. Several experiments conducted at the University of Akron [8,67], wear lab have observed that typically, the debris generated during the wear studies show bimodal distribution. Padovan et al [8] showed that the peak of the distribution corresponds to effective diameters of 1-10 microns and corresponding aspect ratios of 1-2. The second peak corresponds to an effective diameter of 100 to 300 microns and much higher aspect ratios. Here, the larger debris is more of the typical 'sausage shaped' agglomerates, whereas the smaller debris is the result of actual intrinsic wear. In order to understand the initiation of defects and resulting debris, observations at microscopic scales become important. Figure 2.22 and Figure 2.23 show representative crosssectional micrographs (SEM) of ESBR and SSBR vulcanizates [66]. The images indicate distinctive domains that create a 'grainy' appearance at the micron levels. It is not known if these grain boundaries are the source of crack initiation at the microscopic levels. Qureshi [66] however shows that the grain boundaries are mechanically stable for the range of shear rates typically experienced in the processing of rubber in a Banbary mixer. This implies that these grain-boundaries will survive the manufacturing processes for rubber product manufacturing. Furthermore, when Qureshi [66] reports that when a dull blade is used to abrade the surface of a vulcanizate, a debris particle with a typical size of 1 micron is generated after 1000 cycles.

The grainy structure observed in these micrographs is also found to be affected by processing conditions. Specifically mixing conditions in a Banbary type blender affect the nature of the distribution.

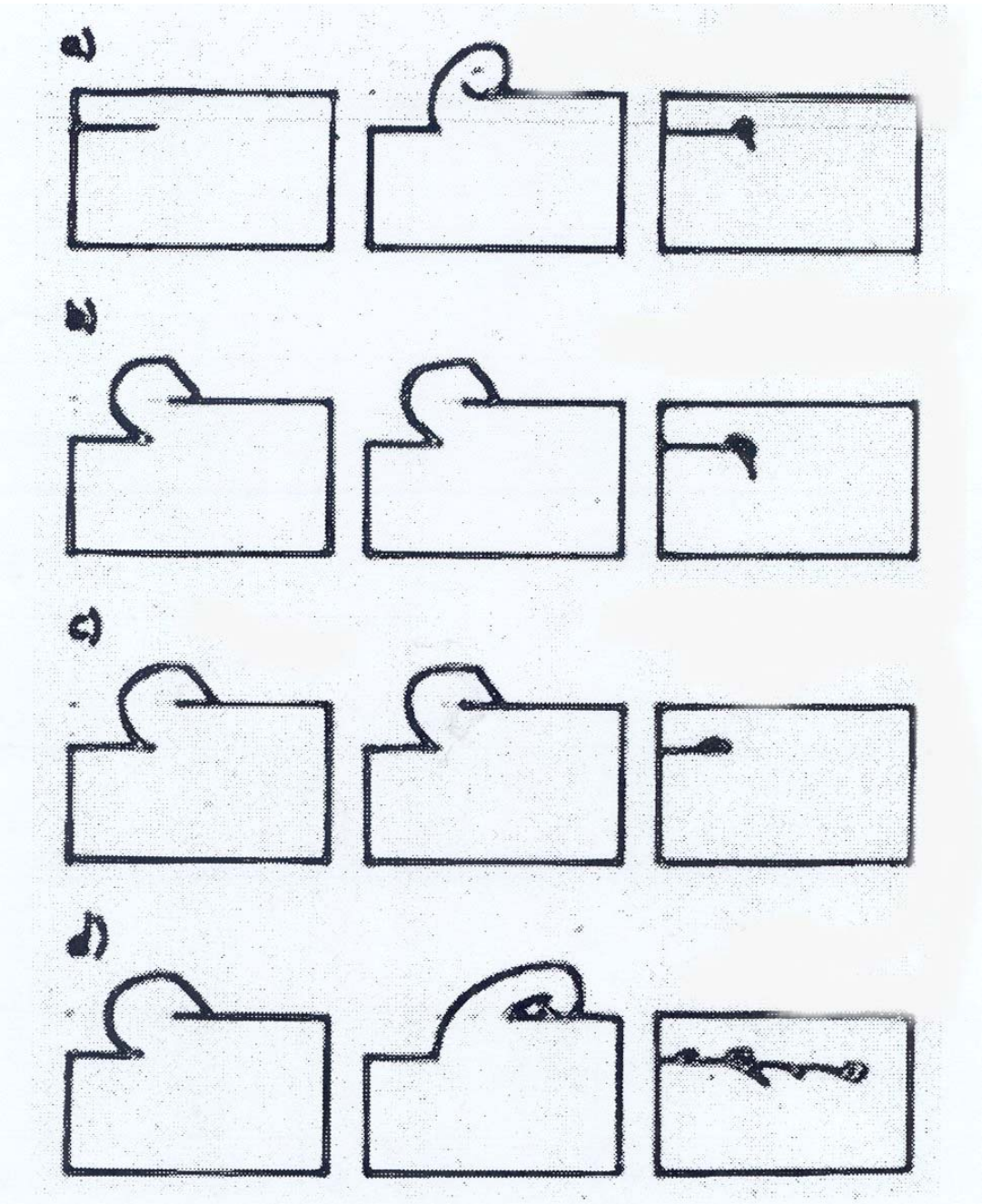

FIGURE 2.21: Flap growth stages in a rubber block. From Gerrard [65]

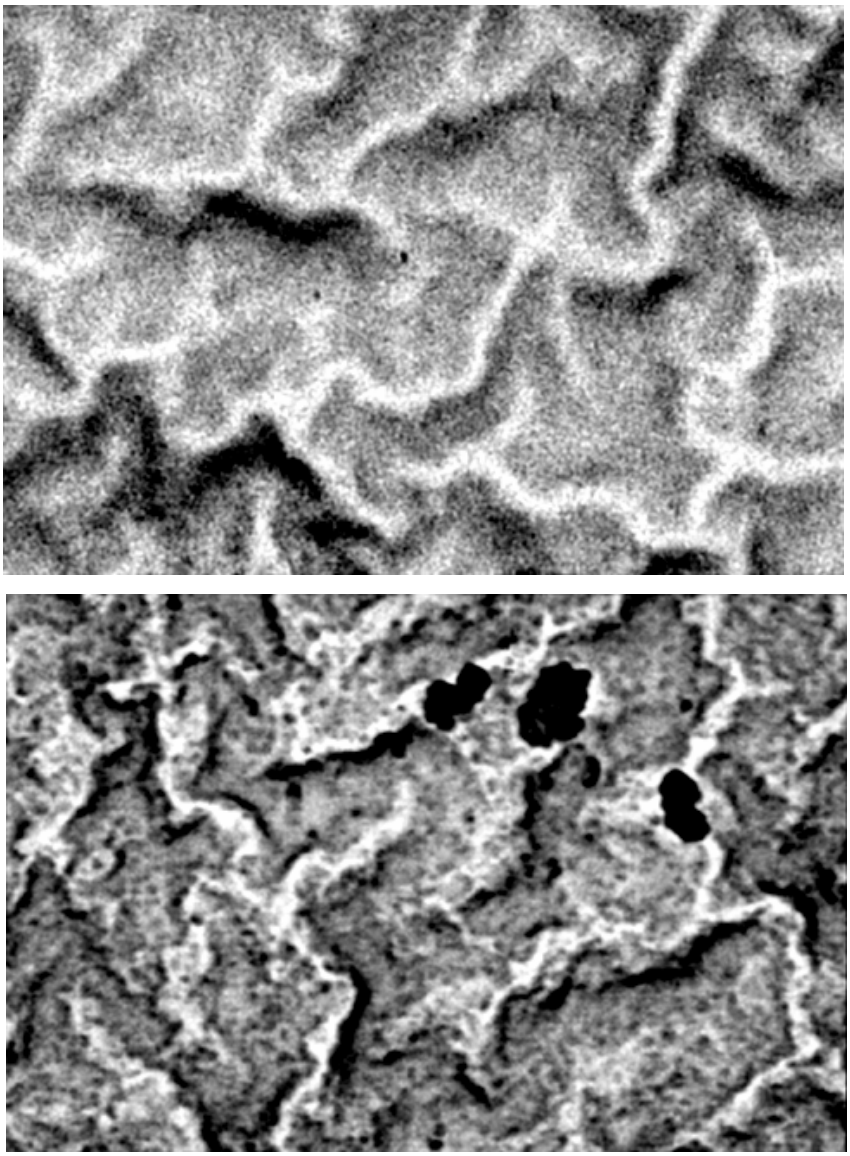

FIGURE 2.22: Negative images of Mixing zones after processing in Banbary Mixer
Top: ESBR, Bottom: SSBR (Scale: 1 inch = 5 microns) From Quereshi [66]

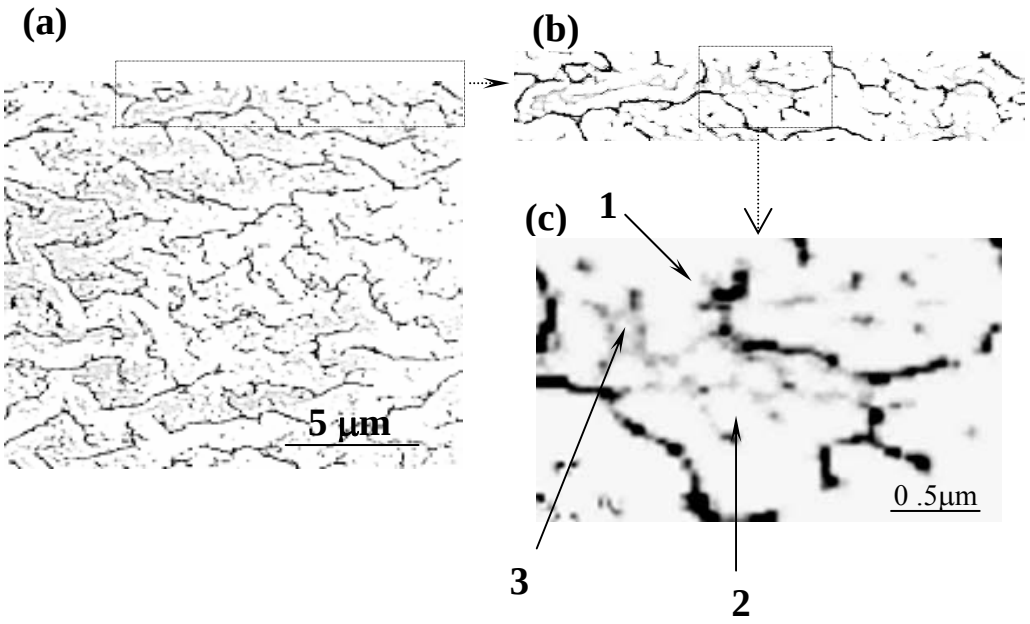

FIGURE 2.23: Expanded view of cross section of SSBR stock. (a) cured stock (b) top layer (expanded) (c) components of filled rubber 1: rubber 2:secondary rubber particles 3. rubber-filler aggregate. From Qureshi [66]

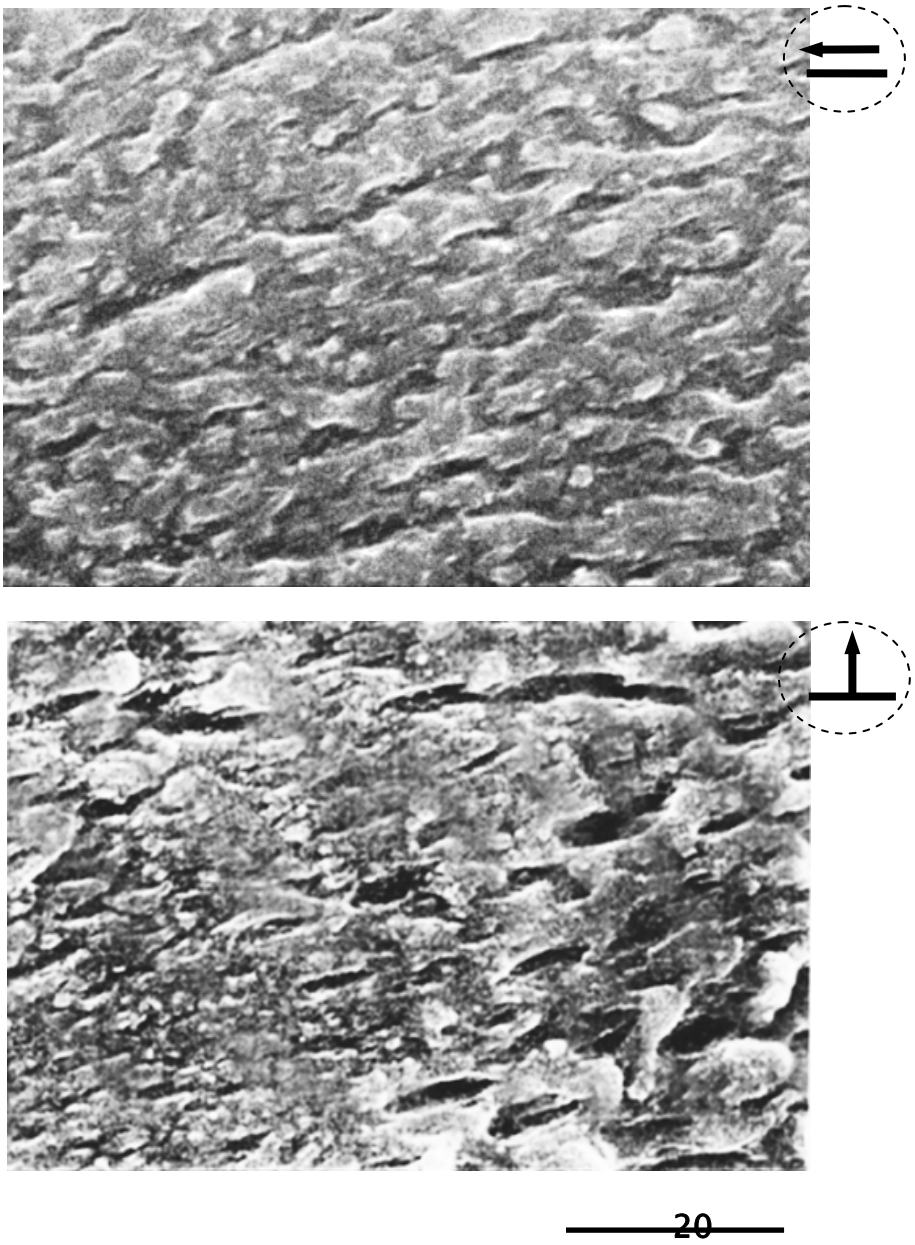

FIGURE 2.24: Effect of processing on mixing zones and damage. Top: Mixing direction parallel to slip direction Bottom: Mixing direction perpendicular to slip direction. From Qureshi [66]

The effect of the slip direction on a wear (abrader) machine and the processing conditions in a Banbary are shown in Figure 2.24. It should be noted that the damage in Figure 2.24 is at a scale of 4 times to that of the characteristic dimensions in the grainy structure (Figure 2.23).

When the process of wear is compared for ESBR and SSBR, more individual intrinsic particles and smaller ridges are formed in ESBR as compared to SSBR. Coincidentally, a filled SSBR stock shows less wear rating as compared to that in ESBR stock during the initial stages of wear and similar or slightly higher wear in long range testing

These observations shed light on the process of wear as it is initiated at the microstructure. Gent [6] has proposed a mechanism by which unbounded elastic expansion at the microscopic voids may initiate the fracture process. However, this is an extrapolative speculation from observations related to spalling and resulting crack-initiation under pressurized nitrogen in rubber. Such extension to crack initiation in a general rubber component may be erroneous as the efforts in this area originated in seals where the foam like structure lends itself to cavities.

2.5.2 Proposal

The experimental evidence presented in the previous section provides details of the micromechanical interactions in a wear process. These observations confirm that a wear is an 'evolutionary' process that happens over scales that range from microns to millimeters. However, a number of questions related to the exact nature of this process remain unanswered. We propose a numerical approach to investigate these questions.

The experiments related to macroscopic wear (section 2.5.1.3) raise following questions:

(1) How does stress field around a penetrating asperity change in the presence of cracks? How does it change when an asperity is approaching or moving away from a defect? What is the effect when an approaching asperity loads one of the faces of the crack?

(2) What roles do asperity size, crack size and depth of penetration play in this?

(3) How do multiple cracks of different scales affect each other in presence of an asperity induced stress field?

(4) How does the evolution of pattern wear lead to particle removal at certain size and scale?

Answering the above questions will help us understand the evolution of pattern wear at the microscale. Additionally, experimental observations on rate of wear and changing slip direction leads to following questions:

(1) How does change in slip direction affect the stress distribution at an asperity level?

(2) Can we deduce a relationship between wear and slip direction from answering the previous question?

Lastly, the microscopic observations described in section 2.5.1.3 raise the following questions:

(1) How do grain boundaries affect/assist the crack initiation process at microscopic level?

(2) How do the variation in material properties and microstructure affect the asperity interaction?

(3) What role is played by the filler particles and the occluded rubber?

(4) The typical asperity interaction in real life is a highly dynamic event and may involve strain rates from 50 1/s to 10^6 1/s. How is the mechanical response affected over the range of strain rates involved?

To answer these above set of questions, numerical models at three different geometric scales are proposed. They are as follows:

(1) An asperity-crack defect interaction model for a general 'homogeneous' material, will be used to study the mechanics of wear at the macroscopic (mm) level. This is further discussed in section 3.3

(2) A three dimensional asperity- flap interaction model that allows us to study the dynamics of change in slip direction.

(3) A two-dimensional model at the microscopic (micron) level that includes the non-homogeneity due to the grain structure described in section 2.5.1.3.

CHAPTER III

2D ASPERITY CONTACT AT MACROSCALE

In this chapter, an asperity contact is modeled with an elastomeric space in the vicinity of a crack. The primary objectives of this study are (1) to quantify the effects of an asperity contact in the vicinity of a preexisting crack, (2) to estimate the event of a new crack initiation in the vicinity of the crack and (3) to identify the influence of principle physical parameters involved, viz. material properties, friction and characteristic dimension of asperities and crack(s) involved in the process. In section 3.1 the assumptions involved in the Asperity contact model are discussed.

3.1 Assumptions For the Steady State Asperity Contact Model

There are a number of issues that complicate the modeling of an asperity with an elastic half-space. The complications are a direct result of the nonlinear material properties of rubber, and friction. Also, the contact mechanics between the asperity and the elastic half space as well as two walls of a crack surface create nonlinear constraints on the problem. The simplifying assumptions involved in the steady state asperity contact model are as follows:

(1) 2-D Geometry: A 3-D contact model create a problem with large number of degrees of freedoms and constraint equations in the form of contact. The 3-D contact problem creates particular meshing challenges that either increase the solution time drastically or create un-resolvable contact when the extent of deformation near the cracks is large.

With this in mind, the asperity interaction with an elastic half space with a crack is modeled as a 2D problem. Both the plain strain and the plain stress cases are considered. When the asperities are closely spaced specially along the lateral direction and the lateral crack dimension is substantially larger than the crack depth into the material, the loading case resembles closer to a plain strain case. On the other hand, if the lateral dimension of the crack is much smaller compared to the depth of the crack into the surface, the loading condition of the asperity can be effectively approximated as a plain stress case. In reality, the 3D stress state in the elastic half space, is a combination of the plain stress and the plain strain cases. However, a 2-D approximation still allows us to investigate possible stress relief in the vicinity of a crack.

(2) Steady state loading: In this particular model, a steady state asperity loading is considered. The effect of inertia will be considered in a later section

(3) Material property parameters: Rubber may undergo large deformations under loading from the asperities. This results in a peculiar stress distribution and affects the pattern wear accordingly. This behavior is further complicated by inhomogeneity and nonlinearity built into a commercial application such as a tire construction. For example, fillers such as carbon black embedded in a rubber matrix, affect properties of rubber locally. The resultant change in stress distribution may affect the behavior of the crack-tip [64]. The proposed study will thus include changes in asperity-crack interaction under the presence of fillers. Also, dissipative effects such as Viscoelasticity and Mullins effect are assumed to be small for steady state problem involving gradual loading. A Mooney Rivlin model will be used to describe the nonlinear behavior of the rubber and is discussed in section 3.3.

(3) Crack Geometry: In all the models to be analyzed, defect will be represented by a crack with a blunt tip (circular geometry). The radius of curvature of the tip is much smaller than the overall dimensions of the crack. It should be noted that a blunt crack also has computational advantages. Typically, a sharp crack limits computations to the realm of linear elastic fracture mechanics. This precludes large nonlinear deformations that are common in elastomers. Also, a sharp crack is usually modeled using quadratic elements with quarter points to obtain the stress singularity at the crack tip. This introduction of quadratic elements leads to restrictions for a generalized contact problem. At the same time, a blunt crack is a fairly good approximation for elastomers as evident from several experimental as well as numerical research efforts [49]. Figure 3.1 shows the typical curvature of a crack tip in rubber under extremely small (<20%) bulk strain. Additionally it is assumed that all the cracks in the elastic half space are much smaller in dimension than the surface crack of interest.

3.2 Methodology

A finite element code in the ABAQUS environment is used to investigate the problems described in the previous section. A variational total Lagrangian approach will be used. This method is found particulary suitable for nonlinear and hyperelastic materials. The total Lagrangian method is also proved economical for problems envolving relative large rotations but small to moderate amount of strains. This includes nonlinear phenomena such as plasticity and creep. It should be noted, that these procedures are valid for both static and dynamic problems.

In the total Lagrangian approach, the equilibrium can be expressed by the principle of virtual work as:

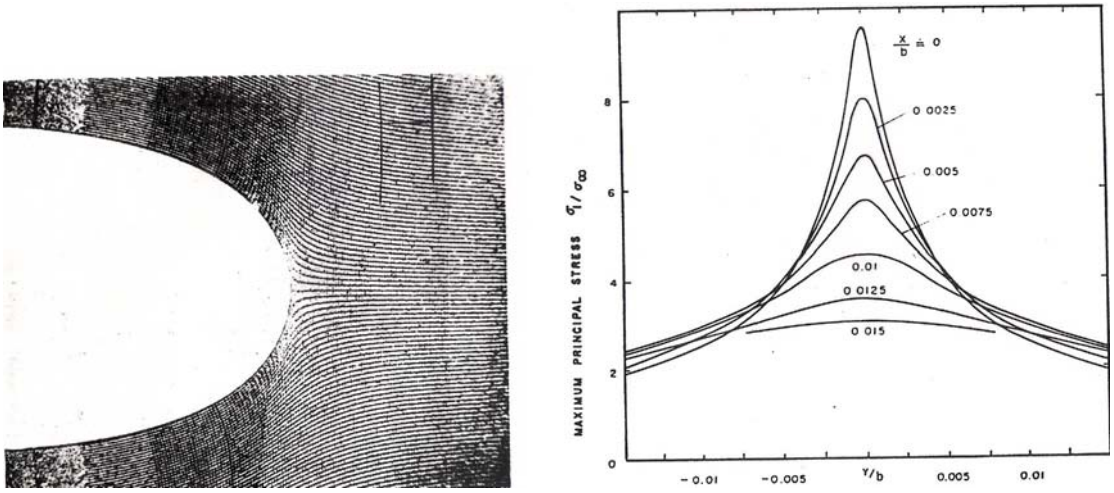

(A) (B)

FIGURE 3.1 Crack tip stress distribution from experimental results.
(A) Close up of a crack tip from experiment [53] (B) Maximum Principal Stress Distribution along the crack for rectangular coordinates [54]

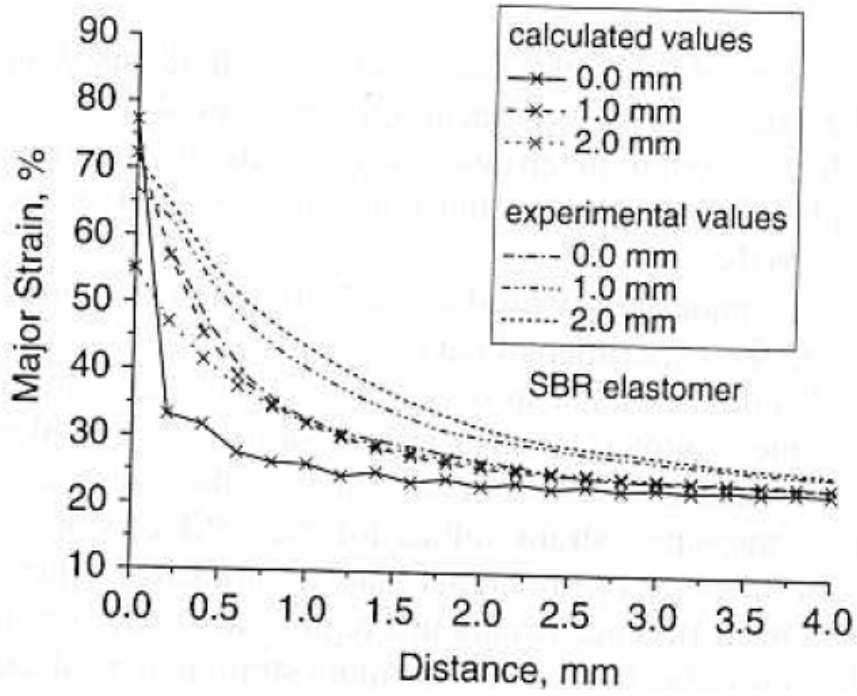

FIGURE 3.2: Influence of crack tip radius on Maximum Principal Strain along the crack axis from experiments [129].

$$\int_{V_0} S_{ij}\delta E_{ij}dV = \int_{V_0} b_i^0 \delta\eta_i dV + \int_{A_0} t_i^0 \delta\eta_i dA \qquad 3.1$$

Here S_{ij} is the symmetric second Piola-Kirchhoff stress tensor, E_{ij}, is the Green-Lagrange Strain, b_i^0 is the body force in the reference configuration, t_i^0 is the traction vector in the reference configuration, and η_I is the virtual displacements. Integration is carried out in the original configuration at *t=0*. The strains are decomposed in total strains for equilibrated configurations and the incremental strains between *t=n* and *t=n+1* as:

$$E_{ij}^{n+1} = E_{ij}^{n} + \Delta E_{ij} \qquad 3.2$$

while the incremental strains are further decomposed into linear ΔE_{ij}^{1} and nonlinear ΔE_{ij}^{n1} parts as:

$$\Delta E_{ij} = \Delta E_{ij}^{1} + \Delta E_{ij}^{n1} \qquad 3.3$$

where ΔE^1 is the linear part of the incremental strain expressed as:

$$\Delta E^{1} = \frac{1}{2}\left[\frac{\partial \Delta u_i}{\partial X_j} + \frac{\partial \Delta u_j}{\partial X_i}\right] + \frac{1}{2}\left[\left(\frac{\partial u_k^n}{\partial X_i}\right)\left(\frac{\partial \Delta u_k}{\partial X_j}\right) + \left(\frac{\partial u_k^n}{\partial X_j}\right)\left(\frac{\partial \Delta u_k}{\partial X_i}\right)\right] \qquad 3.4$$

The second term in the bracket in Equation 5-11 is the initial displacement effect. ΔE^{n1} is the nonlinear part of the incremental strain expressed as:

$$\Delta E^{n1} = \frac{1}{2}\left[\left(\frac{\partial \Delta u_k}{\partial X_i}\right)\left(\frac{\partial \Delta u_k}{\partial X_j}\right)\right] \qquad 3.5$$

Linearization of equilibrium of Equation 5-9 yields:

$$\{K_0 + K_1 + K_2\}\delta u = F - R \qquad 3.6$$

where K_0 is the small displacement stiffness matrix defined as

$$(K_0)_{ij} = \int_{V_0} \beta^0{}_{imn} D_{mnpq} \beta^0{}_{pqj} dV \qquad 3.7$$

K_1 is the initial displacement stiffness matrix defined as

$$(K_1)_{ij} = \int_{V_0} \{\beta^u{}_{imn} D_{mnpq} \beta^u{}_{pqj} + \beta^u{}_{imn} D_{mnpq} \beta^0{}_{pqj} + \beta^u{}_{imn} D_{mnpq} \beta^u{}_{pqj}\} dv \quad 3.8$$

in the above equations, $\beta^0{}_{imn}$ and $\beta^u{}_{imn}$ are the constant and displacement dependent symmetric shape function gradient matrices, respectively, and D_{mnpq} is the material tangent. K_2 is the initial stress stiffness matrix:

$$(K_2)_{ij} = \int_{V_0} N_{i,k} N_{j,\ell} S_{k\ell} dV \quad 3.9$$

in which S_{kl} is the second Piola-Kirchhoff stresses and $N_{i,k}$ is the shape function gradient matrix. Also, δu is the correct displacement vector. F and R are the external and internal forces, respectively.

This Lagrangian formulation can be applied to problems if the undeformed configuration is known so that integrals can be evaluated, and if the second Piola-Kirchhoff stress is a known function of the strain. For solids, each analysis usually starts in the stress-free undeformed state, and the integrations can be carried out without any difficulty. For viscoelastic fluids and elastic-plastic and viscoplastic solids, the constitutive equations usually supply an expression for the rate of stress in terms of deformation rate, stress, deformation, and sometimes other (internal) material parameters. The relevant quantity for the constitutive equations is the rate of stress at a given material point.

The second Piola-Kirchhoff stress for elastic and hyperelastic materials is a function of the Green-Lagrange strain defined below:

$$S_{ij} = S_{ij}(E_{kl}) \quad 3.10$$

If the stress is a linear function of the strain (linear elasticity)

$$S_{ij} = D_{ijkl} E_{kl} \quad 3.11$$

the resulting set of equations is still nonlinear because the strain is a nonlinear function of displacement.

The heuristic contact-mechanical algorithm used in the finite element codes is briefly described in Appendix B. As evident from it, the contact mechanics involved is highly dependent upon the mesh size. The problem of asperity indentation creates large local deformation. Also, there is a high frictional force associated with the contact. Material may also experience self contact under these conditions. When the material (rubber) is involved in intermittent contact with the asperity, the problem may become unstable. Also, a large frictional force, may distort elements and require remeshing. Additionally a complicated friction model such as a stick-slip model may create numerical instabilities. A simple Coulomb-Type friction model is used to reduce the complexity of the model.

3.3 Material Model

Considering the steady state nature of the indentation problem, the elastomeric half space is modeled with a hyperelastic material. Strain-energy function, U, the energy stored in a deformed body, can be used to obtain the stress-strain relations for homogenous, isotropic, and elastic materials. From the principal of material objectivity, the strain energy function is typically expressed as a function of the invariants of the strain measure. An example of such strain energy function would be a generalized polynomial of the invariants.

$$U = C_{10}(I_1 - 3) + C_{01}(I_2 - 3) + C_{20}(I_1 - 3)^2 + C_{11}(I_1 - 3)(I_2 - 3) + ... + C_{ON}(I_2 - 3)^N$$

where:

$I_1=\lambda_1^2+\lambda_2^2+\lambda_3^2$ $I_2=\lambda_1^2\lambda_2^2 + \lambda_2^2\lambda_3^2 + \lambda_3^2\lambda_1^2$ $I_3= \lambda_1^2\lambda_2^2\lambda_3^2$ (3.12)

and "λ_i"are principal extension ratios. For incompressible materials such as rubber, $I_3=1$.

The simplest hyperelastic representation, Neo-Hookean is defined as:

$$U = C_1(I_1 - 3) \tag{3.13}$$

where C_1 is assumed to be constant. A first order polynomial function for energy is known as Mooney-Rivlin function as:

$$U = C_1(I_1 - 3) + C_2(I_2 - 3) \tag{3.14}$$

Higher order polynomials can be constructed. For instance, a second order polynomial may be:

$$U = C_{10}(I_1 - 3) + C_{01}(I_2 - 3) + C_{20}(I_1 - 3)^2 + C_{11}(I_1 - 3)(I_2 - 3) + C_{02}(I_2 - 3)^2 \tag{3.15}$$

It can be shown [141] that stress can be defined as $S = \frac{\delta U}{\delta \lambda}$ where "λ" is principal stretch. For the case of uniaxial simple tension, the stress derived from Neo-Hookian relation has the form:

$$S = 2C_{10}(\lambda - \lambda^{-2}) \tag{3.16}$$

and from the Moony-Rivlin representation:

$$S = 2\lambda(C_{10}\lambda - C_{10}\lambda^{-2} - C_{01}\lambda^{-3} + C_{01}) \tag{3.17}$$

and finally from second order polynomial:

$$S = \frac{2(1-\lambda^{-3})}{\lambda^2}[2C_{20}\lambda^5 + 3C_{11}\lambda^4 + (C_{10} - 3C_{11} - 6C_{20} + 4C_{02})\lambda^3 + (C_{01} - 3C_{11} + 4C_{20})\lambda^2 +$$

$$3C_{11}\lambda + 2C_{02}] \tag{3.18}$$

These stress-strain relations can be used for finite deformation analysis for elastic materials such as rubber vulcanizates. Due to high compressive strains involved in an asperity penetration problem, a small compressibility consistent with literature data [90,93-95]. is included in the Mooney Rivlin material model.

Table 3.1 Composition of different elastomers considered in the numerical simulations
.

Ingredients	SBR1	SBR2	SBR3
SBR 1502	100.00	-	-
SBR 1500	-	100.0	100.00
Zn0	3.00	3.5	3.5
Stearic Acid	1.0	2.5	2.5
Sulfur	1.80	2.0	2.0
TBBS	1.20	-	-
TMTD	0.10	-	-
CBS	-	1.1	1.1
N990 (MT Black)	-	31	10

Table 3.2**:** Material properties for the elastomer compositions shown in Table 3.1.

Vulcanizate	C1 (MPa)	C2 (MPa)	E (MPa)	σ @ break (MPa)	ε @ beak %
SBR1	0.113	0.237	1.92	1.38	272
SBR2	2.0	2.9	29.4	6.8	-
SBR3	1.7	2.0	22.2	4.8	-

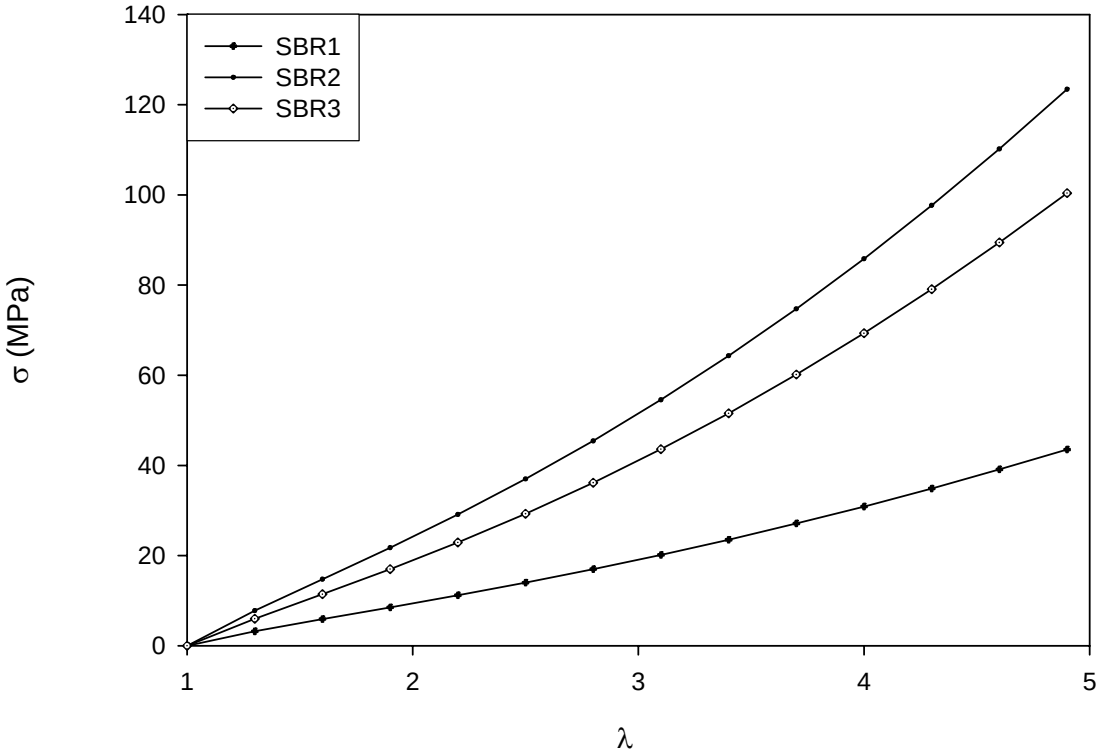

FIGURE 3.3: Cauchy stress vs stretch ratio for the filled and unfilled SBR grades listed in Table 3.1

3.4 Preliminary Results

We now briefly discuss the results of FEA simulations for a general asperity-rubber interaction model. Figure 3.4illustrates the simple geometry for the study of asperity interaction with a defect. This model is used for a parametric study where the diameter of the asperity and length of the defect are varied. The asperity is considered 'rigid' for all practical purposes. The stress distribution in the vicinity of an asperity and the defect are calculated using a FEA analysis for frictional and frictionless conditions. The asperity radius of 7.5, 10 and 15 mm are used. Also, the defect size is varied as 10, 15 and 20 mm. This is a rather large asperity dimension and is chosen to replicate interaction at the macro-scale.

As shown in the figure, two types of loading conditions are analyzed. These loading conditions are idealization of what happens when an asperity from a hard surface (road) comes in contact with the rubber (tire). One case involves direct (vertical) penetration of asperity into a rubber block (Loading A). The second loading involves asperity travel along the surface at a fixed depth of penetration (Loading B).

For the pure penetration loading, the sample rubber block is fixed at the bottom edge. The length of the block is chosen such that the boundary conditions on the two edges do not affect the stress distribution near the defect and the site of penetration. When the asperity is moving away from the defect, the boundary towards the direction of motion is also restrained. Plain strain elements (CPE4R) with reduced integration are used with a static viscous stabilization parameter of $2x10^{-3}$ and a hourglass stiffness of 0.15.

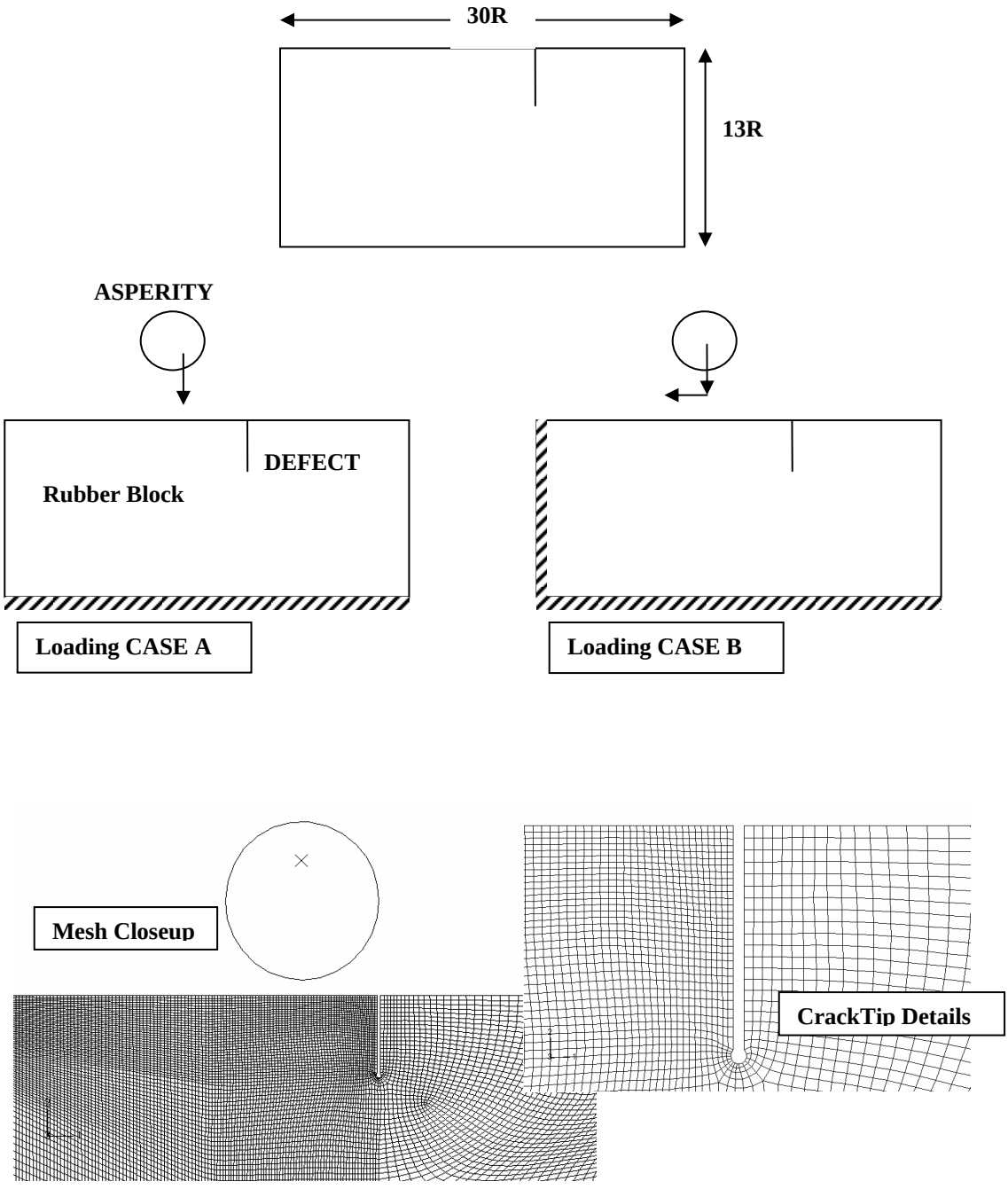

FIGURE 3.4: Boundary conditions and mesh details for asperity loading near a defect in a rubber block.

3.4.1 Stress State Under Asperity Penetration (Loading A)

These simulations are done to observe the effect on stress field due to a defect at a relatively large distance. The important areas where stress distribution is of interest are: (1) Along the wear surface (from the point of asperity contact to the defect site (2) Through the bulk (along the line of contact from the asperity (3) Along the crack tip. These three paths are labeled in Figure 3.5 as path 1, 2 and 3.

(1) Comparison of stress state when there is no defect present.

Figure 3.6 shows the stress distribution along the wear surface (path 1), *when there is no defect present* in the rubber block. The total stress distribution is described by the normal stress and the tangential stress. In this situation, the tangential stress is identical to the Maximum Principal stress. The stress quantities are non-dimensionalized by the ratio of the Reaction force on the asperity and the effective cross sectional area. The distance along the wear surface is non-dimensionalized with division by the asperity radius. As Figure 3.6 shows, the normal and the tangential stresses along the wear surface increase as the depth of penetration increases. Also, the tangential stress along the wear surface shows change in compressive stress zone for higher depth of penetration for frictionless conditions. When friction is introduced, the stress distribution along the wear surface shows a sharper variation in the contact zone. Figure 3.7 shows identical simulations in the presence of a defect at a large distance (roughly 6R). At this large distance from the defect, the peak normal and tangential stresses are roughly the same (within 10%) of that of the virgin material (no defects present). However, the contact zone (area) is slightly larger in case when the defect is present. This is because of the larger deformation of the material under the presence of a defect.

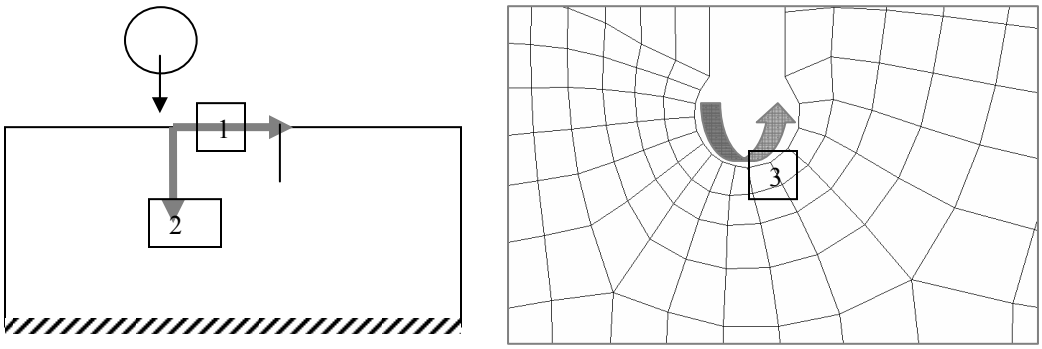

FIGURE 3.5: Paths for stress distribution for plots. (1) Along the wear surface from asperity contact point to the defect (2) Through the bulk in a direction perpendicular to the direction of asperity travel (3) Along the crack-tip.

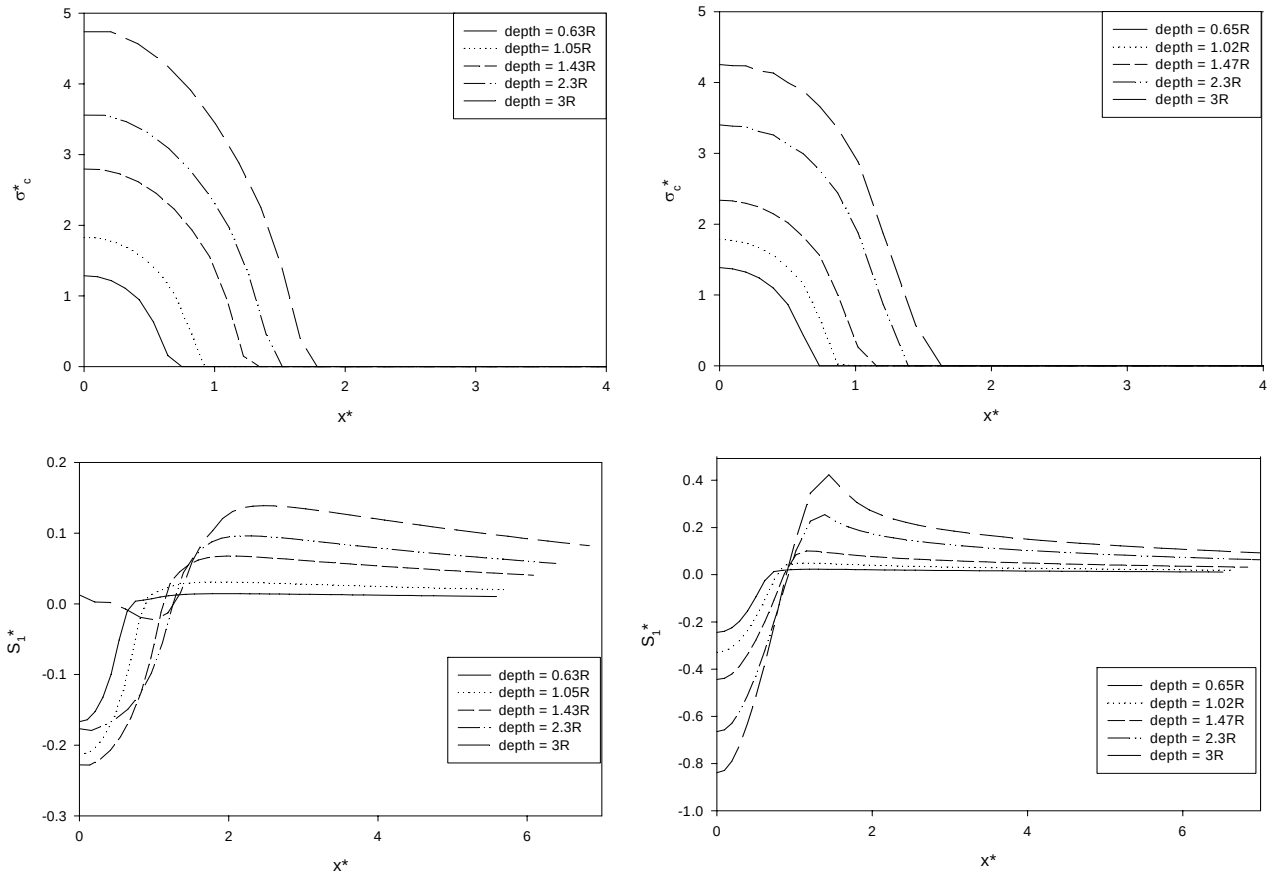

FIGURE 3.6: Stress state under asperity penetration. (Top) Variation of dimensionless Normal Compressive Stress with depth of penetration for Frictionless (left) and Frictional (right, μ=0.5) conditions. (Bottom) Variation of dimensionless Maximum Principal Stress with depth of penetration for frictionless (left) and frictional (right, μ=0.5) conditions.

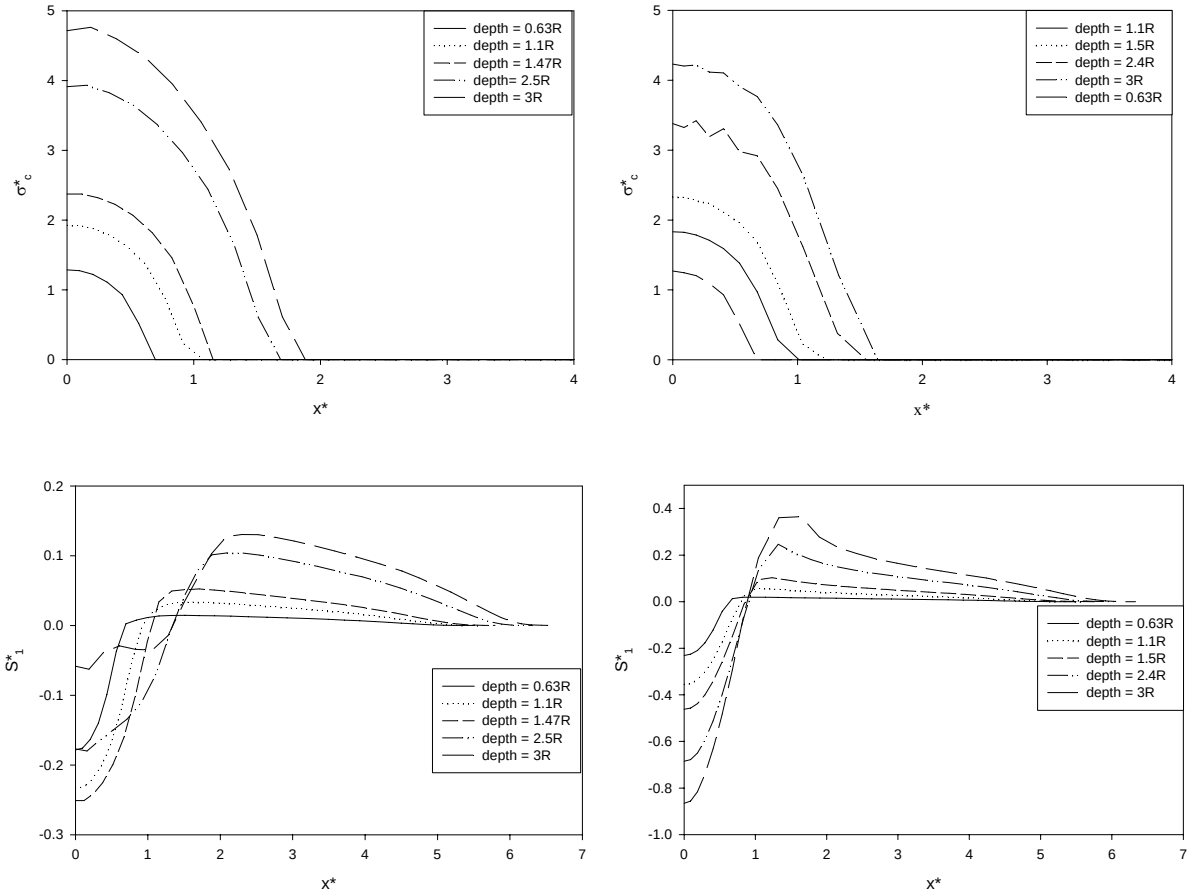

FIGURE 3.7 Stress state under asperity penetration in the vicinity of a defect (see Figure 3.9). Top Variation of dimensionless Normal Compressive Stress with depth of penetration for Frictionless (left) and Frictional (right, μ=0.5) conditions. Bottom Variation of dimensionless Maximum Principal Stress with depth of penetration for frictionless (left) and frictional (right, μ=0.5) conditions

Also, at the surface where the defect is located, the boundary conditions are stress free. This changes the overall stress distribution along the wear surface as well as the contact area. It should be noted that the tangential stress (Maximum principal stress along the wear surface) is one of the indicators of the failure of material, and may cause tear or propagation of an existing defect.

(2) Effect of defect size.

Figure 3.8 shows the stress variation along the wear surface under the asperity penetration of 3R as the length of the defect is varied while keeping the other dimensions the same. There is virtually no variation in the normal stress even at this large depth of penetration. However, the peak tangential stress (Maximum principal stress) shows significant reduction (roughly 25%) as the defect length increases from zero (virgin material) to 20mm (2R). This shows that for a large enough depth of penetration, the stress distribution resulting from an asperity will be affected if the size of the defect is large, even if the defect is far from the point of contact (6R). Conversely, at these high depth of penetrations, the crack-tip will show significant tensile stresses. Figure 3.9 shows the variation of the tangential stress along the crack tip for frictional and frictionless conditions for a defect length of 10mm (1R). In this figure, the distance is non-dimensionlised with the radius of the crack-tip. Please note that even when an asperity penetration is at a large distance, the peak stresses along the crack tip are roughly 75% of those at the contact interface (figure 3.6 and 3.7). This is because of the large deformation of the material in the presence of the defect.

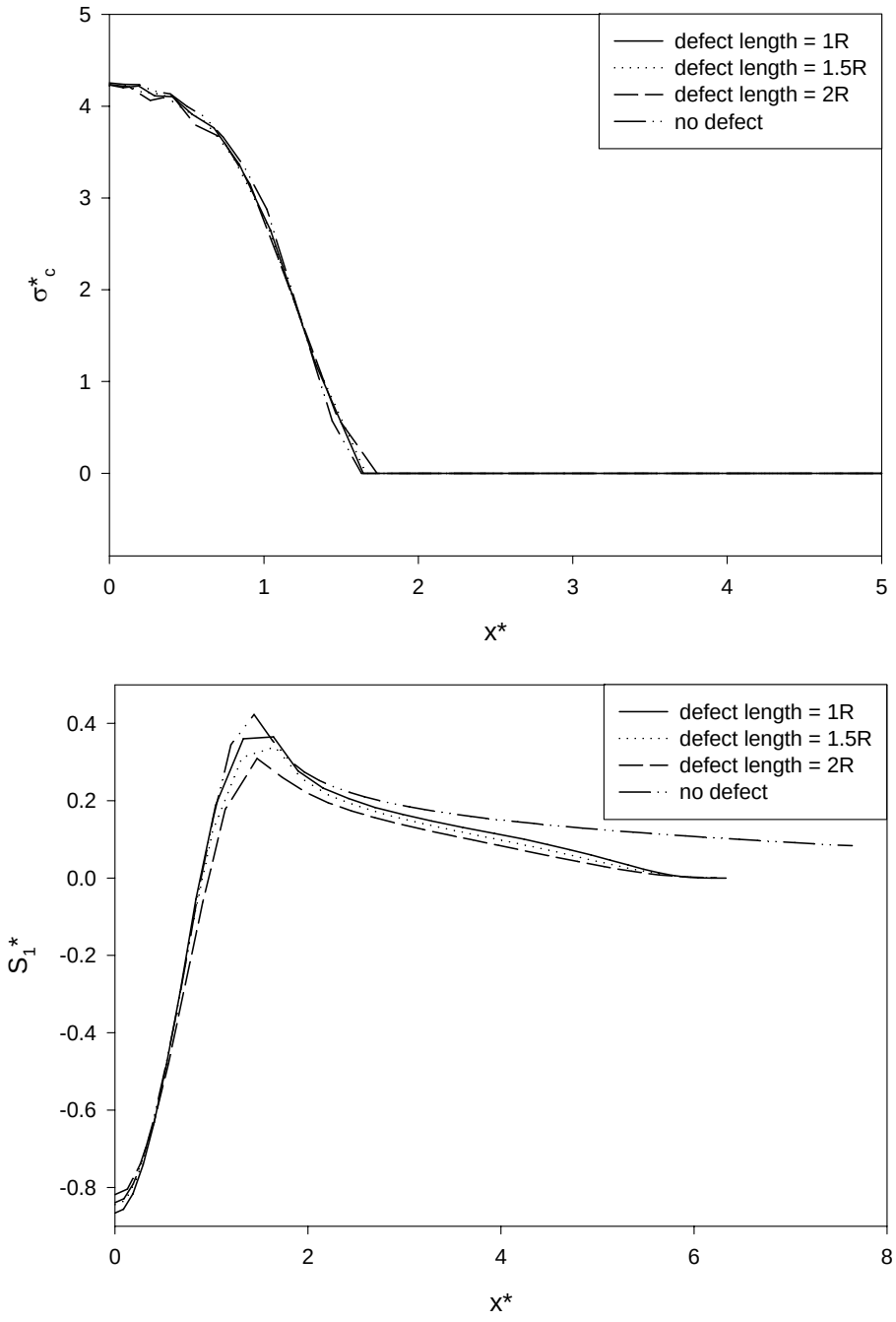

FIGURE 3.8: Comparison of radial (pressure) stress on asperity. Top and maximum principal stress Bottom under the loading conditions shown in Figure 1 for different lengths of defects at a fixed distance.

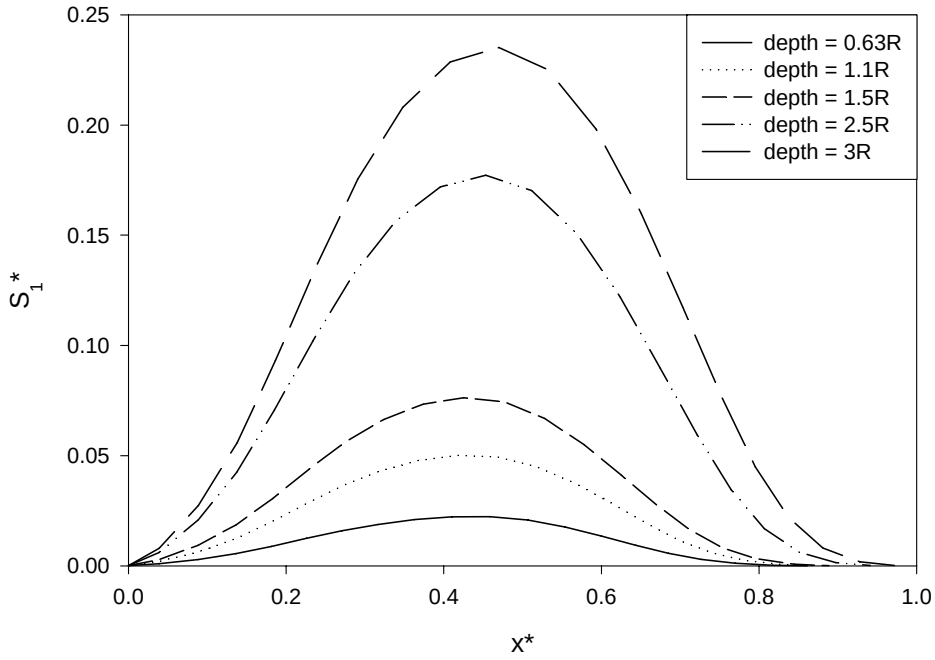

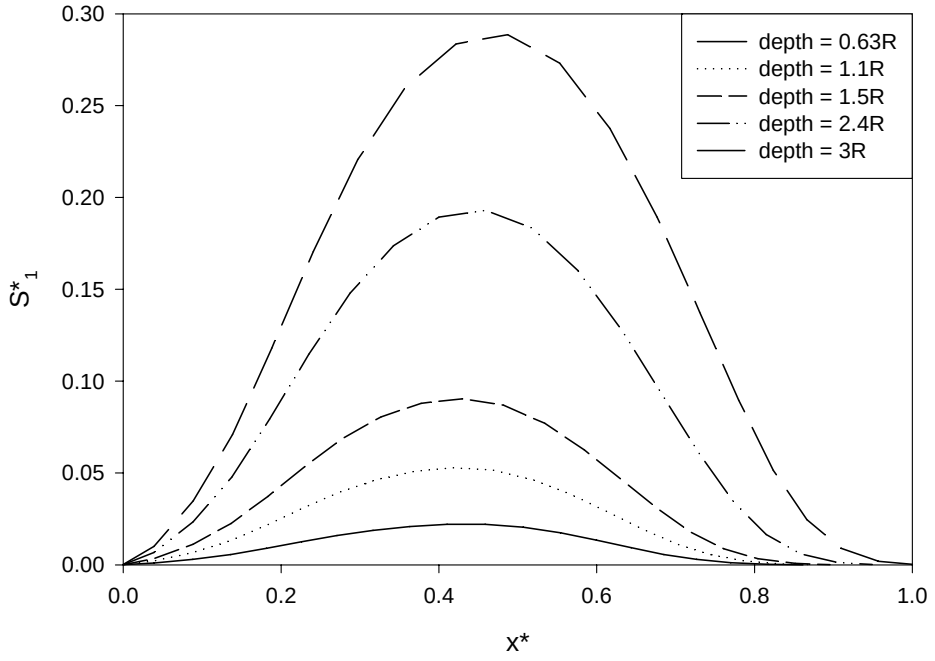

FIGURE 3.9: Maximum principal stress distribution for the 'crack tip' at varying depth of penetrations. **(**Top): Frictionless (Bottom)**:** With friction (μ=0 .5)

Figure 3.10 shows the variation of peak tangential stress at the crack tip for varying defect length. The peak tangential stress falls more than twice as the length of the defect goes from 1R (10mm) to 2R(20mm).

(3) Effect of friction coefficient

As observed in Figures 3.6 and 3.7 the presence of friction increases the peak stresses along the wear surface as well as the crack-tip. This is illustrated in figures 3.11 and 3.12. However, the increase in friction coefficient from 0.5 to 1.5 does not affect the peak tangential stresses along the wear surface as well as the crack tip significantly. This is because the loading is perpendicular to the surface and there is very little motion in the direction of friction.

(4) Effect of asperity size

Figure 3.13 shows the effect of asperity radius on the stress along the wear surface and the stress along the crack tip. As the asperity radius increases, the corresponding contact area increases for a given depth of penetration. This increase causes a reduction in the peak tangential (maximum principal) stress. Furthermore, the location of peak stress moves further away from the center of the asperity ($x^*=0$) as the contact area increases. Similarly, an increase in asperity radius corresponds to an increase in the peak tangential stress along the crack-tip. This is because a larger asperity has a larger 'zone of influence' for a given depth of penetration.

(5) Strain energy density distribution

Strain energy distribution represents the energy available for the deformational work and is an important quantity in the determination of possible crack propagation or material failure.

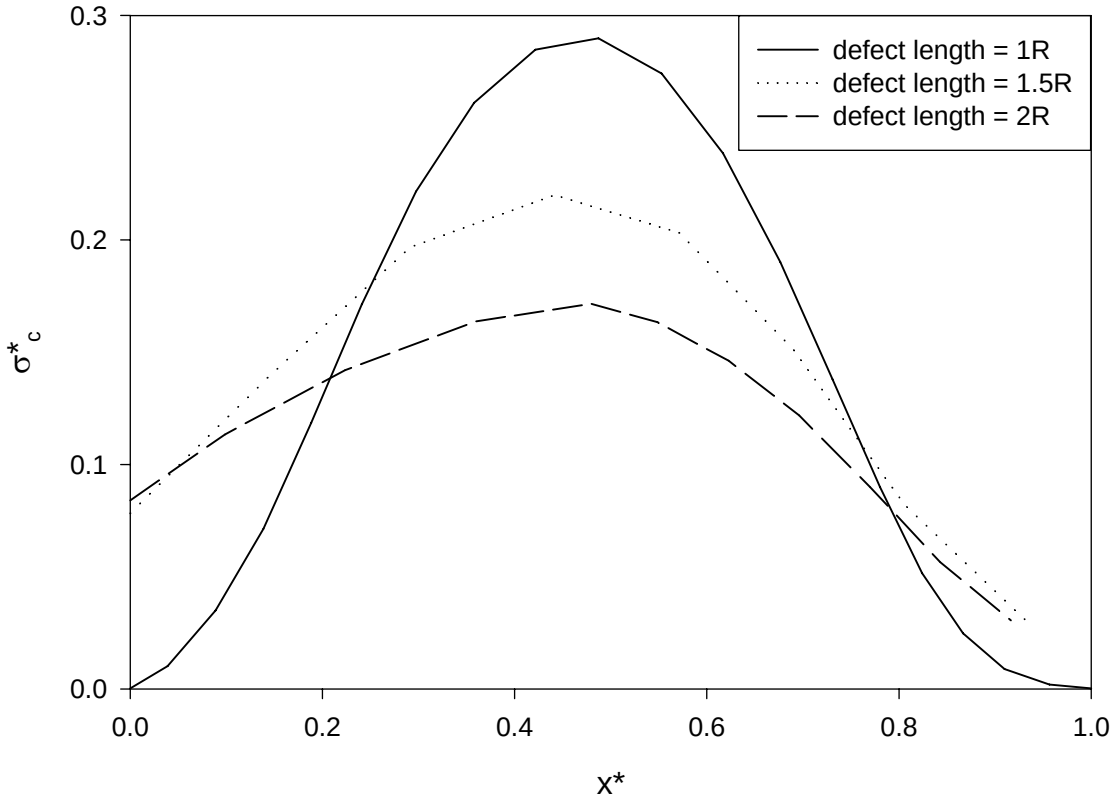

FIGURE 3.10: Maximum principal stress distribution for the ‘crack tip’ for varying sizes of defect.

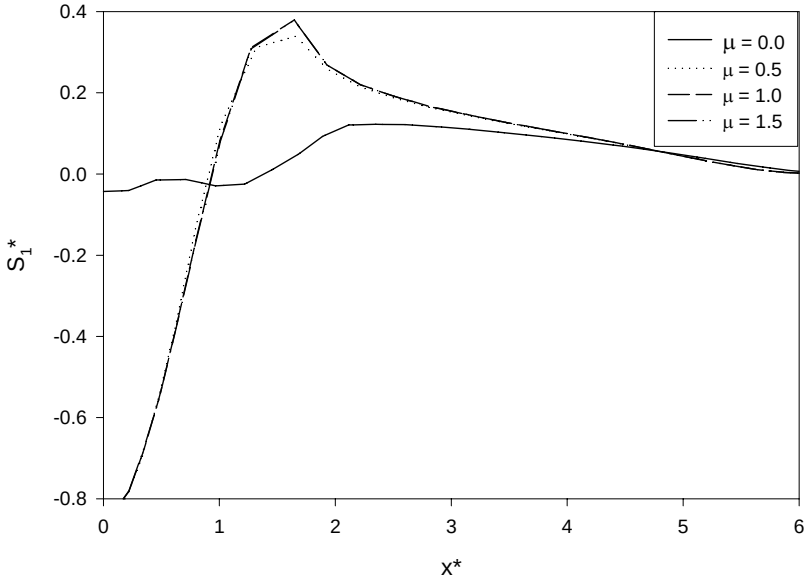

FIGURE 3.11: Comparison of maximum principal stresses for various friction coefficients at the depth of penetration = 3R and defect length of 1.5R along the wear surface (path 1).

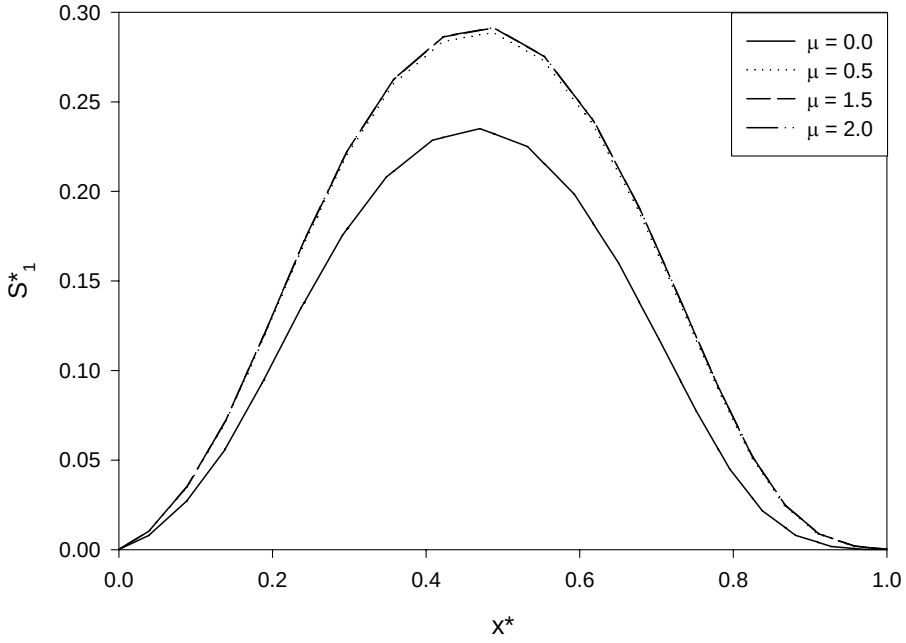

FIGURE 3.12: Comparison of maximum principal stresses for various friction coefficients at the depth of penetration = 3R and defect length of 1.5R along the crack-tip (path 3).

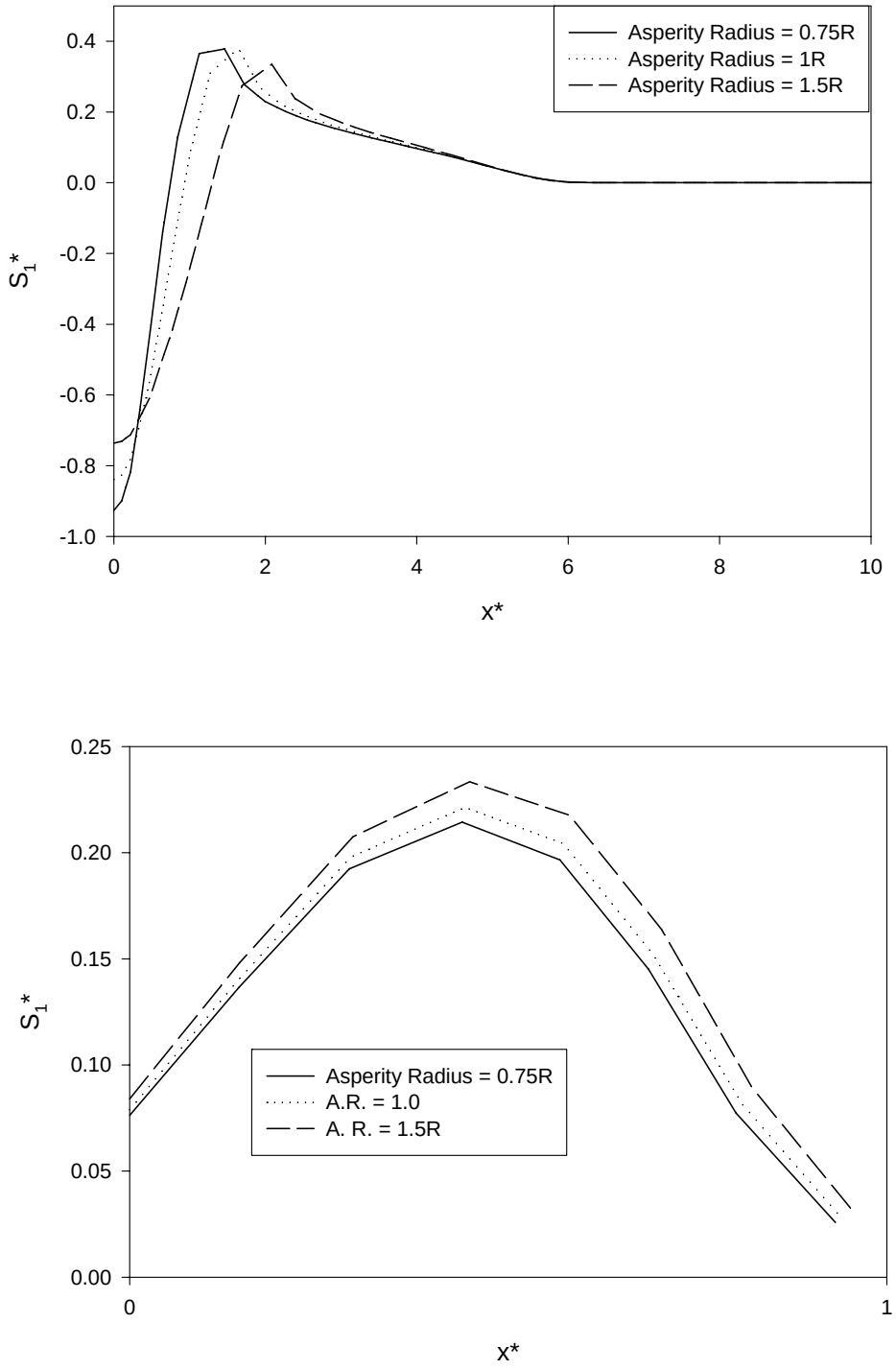

FIGURE 3.13: Comparison of Maximum principal stresses for varying asperity radius at the depth of penetration = 3R and defect length of 1.5R for Top along the wear surface, and Bottom along the crack tip.

Figure 3.13 represents the variation of strain energy density along the wear surface as well as the crack tip. It may be noted that even though the peak tangential stress observed at the crack tip is comparable to the tangential stress along the wear surface (contact area), there is a large difference in the corresponding strain energy density distributions. This is because at such large distances from the asperity, the deformations at the crack tip are relatively low. This graph shows the importance of both the tangential stress and the strain energy density quantities in determination of possible failure.

(6) Stress Distribution through the bulk along the line of penetration.

Another important area where stress distribution under asperity penetration is important, is along the line of penetration. This is shown as Path 2 in figure 3.5. Figure 3.14 shows the normalized tangential stress as well as the strain energy density variation along the line of contact for friction . It is easy to see that the peak tangential stress is significantly higher than that along the wear surface or the crack tip. However, the peak tangential stress occurs just under the wear surface (<0.5R) and very close to the contact region. Also, the strain energy density is correspondingly higher compared to that on the wear surface as well as the crack tip. It should be noted that these high stresses under the subsurface are due to the particular nature of loading. A direct vertical asperity penetration is an idealization. The closest situation that corresponds to this type of loading is when a tire is coming in contact with an asperity on the road. However, once the contact is established, the asperity 'drags' along the wear surface in the direction of motion. Results for such type of loading (loading B in Figure 3.9), are presented in the following section.

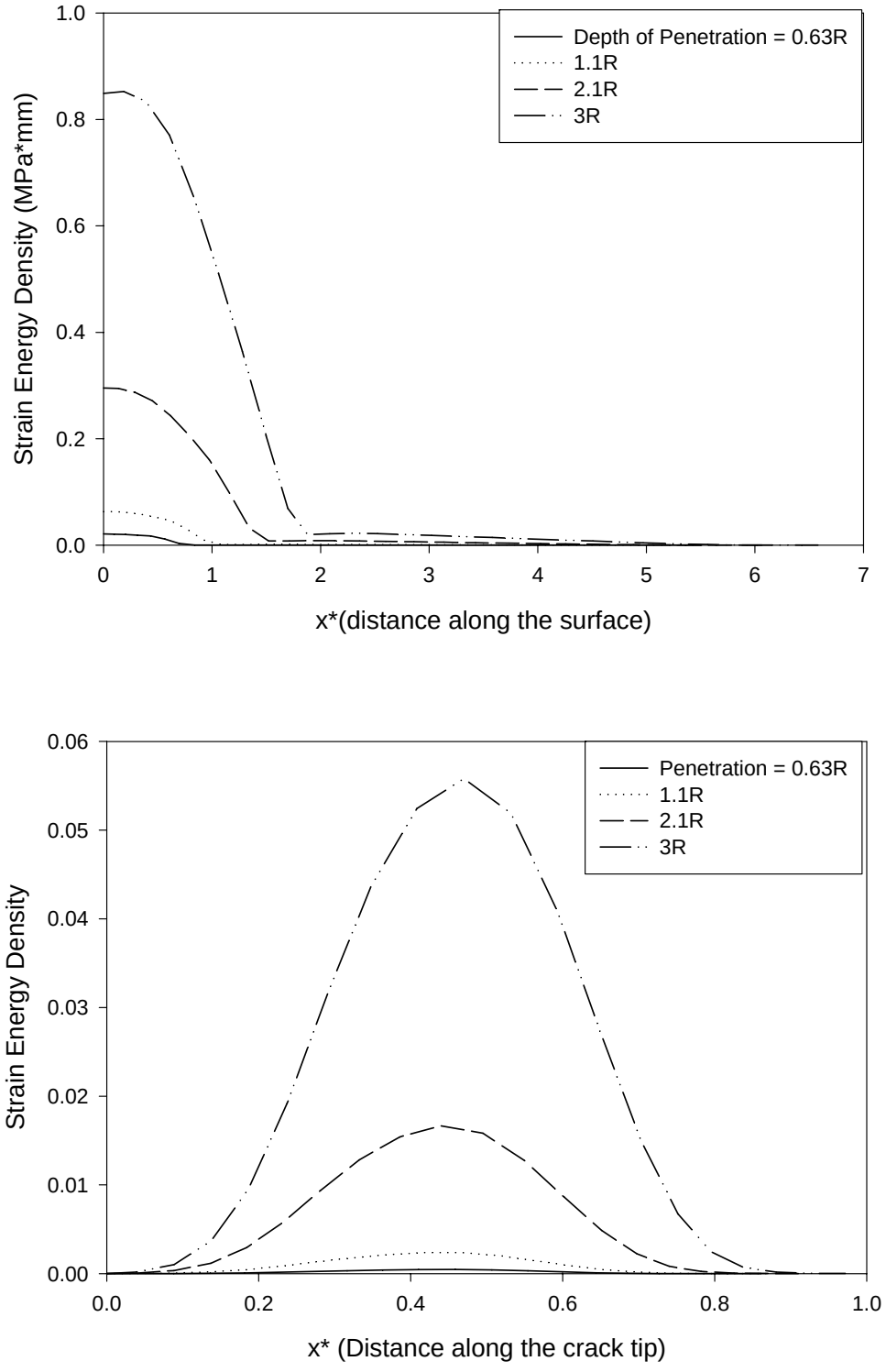

FIGURE 3.14: Variation of Strain Energy density along the wear surface Top, and along the crack tip surface Bottom.

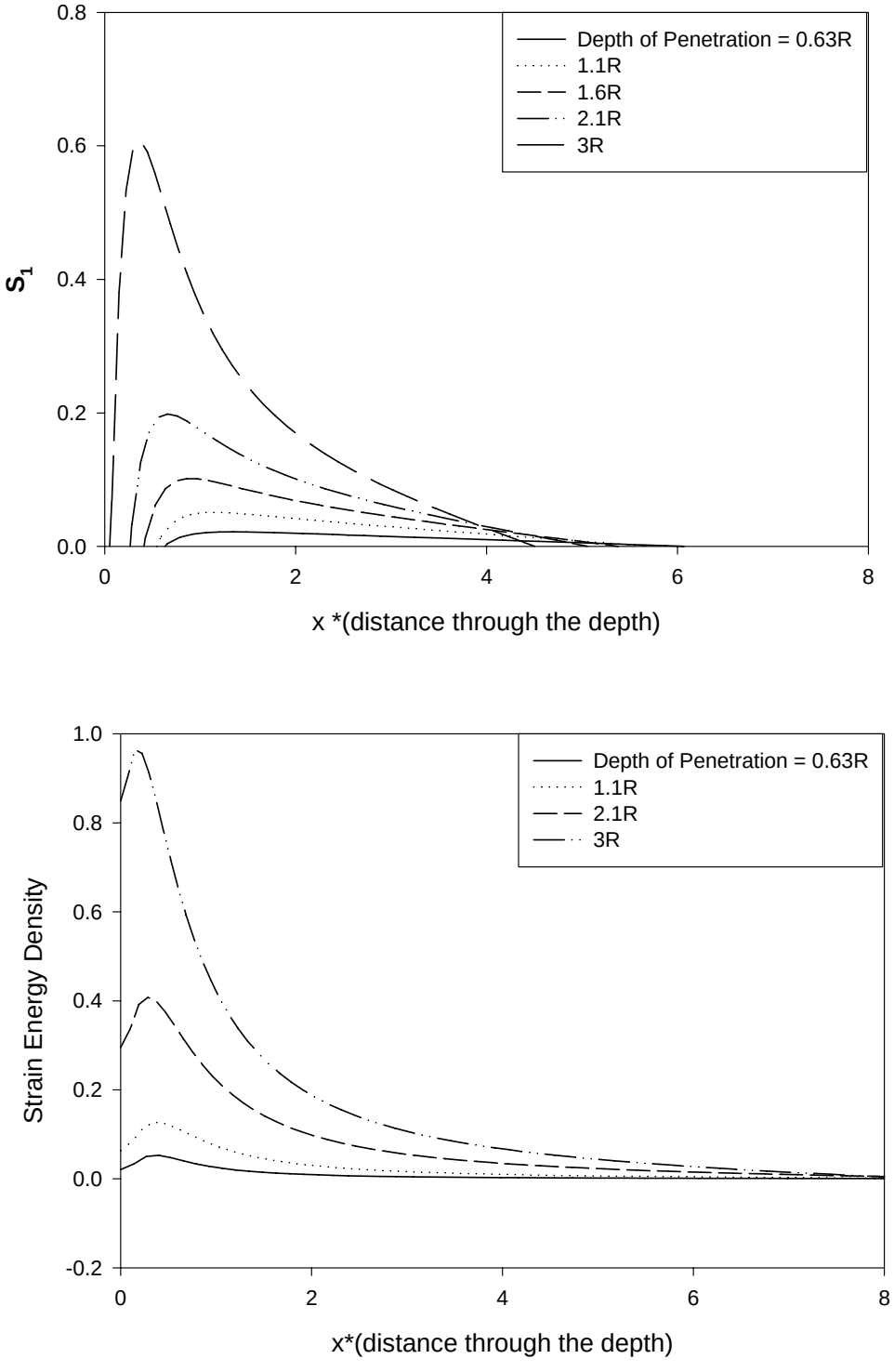

FIGURE 3.15: Variation of Maximum principal stress, Top and Strain Energy density through the depth at the point of penetration, Bottom.

3.4.2 Stress State Under Asperity Travel at a Fixed Depth

Figures 3.16 A-B show the Maximum Principal stress contours when an asperity of radius R (R=10mm) penetrates at a distance R to a depth R from a blunt crack of length R and the crack tip radius <<0.1R. A Coulomb friction model with friction coefficient of 1.0 is used for surface interaction. When an asperity penetrates close to a crack defect, there is large deformation. The contact area is no longer symmetric as in the case of Loading A. This deformation also leads to contact between the two walls of defect and resulting closing of the crack. There is also large rotation at the crack-tip after the penetration reaches beyond certain depth. The asymmetry of the contact area is also present in the maximum principal stress along the wear surface. As Figure 3.17 (Top) shows, with the increasing depth of penetration, the asymmetry in stress decreases slightly. This is however is not the case of the strain energy density distribution along the wear surface (Figure 3.17-Bottom). As the depth of penetration increases, the asymmetry in SED increases dramatically due to larger strain in the defect region. This shows the significance of choosing the appropriate failure criteria in this situation.

Figure 3.18 shows the Maximum Principal Stress and SED distribution along the crack-tip during the penetration. The peak stresses in this case are much higher compared to Loading A and the distribution is affected by the large self contact of the two walls forming the crack. This creates a large compressive stress on one side of the crack tip and a large tensile stress along another side of the crack-tip. The SED distribution shows similar variation but two positive peaks. Figures 3.19 A-B show the Maximum principal stress contours as the asperity travels away from the defect at a fixed depth of penetration R.

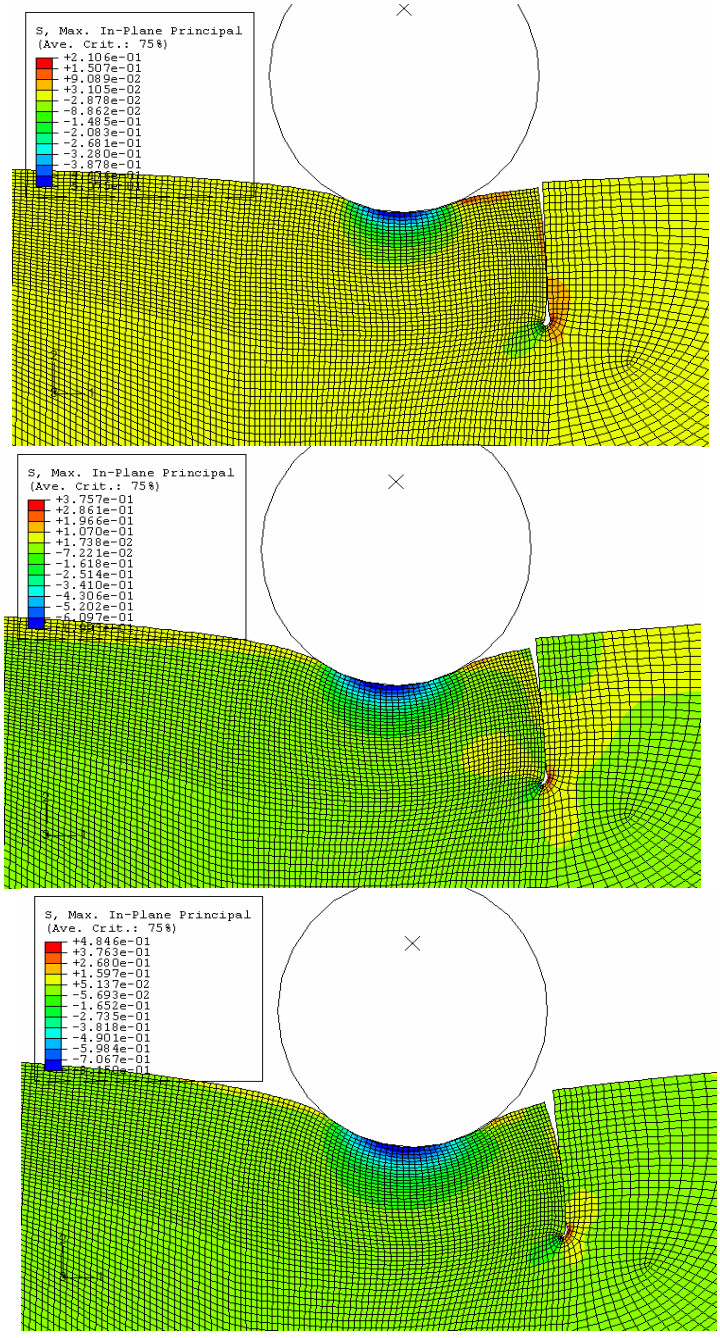

FIGURE 3.16: Maximum Principal Stress contours with asperity of radius R penetrating at a distance R from the defect to a depth of penetration of (A): Top: 0.3R Middle: 0.55R Bottom: 0.7R

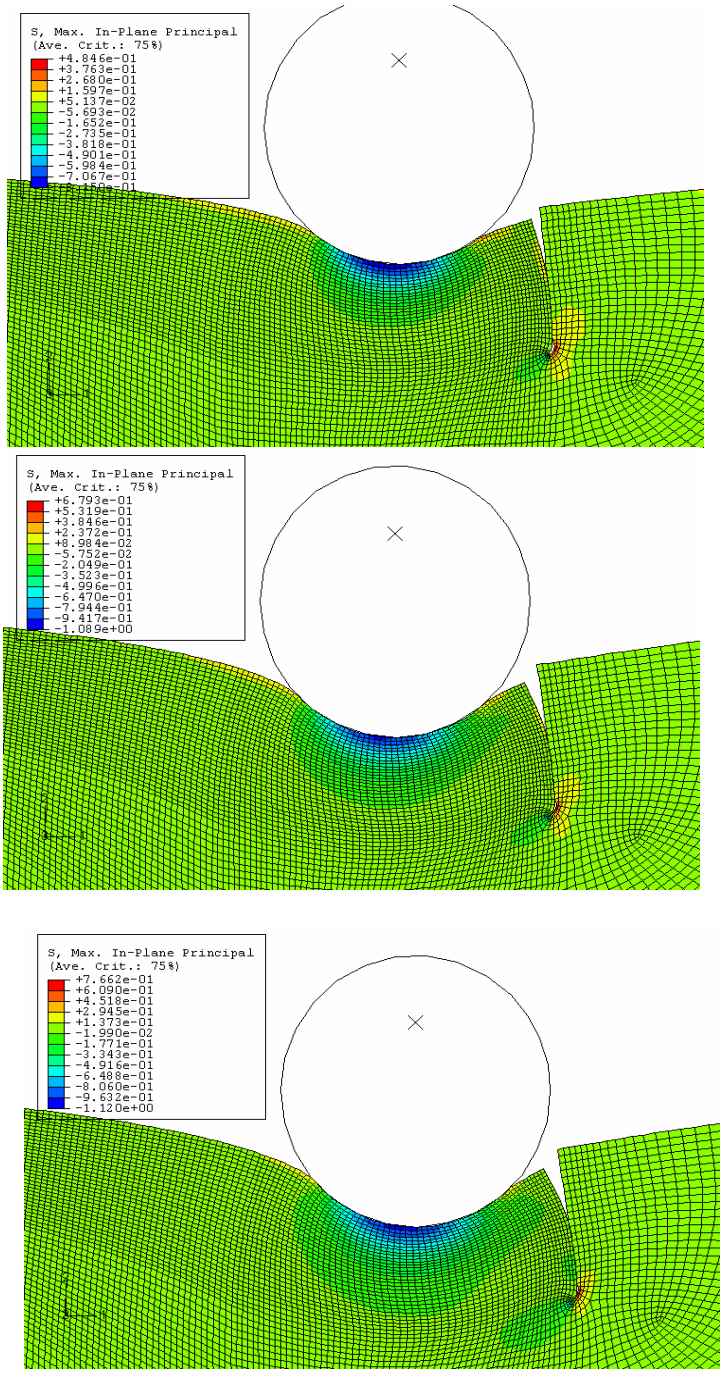

FIGURE 3.16 : Maximum Principal Stress contours with asperity of radius R penetrating at a distance R from the defect to a depth of penetration of (B): Top: 0.9R Middle: 0.95R Bottom: 1R

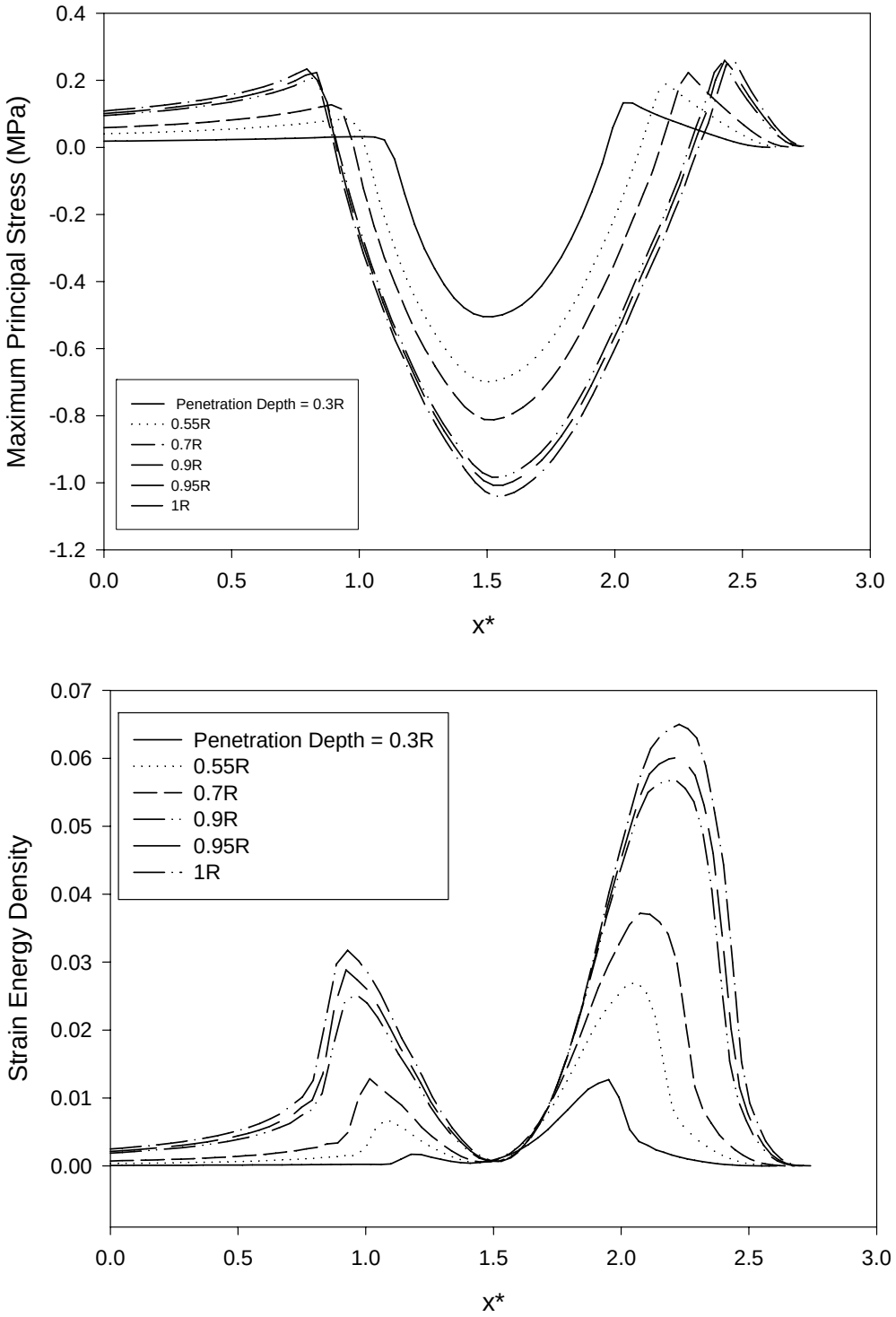

FIGURE 3.17: Top: Variation of Maximum Principal Stress and Bottom: strain energy density along the wear surface for asperity penetration at a distance R from the defect.

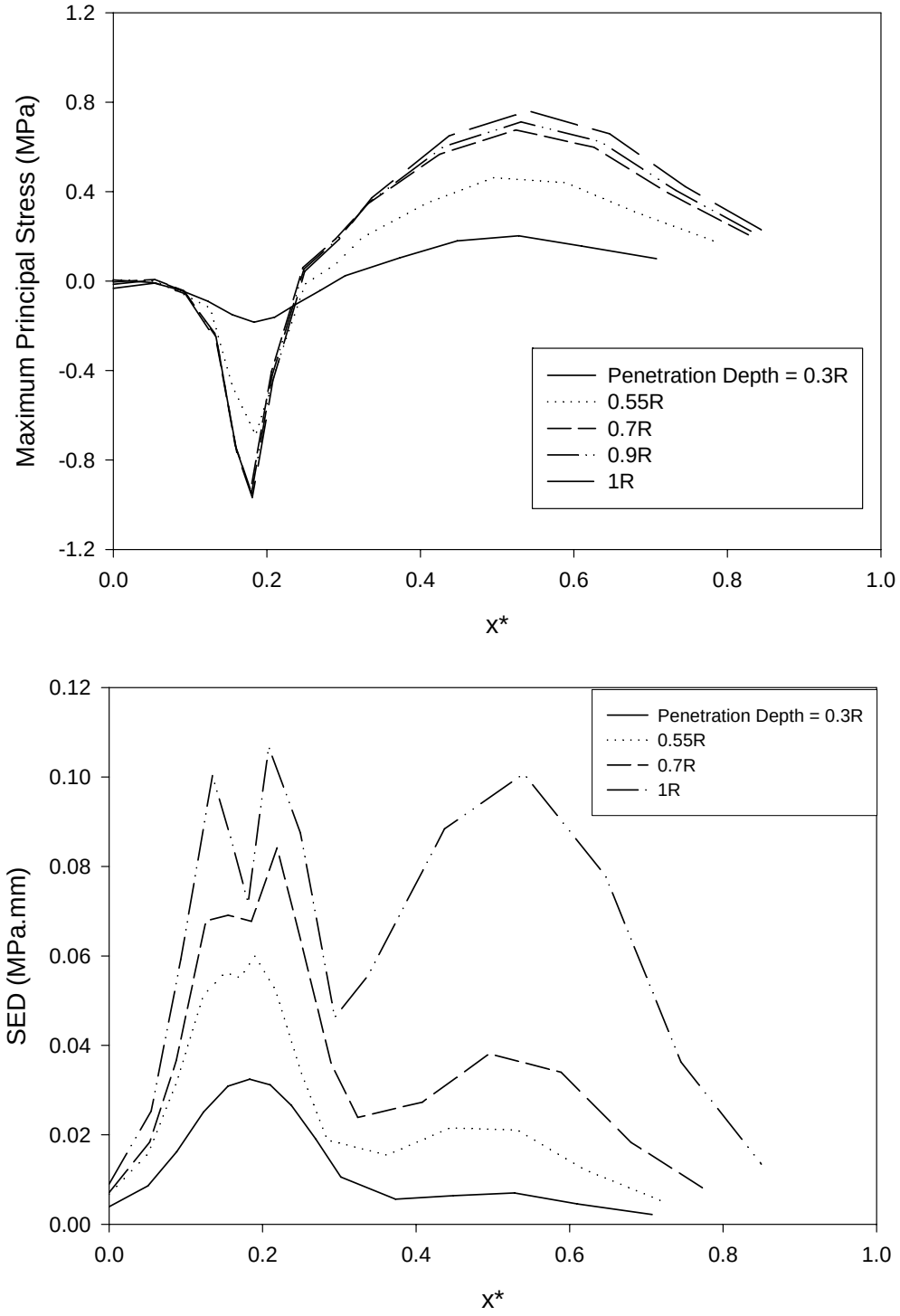

FIGURE 3.18: Top: Variation of Maximum Principal Stress and Bottom: strain energy density along crack tip for asperity penetration at a distance R from the defect.

As the asperity moves away from the defect, the high stress zones in the contact area show changes. This is because of the higher friction forces involved in translational motion. Similarly, the crack-tip 'opens up' as one of the walls is gradually pulled away in the direction of motion. As the travel continues, the effective contact area decreases. This is seen from the variation of maximum principal stress along the wear surface (Figure 3.20 Top). As the shearing action continues with the travel, the peak in the maximum principal stress becomes sharp. The initial negative (compressive) principal stress zone in the contact area changes to a tensile stress zone as the shearing continues. However, the maximum principal stress is no longer 'tangential' to the wear surface but is at an angle (<30 deg) to the wear surface. With the increasing travel distance, the mesh may show some shear distortion. This creates the onset of distortion related instability and reflects in the lack of smoothness of the maximum principal stress variation along the path. The strain energy density variation along the wear surface shows a sharp peak at the leading edge of the asperity, indicating the excessive local deformation.

As the crack-tip opens under shearing, the self-contact between the crack walls diminishes and the maximum stress as well as the deformation grows rapidly. Figure 3.21 shows the corresponding variation in maximum principal stress as well as strain energy density. It should be noted that the non-dimensionalized length of the path increases significantly indicating large circumferential strain. This causes high strain energy density as well as tensile stresses that are several times that experienced by the wear surface. Such a deformation is likely to lead to propagation of the defect (crack) than cause any new cracks of the same geometric scale at the wear surface.

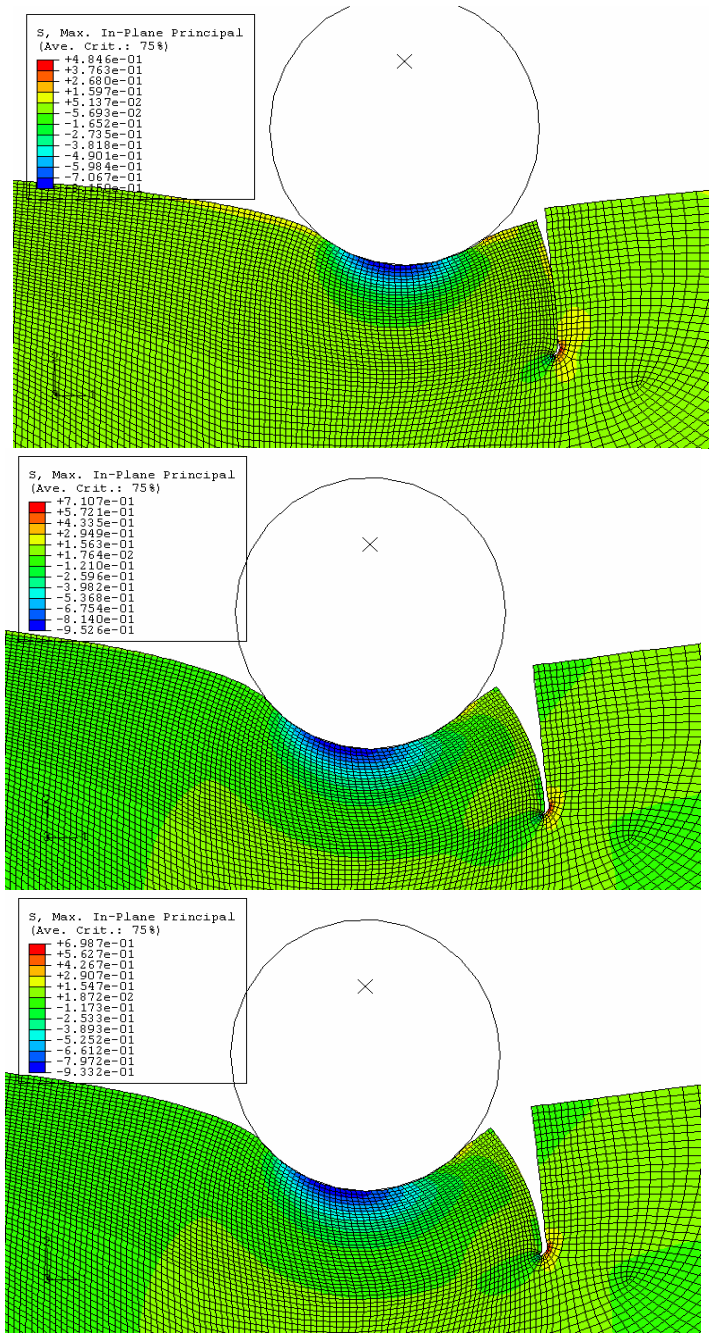

FIGURE 3.19: Maximum Principal Stress contours with asperity moving away from a defect for depth of penetration of 1R at a distance of (A): Top:0.04R Middle: 0.045R Bottom: 0.1R

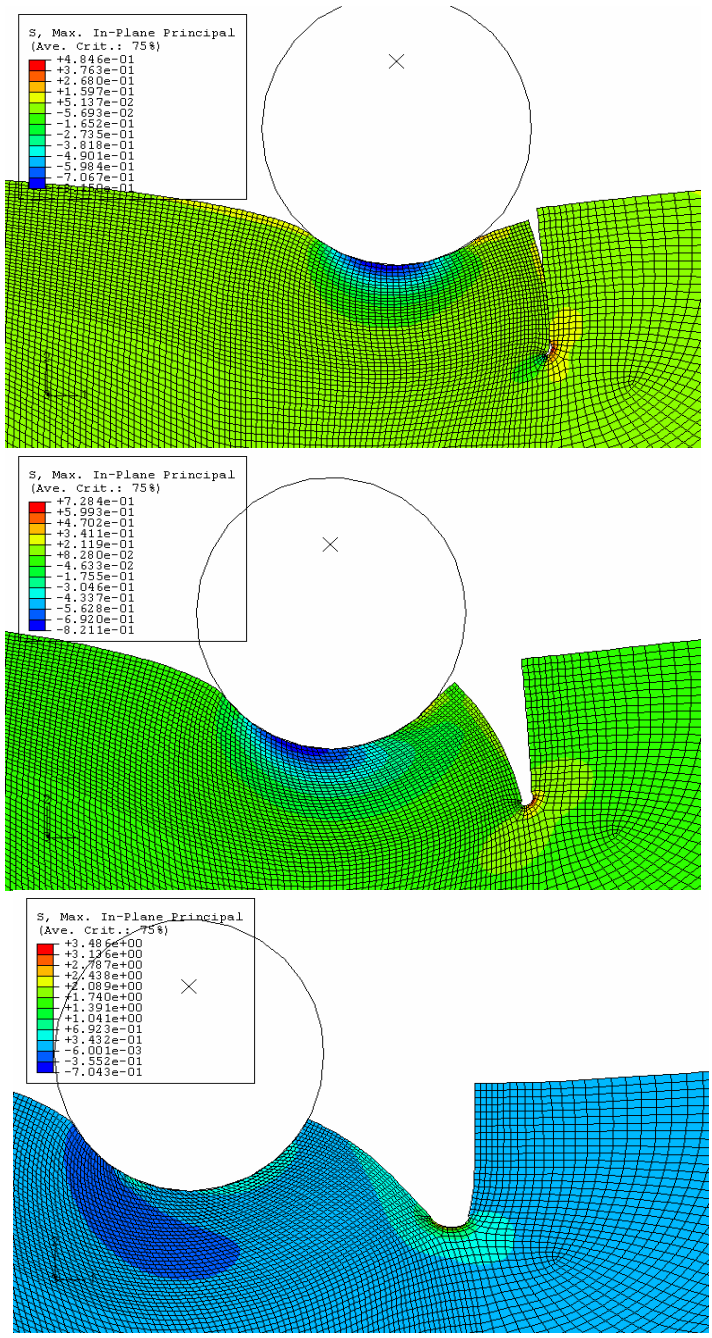

FIGURE 3.19: Maximum Principal Stress contours with asperity of radius R moving away from a defect for depth of penetration of 1R at a distance of (B): Top: 0.26R Middle**:** 0.3R Bottom:0.36R

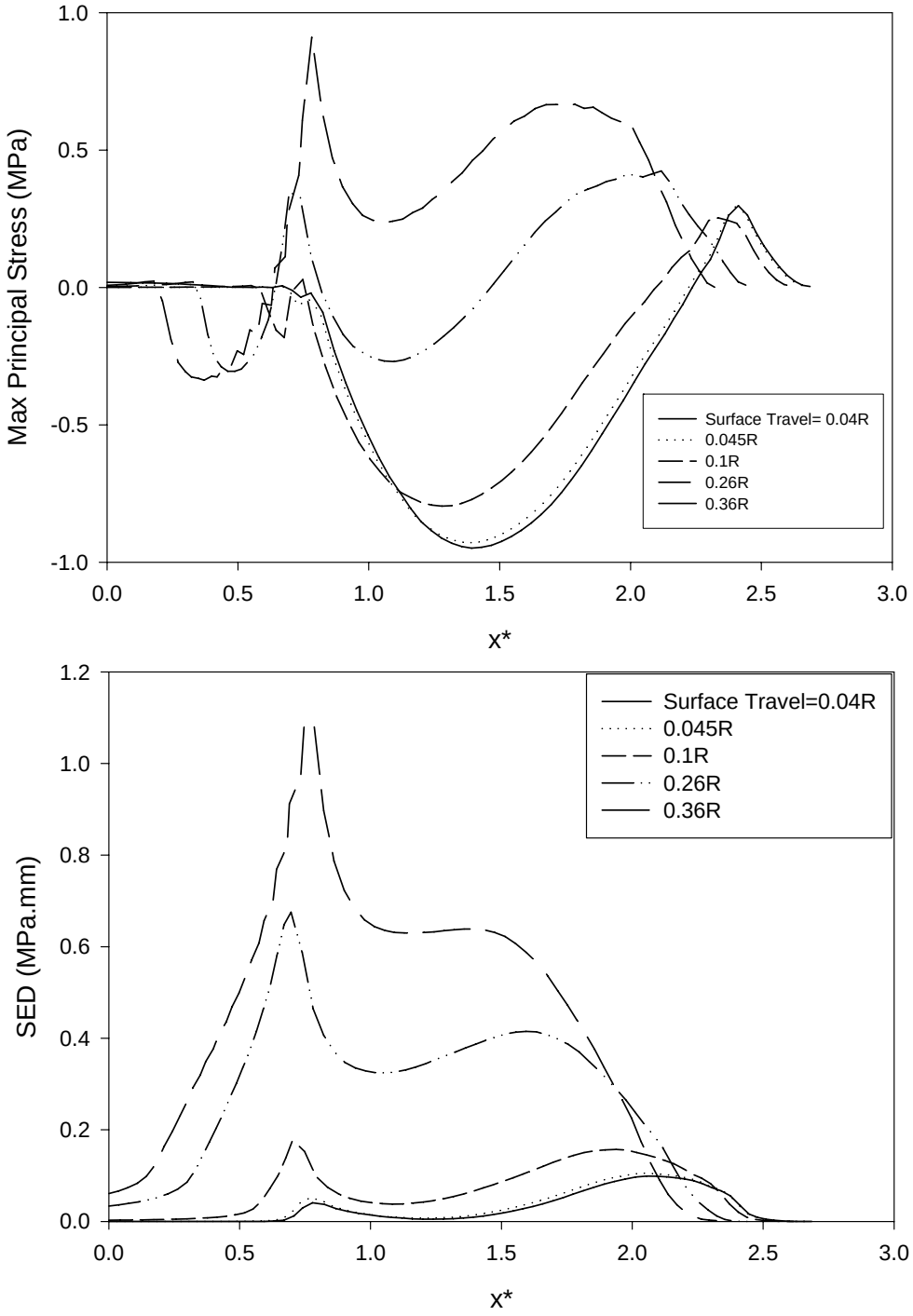

FIGURE 3.20: Variation of Top: Maximum Principal Stress and Bottom: strain energy density along wear surface for asperity travel away from the defect at penetration R.

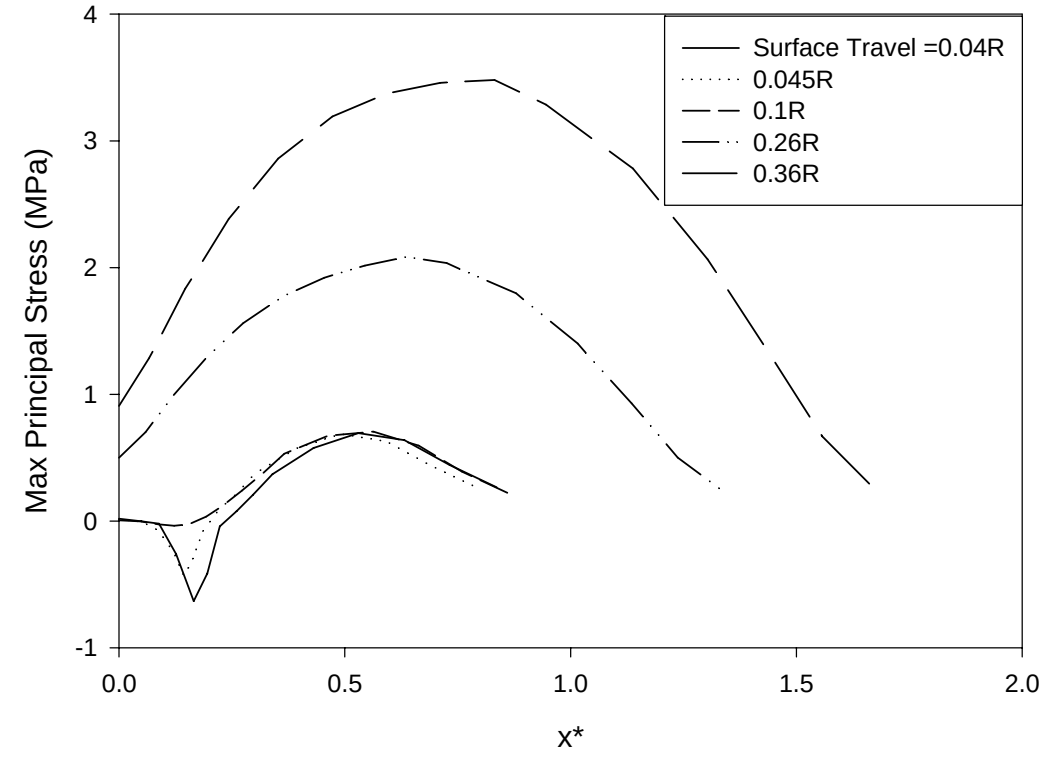

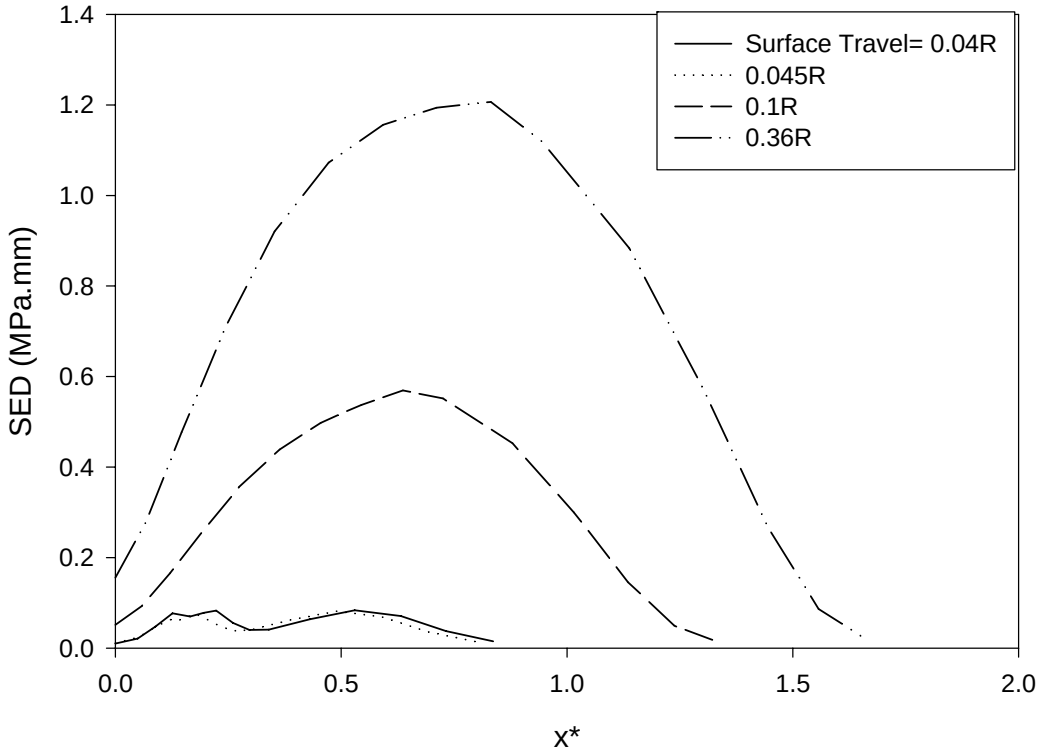

FIGURE 3.21: Variation of Maximum Principal Stress Top and strain energy density Bottom along crack tip for asperity travel away from the defect at penetration R.

The high shear distortion of the mesh limits the maximum translational displacement for a single run. Typically, the problem can be solved by remeshing the deformed geometry. However the nonlinear nature of the problem creates difficulties in remapping and equilibriating the stress on to the new mesh. One of the primary objectives of the study is to find the minimum distance from the defect at which the stress relief caused by the defect is negligible. In order to achieve this, a number of simulations were conducted where the asperity penetrates a certain interval from the defect and follows it by a travel away from the defect. The distance traveled by the asperity is sufficient to establish a steady shear deformation. Figure 3.21 shows the maximum principal stress and strain energy density data along the wear surface as the asperity travels away from the defect at a fixed depth of penetration of R. For distances up to 1.5R from the asperity, the maximum principal stress is much smaller compared to the corresponding stress when the asperity is not present. As soon as one moves away from the defect, the peak stress along the wear surface reaches levels that are close to the case when there is no defect. This distance may be roughly approximated as 3.3~3.5R. The same variation is also found in the strain energy density along the wear surface. The variation in the peak stress and SED along the crack-tip is a little different. For distances up to 2.3~2.5R there is actually increase in the crack-tip stress as the asperity travels away from the defect. When the asperity is really close to the defect, the peak stresses are affected by the closing of the crack. However, beyond a certain distance (in the present case, roughly 2.5R), the peak stresses start decreasing as the asperity is now further away from the defect.

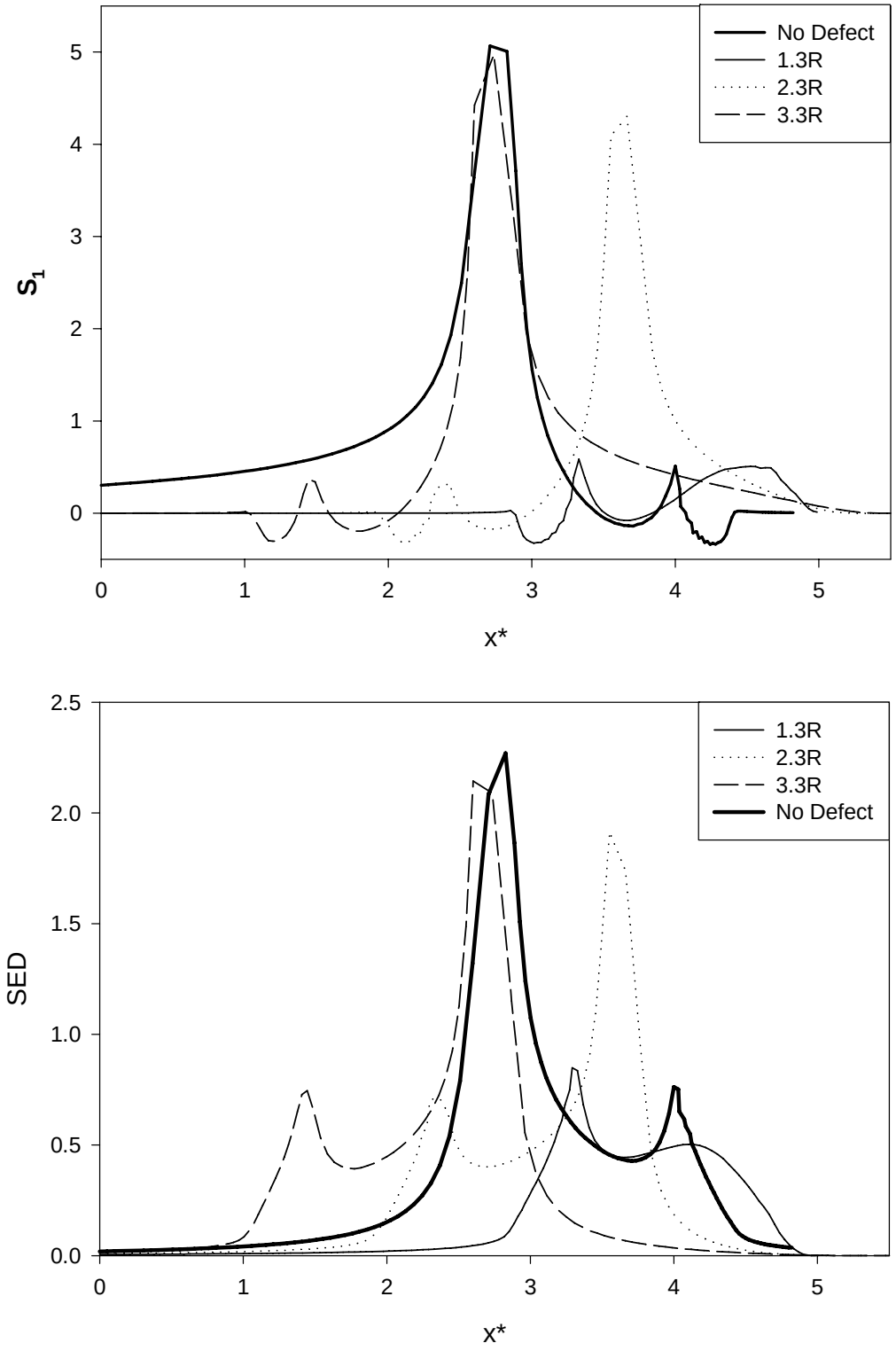

FIGURE 3.22: Variation of Maximum Principal Stress Top and strain energy density Bottom along crack tip for asperity travel away from the defect at penetration R

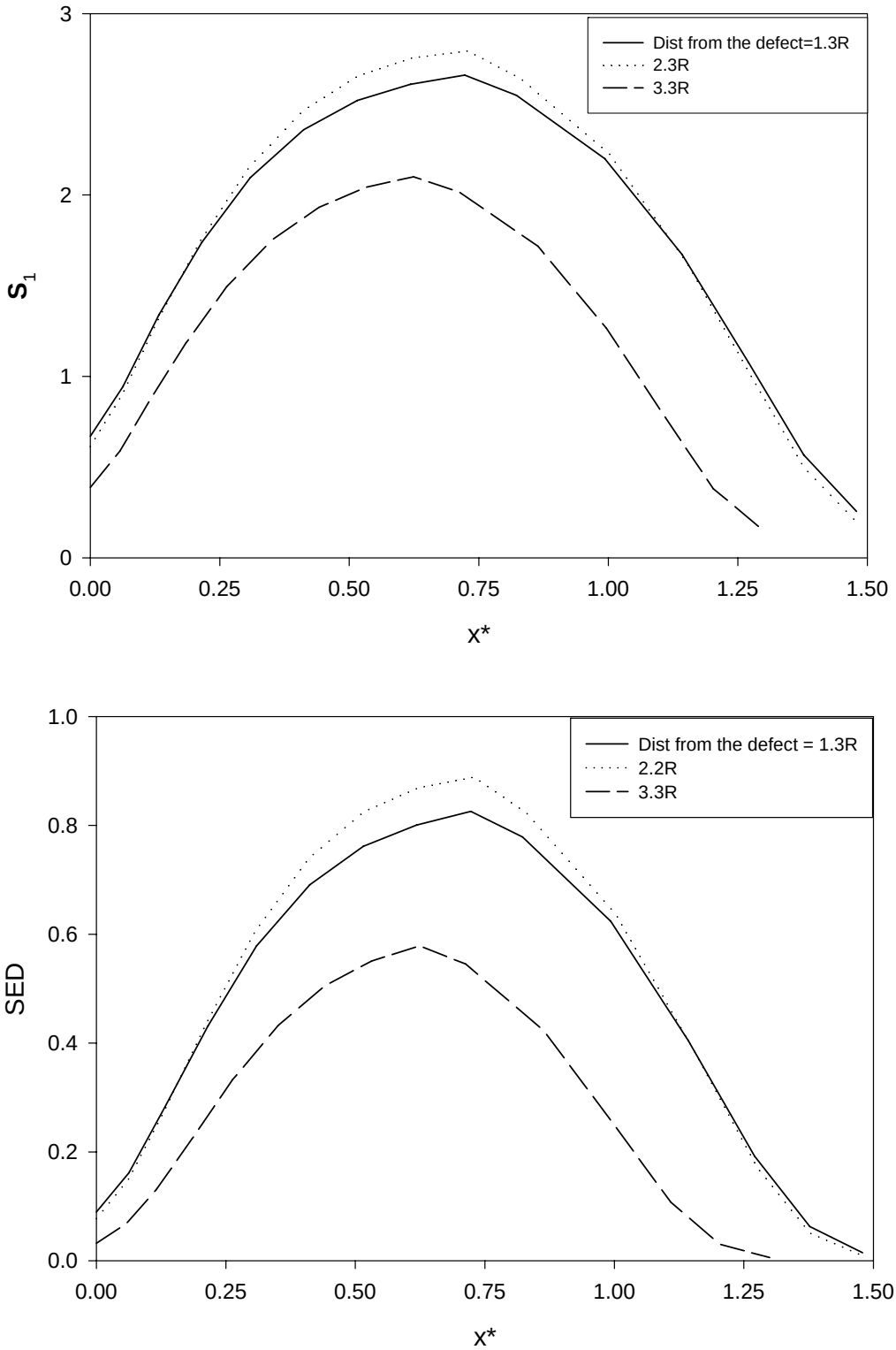

FIGURE 3.23: Variation of Maximum Principal Stress, Top and strain energy density, Bottom along crack tip for asperity travel away from the defect at penetration R.

There is a clear picture that emerges from the figures 3.20 and 3.21. When the asperity is traveling away from a defect, at small displacements, a large part of the deformational energy is concentrated at the crack tip and the wear surface records relatively low stresses. As the asperity moves away from the defect, the deformational energy is predominantly at the wear surface where as the crack-tip shows lower stresses. This means that in the particular case, up to a travel of 2.5R, the likelihood of the existing defect to propagate is much larger than that of a new defect formation at the wear surface. This means that the minimum distance between the next defect is likely to be at least 2.5R assuming homogeneous material properties.

The above quantitative observations are strictly true for the simulated problem where the asperity size, the depth of penetration and the crack defect length are exactly equal (R). However, the qualitative observations should hold true even when there is a change in one of the relevant parameters.

3.4.3 Observations for Stress Fields Around Asperity Penetration in Filled Rubbers

The general observations regarding stress fields under asperity penetration and translation in previous sections were for straight cracks in unfilled material (SBR1). These qualitative observations are equally valid for filled materials (SBR2, SBR3). Figure 3.24 and 3.25 are the Maximum Principal Stress contours for penetration of an asperity near a crack oriented at 30^0 to the vertical for the material SBR2. Figure 3.26 and 3.27 are the corresponding Maximum Principal Stress Contours for penetration and translation away from the crack at conditions identical to those in Figures 3.24 and 3.25 but for an asperity size that is twice that of the asperity in Figures 3.24 and 3.25.

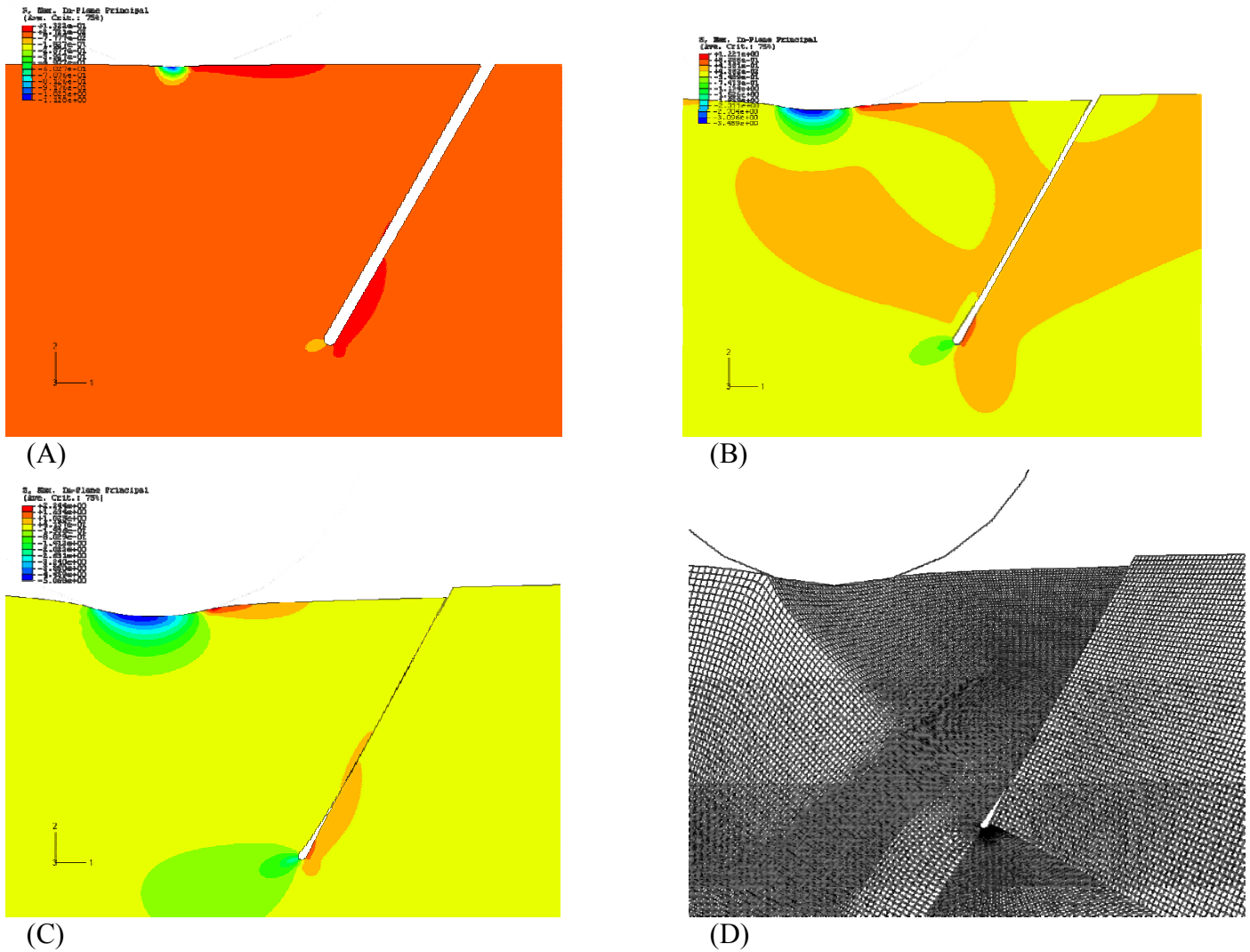

(A) (B)

(C) (D)

FIGURE 3.24: Asperity radius 0.75R. Penetration Step Frames 0, 1, 2, and deformed mesh for frame 2, μ=1.0

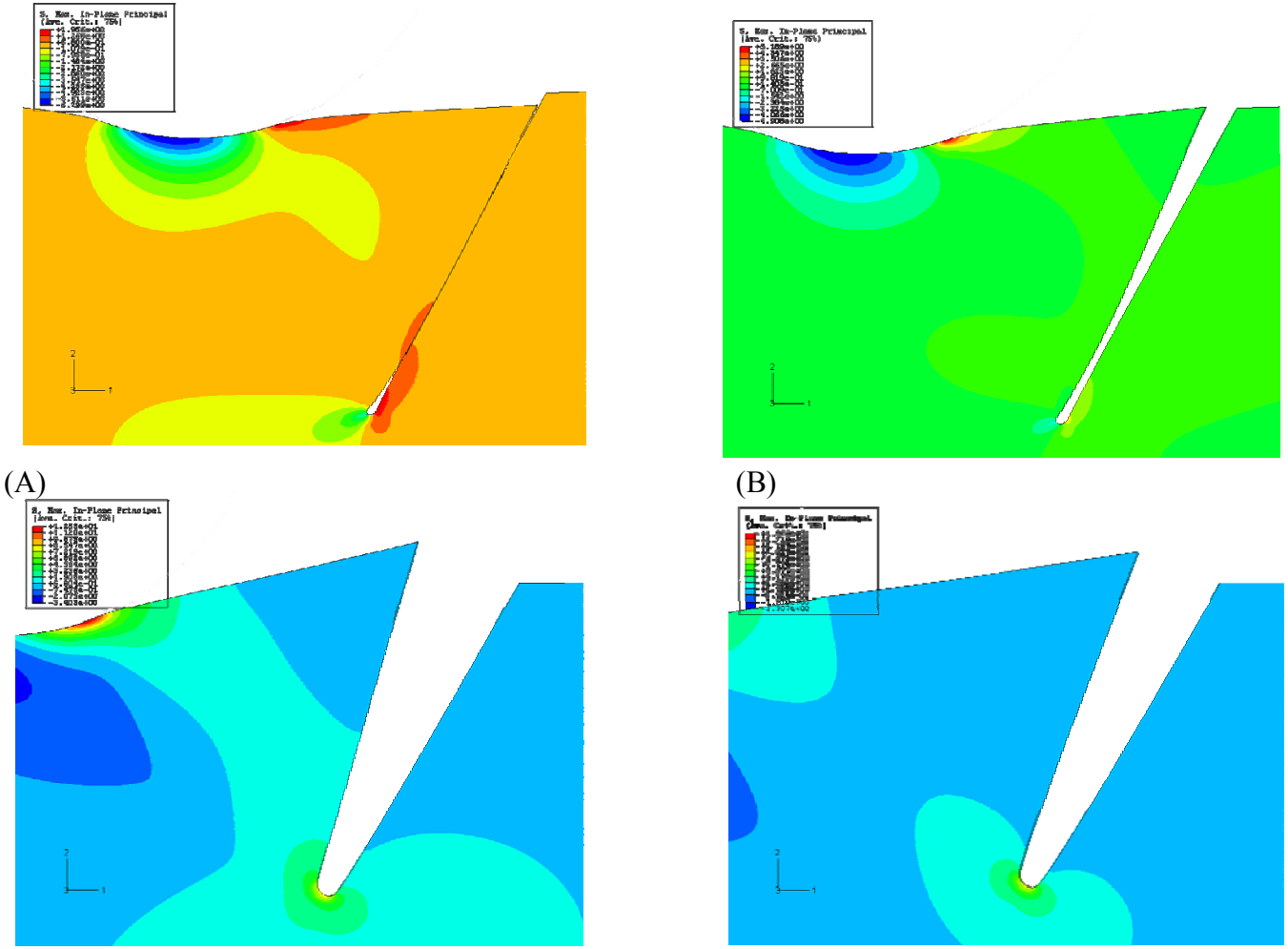

(A) (B)

(C) (D)

FIGURE 3.25: Asperity with Radius 0.75 R receding from Crack frames 0, 1, 2, 3, friction coefficient 1.0

When a crack at an angle to the perpendicular to the crack surface is introduced, it changes the nature of the contact mechanics at the asperity, rubber surface interaction. In particular, the crack walls come into contact more readily than with the crack perpendicular to the surface. The high friction coefficient between the two crack walls (μ =1.0) creates a shearing condition from the contact. The contact pressure transmitted to the walls from the asperity penetration, may also cause the crack-tip to get compressed. Although these phenomena are also evident in a perpendicular crack, they happen to a lesser degree. As the asperity moves away from the crack at a particular depth of penetration, the two sides of the crack that are in contact, slowly open up. This causes change in the stress direction from the compressive to the tensile stress.

Also, for the same depth of penetration, material and friction conditions, a larger asperity tends to have a larger contacting area. When the asperity travels away from the crack, this contact area determines the degree of shear stress area on the surface of the elastomer. This causes a very different contact behavior when traveling away from the crack. Figue 3.25 shows a smaller shearing area, and has lesser influence on the crack-tip. Figure 3.27 shows a larger shear area from a larger asperity that causes a larger adhesion with the crack surface. This results in a larger opening of the crack when the asperity travels away from the crack.

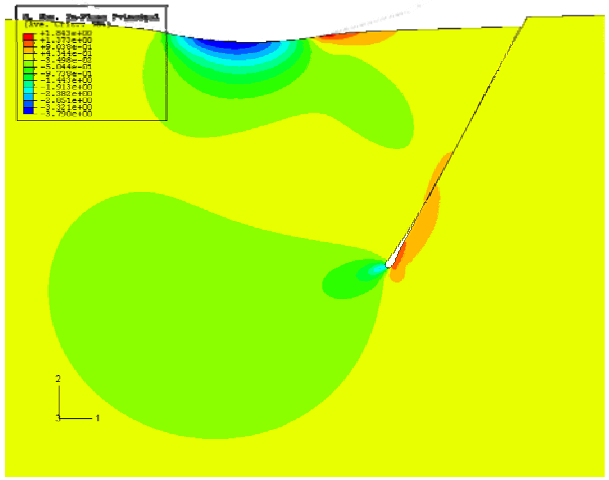

(A)

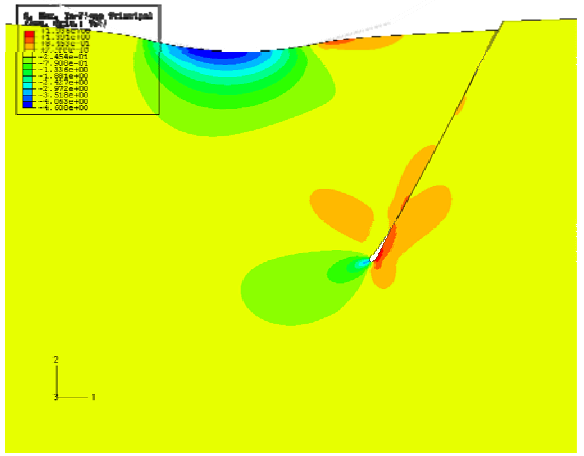

(B)

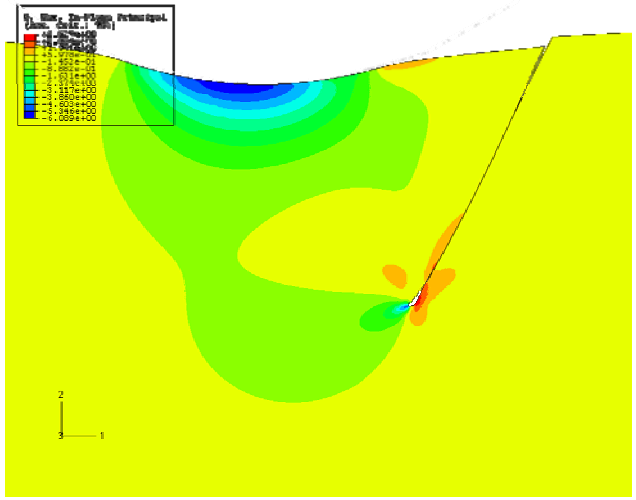

(C)

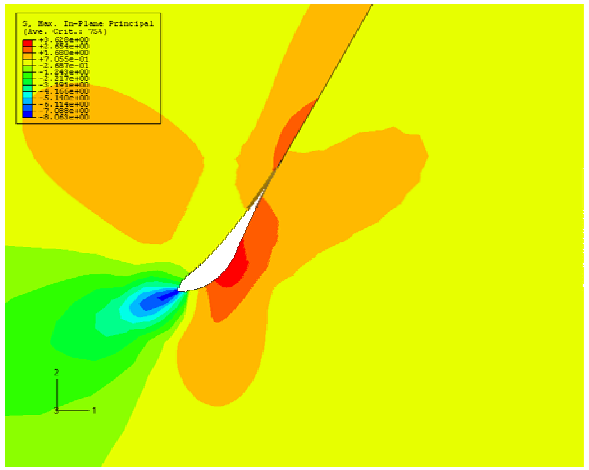

(D)

FIGURE 3.26 Asperity radius =1.5R penetration step. Frames 26, 33, 42, 50

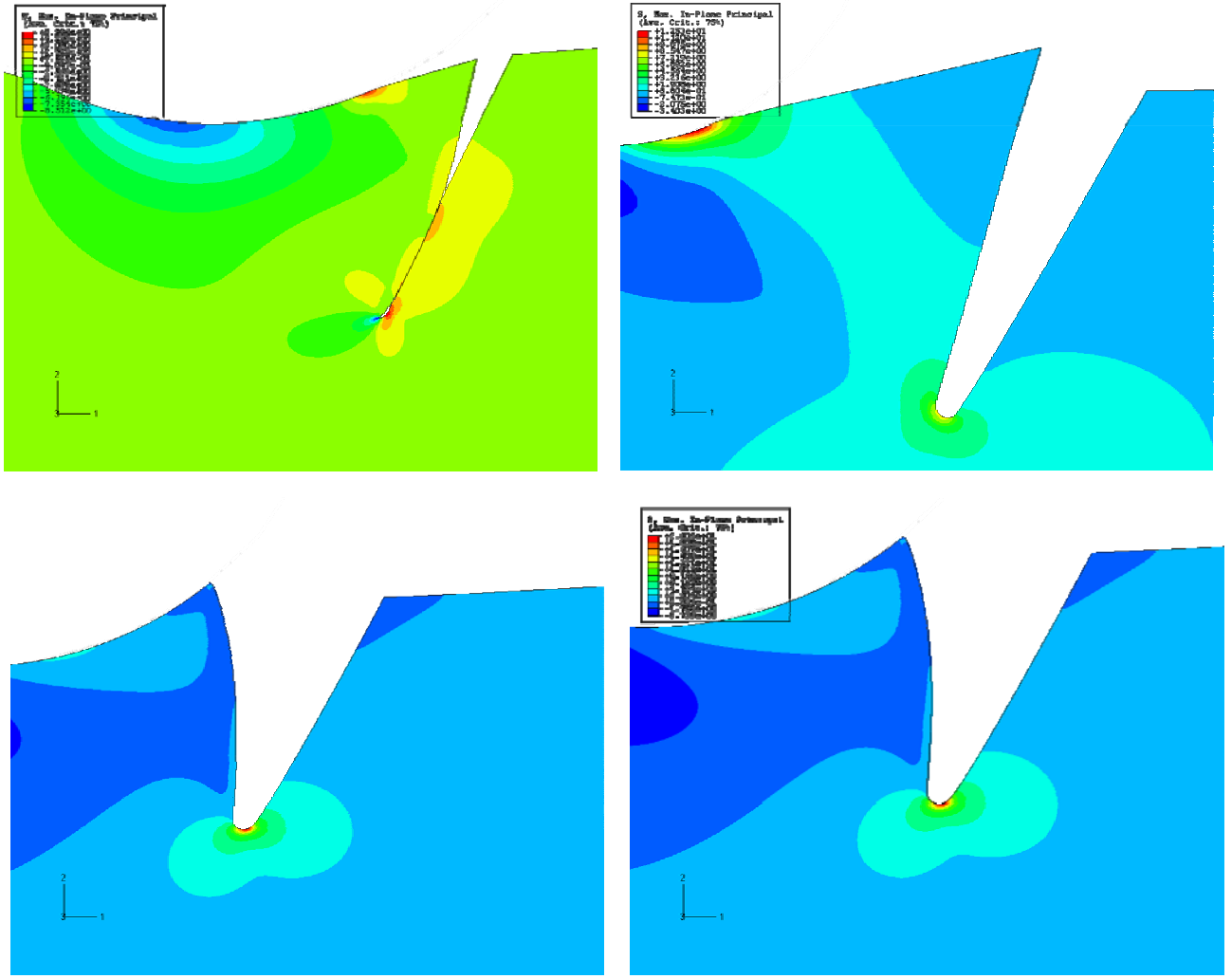

FIGURE 3.27: Asperity radius 1.5R receding awav from crack frames 1,2,4,5, friction = 1.0

CHAPTER IV

ENERGY RELEASE RATE

Chapter III described some general results when a single asperity interacts with a rubber surface in the presence of a crack. In the present chapter, a method is proposed to calculate the possibility of a new crack initiation. This method is the application of the general crack energy release rate approach to the surface cracks. The proposed method is then used to investigate to see if the stress relaxation in the vicinity of a crack influences the crack initiation locally.

Again, the particular asperity loading condition discussed in the previous chapter is considered. Figure 4.1 and 4.3 illustrate the Maximum Principal Stress distribution near an asperity contacting a wear surface, during the penetration (4.1) and the receding (4.3) stage. The asperity is penetrating close to a crack of the size 0.5R, where 1.5 R is the radius of the asperity and the friction coefficient for asperity interaction with the elastomer is 0.5. Figures 4.2 and 4.4 show the corresponding strain energy density plots. From these plots, it is clear that predominantly, the largest maximum principal stresses are found (1) at the crack-tip, (2) the side walls of the crack during penetration stage, and (3) the wear surface in the wake of the asperity in motion. These are the most likely areas of new crack initiation. The experimental data for energy release rate for the cracks in finite elastic bodies is typically available for a few standard cases of stress states. In general, the energy release rate for a complex state of stress is hard to measure.

Fortunately, a close examination of the state of stress at the areas candidate for the high crack propagation rates, are predominantly under tension. Figure 4.5 illustrates the Principal Stress direction at the edge of an asperity contact. The Maximum Principal Stress in this case is the dominant stress and is tangential or nearly tangential to the contact surface in the deformed configuration. Similary, the crack far wall (during penetration) and the crack tip (during receding asperity motion) show areas where, the maximum principal stress creates a near uni-axial tensile zone. This is observed for both the plain stress as well as plain strain elements.

4.1 Crack Initiation Criterion

In this study, the crack initiation event is regarded as crack propagation of a defect that has a dimension of at least one order lower or smaller than the blunt crack modeled in the system. In this sense the criterion for crack initiation is replaced by the criterion for crack propagation at lower length scales. The advantage of this approach is self-evident as there is numerous experimental data in the literature that describes the crack propagation in both filled and unfilled rubber materials [56-60,82]. In comparison, much of the existing crack initiation data mentioned in literature is related to the type of initiation related to the cavitation of elastomeric material. This type of mechanism is plausible in certain applications such as compression seals. However, the mechanism typically results under pure triaxial hydrostatic tension state. This type of stress state is not typical of an asperity elastomer interaction dominated by stress regimes that vary from tensile to shear to compressive. On the other hand, crack propagation has been extensively studied in experiments that include both pure shear and uniaxial tensile stress state.

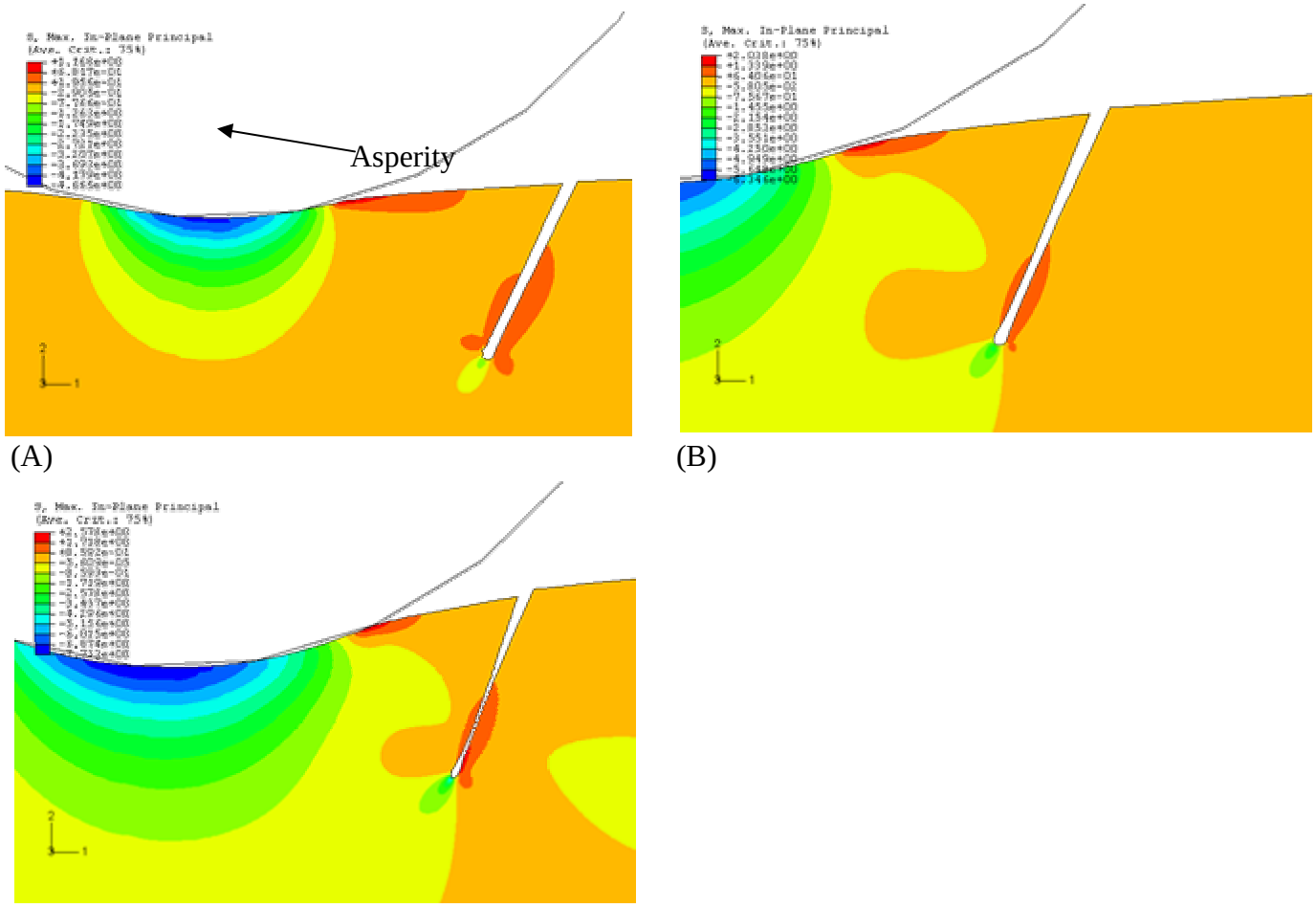

FIGURE 4.1: Variation of Maximum Principal Stress during penetration close to a crack.

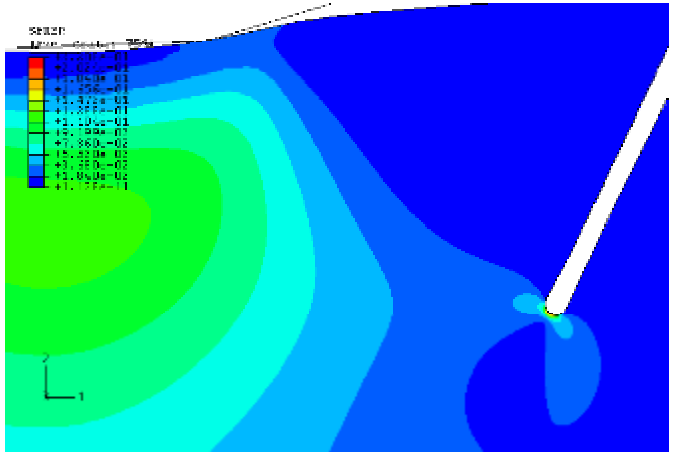

(A)

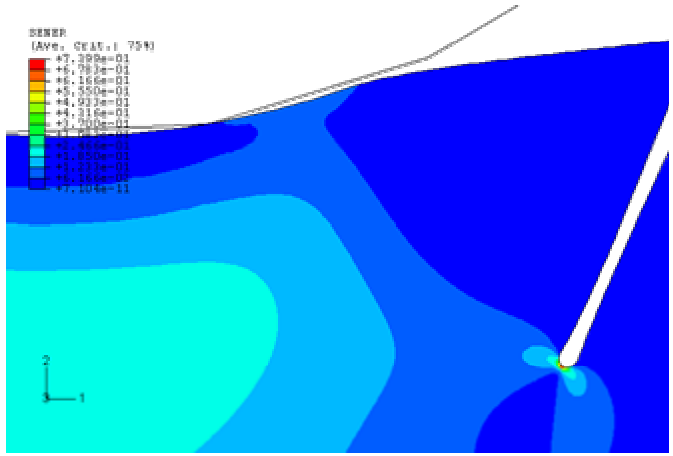

(B)

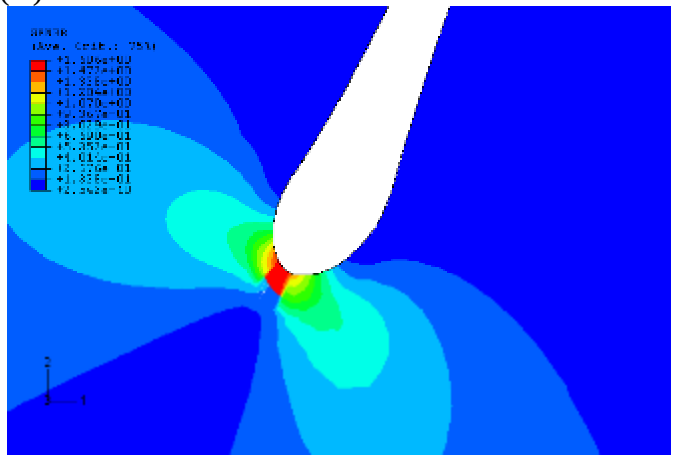

(C)

FIGURE 4.2: Variation of Strain Energy Density during penetration close to a crack. (A) and (B) show successively larger penetration and C shows the crack tip at the maximum penetration.

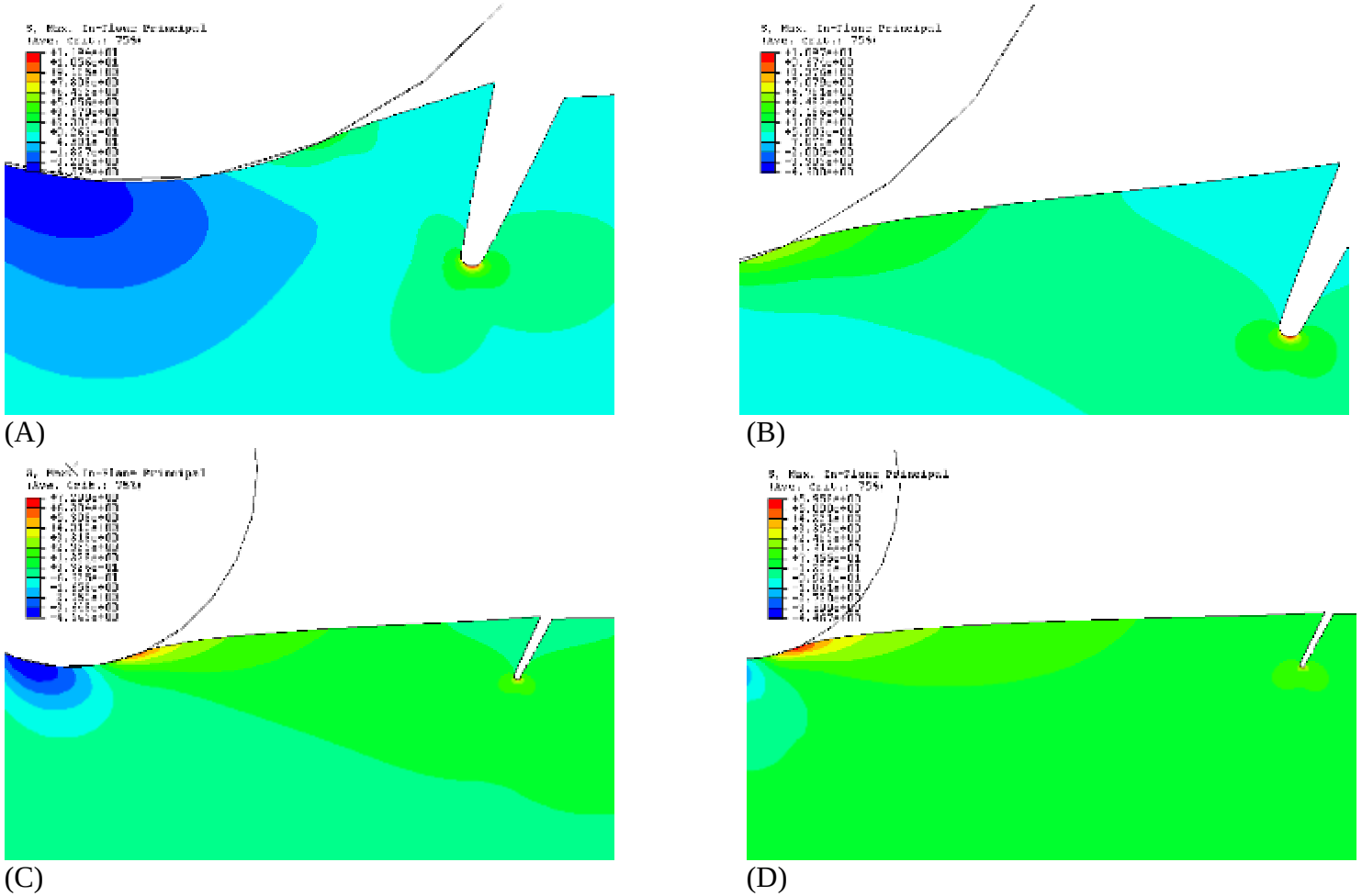

(A) (B)

(C) (D)

FIGURE 4.3: Maximum Principal Stress along the wear surface with asperity moving away from the crack. Radius = 15 mm = 1.5R .

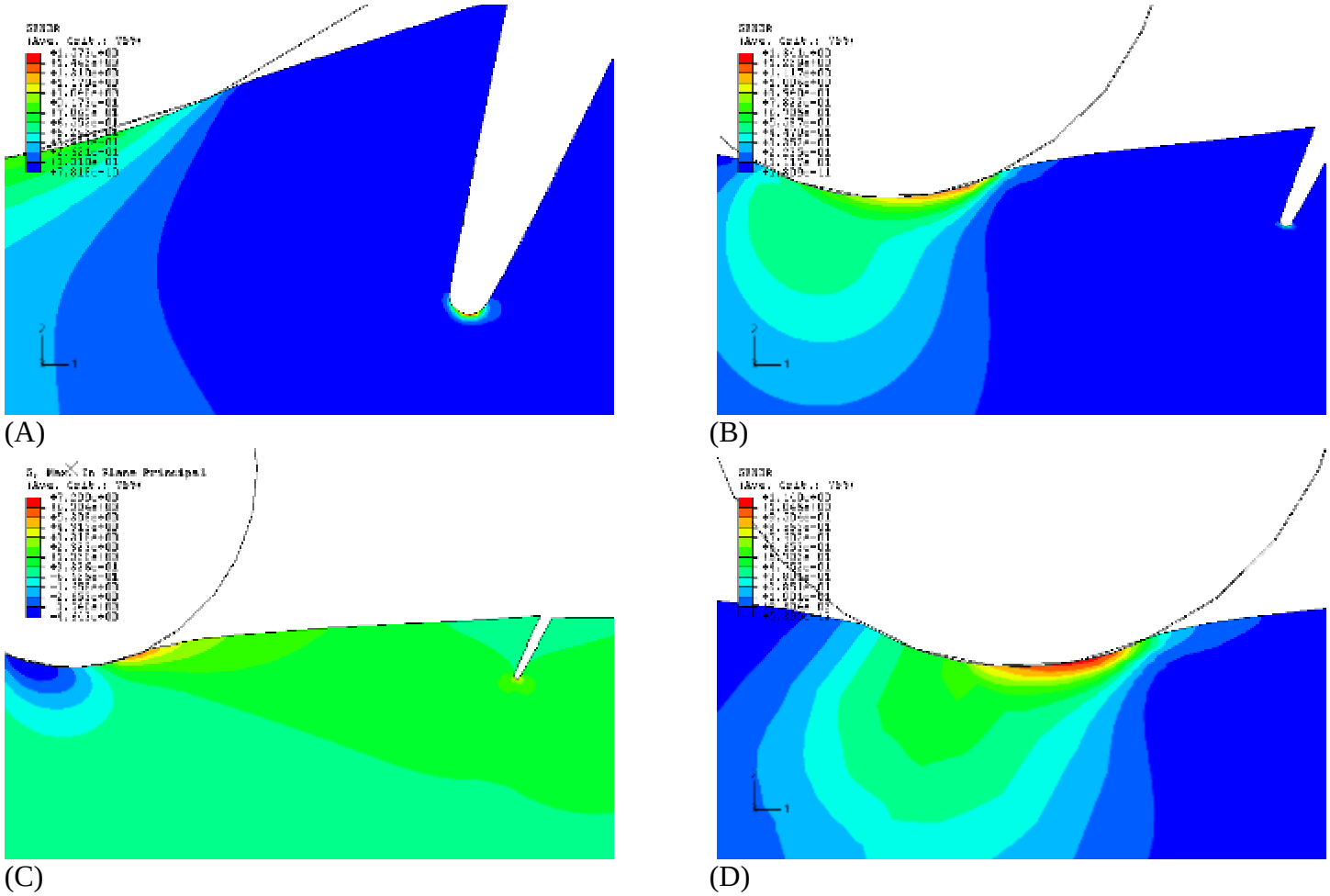

(A) (B)

(C) (D)

FIGURE 4.4: Strain Energy Density distribution with asperity moving away from the crack.

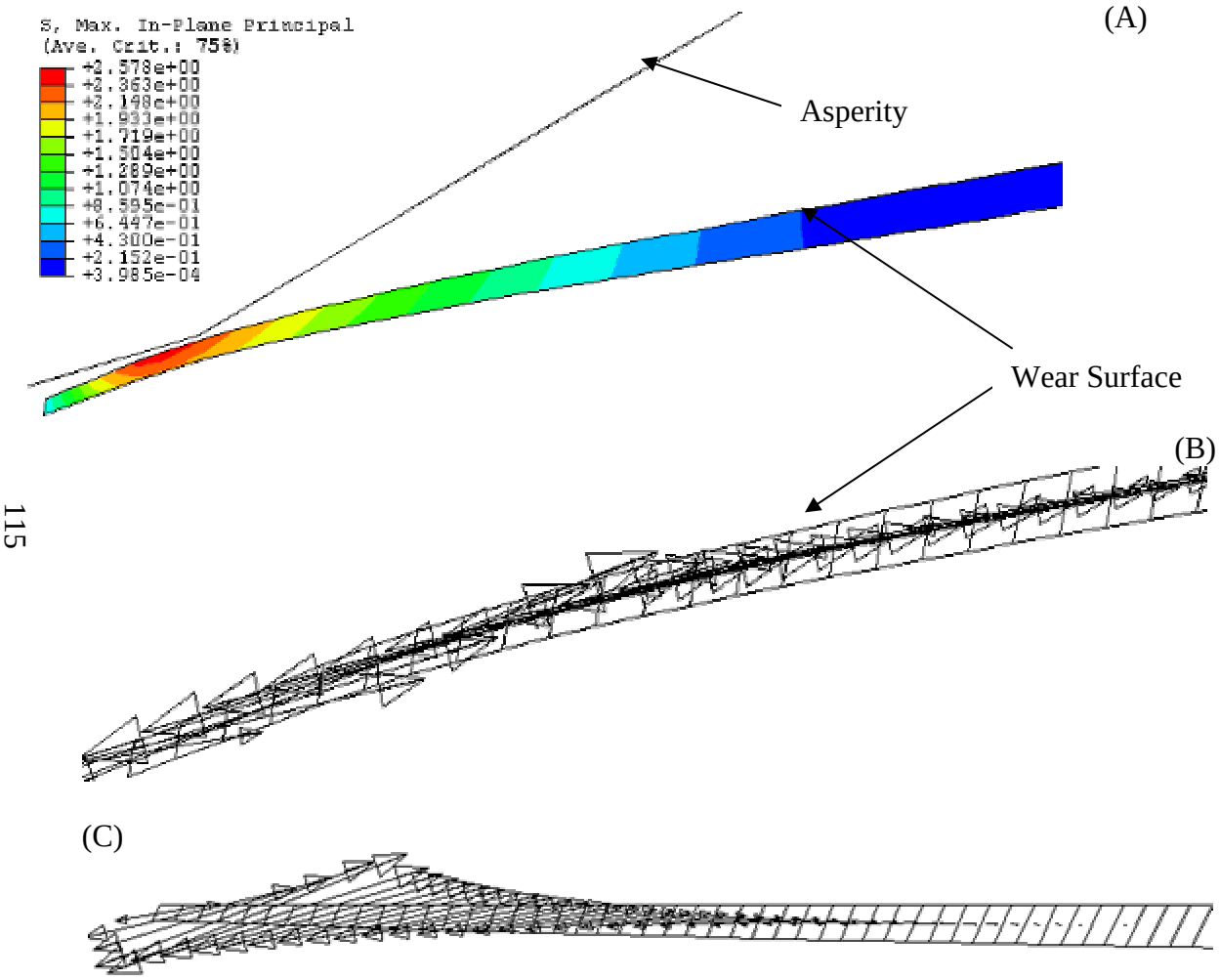

FIGURE 4.5: Maximum Principal Stress along the wear surface. (A) Distribution (B) Orientation in deformed coordinates (C) Orientation in undeformed coordinates.

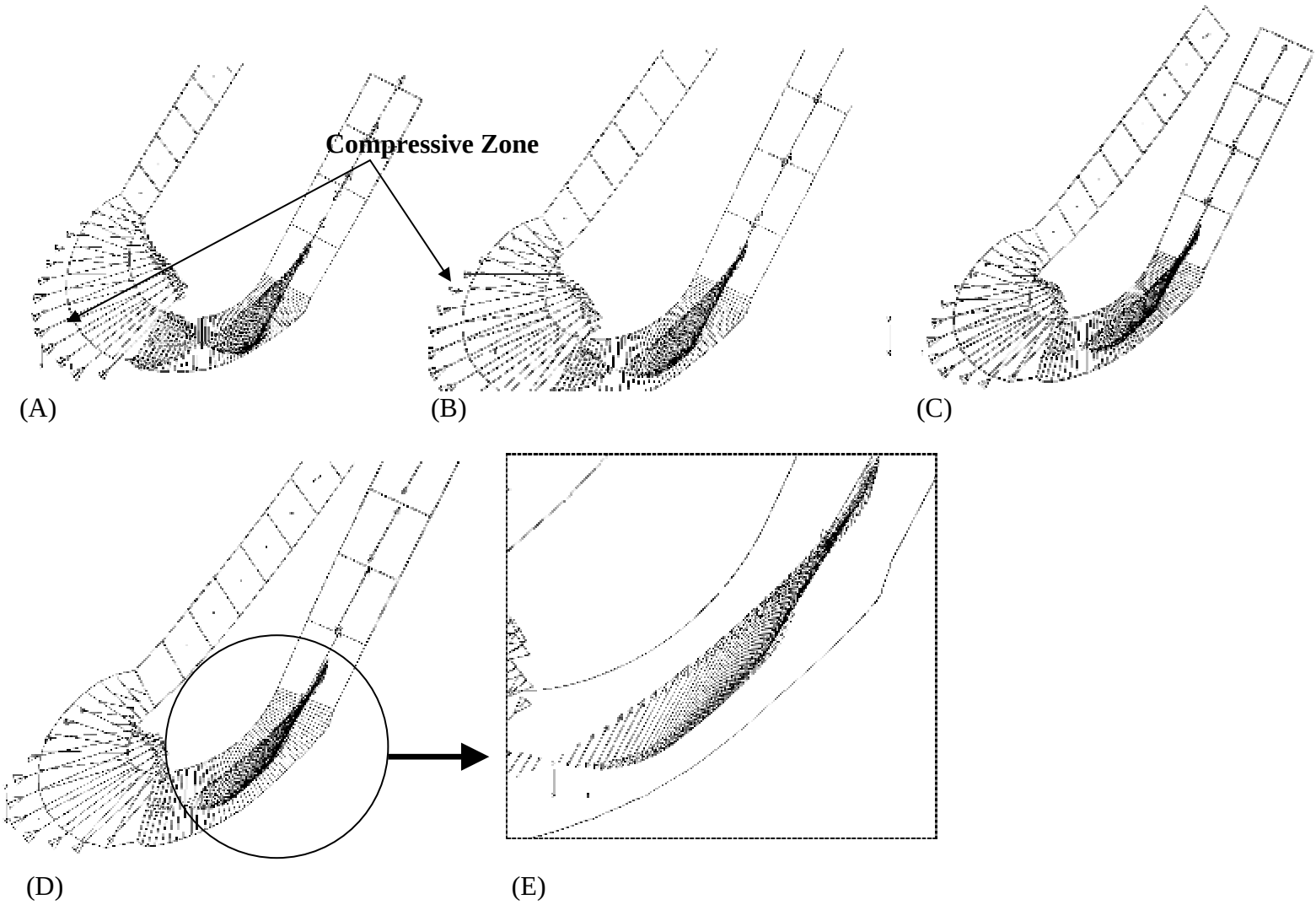

FIGURE 4.6: Maximum Principal Stress Direction around crack tip during asperity penetration close to the crack tip.

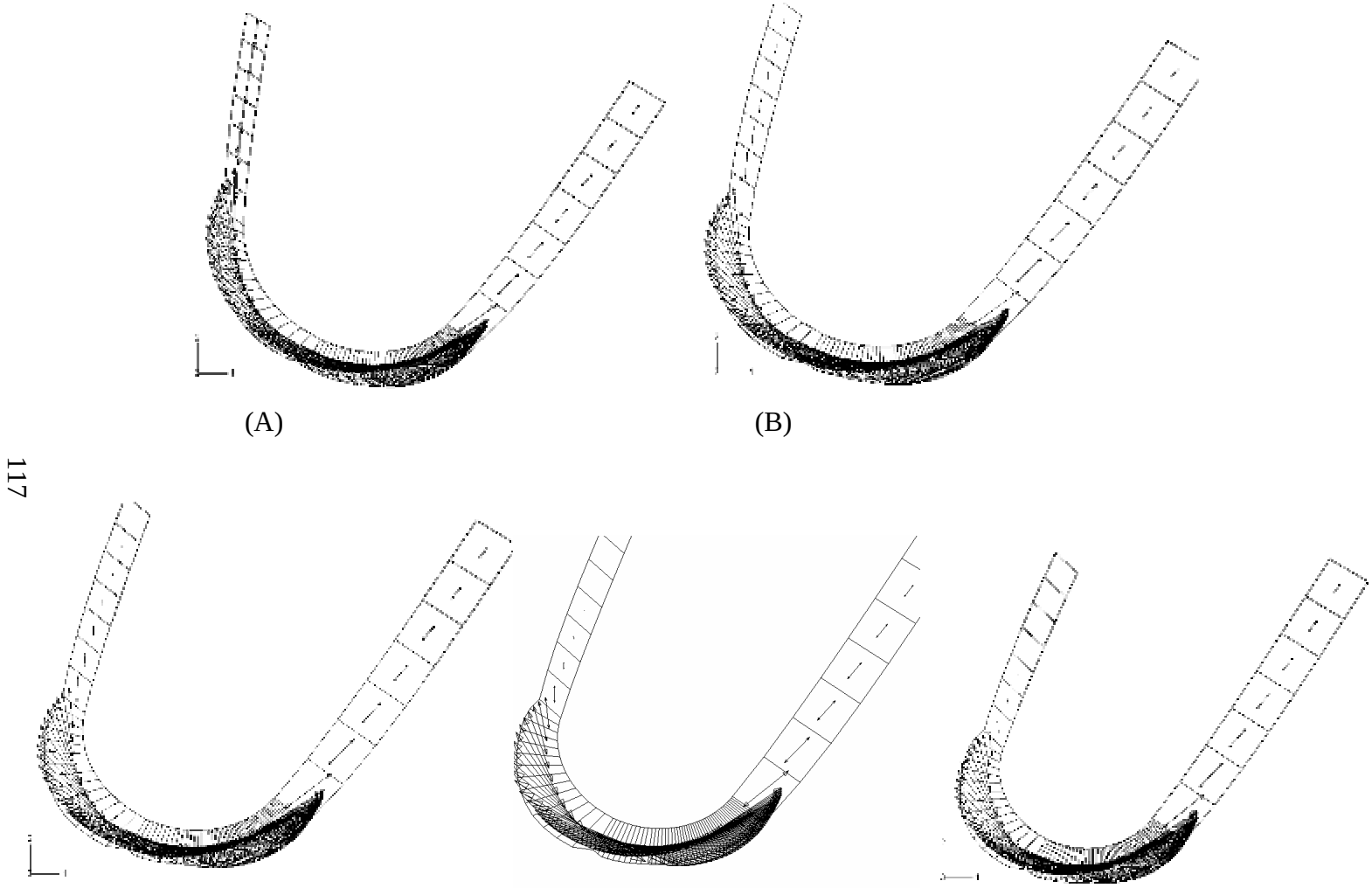

FIGURE 4.7: Maximum Principal Stress Direction around crack tip with the asperity moving away from the crack.

Most crack propagation theories related to rubber use linear elastic fracture mechanics [84, 87]. Appendix C., describes several competing theories in this regard. In this study the following crack propagation criterion is used:

(1) Stress induced crack propagations occurs when the critical Energy Release Rate (Gc) as observed from experiments under identical stress conditions, is reached.

(2) The direction of crack propagation is along the normal to the maximum principal stress at the point in the material where the critical energy release rate is achieved.

(3) In case of a negative Maximum Principal Stress, the crack propagation does not occur.

It should be noted that the above criterion disallows crack propagation under compression which is deemed physically impossible. In other words, the Energy Release Rate itself can not be the sole criterion for the stress induced crack propagation. Figure 4.8 is an illustration of a case where the strain energy density (proportional to crack energy release rate) is very high in a stress field around a crack in the region where the Maximum Principal Stress is predominantly compressive. This typically happens, when an asperity with dimensions roughly the same order as the crack has penetrated within a distance of order O(r) where r is the asperity radius. Thus, it is clear that the maximum strain energy density is highest at the tip of the crack that sees compression. On the other hand, the maximum principal stress has a maximum value on the crack walls away from the tip where the crack walls are touching. These regions see a tensile maximum stress but relatively lower magnitude of deformation as compared to the compressive strains seen at the tip of the crack. In this situation, it is clear that the crack propagation event is most likely at the site of tensile stresses assuming that the high compressive stresses do not

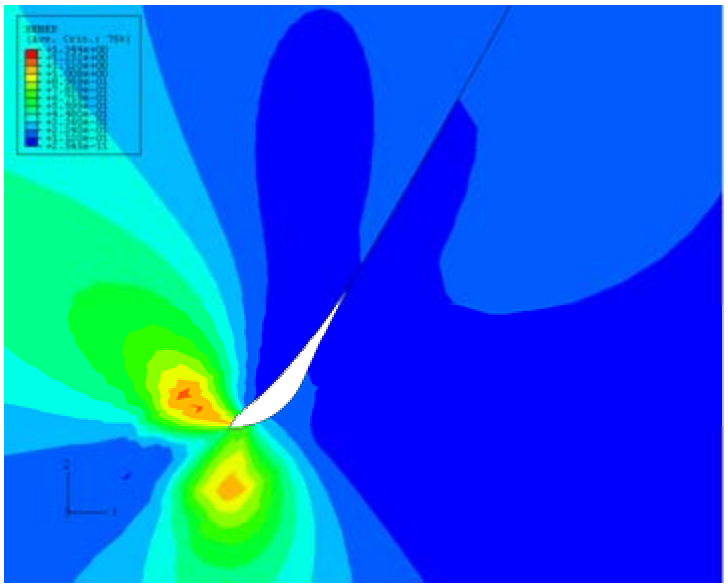

(A)

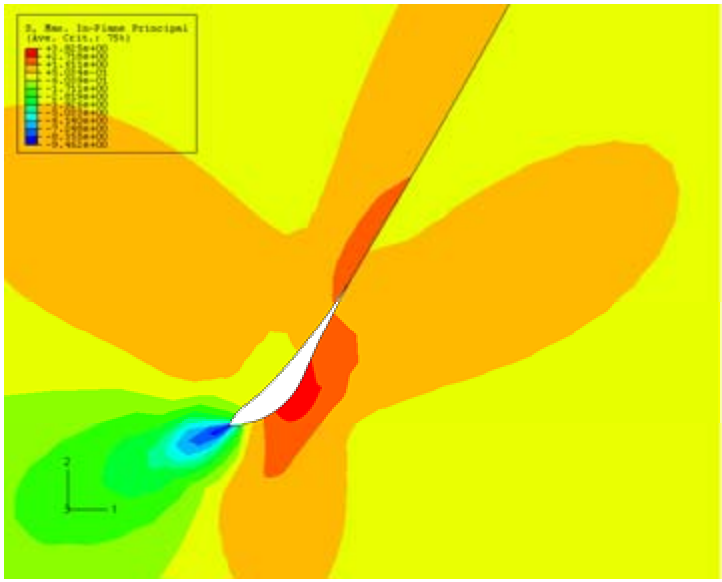

(B)

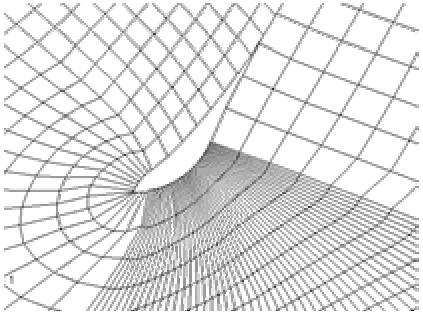

(C)

FIGURE 4.8: Illustration of Maximum Principle Stress and Strain Energy Density as Crack Propagation Criteria. (A) Strain Energy Density Distribution, (B) Maximum Principle Stress Distribution, (C) Deformed mesh around the crack.

lead to areas of weakening such as those found in compression related fatigue. The particular methodology used in the present study is presented in the following section.

4.2 Methodology Used to Estimate the Energy Release Rates in the Surface Cracks

The figure 4.9 shows a sketch of an asperity moving away from a surface crack. As discussed in the previous section, the tensile region in the wake of the asperity has high probability of fracture and related crack propagation. These high tensile stresses are related to the contact and decrease rapidly in the direction of the depth. The Maximum Principle Stress at the surface of the skin is nearly tangential or tangential depending upon the nature of the contact, friction coefficient, the boundary conditions and the errors in the calculation with the FEA method. Figure 4.10 represents the Maximum Principle Stress condition and the Strain Energy Density along a path perpendicular to the Maximum Principle Stress directions near the surface (Figure 4.9). The figures in 4.10 are shown for 3 such paths for 3 successive nodes (618, 619,620) along the wear surface when the particular nodes are near a receding asperity. Note that these 'path plots' are at a particular incremental solution during a static analysis. Figure 4.10 shows that very near the surface, the elements with nodes 618, 619 and 620 have similar Maximum Principle Stress, with an error less than 20%. Both the Minimum Principle Stress and the out of plane stress (for Plain Strain elements) are comparatively smaller than the Maximum Principle Stress (within 5 to 10 %). This state of stress for the few (usually up to 3) adjacent surface elements can be approximated to those observed in a tensile notched specimen shown in Figure 4.11

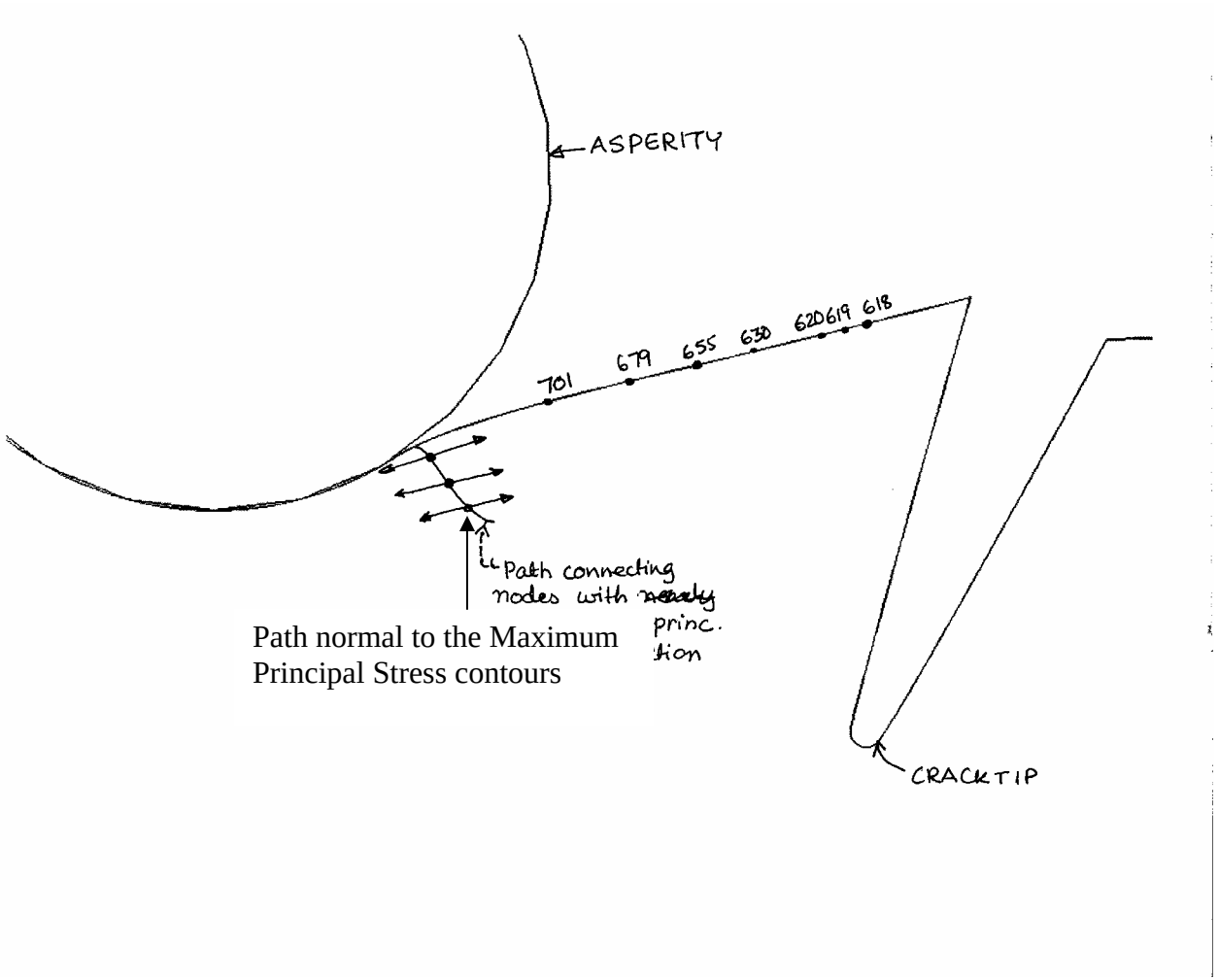

FIGURE 4.9: Illustration of proposed computation scheme of the Energy Release Rate for wear surface crack. The solid dots represent nodes.

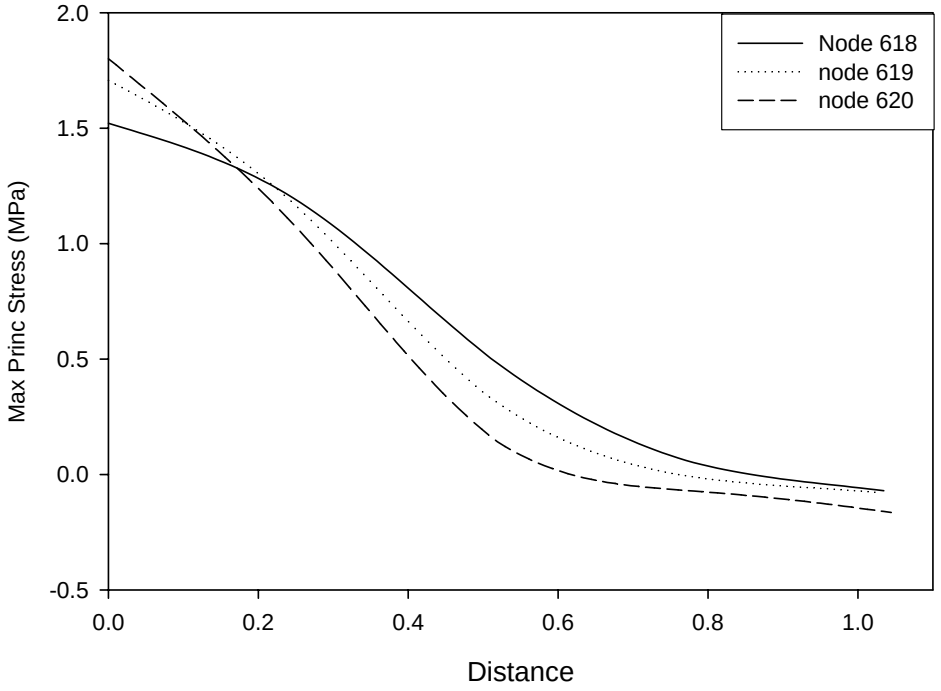

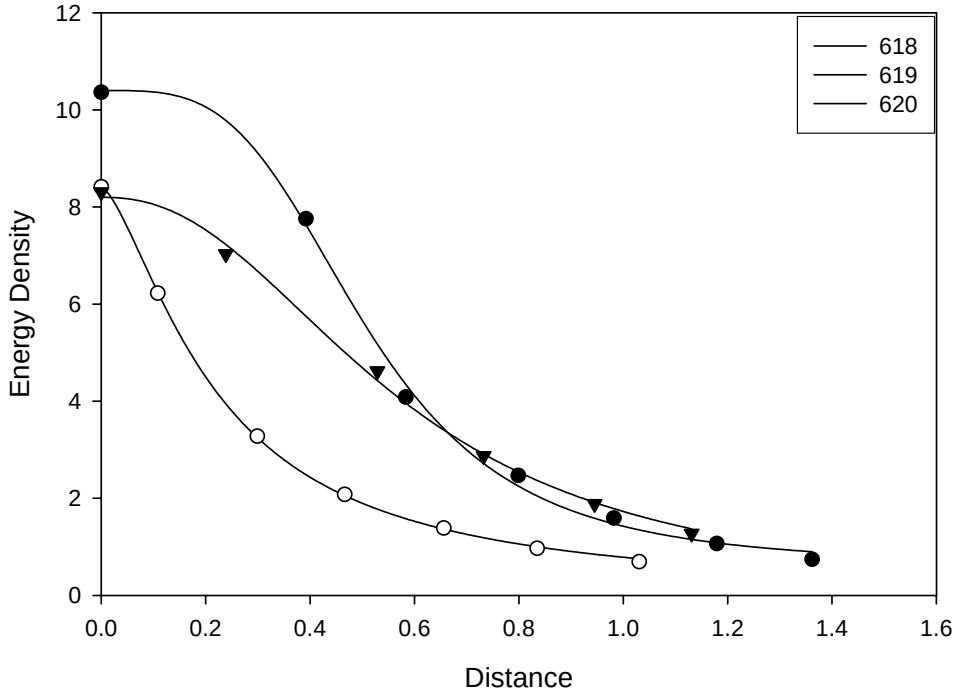

FIGURE 4.10 Top : Maximum Principal Stress and Bottom Strain Energy Density along a Path for 3 adjacent nodes on the wear surface

The tensile notched specimen (Figure 4.11) is a well-established geometry in the field of fatigue and crack propagation. Figure 4.11 shows the typical data for crack growth rate vs. the crack energy release rate (G) for such a specimen at different applied speeds. Such a curve is also found to be invariant under the type of loading conditions (Pure shear, uni-axial tension) and the geometry of the experiment, and is considered to a material property as such. The limiting value of strain energy release rate is $G_{0,}$ beyond which the crack growth rate is dependent on the strain rate energy release rate. This limit is a critical transition limit above which the rate of crack growth is several orders higher and is sighted [82] as the major failure mechanism in elastomers.

Lake et al [82] also provide evidence that the energy release rate approach at low deformation rates can be extended to high strain rates for a satisfactory match with experimental data with high strain rate. These experiments typically are conducted for relatively thin specimens. However, at high strain rates, the thickness has virtually no effect on the crack growth resistance. This proves that experiments are influenced by the 'edge effect' in the small thickness specimen. Lake et al [82] also points out the effect of transverse stresses leading to cavitation at small specimen thicknesses.

In the present study, it is assumed that the nearly uniform tensile area on the surface will experience failure dependent on the energy release rate at the edge crack. Such an event is similar to the specimen shown in figure 4.11 and has the energy release rate:

$$G = 2 \cdot KWc \qquad 4.1$$

.

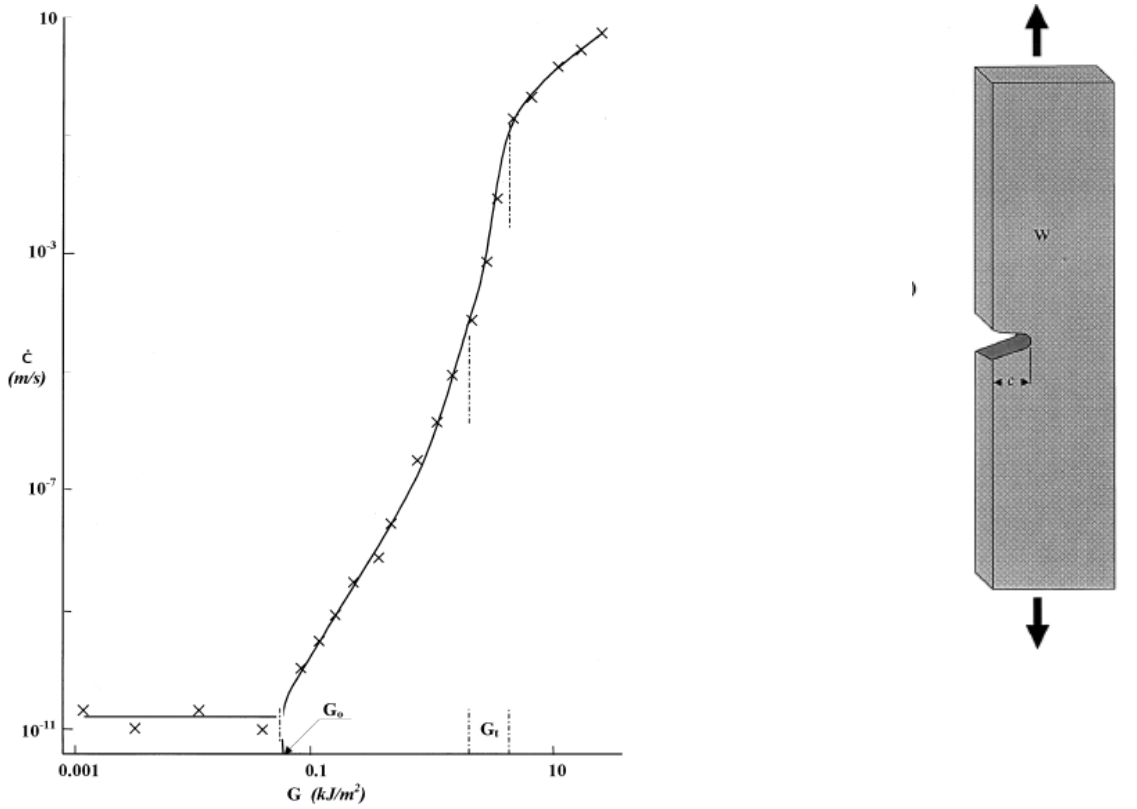

FIGURE 4.11: Crack growth rate vs. Energy release rate curve for SBR (Left) from a tensile specimen (Right) From Lake et al [82]

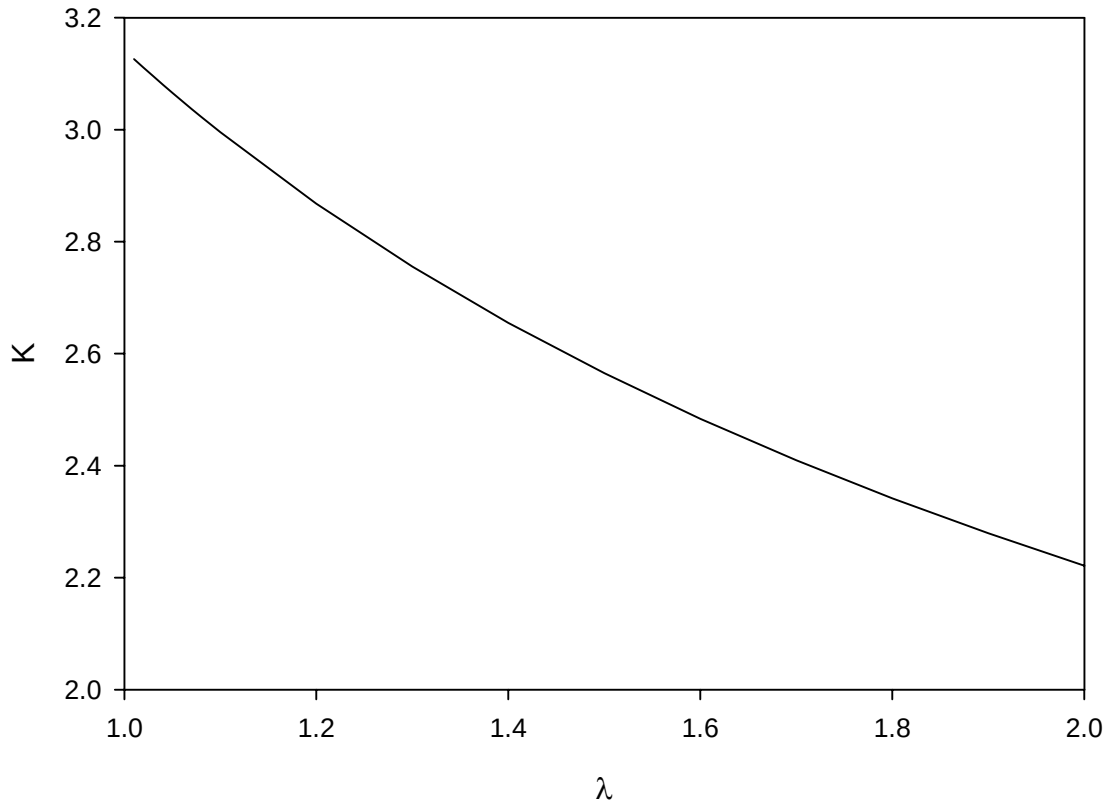

FIGURE 4.12: Dependence of ‘K used in the energy release rate (G) calculation on the stretch ratio (l)

Here, K is an amplification factor (a constant), W is the far field strain energy density in the specimen away from the crack and c is the length of the crack. This is a good approximation, provided that $c < 0.3w$, where 'w' is the test piece width. The variation of 'K' the amplification factor is a function of the stretch ratio, and is plotted in Figure 4.12. Since the results of the present simulations indicate that the uniformly tensile stress condition is valid at the surface in an area about 3 elements long and 2 elements wide, it is safe to say that cracks with lengths smaller than 0.3 times the width of the single element can be used for the calculations of the energy release rates. Thus, for the paths shown in Figure 4.10, a representative energy release rate can be calculated using an integration procedure showed in Figure 4.13. The hatched area under the curve in Figure 4.13 represents the strain energy release rate for a crack length of Δx. The important assumption here is that the advance of the crack is small enough such that the effective tensile state in the specimen is unchanged.

The exact procedure used to calculate the energy release rate in this manner, is summarized below.

(1) The data at 3 adjacent surface nodes with highest strain energy density and near uniaxial tensile state was collected at each position of the asperity as it moves away from the crack.

(2) Using python scripts, the data for strain energy density was integrated over a distance of a crack length. $\Delta x = 0.3l_e$ where l_e is the length of the element in the direction perpendicular to the surface. The average crack energy release rate at a surface node is calculated as the average of the energy release rates for the 3 adjacent nodes. The Figure 4.15 (top) shows the energy density plots along the

principal stress contour paths for a number of adjacent nodes as shown in Figure 4.9. Figure 4.15 (bottom), shows the effective energy release rate along the surface of the rubber specimen as the asperity moves away from the crack.

(3) The integrated data represents the energy release rate per unit amplification factor (K). Assuming that the cracks with length scale of the order of the element length are uniformly distributed in the specimen in every direction and have differing crack tip radius, they may have differing amplification factor K. The cracks that release the critical crack energy release rate G_0 will propagate at a very high rate. The experimental data for the two filled rubbers used in this study is shown in Figure 4.14 (A). Figure 4.14 (B), illustrates the typical crack speed limit for a Mooney-Rivlin type material, which is the transverse elastic velocity.

(4) These cracks at smaller length scales than the existing crack in the specimen, will cause 'crack initiation' at a length scale at a higher order length scale, if they continue to grow at a high energy release rate.

4.3 Energy Release Rates Along the Crack Surface for a Moving Asperity

Figure 4.16 (Top) shows the energy density distribution along the surface nodes for a moving asperity, for different friction conditions. The data for distance from the crack (x axis) is non-dimensionalised with the radius of the asperity. The corresponding energy release rate per unit amplification factor is shown in Figure 4.16 (Bottom). This result is for the plain strain case simulation. Figure 4.17 shows the nondimensionlized energy release rate per unit amplification factor for both plain strain and plain stress case.

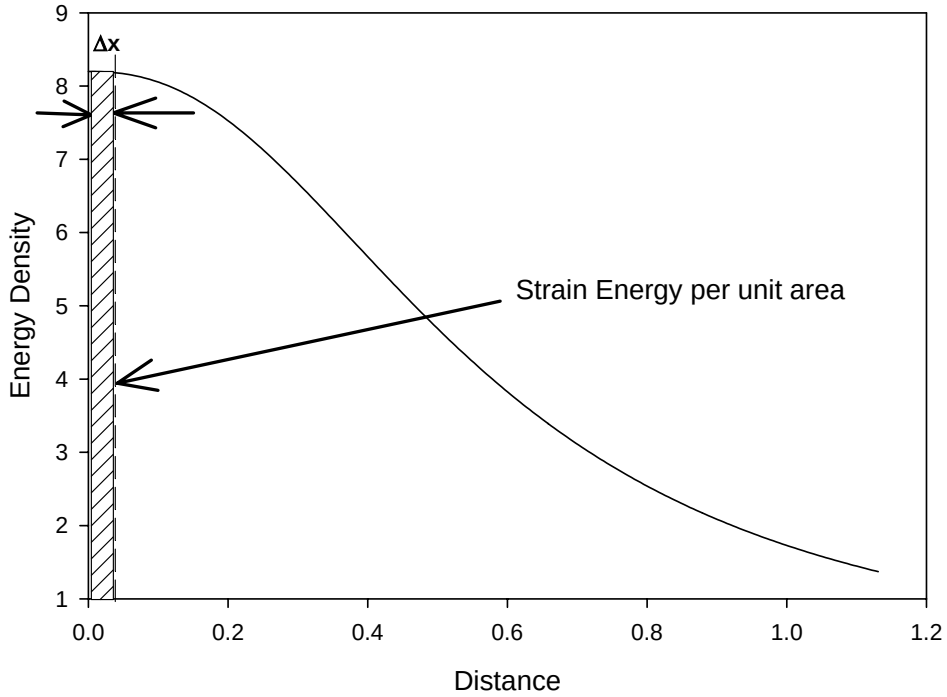

FIGURE 4.13: Illustration of energy release rate (G) calculation

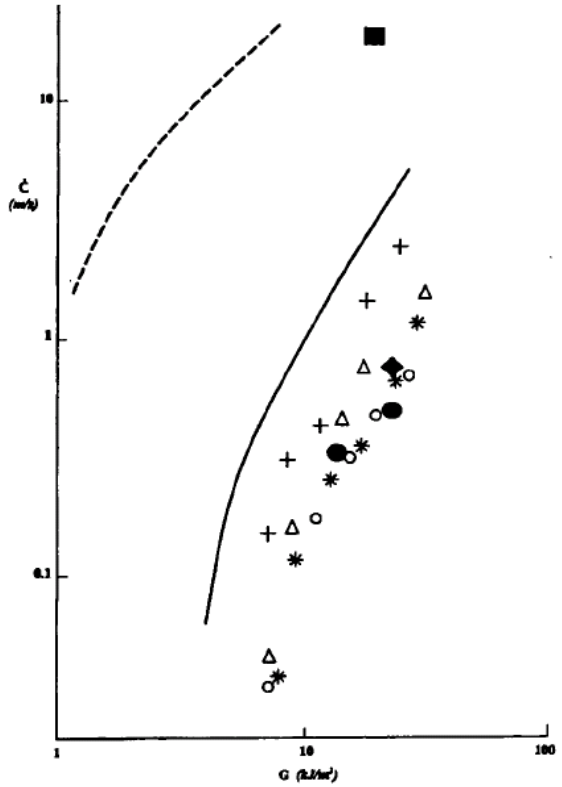

(A)

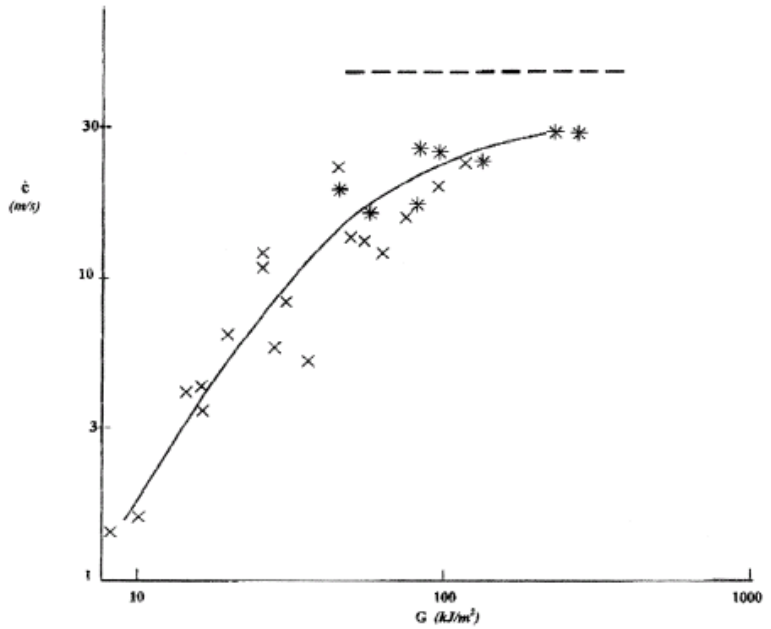

(B)

FIGURE 4.14: (A) Crack growth rate vs G data for SBR1 and SBR2 (B) Crack growth rate vs G data and wave velocity (dashed line). From Lake et al [82]

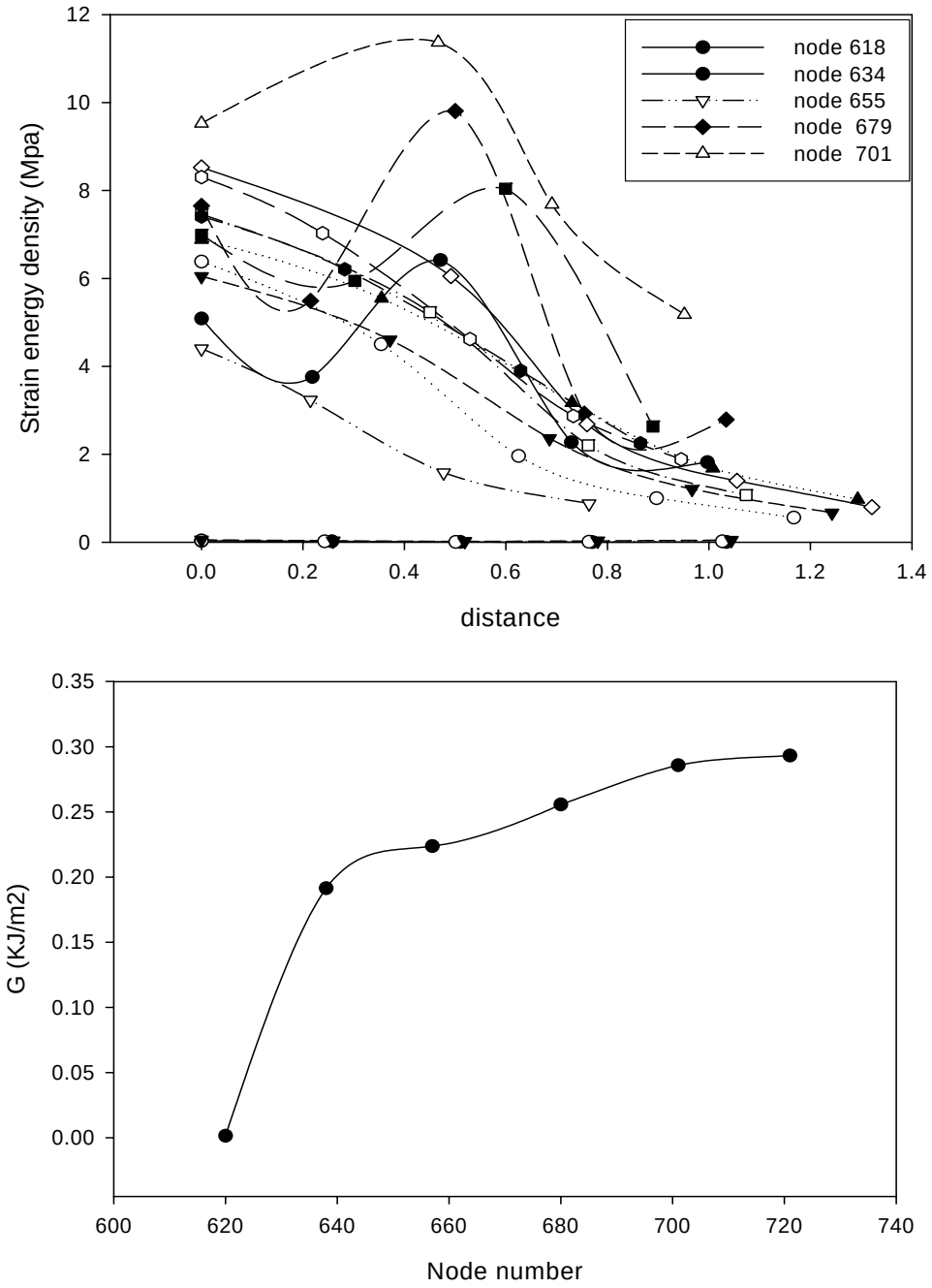

FIGURE 4.15: Top: 'Path' plots along the maximum principle stress contours along the wear surface Bottom: Averaged energy release rate along the path (increasing node numbers)

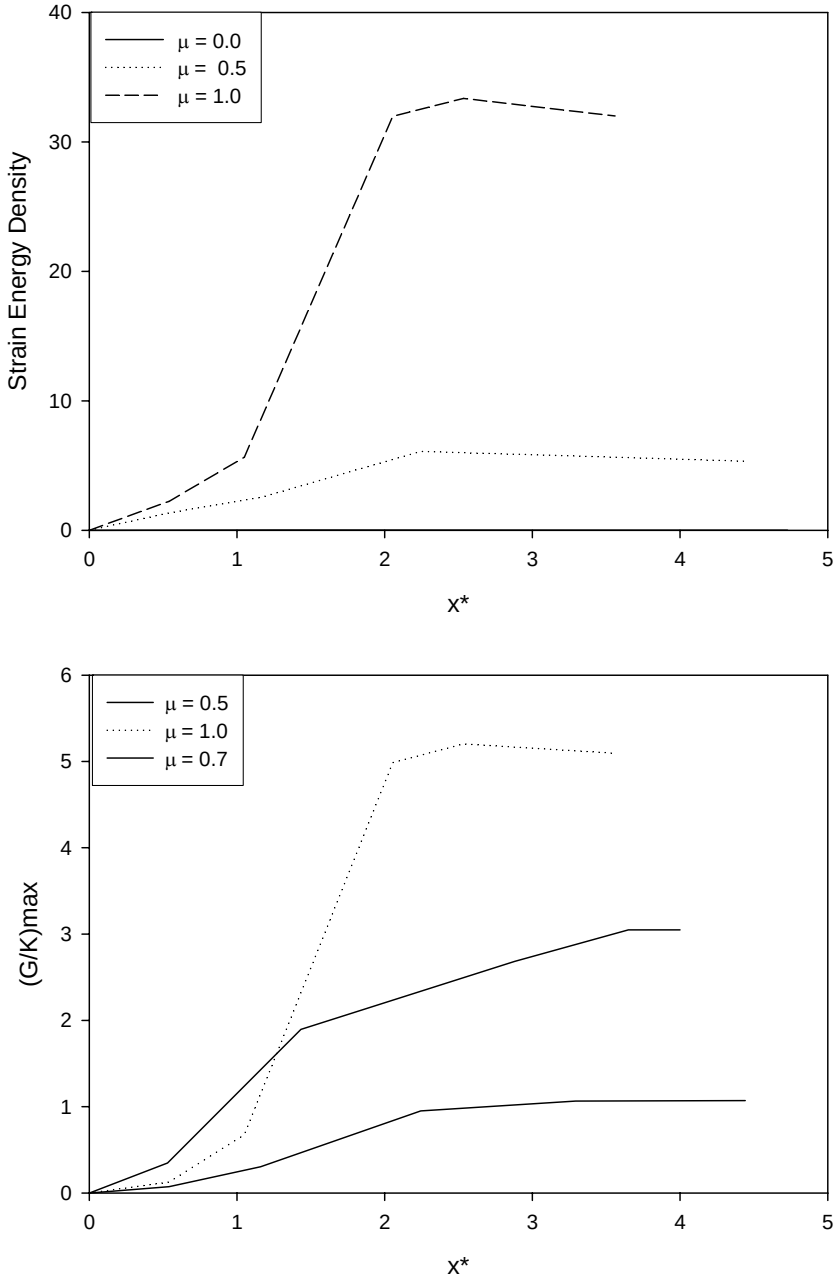

FIGURE 4.16: Top: Maximum Strain Energy Density along the wear surface going away from the crack. Bottom: Maximum estimated Strain Energy release rate along the wear surface for differing friction values (Plain Strain case).

Here the data for energy release rate is non-dimensionlized using the energy release rate at a very small deformation rate (G_c), which is also referred as the tear strength for the material.

Figures 4.16 and 4.17 give us a unique and hitherto unexplored way of presenting energy release rate data along a wear surface. It is easy to see that the energy release rate increases steadily along the asperity motion direction, and reaches a plateau after certain distance. At higher coefficient of friction, the data the rise in the energy release rate is higher than that at the lower coefficient of friction.

Figure 4.17 shows that the critical strain energy release rate corresponding to the tear strength is not achieved in the plain strain case, unless the friction coefficient reaches a high value. At coefficient of friction equal to unity, value equal to the 80% of tear strength is achieved by the energy release rates. This is significant as even with a amplification factor of K=2, the corresponding energy release rate is sufficient to start crack growth. In the plane stress case, the energy release rate is much smaller for the same depth of penetration and frictional condition. This implies that for cracks with larger lateral dimensions, higher energy release rates are achieved than those for the cracks with smaller lateral dimensions, for the same friction conditions and penetration of depth.

Figure 4.18 similarly shows the dimensional and non-dimensionalized energy release data along the direction of asperity travel for the two different filled rubber materials SBR2 and SBR3. The two different materials have different filler content (30 vs 10%) and have different tear strengths.

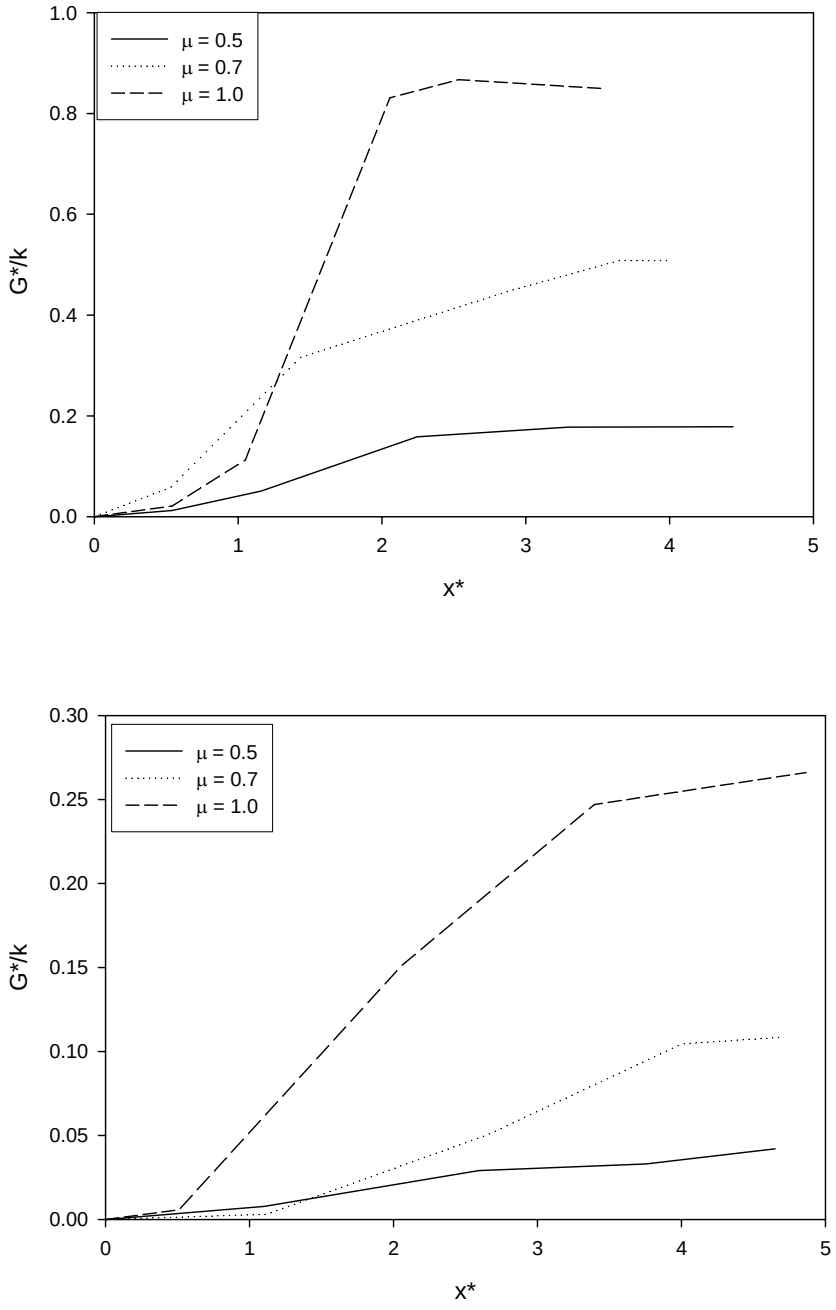

FIGURE 4.17: Variation of non-dimensional strain energy release rate as asperity moves away from a crack. Top: Plain Strain case. Bottom: Plain Stress case.

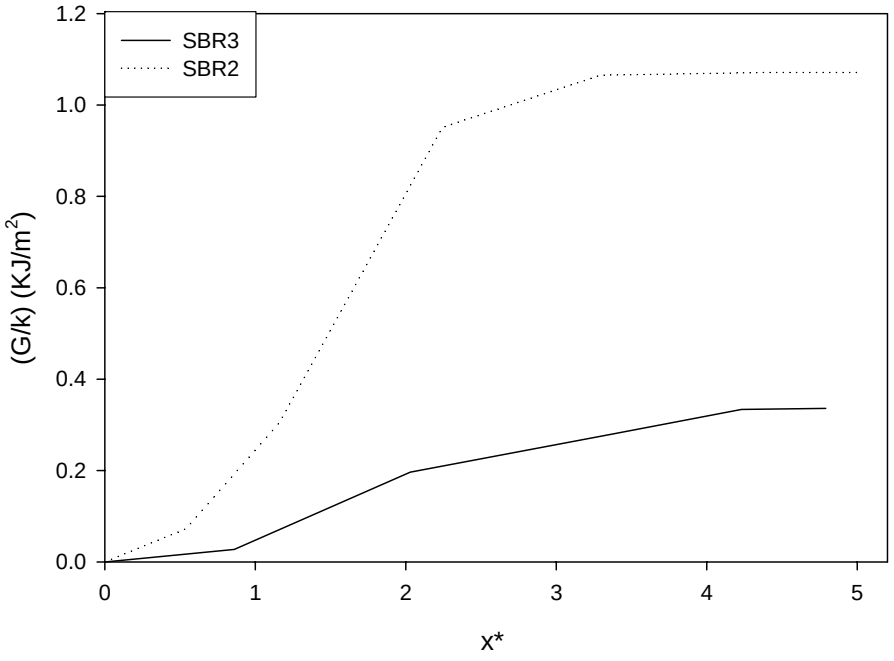

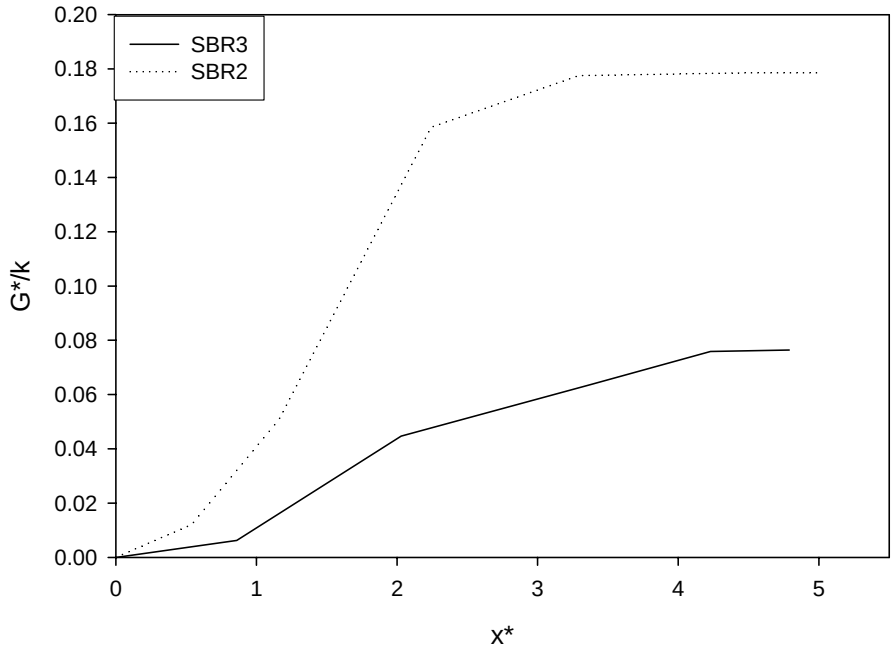

FIGURE 4.18: Variation of Strain Energy Release rate for two different SBR grades (1R, μ =0.5), (Top) and Non-dimensional StrainEnergy Release rate (Bottom).

The effect of geometric factors on the surface energy release rates is seen in Figures 4.19 and 4.20. With the increasing asperity radius, the energy release rate decreases at a given distance from the crack, for the same depth of penetration and friction condition. This is consistent with the fact that a smaller radius of asperity causes larger local curvature for the same depth of penetration, resulting in a larger tensile stress near the trailing edge of the asperity. Conversely, as asperity size decreases with respect to the preexisting crack size in the model, the stress field around the asperity is less influenced by the preexisting crack in the vicinity.

As the crack angle with respect to the direction transverse to the surface increases, the energy release rate at the surface decreases. This is consistent with the observation of the stress fields in the perpendicular orientation of crack (0^O) vs the stress fields when the crack is oriented at an angle to the surface that is smaller. Although the far-field stress energy release rate, indicated by the plateau region in Figure 4.20 is consistently smaller as crack gets shallower, the energy release rate in the vicinity of the crack ($x^* < R$), has no such consistent trend. This is largely due to the complex geometric and contact effects in the region.

4.4 Crack Spacing

The crack energy release rates estimates along the surface of the crack represent the statistical distribution of probable crack propagation along the surface of the crack. Assuming that the tear strength is the defining criteria, and a nominal value of K=2, Figure 4.21 shows the energy release rate data for different coefficient of friction for the same depth of penetration (0.5R). The solid horizontal line corresponds to the tear strength for the material ($Gc = 6\ KJ/m^2$).

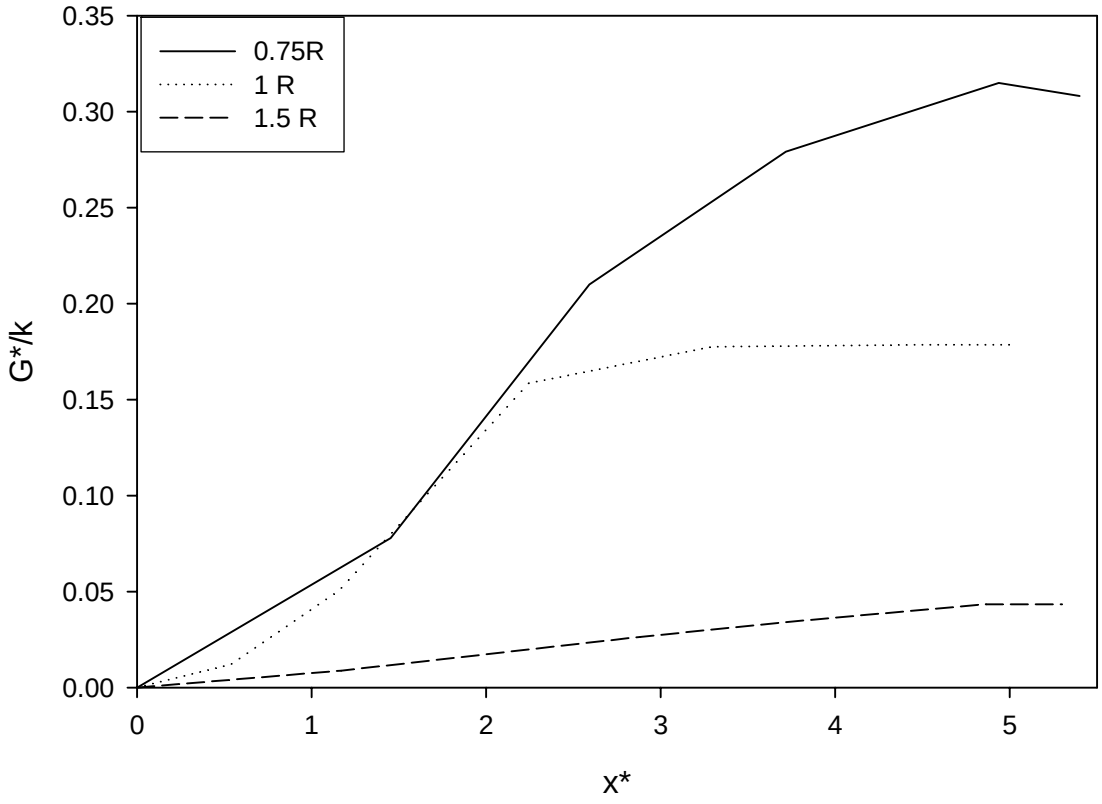

FIGURE 4.19: Effect of Energy Release Rate (dimensionless) distribution in the wake of an asperity traveling away from the crack for different asperity radius ($\mu = 0.5$).

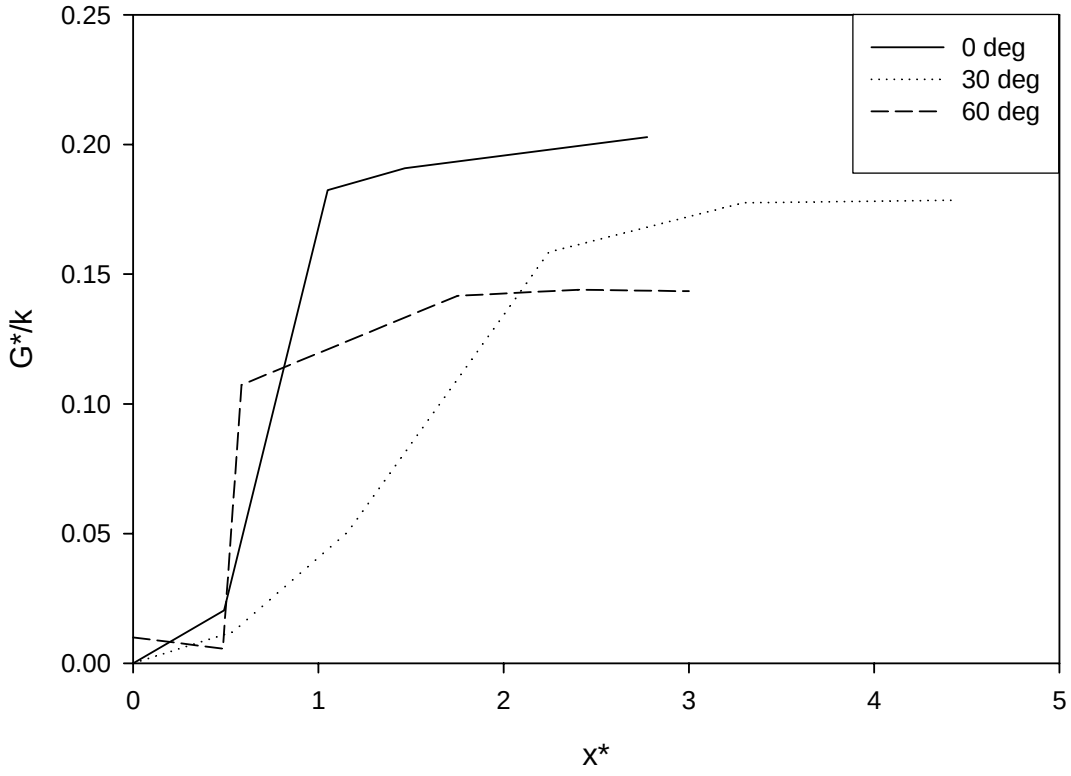

FIGURE 4.20: Non-dimensional energy release rate along the wear surface for a moving asperity for varying crack orientation angle. Crack orientation angle is measured with respect to the conventional vertical line and angle measurements are clockwise positive.

Using the tear strength as a criteria for further crack propagation at smaller scale. The points A and C represent the crack spacing represent the probable crack spacing between the existing crack and a new crack for the friction coefficients 1.0 and 0.7 respectively. Note that, for the same depth of penetration, with a lower friction (0.5), the energy release rates are less than 30% of that required for the crack propagation at surface. In the present simulations, care was taken so as to eliminate errors from the high distortion in the elements at higher frictions. This limits the data for the higher friction cases at a large distance from the crack, where the finite element model has larger element size for computational economy.

The above definition of crack spacing, relies upon crack propagation when the asperity is moving very slowly, and the crack propagation happens in a single pass. There are several other possibilities dependent upon the nature of asperity loading condition. If the results from the conditions in Figure 4.21 were to be extended to a case when the moving asperity repeated traverses the surface, the cyclic loading conditions can be applied. The typical cyclic loading data for the materials under consideration correlates the data for crack length increase per loading cycle. Figure 4.22 shows the results of crack growth per loading cycle as an asperity traverses away from the crack. The line corresponding to crack growth of 1mm/Kcycle is arbitrarily defined as the new crack initiation threshold. This corresponds to 10% of the length existing crack in the model. Using this threshold as acceptable definition of the new crack growth, it can be seen that, even at low friction coefficient of 0.5, a new crack may appear, although at a much larger distance from the existing crack (point C). In comparison, the repeated

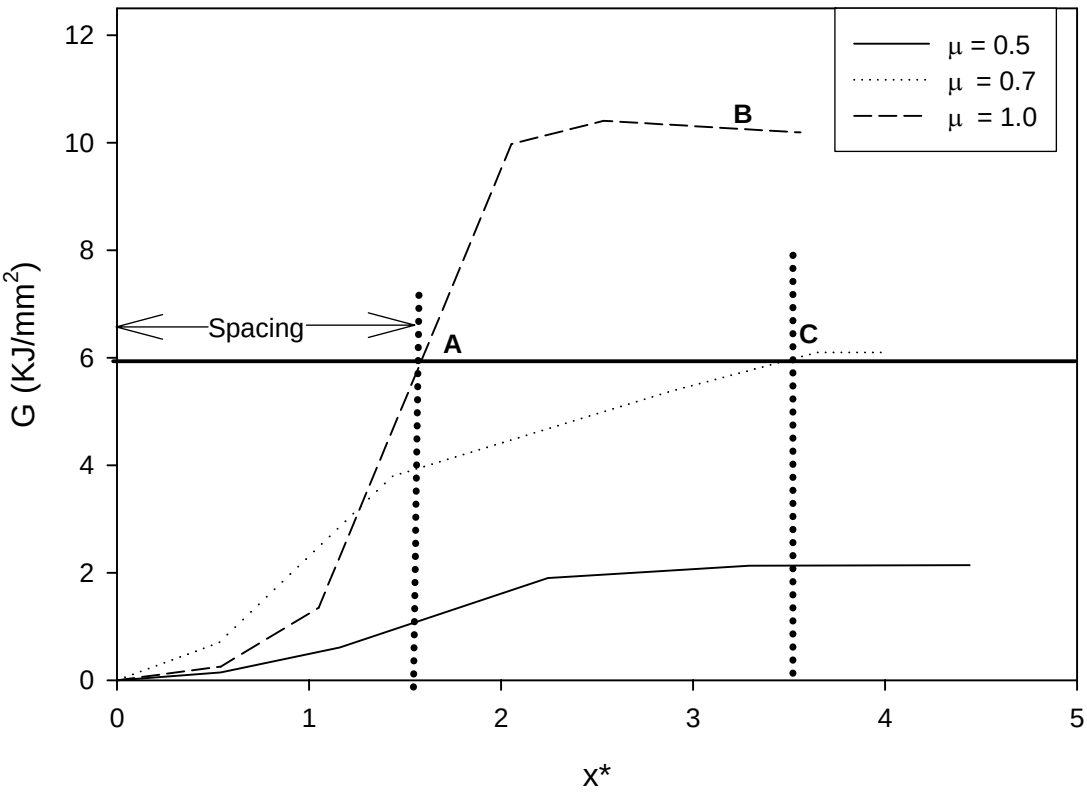

FIGURE 4.21: Spacing measure based on G dependant crack growth rate for different friction coefficients. A, Crack Initiation distance for $\mu = 1.0$. B, Plateu region of the Energy release rate. C Crack initiation distance for $\mu = 0.7$

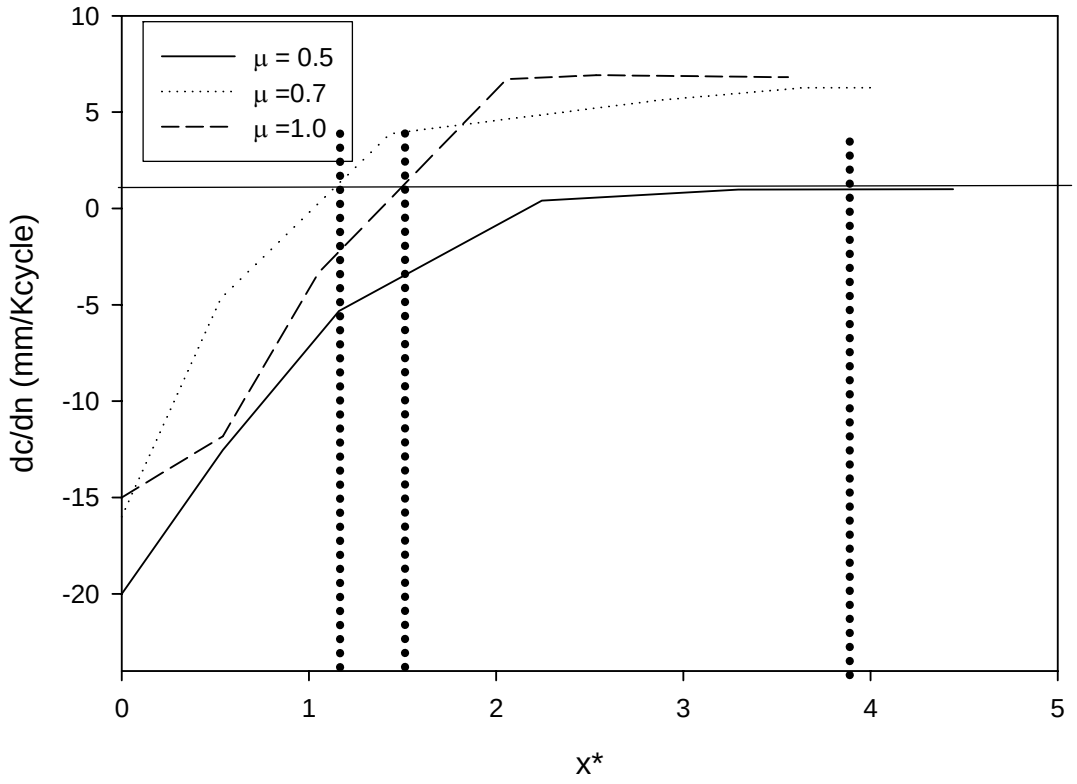

FIGURE 4.22: Spacing measure based on crack growth under cyclic loading for different friction coefficients. The solid dotted lines indicate the critical distance at which the crack initiation happens.

loading, creates smaller spacing at higher friction (points A and B) keeping other conditions the same.

4.5 Stress Variation Along Crack Tip

Crack-tip is another area where stress concentration can be found. As seen in Figure 4.6-7, this is also a surface area where the stress undergoes highly uniaxial stress distribution during asperity penetration and travel away from the crack.. Figure 4.23 shows the evolution of crack-tip stress (Maximum Principal) as the asperity recedes from the crack. Figure 4.24 shows the Maximum Principal Stress distribution around the crack-tip with the asperity traveling away from the crack. After a certain critical distance, the peak of the distribution starts to decrease as the asperity is at a larger distance from the crack. Coincidentally, the Maximum Principal Stress and the Strain Enregy density distribution in the wake of the asperity contact, starts increasing dramatically.

This is consistent with the conjecture in the earlier section (3.4.3) that as the asperity moves away from the crack, a larger portion of the deformational strain energy contributes to wards surface cracks in the wake of the asperity. The distance at which the peak crack tip stress is achieved is determined by geometrical factors (angle of the crack, length and depth of penetration) along with the material properties.

The strain energy release rate calculations similar to those described in section 4.4 were applied to the crack-tip stresses. From Figure 4.24, it is obvious that the Maximum Principal Stress is about 7-8 times as large as the Minimum Principal Stress and about 2 times as large as the Out of Plane Stress.

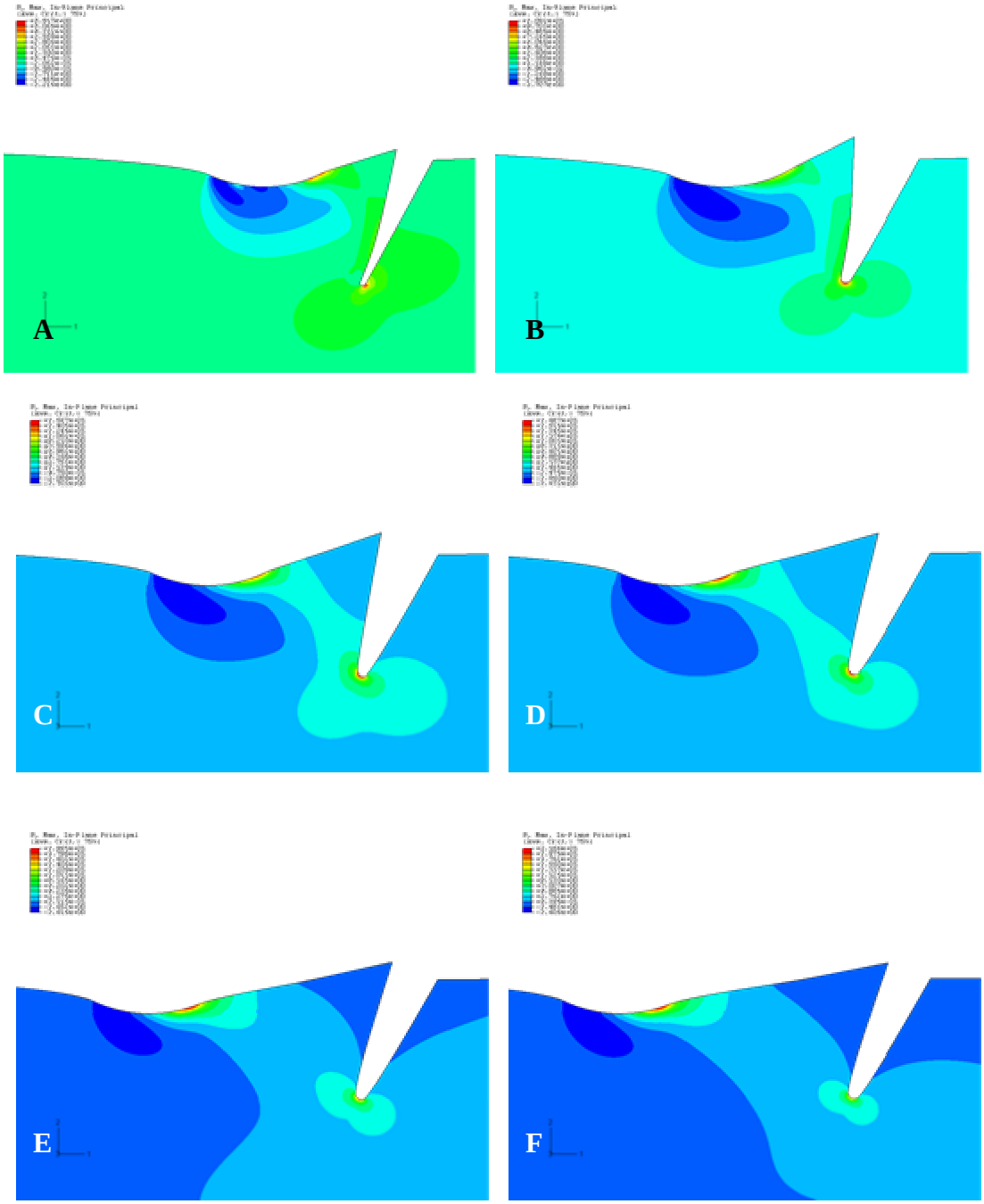

FIGURE 4.23: Crack tip influence on stress field as the asperity moves away from the crack.

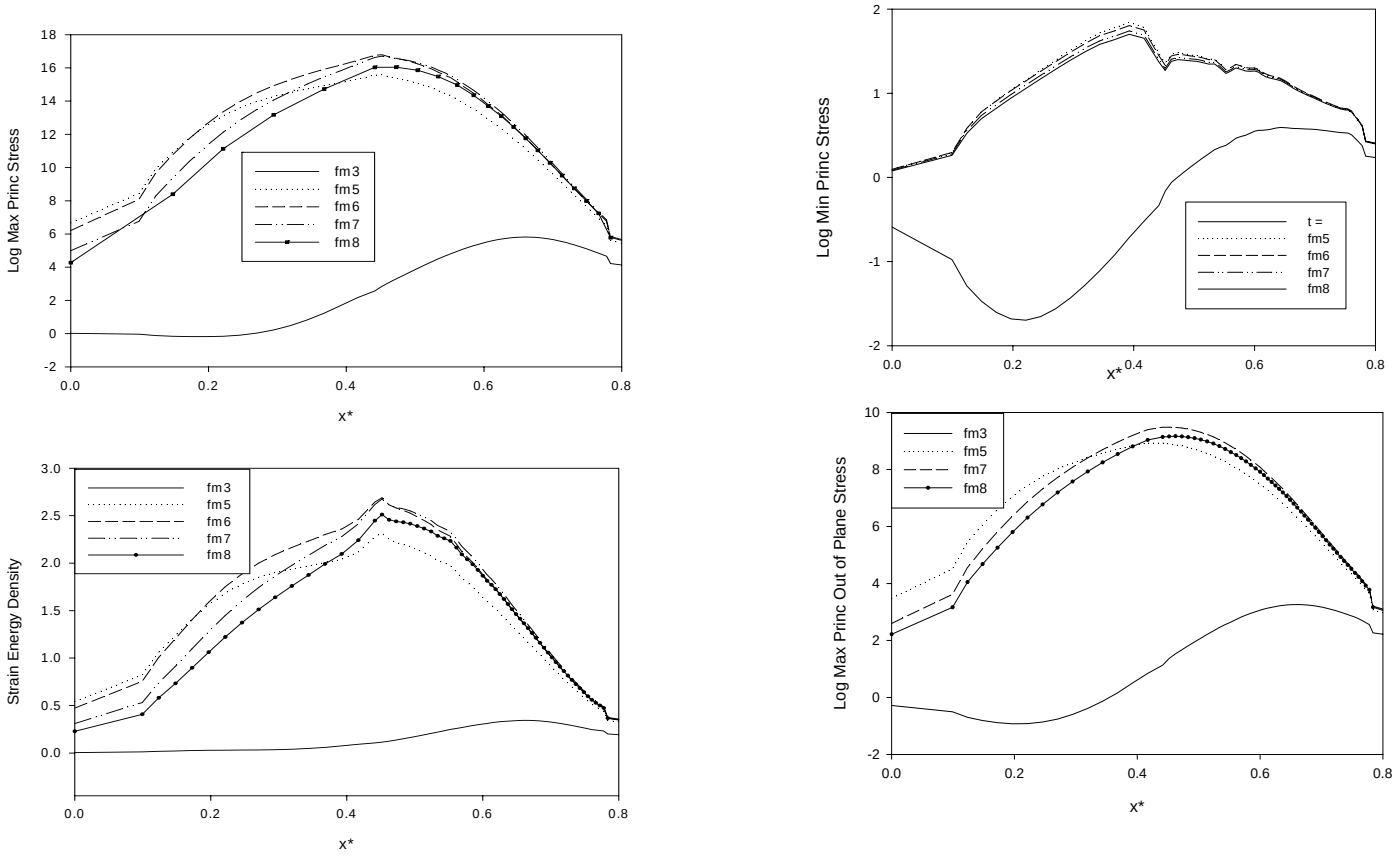

FIGURE 4.24: Principal Stress Components and Strain Energy Density evolution with moving away asperity.

Figure 4.25 shows the deformed mesh around a crack tip with node locations marked. During asperity penetration, the maximum energy release rates are observed predominantly at the far crack wall represented by node 2585. As the asperity moves away from the crack the location of the maximum energy release rate shifts towards the center of the crack tip (2615).

Figure 4.26 shows the variation of non-dimensional energy release rates for the node 2585 with increasing depth of penetration. Observe that at least for small depth of penetration (0.5R) , the energy release rates at the crack tip, are much smaller than the tear strength required for local crack propagation. However, the possibility of fatigue related crack initiation and propagation can not be ruled out. Also, the crack propagation may occur at different location and direction at the crack tip based on the nature of asperity loading.

4.6 Asperity Approaching a Crack

The last two chapters have primarily focused on asperity penetration near a crack followed by the asperity travel away from the crack. Several instances of the event when the asperity approaches a crack were also studied. Figure 4.27 shows some scenarios where a crack is approached by a penetrating asperity. In all these cases, the crack walls tend to close on each other resulting in a large contact pressure between the walls of the crack. As the asperity comes in contact with the wear surface where the edge crack is, there are severe computational difficulties. These result largely from the incompressibility of the material as the large contact forces between the two sides of the crack create large volumetric strain. The problem is not completely alleviated by the introduction of a finite compressibility. Additionally there are severe contact related

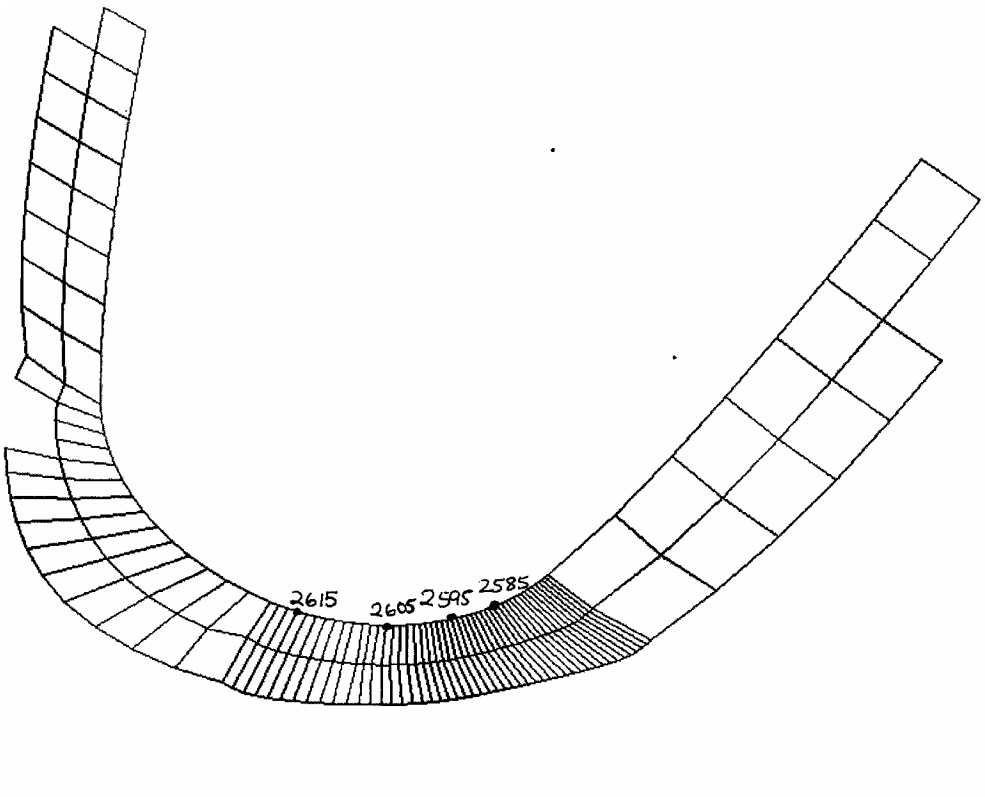

FIGURE 4.25: Deformed crack tip mesh, with critical nodes on the tip identified

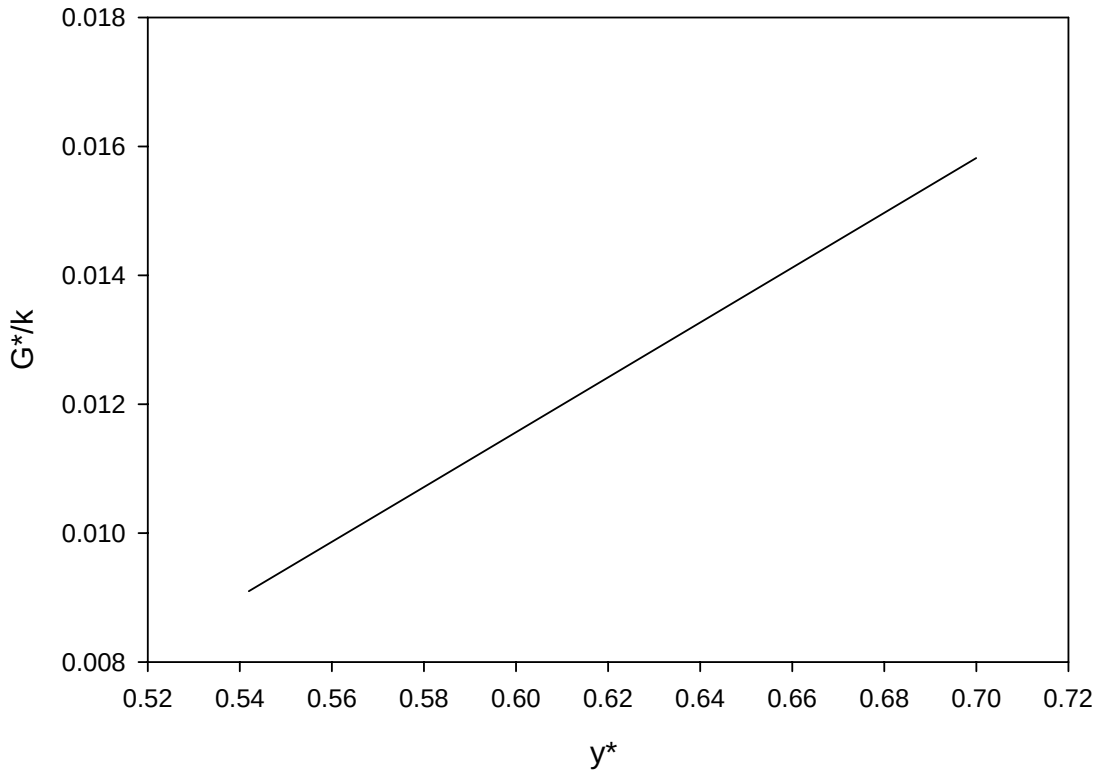

FIGURE 4.26: Non-dimensional Energy release rate vs Non-dimensional Depth of Penetration at a far-wall crack tip node 2585 (see figure 4.25).

iterations that lead to poor convergence properties. This is because the number of contact constraints increase dramatically. Certain nodes located on the crack surface and the wear surface are over-constrained when the contact between crack walls, crack walls and the asperity, crack walls and wear surface on either side of the crack walls become active. Convergence may still be achieved still by running the problem in stages where selective contact conditions are turned on or off based on the state of the solution and physical intuition. However, in most flat (or straight) wear surfaces, this is an exercise that yields very little additional information. As the crack is closed on the asperity approach, the effective crack dimension is reduced by a large extent and it can be safely assumed that the crack does not affect the stress field around the asperity contact area for a period of time as the asperity approaches, passes and moves to the other side of the crack. Once the asperity has passed on to the other side, the crack may again open from the shearing load. This problem then again reverts to the problem of an asperity moving away from the crack, however, with a difference that the crack is 'closed' in the initial period when the asperity is moving from the crack. In such an event, the crack-spacing may be different from the event when the crack is not closed when the asperity starts moving away from the crack.

However, if the wear surface is not straight or flat and if the walls of the edge crack are not 'even' or flush at the wear surface, other contact scenarios come into play. One interesting scenario is shown in the sketch 4.27(D). Here, the asperity may load the crack wall as it approaches the edge crack. In this case, the stresses and the energy release rate at the crack tip have potential to reach the critical limit for the crack.

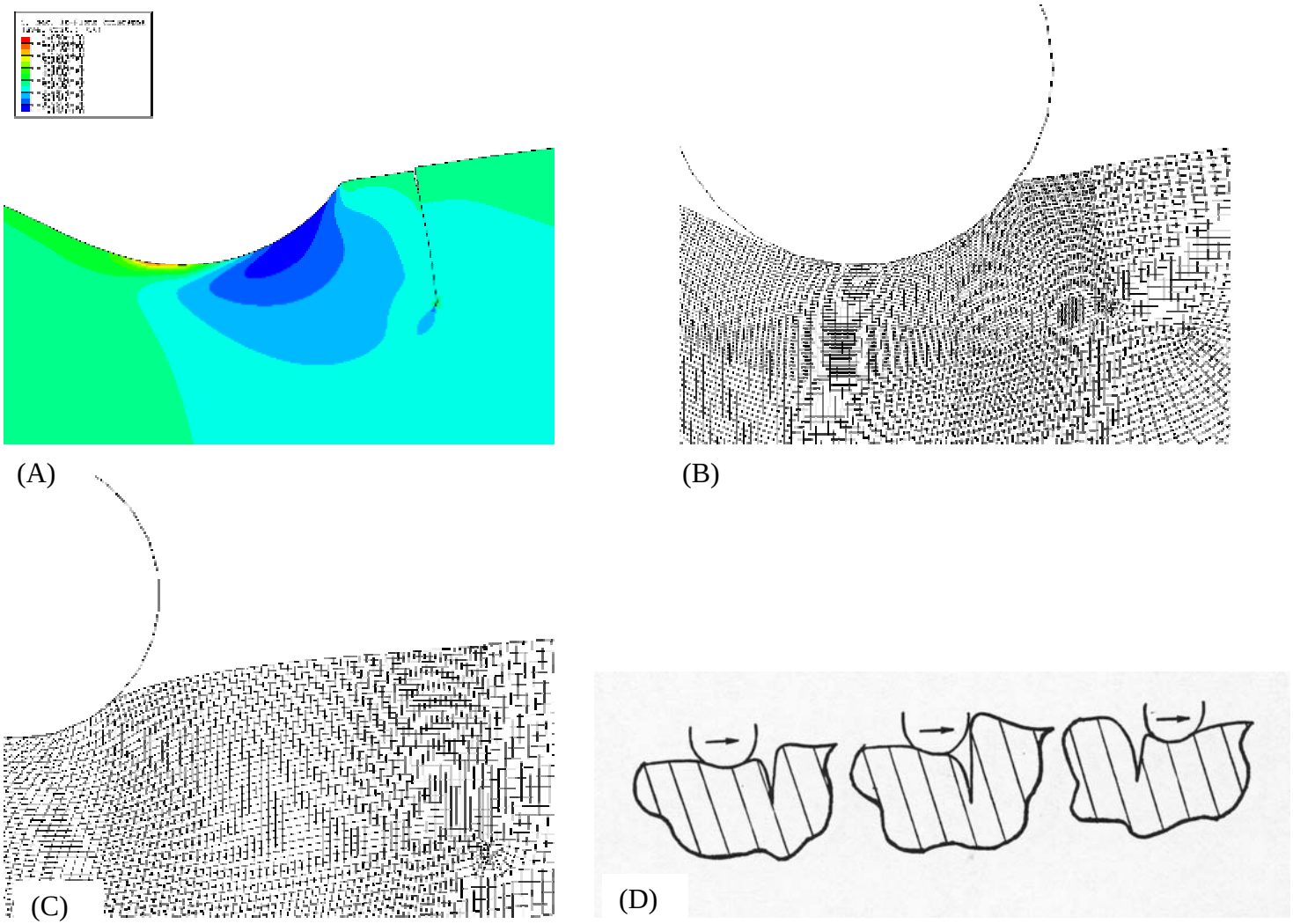

FIGURE 4.27: Scenarios for asperity approaching a crack (A) Max Principal Stress Contour (B) and (C) two different deformed mesh configurations and (D) Possible scenario where asperity loads a crack wall [64]

4.7 Comment on Cavitation Damage in Asperity Loading

As the asperity penetrates close to a crack and moves away from it, there are several areas where there is a likelihood of large hydrostatic forces. Also, for plain strain case corresponding to cracks with large lateral dimension, there are large transverse stresses that Lake et al [82] link to cavitation phenomena. For all the simulations in this study, a cavitation parameter was calculated as:

$$\Phi_c \cong (4\sigma_1 - \sigma_2 - \sigma_3)(4\sigma_2 - \sigma_3 - \sigma_1)(4\sigma_3 - \sigma_1 - \sigma_2) - 5\mu^3 \qquad (4.2)$$

Where the stresses represent the principal stress components and μ is the NeoHookean shear modulus. The cavitation condition is then given by :

$$\Phi_c \geq 0 \qquad (4.3)$$

Figure 4.28 shows the plot of some representative crack tip nodes during the asperity penetration near the crack. Note that the cavitation parameter is rather small, even for a depth of penetration corresponding to 70% of the asperity radius and large friction coefficient. So at least for the materials involved in this study, there is no evidence of possible cavitation damage for the asperity loading conditions specified. This also provides indirect justification for using the tensile test data from relatively thin samples, and applying it to plain strain case without accounting for the effect of lateral stresses on energy release rate.

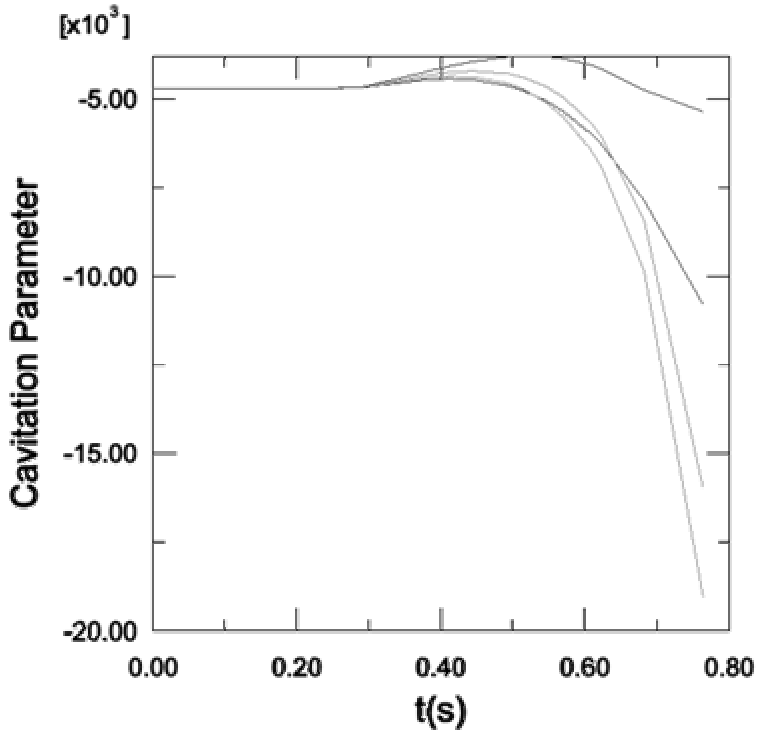

FIGURE 4.28: Cavitation Parameter for elements around the crack tip for an asperity penetration near a crack (length R) for a depth of penetration of 0.7 R and friction coefficients: μ=0.5. for rubber asperity and μ= 1.0 for rubber to rubber interaction.

CHAPTER V

DYNAMIC ASPERITY LOADING

In this chapter we discuss the effect of dynamic loading in the asperity interaction with an elastomeric surface. An explicit dynamic methodology is used in the ABAQUS environment for this purpose.

5.1 Explicit Dynamic Method in FEA

Most asperity interactions in real life are dynamic events. In this chapter, we investigate the effects of dynamic asperity interaction with the wear surface. The dynamic asperity interaction model is simulated using the explicit dynamic procedure available in the commercial code ABAQUS. The method has particular advantage with respect to the implicit method described earlier as it does not require formulation of a stiffness matrix [128]. At the beginning of each time increment, the program computes the dynamic equilibrium as described in equation 5.1.

$$\ddot{u}^{N}_{(i)} = \left(M^{NJ}\right)^{-1}(P^{J}_{(i)} - I^{J}_{(i)}) \qquad 5.1$$

Here $\boldsymbol{u}$ represents displacement, M is the nodal mass matrix , P represents the externally applied force(s) and I is the internal element force. The nodal mass matrix is a diagonal matrix and allows for easy inversion resulting in inexpensive nodal calculations. The specific steps involved in an Explicit method are as follows:

(1) Calculation of accelerations at the nodes as described in equation 5.1. This is then

(2) used to calculate the nodal velocity and displacement using a central difference operator as follows:

$$\dot{u}^{N}_{(i+\frac{1}{2})} = u^{N}_{(i-\frac{1}{2})} + \frac{\Delta t_{(i+1)} + \Delta t_{(i)}}{2}\ddot{u}^{N}_{i}, \qquad u^{N}_{(i+1)} = u^{N}_{(i)} + \Delta t_{(i+1)}\dot{u}^{N}_{(i+\frac{1}{2})} \qquad 5.2$$

Here, the subscript ***i*** indicates the quantity at time *t* and *(i + 1)* represents the time $t+\Delta t$ where Δt is the time step used for the analysis.

(2) The displacement related quantities estimated in the step 1 are used to estimate the element strain rates at the integration points and corresponding strain increments ($d\varepsilon$) for the element. The element stress quantities are determined using the relation:

$$\sigma_{(t+\Delta t)} = f(\sigma_{(t)}, d\varepsilon) \qquad 5.3$$

(3) The updated stress variables for the element are used to assemble the nodal internal forces.

(4) Repeat the calculations again from Step 1 with ***t*** set to ***t*** + ***Δt***

For the above method to be successful, the time increment required is typically very small. However, individual increments are very inexpensive, allowing for smaller computation times. For more details regarding this method the reader may refer to ABAQUS user manual [128] or standard FEA textbooks.

Stability of the Explicit Method [128]:

The explicit method described above is only conditionally stable with the maximum time step allowed for an increment limited by the following criterion:

$$\Delta t \le \frac{2}{\omega_{\max}}\left(\sqrt{1+\xi^{2}_{\max}} - \xi_{\max}\right) \qquad 5.4$$

Here the highest frequency of the global model determines the time step.

In a discrete method, this is done on a element by element basis. Typically, the highest frequency is associated with the dilatational mode. At an element level, the maximum time step requirement for stability simply reduces to:

$$\Delta t_{\text{stable}} = \frac{L^e}{c_d} \tag{5.5}$$

Where L^e is the characteristic element length and c_d is the characteristic dilatational wave speed of the material. . The characteristic element dimension is based on an analytic upper bound expression for the maximum element eigenvalue. For example the 4-node plain strain quadrilateral (Abaqus CPE4R element), has a characteristic element dimension defined as:

$$L_e = \frac{A}{\sqrt{B_{iI} B_{iI}}} \tag{5.6}$$

where B_{ij} is the element gradient operator and A is the area of the element.

For a typical elastic material, the dilatational wave speed is given by:

$$c_d = \sqrt{\frac{\hat{\lambda} + 2\hat{\mu}}{\rho}} \tag{5.7}$$

The effective Lame's constant in the equation 5.7 are determined using a hypoelastic material relationship for the bulk modulus.

$$3\hat{K} = 3\hat{\lambda} + 2\hat{\mu} = \frac{\Delta p}{\Delta \varepsilon_{vol}} \quad ; \; 2\hat{\mu} = \frac{\Delta S : \Delta e}{\Delta e : \Delta e} ; \; \hat{\lambda} + 2\hat{\mu} = \frac{1}{3}\left(3\hat{K} + 4\hat{\mu}\right) \tag{5.8}$$

Here K is the effective bulk modulus determined by using the incremental hydrostatic component of the total stress and the volumetric strain.

The introduction of such pure hypoelastic compressibility law as described above

creates a need for damping at high speed (frequency) dynamic events. This damping is introduced in the form of the bulk viscosity. These viscosity parameters (b_1 and b_2) are defined by a linear (b_1) and a quadratic expression (b_2) between an artificial bulk pressure (p_{bv}) and the volumetric strain rate (ε_{vol}) as described in the equations 5.9 and 5.10 respectively.

$$p_{bv1} = b_1 \rho c_d L_e \dot{\varepsilon}_{vol:} \quad 5.9$$

$$p_{bv2} = \rho(b_2 L_e \dot{\varepsilon}_{vol})^2 \quad 5.10$$

The quadratic version of the bulk viscosity is only used for the plain stress reduced integration elements (ABAQUS CPS4R element). The effective damping introduced by the bulk viscosity approach is given by:

$$\xi = b_1 - b_2 2 \frac{L_e}{c_d} \min(0, \dot{\varepsilon}_{vol}) \quad 5.11$$

The linear bulk viscosity is related to the high frequency oscillations for an element and the quadratic bulk viscosity is related to the collapsing of an element under concentrated pressure wave (shock). Note that the bulk viscosity pressure is purely a numerical artifact and has no bearing on the hydrostatic component of stress derived from a material constitutive law.

5.2 Material Properties Under Dynamic Conditions

For the dynamic simulations, the dynamic response of material needs to be characterized. Data from high strain rate experiments for elastomers is scarce. In light of this, the present investigation is restricted to the high strain rate data for unfilled polymers from Bekar et al [124]. The Figure 5.1 shows the data for unfilled SBR at strain rates ranging from 1 s^{-1} to 480 s^{-1} . These experiments were conducted with a rapid

imaging system while stretching a rubber specimen at high strain rate. The Cauchy stress vs stretch ratio (λ) data also shows that the breaking stress has an envelope for the particular unfilled SBR grade. Thus, the breaking stress increases with the increasing strain rate in the beginning and then decreases with increasing strain rate after reaching a peak value.

Typically, the dynamic response of elastomers is highly viscoelastic. So a multimode Maxwell Model was attempted to characterize the data shown in Figure 5.1 However, this attempt was not successful in providing reasonable viscoelastic parameters that could be simulated using the explicit dynamic scheme described before. Largely, this was attributed to the lack of unloading data in reference [124]. Additionally, in the case of viscoelastic constitutive models, the explicit scheme described in the previous section has a more stringent stability requirements for the maximum time step used. This is counterintuitive to the idea that damping typically adds stability to the system. However, the logic is easily explained by equation 5.4.

With the limitations described above, the material was modeled as a strain rate dependent hyperelastic material ('weak' Voigt Model)l. Thus, the stress-strain curves at constant strain rates were approximated by a Mooney Rivlin type hyperelastic law with different set of material coefficients at different strain rates. The data was approximated by a Mooney Rivlin type equation very well through most of strain (stretch ratio) ratio (Figure 5.1). However at higher strain rates, the data was only poorly approximated by the Mooney-Rivlin type equation at small strains. Note that the experimental data reported by Bekar [124] covers a wide range of strain, measured using imaging strain. The data has relatively large error for small strains (less than 0.25%) for both the stress

and the strain conditions. Nevertheless, at high strain rates, there is a very large instantaneous elastic Component, resulting in a stiff response. The small strain data is shown in Figure (5.1, Bottom) with the curve fit for Mooney Rivlin model.

The Abaqus Explicit code is limited in convergence properties for incompressible or near incompressible material models. This is explained easily by the hypoelastic compressibility equation 5.4. For this purpose, a compressibility related term of 5.55556E-02 is added to the Mooney Rivlin Strain Energy potential for the plain strain models. Similarly for plane stress elements a term equal to is added. This creates significant compressibility in the material model. This can be rectified by using a mixed element formulation with pressure as an independent variable similar to those in fluid dynamic simulations along with the usage of special techniques related to Nonlinear Hyperbolic Partial Differential equations such as the Streamline Upwind Petrov Galerkin method (SUPG). However, this is seriously lacking from the present day FEA codes for solid mechanics that use the general Lagrangian description.

5.3 Implementation of the Constitutive Law for the Dynamic Behavior of the Material

From the discussion in previous section, a strain rate dependant hyperelastic model was implemented in ABAQUS as a user subroutine (VUMAT). The subroutine calculates the Cauchy stress for a given strain increment defined by the symmetric part of the deformation gradient. All the strain measures are calculated using configuration at mid-step time increment and the tensor quantities are calculated based on a corrotational coordinate system at the integration point. This may introduce its own problems at high strain rates [125,126]. The user subroutine reads the material state of stress at a given

integration point at the previous increment as well as the stretch and rotation information at the beginning and the end of the latest increment.

The user subroutine then updates the stress conditions to the new time step using a Mooney Rivlin type constitutive law where the material parameters are interpolated from the closest strain rates from the experimental test data. For the strain rates higher than the experimentally tested strain rates, the Mooney Rivlin coefficients are obtained by extrapolation.

5.4 Frictional Law

The data for elastomeric friction at high speeds, is not easily available despite several comprehensive works [17-20]. In the present simulation, a proposed Stick-Slip model by Leonov et al [23, 24] is used along with a constant friction Coulomb model for the comparison. The data for slip speed dependence of friction based on the Leonov model is shown in Figure 5.2 for the constitutive parameters m and n. The pressure dependence is approximated by a linearly decreasing law from literature [17,19]. Although, the proposed model by Leonov et al [24,23] includes a critical shear stress and speed at which the slip occurs, this is conveniently not included in the present model in order to avoid numerical instabilities related to the contact. Note that there is a serious lack of friction data in the literature, let alone the data for the particular grade of SBR under consideration. So the friction models used here are strictly to estimate the qualitative nature of wear surface interaction.

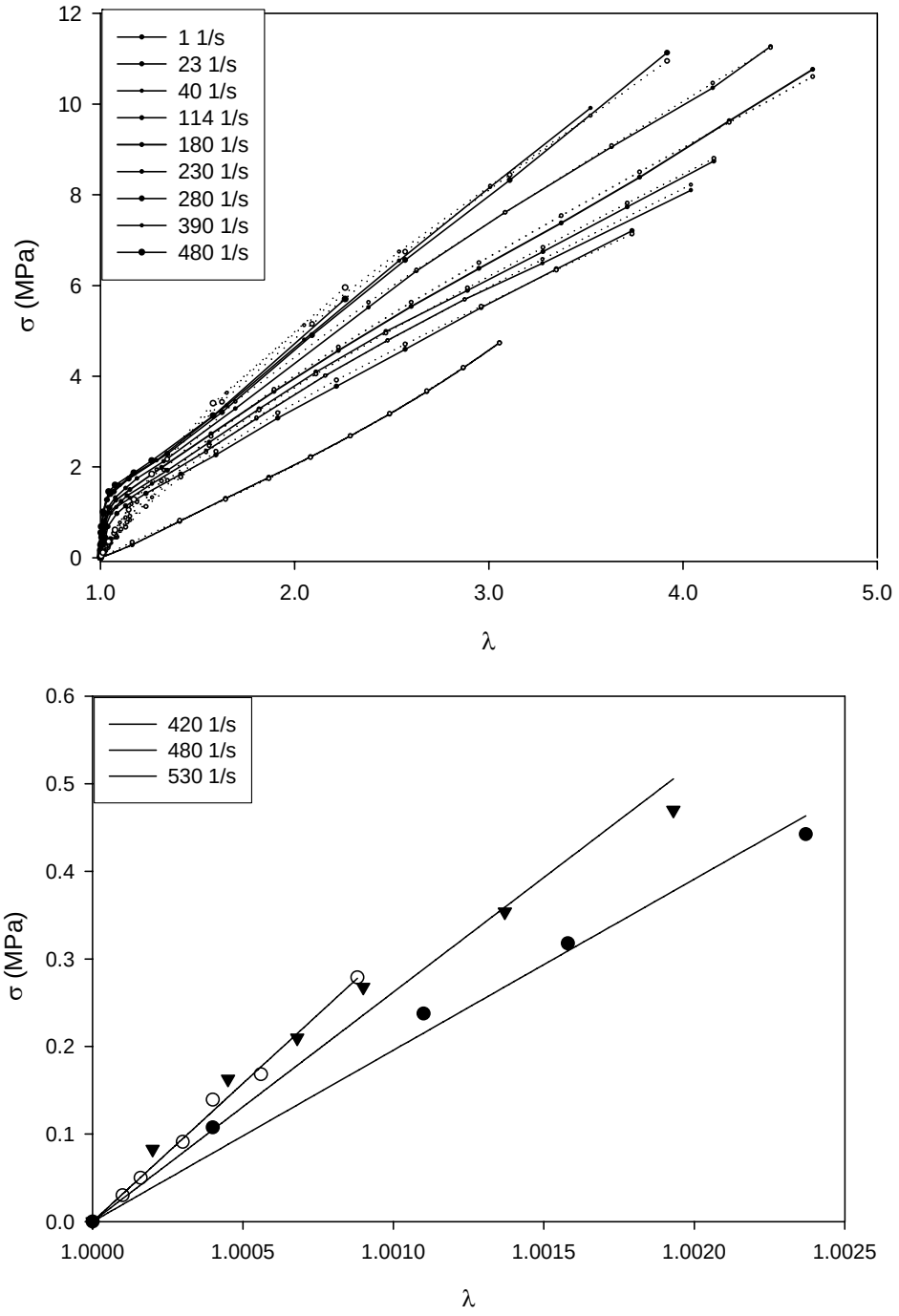

FIGURE 5.1: Cauchy Stress vs Stretch Ratio from constant strain rate experiments. The data is from Bekar et al [124]. The curve fits show rate dependant hyperelastic fits. Top: Data

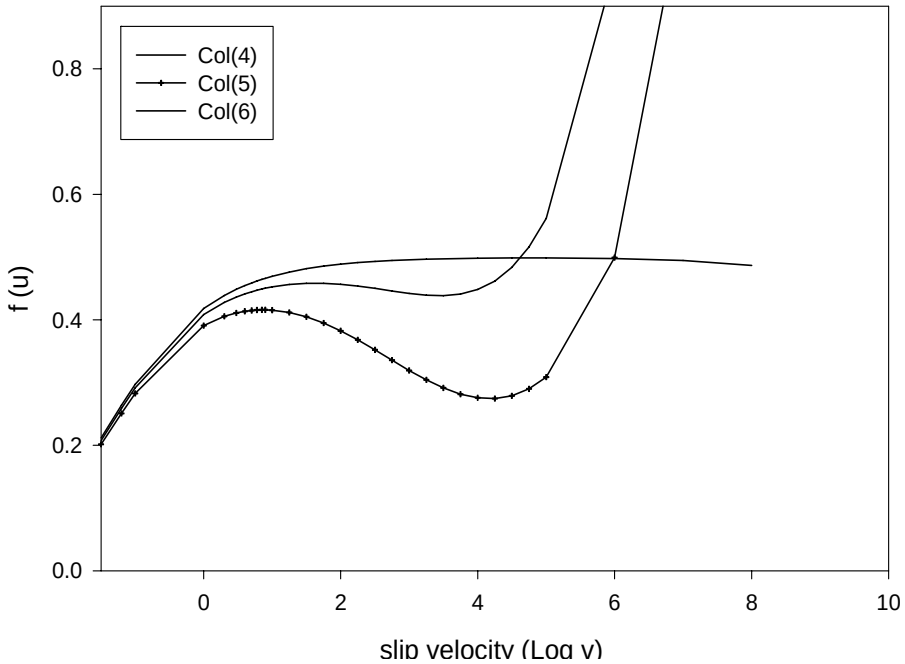

FIGURE 5.2: Friction dependence on sliding velocity [102] for various constitutive parameters m and u

5.5 Results from the Dynamic simulations

The asperity loading discussed in the previous chapter was studied for three different speeds, viz. 1 km/hr, 10 km/hr and 18 km/hr. The Figure 5.3 shows the typical strain history and strain rate history for few representative nodes along the wear surface as the asperity penetrates and travels away from the crack. Similarly, figure 5.4 shows the corresponding strain and strain history for representative crack tip nodes.
Note that, the crack tip nodes achieve severe high strain rates (of the order of $1200s^{-1}$) during asperity penetration as well as travel step. The strain rate dependant material properties are largely responsible for this.

A few animations are provided on a separate compact disc (CD) along with this dissertation. The animations show the maximum principle stress as well as the stress distribution for the different speeds as well as frictional conditions. Three different frictional conditions were considered. The first one was implemented with a Coulomb type constant friction coefficient of 1.0, the other two cases used the velocity dependence represented by the Col(6) in figure 5.2 but with a steady state friction coefficient of 0.3 and 0.5 when the contact pressure is of the order of the elastic modulus of the material at low strain rates.

5.5.1 Contact Area and Contact Pressure

Figure 5.5 shows the evolution of the contact area for the two different asperity velocities 1km/hr (Top and Middle) and 10 km/hr (Bottom). The top two frames show contact area evolution for the speed of 1 km/hr but for two different friction models. The first half of the time represents asperity penetration, where the contact area

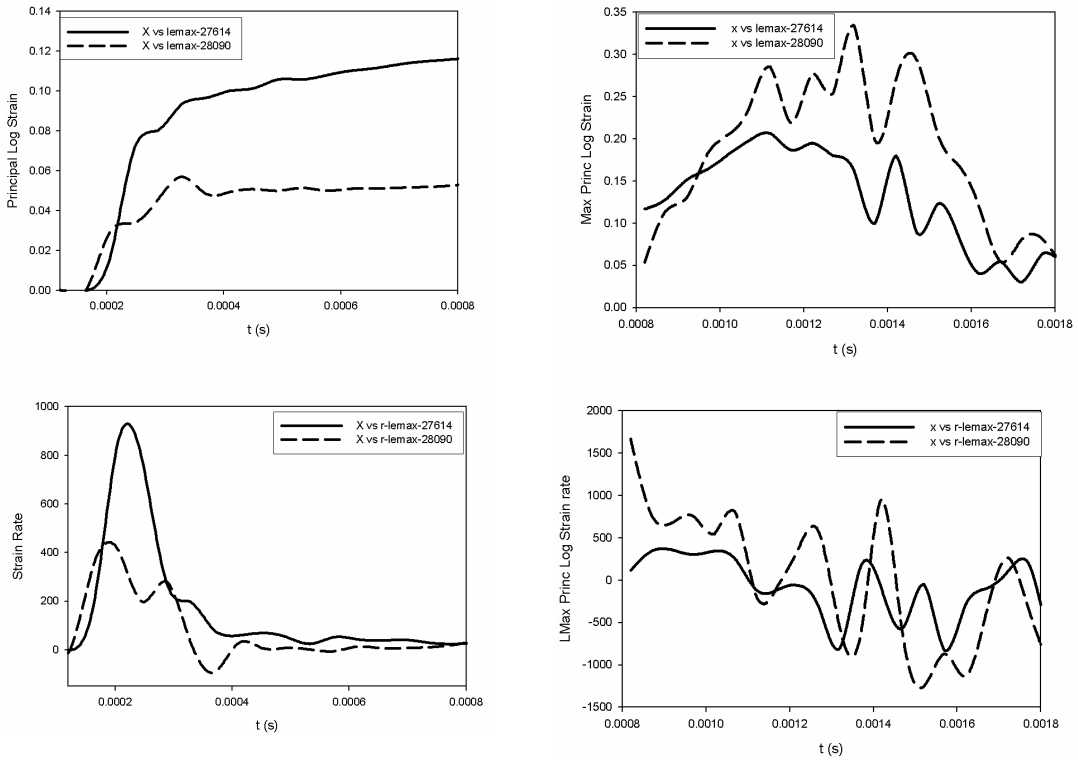

FIGURE 5.3: Principle strain measures and strain rates for asperity penetration for selective surface nodes (Left) and for a receding asperity (Right).

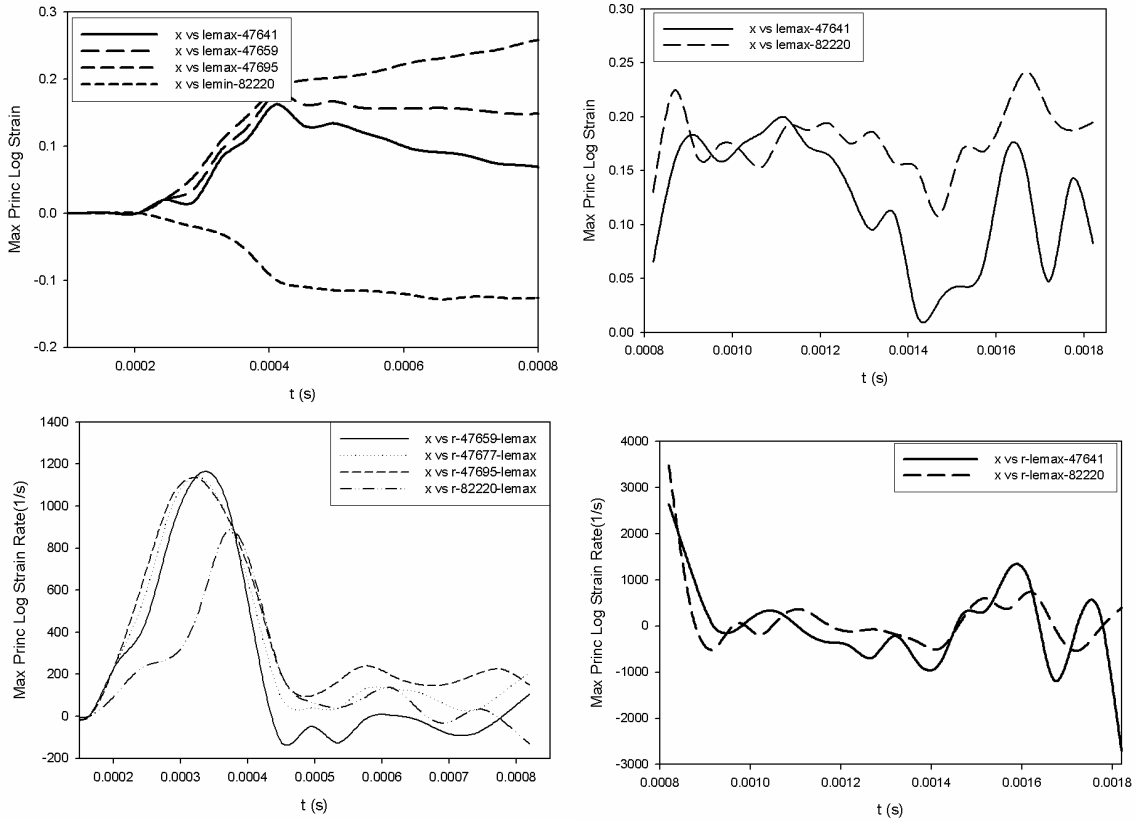

FIGURE 5.4: Principal strain measures and strain rates for asperity penetration for selective crack tip nodes (Left) and for a receding asperity (Right).

increases continuously. In the second interval of the time, the contact area shows slight increase at the lower speeds. In the case of Coulomb friction with a high friction coefficient, there are significant oscillations corresponding to the distortion of the elements due to high friction coefficient. In the case of velocity–pressure dependent friction model at the low velocity, the friction coefficient is moderate and the distortions are far less.

When the speed increases considerably to 10 km/hr, the qualitative behavior of the contact area is similar, however a smaller contact area is reached (nearly half that at 1 km/hr) at the same depth of penetration. When the asperity is traveling away from the crack, the contact area steadily decreases with large oscillation. The reduced contact area during the penetration is due to the increased stiffness of the material at higher strain rates. The decrease in the contact area during asperity travel away from the crack, is due to loss of contact in the contact area at high speed (10 km/hr).

This is observed in Figure 5.7 where the contact pressure distribution gradually shows oscillations along the contact path. As asperity moves away from the crack, there are more than one peaks for contact pressure in the contact patch. Eventually, there are some nodes where zero contact pressure is achieved. This symbolizes the loss of contact. The resulting 'wave' like instability in the contact area leads to the decrease in the contact area.

This unstable behavior in the contact region is nothing but the Schallamach wave as described in the literature [1, 18]. Note that at high strain rates, the unfilled SBR modeled in this simulation has relatively high stiffness, even then, the Schallamach

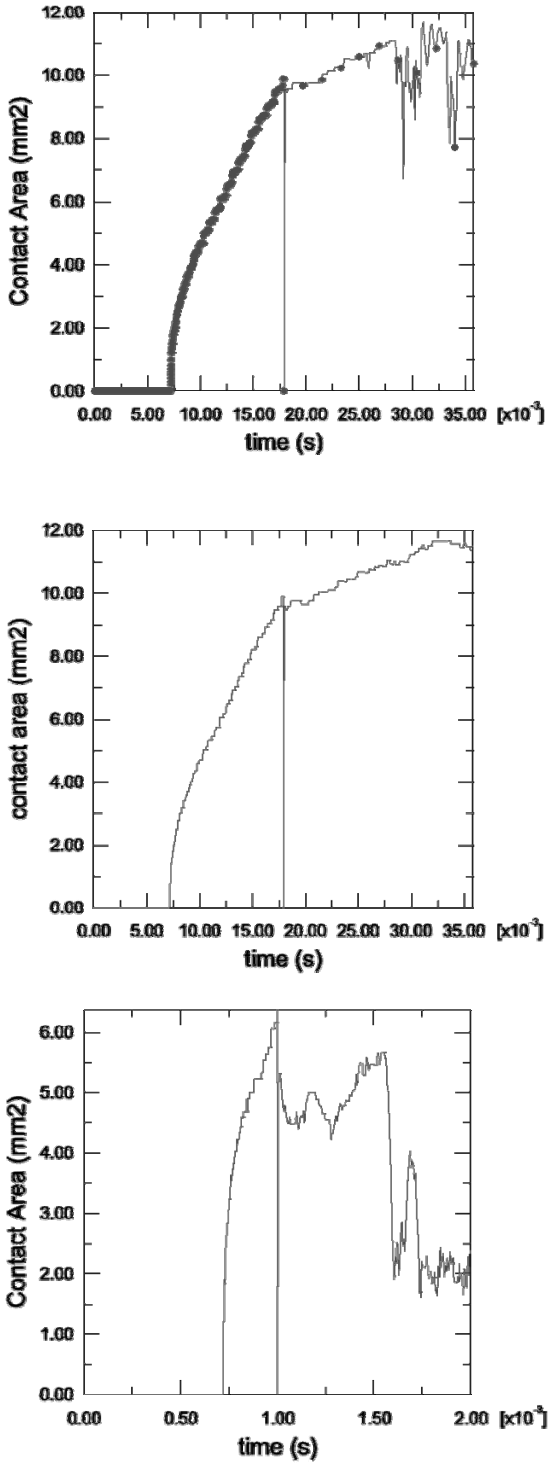

FIGURE 5.5 : Contact area for the asperity during loading. (Top) μ =1.0 , Colomb, velocity =1 km/hr. (Middle) Speed and Pressure dependent friction with static friction coefficient = 0.5, velocity =1 km/hr. (Bottom) Frictional condition same as the middle plot, velocity = 10 km/hr

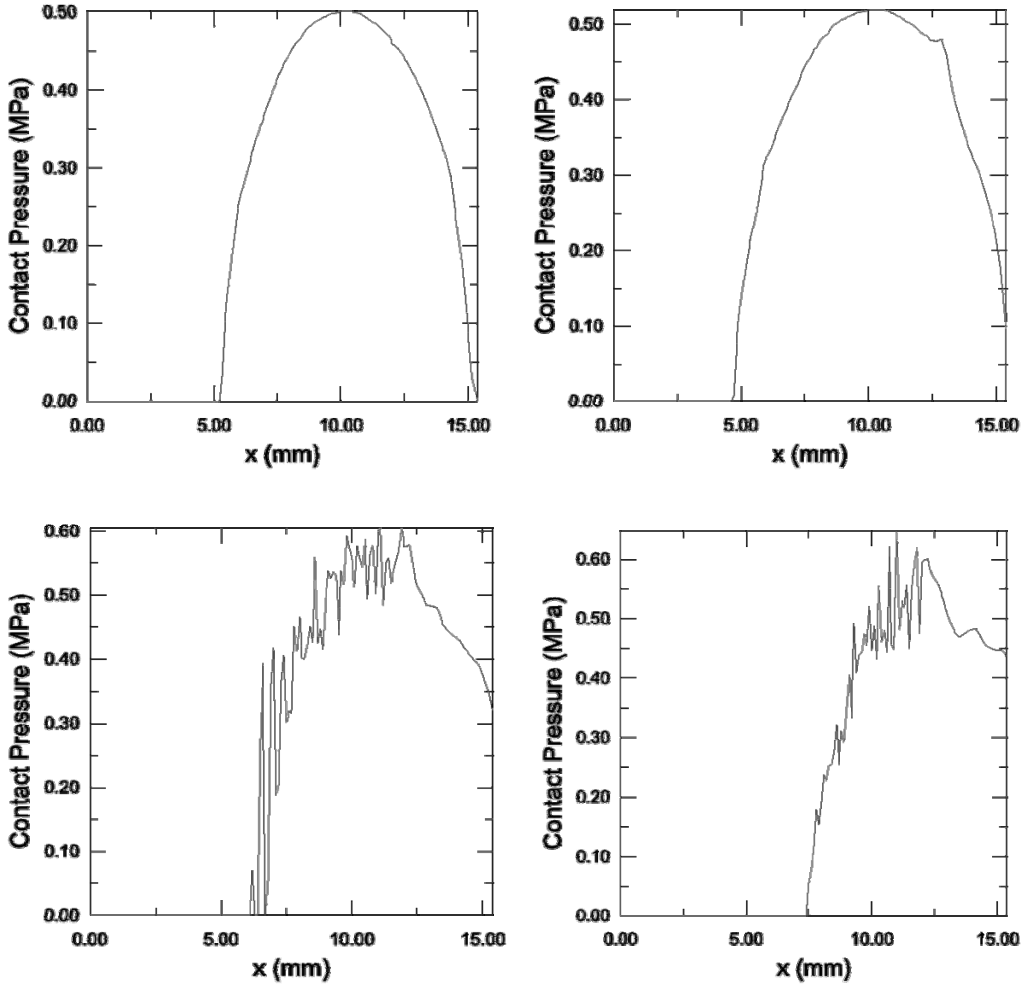

FIGURE 5.6: Contact pressure distribution in the contact area as the asperity moves away from the crack progressively from: Top Left: when the asperity is closest to the crack, to Bottom Right: when the asperity is furthest from the crack μ =1.0 , Coulomb, velocity =1 km/hr.

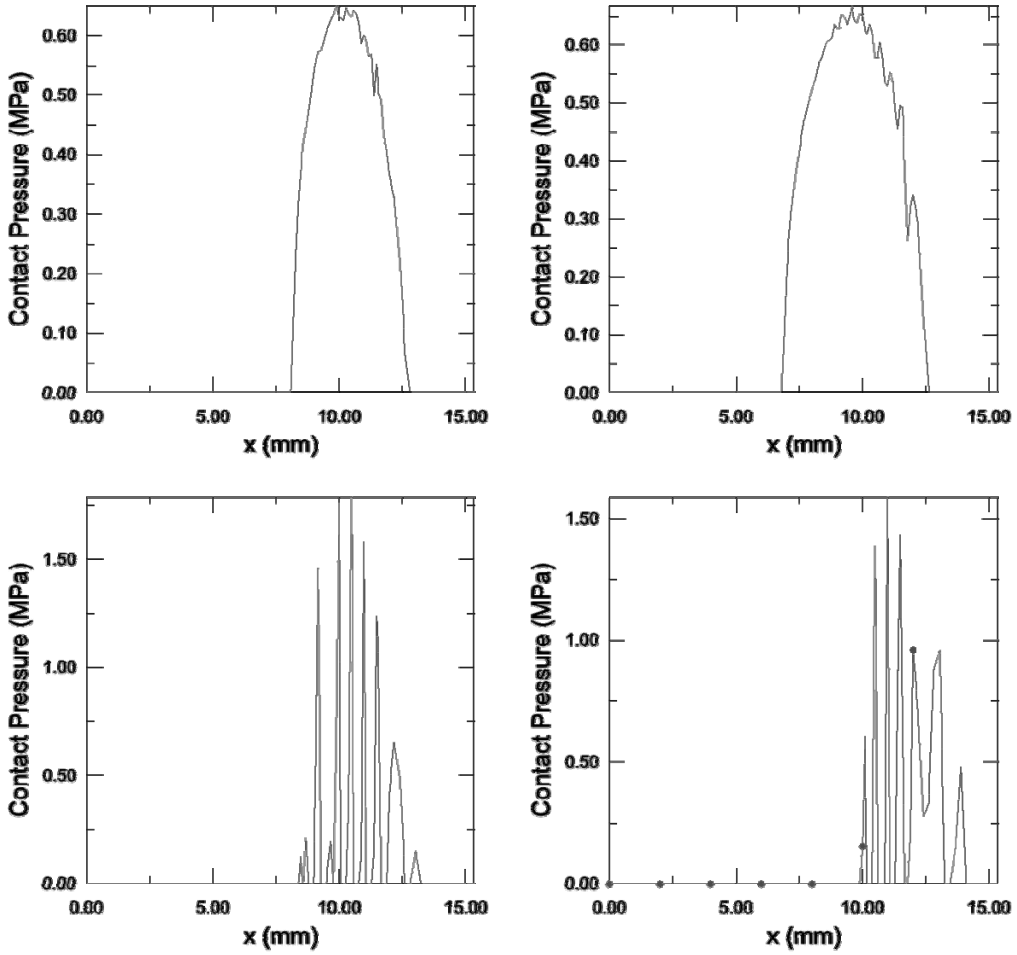

FIGURE 5.7: Contact pressure distribution in the contact area as the asperity moves away from the crack. From Top Left when the asperity is closest to the crack to Bottom Right when the asperity is furthest from the crack static μ =0.5, velocity dependent friction. Asperity Velocity =10 km/hr.

waves are readily propagated at the given depth of penetration. At the same time, the present simulation suffers from modeling dissipation based on loading alone. This may result in exaggerated wave phenomenon in the trailing edge of the asperity. Even at the low speed of 1 km/hr, at a high Coloumb friction coefficient of 1.0, there is a stress wave in the wake of the asperity. This is evident in the stress contours of Figure 5.8. However, this elastic wave is quickly dampened by the relatively high deformation of the material at the low strain rates.

5.5.2 Stress Distribution During Dynamic Asperity Loading and Crack Growth

Figure 5.9 shows the Maximum Principal Stress history for few select elements along the wear surface for 1 km/hr and 10 km/hr. The distribution shows the dynamic nature of the stress experienced by the wear surface. Unlike the static asperity loading case, in the case of dynamic asperity loading, the stress experienced by the wear surface is highly biaxial. There are no distinct areas near the trailing edge of the asperity where a near uniform tensile stress zone exists. This is partly due to the stress wave generated by the dynamic loading. This creates a highly complicated multiaxial and dynamic stress state. Thus a stress initiation/ propagation like criterion as described in Chapter IV is not applicable in the case of dynamic loading. One plausible proposal would be to decompose individual strain energy histories at a point, into Fourier series. This can be then treated as a superimposition of several independent fatigue loading conditions. The energy release rate and the crack growth rate may be then estimated as a sum of the individual components. The stress wave propagation may introduce an additional factor that influences crack spacing in a dynamic event Specially, in the contact region, the

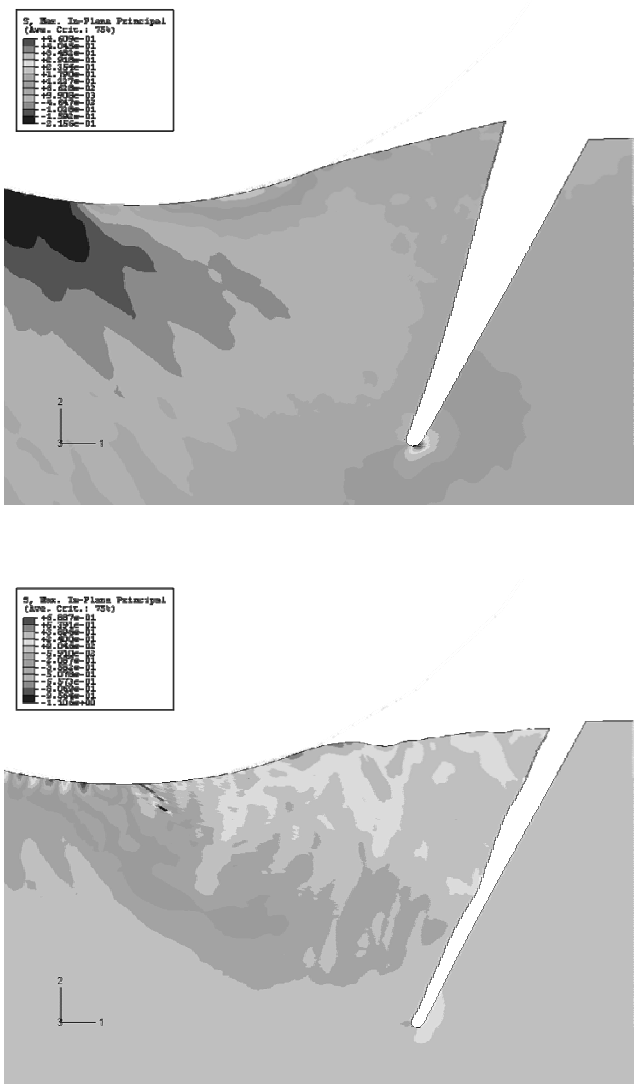

FIGURE 5.8: Maximum Principle Stress distribution as the asperity moves away. (Top) when the asperity is closest to the crack. (Bottom) when the asperity is furthest from the crack static μ =1.0, velocity dependent friction. Asperity Velocity =1 km/hr.

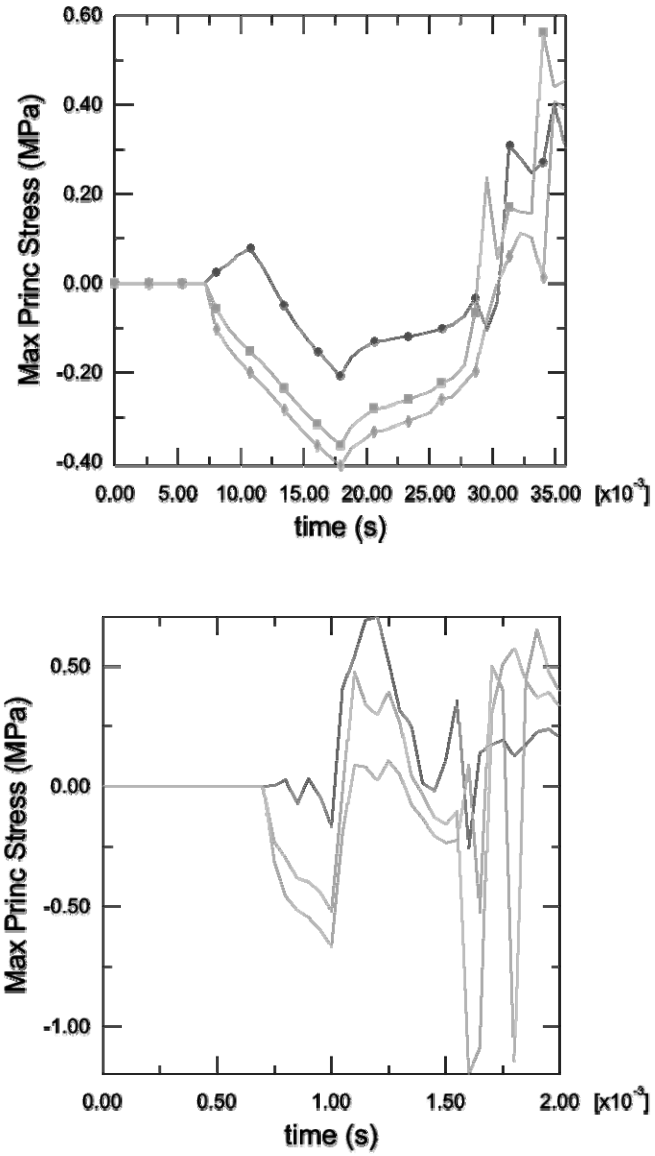

FIGURE 5.9: Maximum Principle Stress history for select wear surface nodes during asperity penetration and travel away from the crack. (Top) static μ =1.0, Coulomb friction. Asperity Velocity =1 km/hr. (Bottom) velocity dependent friction with μ =0.5 and asperity velocity = 10 km/hr

Schallamach wave results in large local deformation that is likely to create a particular spacing associated with the wavelength involved. This wavelength is a function of the material properties, the asperity loading speed and the frictional characteristics.

5.5.3 Energy Distributions

The global energy distributions for a dynamic loading gives important insight into the quality of simulations. Figure 5.10 and 5.11 shows such energy distributions for Asperity velocity of 1 km/hr and 10 km/hr respectively. The figures show that the artificial energy component for the entire model is negligible compared to the total deformational energy as well as the frictional dissipation in the model. This shows that the usage of artificial numerical parameters used to stabilize the system such as the bulk viscosity and the hourglass stiffness, has very little contribution to the solution of the problem. Only, in the case of the Coulomb friction model for asperity speed of 1 km/hr, there is significant artificial energy that is comparable to the frictional dissipation. This is due to the high element distortion in the model that is countered by high hourglass stiffness. Even then, the total deformational energy is substantially higher than the artificial energy. Still, this particular simulation may lack accuracy in the vicinity of the asperity contact. It is also interesting to see that the frictional energy dissipation is larger in case of the velocity dependent friction model as compared to the Coulomb friction model even at low speed of 1 km/hr. At the same time, the frictional energy dissipation at higher speed of 10 km/hr is in a much larger proportion than the total deformational energy. Also, the total deformational energy is at 10 km/hr is substantially smaller (almost 20%) than that of the total deformational energy at the speed of 1 km/hr.

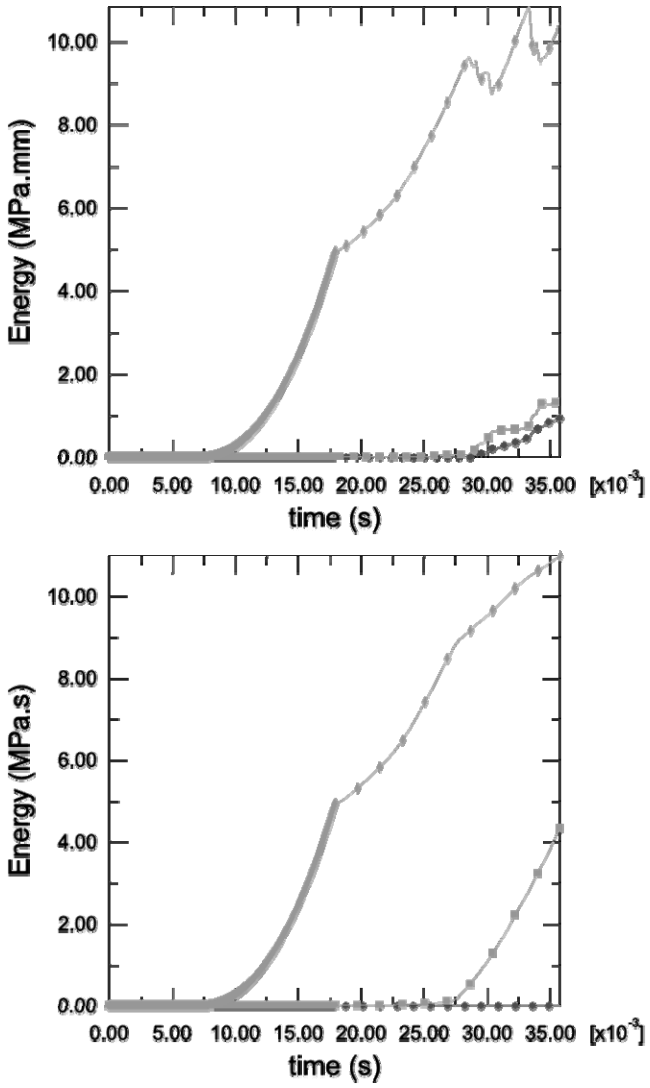

FIGURE 5.10: Strain energy, frictional dissipation and artificial energy (numerical error induced for the model during asperity loading. (Top) static μ =1.0, Coulomb friction. Asperity Velocity =1 km/hr. (Bottom) velocity dependent friction with μ =0.5 and asperity velocity = 1km/hr

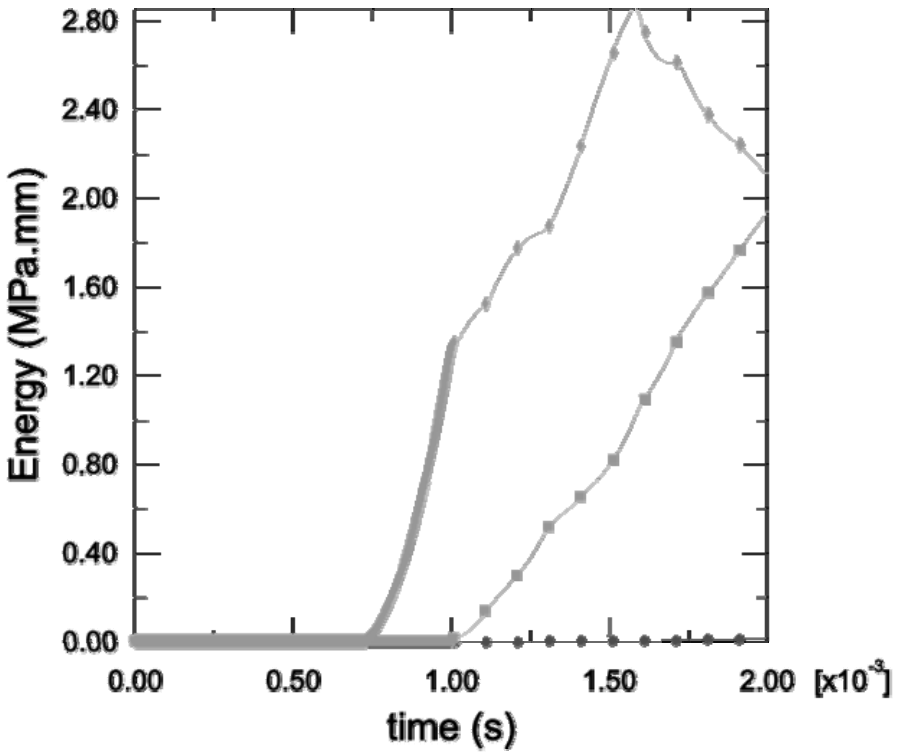

FIGURE 5.11: Velocity dependent friction with static μ =0.5 and asperity velocity = 10 km/hr

CHAPTER VI

OTHER ASPERITY INTERACTIONS

6.1 Asperity Interaction at a Micron Scale

The results of the analysis in previous sections is applicable to asperity interactions at any scale as long as the material parameters are appropriately scaled. Note that the typical results of a Finite Element simulation are *unitless*. This assumption is valid as long as the assumption that the medium is homogeneous media and can be treated as a 'continuum'. This is typically true for scales greater than a certain small length scale.. Below this scale, the medium can no longer be treated as a continuum. The sketch shown in Figure 6.1 refers to polymeric solutions [130]. In case of filled polymers, it is reasonable to assume that the material is no longer a homogeneous continuous media at the scale of 10s of microns. As the Figure 2.23 illustrates, at this resolution, there is appearance of distinct 'grain boundaries' in a filled elastomer. Also, there are regions within the media that show localized inhomogeneity, in the form of filler or occluded rubber.

In this section we discuss some first approximation model of asperity interaction at micron scale. From the SEM photographs (Figure 2.23), an attempt is made to model the microstructure at this level. The principle assumptions in these models are as follows: (1) The media is divided into principal two domains. These domains are the Carbon Filler particle with occluded rubber, and the bulk rubber. These two domains are

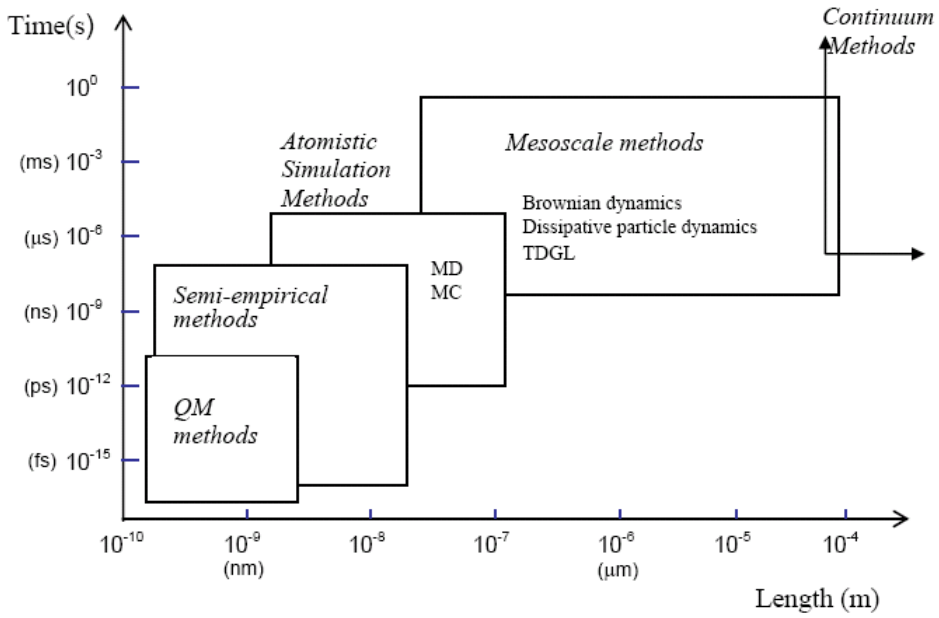

FIGURE 6.1: Chart of Simulation Methods and Scales.

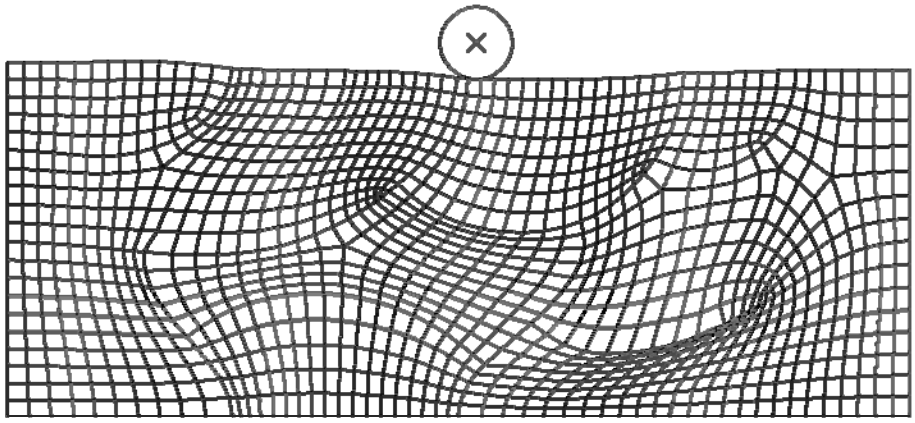

FIGURE 6.2: Mesh for the microscale model for asperity elastomer interaction.

individually modeled as continuous media with homogeneous material properties. Nano indentation studies at small scales show that the material properties at the microlevel are usually radically different than the material properties (eg modulus) at the micro level [119]. However, for the sake of simplicity, it is assumed that the rubber in the micromodel can be modeled as a hyperelastic material with the parameters obtained from the tensile test at the macro-scale.

(2) Although there are 'grain boundaries' in the microstructure that are essentially 'built in' microcracks in the rubber, they may be acted upon by strong cohesive forces. The magnitude of these cohesive forces is not found in a reliable fashion at present. In order to simplify this aspect of modeling, the grain boundaries are essentially assumed to act a material of weak modulus. It is assumed that the modulus of this material is one order less than that of the initial modulus of the bulk rubber.

(3) The carbon filler is assumed to be a linearly elastic material with a modulus equivalent to the bulk macroscopic properties of Carbon.

(4) The boundaries between Carbon black and the rubber are modeled using a 'tied contact'. This is a reasonable assumption as typically, the Carbon filler has some occluded rubber around it. Usually, there is a strong binding between the occluded rubber and the carbon filler.

(5) Just as material properties at microscale are not known, the frictional properties between a hard asperity and the elastomer is not known. Recently there have been efforts to measure the frictional properties of some inorganic substances at such low scales[123].

But efforts to measure friction in polymers at the microscale are virtually nonexistent. A nominal friction coefficient of 0.5 is assumed for the present simulations.

(6) The asperity is considered to be a rigid body. The Finite Element mesh used for the modeling of this asperity interaction is as shown in figure 6.2

6.1.1 Results

The figure 6.3 shows the Maximum Principal Stress Contours during the penetration stage and the figure 6.4 shows the Maximum Principal Stress Contours during the stage when the asperity horizontally at a fixed depth of penetration. The level of the maximum level of stress at this particular depth of penetration is of the order of a 0.5 MPa.
The animations micro1.avi, micro2.avi and micro3.avi in the directory Chap6-gfx\Microscale provided with the accompanying Compact Disc shows the particular nature of the asperity interaction at the microscale.

Micro1.avi shows the penetration of a microscopic asperity on a model. The penetration at this small scale is substantially different than that observed at larger scale. There is very little local deformation in the contact region, as the entire domain bounded by weaker grain boundaries, behaves semi-rigid in its deformation. Additionally, the material shows oscillations in the direction of the asperity travel. This is partly influenced by the contact mechanics, where the asperity senses a sudden change in stiffness while going over the surface defects. The grain boundaries modeled by a weaker material show substantially high strains, specially when under shear. The presence of such grain boundaries transfers the deformation behavior to the interior of the body away from the surface. Micro2.avi shows the same information as in previous video, but with the so called ‘grain boundaries’ suppressed from the view. Typically the

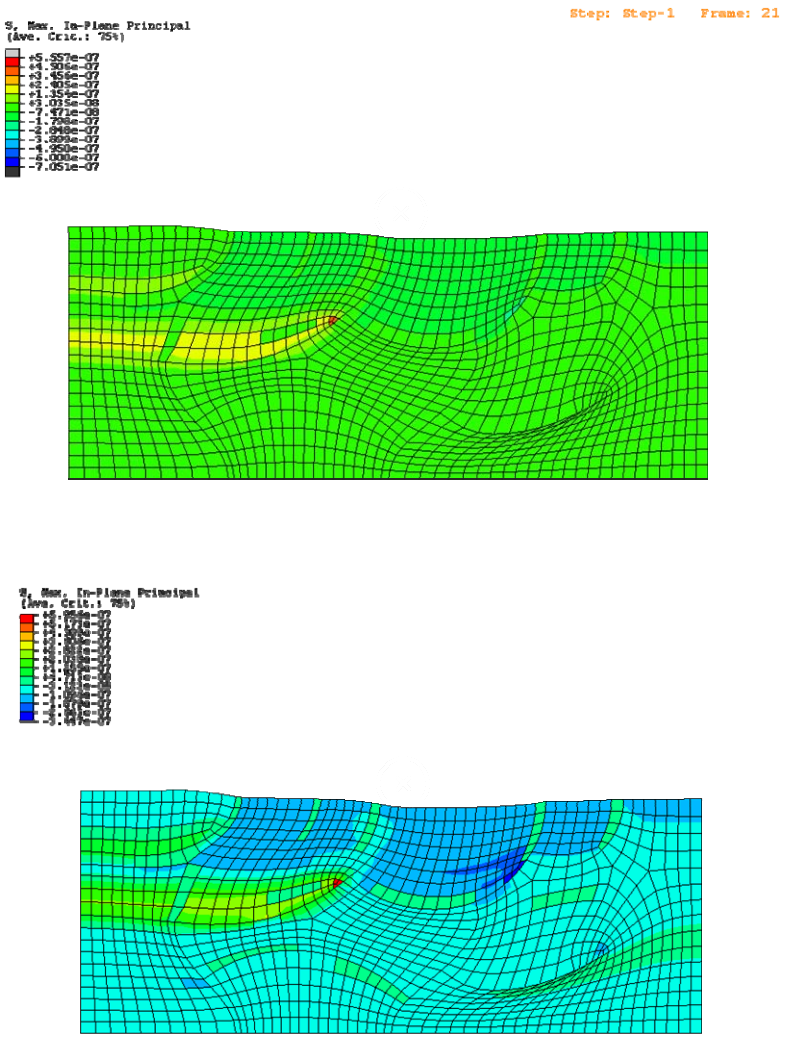

FIGURE 6.3: Maximum Principal Stress contours for asperity penetration

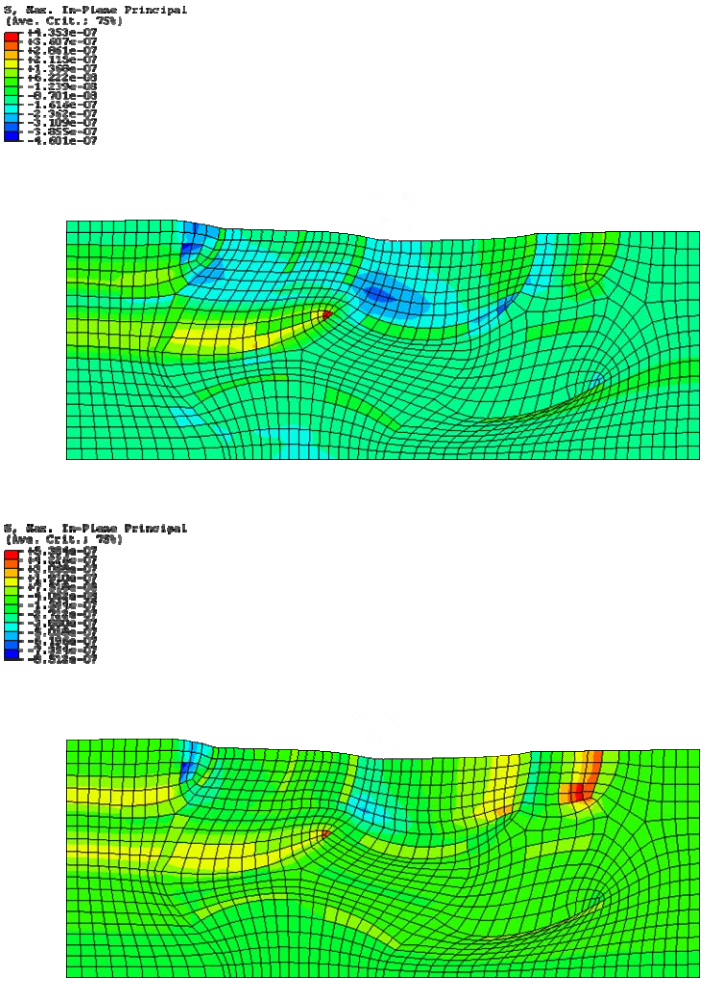

FIGURE 6.4: Maximum Principal Stress contours for asperity moving away from Top penetration location, to the left Bottom.

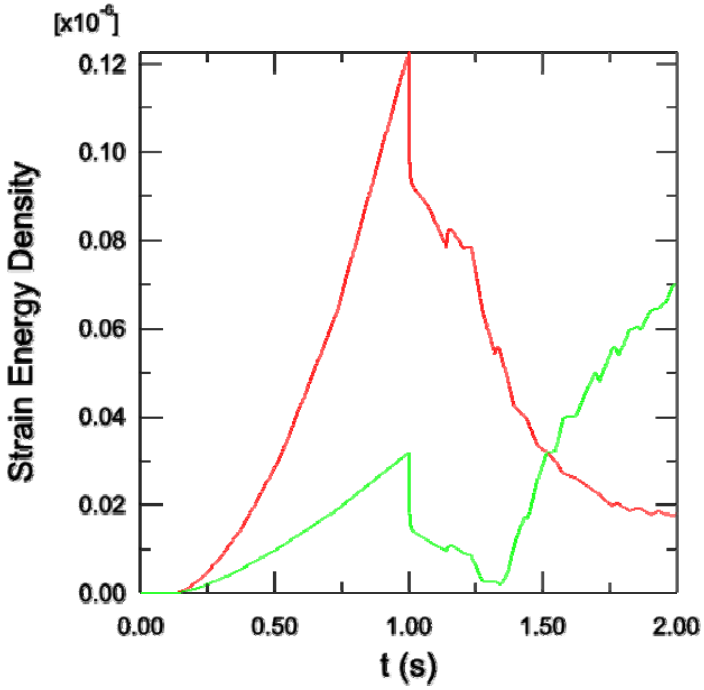

Figure 6.5: Strain Energy Density distribution near carbon filler particles.

high concentration of stress is around the carbon articles and the occluded rubber interface. Also, the grain boundaries near the surface may get stretched under the action of asperity motion.

The file Micro3.avi shows the corresponding Maximum Principle Logarithmic strains.

With the above observations, it is possible to conjecture that the dynamics of the micro-scale behavior is substantially different than that at a larger scale. However, the experimental data for material properties at a smaller scale are nearly non-existent.

The strain energy density plots for the material show that the majority of the strain energy is located around the filler particles with occluded rubber. The figure 6.5 shows the plots of the strain energy density with time for representative nodes. These high strain energy density areas are partly exaggerated by the tied contact approach for connecting between the rubber and the particles under consideration, which is only an idealization. Several researchers [131,132,136] have studied the critical values of surface energies involved in filler-filler and filler-polymer interactions. If the deformational energy exceeds the interaction energy for filler and or polymer, a rupture may result. Since the high concentration area for stresses is usually in the carbon black and occluded rubber interface, this may result in further propagation of cracks in the occluded rubber and carbon interface.

6.2 Asperity Interaction with a Rubber Flap

In this section, we discuss the particular wear geometry of a rubber flap and its interaction with the asperities. Some of the key features and assumptions of this model are as follows:

(1) The rubber flap is modeled simply as a Gaussian 3D geometry with the dimensions 30 mm (x direction), 20 mm (y direction) and 30 mm (z direction). This geometry reduces the complicated contact mechanics required for a rubber flap, while still retaining the important details. Figure 6.6 shows the schematic of the assembly of a Gaussian rubber flap loaded by an asperity.

(2) The material is considered hyperelastic and is modeled as a Mooney Rivlin material model (SBR3). This is an important simplifying assumption that ignores the viscoelastic properties of the material.

(3) The base of the block is restricted using the boundary conditions.

(4) The asperity is modeled as a rigid body.

Three particular cases were considered. In one case, the asperity is much larger than the Gaussian counterpart and is effectively modeled as an infinite cylinder. In other two cases, two different spheres with different radii are considered

(4) An explicit method is used for these set of simulations for their speed.

6.2.1 Results

Figure 6.7 shows the flap geometry with the asperity modeled as an infinite cylinder moving at 36 km/.hr with no friction between the contacting surfaces. The subsequent panels in the Figure 6.7 show the Maximum Principal Stress contours as the asperity passes the region of contact. Note that the high stress areas are formed in the wake of the moving asperity resulting in a nearly complete tensile stress condition. There are also high stresses where the flap folds over, in the fore position of the Gaussian geometry. Figure 6.8 shows a deformed flap geometry due to a large passing asperity. The corresponding state of the stress on the asperity surface is shown along with it. The

orientation of the principle stresses shows that as the asperity deflects a rubber flap, there is a high state of tensile stress along the direction of motion and in the surface just past the asperity. When the asperity is approaching the flap at an angle, the resulting deformations are drastically different. This is partially due to the change in 'effective stiffness' when the asperity approaches at an angle to the flap. Figure 6.9 shows the Maximum Principle Stress as well as Strain Energy Density distribution. Just as in Chapter 4, the idea of using the strain energy density and Maximum Principal stress criteria, for predicting crack growth and the resulting direction. . Thus, with the large asperity moving 'head-on' to the flap, the likely areas where further crack growth and related wear happens, are the 'aft' end of the flap. However, with the cylinder, moving at an angle of 30 degrees to the flap geometry, results in a significantly different stress distribution. This partially explains the different observed wear rates under different slip conditions for the same flap geometry. At the same time, a simple LEFM type relationship is a poor approximation to measure the complex behavior of such an interaction.

Figure 6.10 shows the global energy plots for the infinite cylinder and flap interaction simulations when the cylinder approaches at 0, 30 and 45 degrees. The peak in the total deformational energy stored in the body corresponds to the time when the asperity has completely passed a flap geometry. Note that, in comparison, the artificial energy introduced by the numerical scheme such as hourglassing effect is much smaller than the total energy. As the asperity completely passes the flap geometry, there is a 'recoil' effect and the flap is suddenly released from its deformed shape. This results in

heavy oscillations leading to the element distortion and hourglassing. Hence, there is an increase in the artificial energy introduced in to the system.

Additionally, interaction of the flap geometry with two different, sized spherical asperities was simulated using a discrete rigid body representation for the asperities. Figure 6.11 shows the corresponding mesh geometry . Figure 6.12 shows the Maximum Principal Stress distribution when the same flap geometry is interacting with two different sizes of the spherical rigid body model. For the larger sphere, the area under biaxial tensile stress, just aft to where the asperity contacts the flap is relatively larger, with correspondingly higher Maximum Principle Stress values. Similarly, the contact area and pressure is distributed over a larger area (Figure 6.12). Figure 6.14 shows the principle zones where the stress levels are particularly high. With the spherical geometry, there is a great deal of stretching in the fore position in the lateral direction creating a biaxial or near biaxial stress condition (Marked as U in figure 6.14). However, the largest stress values are found in the overfold area in the fore direction. The stress state in this region is triaxial (Figure 6.15) and is probably a source of crack generation although the proposed method of tensile test can not be applied for a general stress state such as this. Figure 6.16 shows the Maximum Principle Stress and Strain energy density history at two corresponding mid-nodes in the ‘aft’ position of the model for the two different sphere interactions. Surprisingly, the data shows some really high principal stresses although for a very short period of time at the given speeds.

A dynamic frictional law dependent on the velocity and the friction was introduced to study the effect of friction in the asperity-flap interaction. Figure 6.17 shows the comparison of the principal stresses at the speeds of 36 km/hr and 10 km/hr.

Note that the contact area, and stresses in the contact area change dramatically with increased speed. The Maximum Principal Stress is much higher at the higher speed as the friction coefficient increases accordingly. This emphasizes the role of frictional forces in the growth and propagation of surface cracks. Figures 6.18, compares the strain energy density distribution and the Figures 6.19-6.21 compare the contact pressure and contact shear forces for the two speeds.

Once again, the idea proposed in the chapter 4, to determine the direction and location of crack growths at the surface is very much applicable to this situation. The higher speed simulation (36 km/hr) seemed to suggest higher frictional forces , the total frictional dissipation is actually less in the higher speed simulation as compared to the lower seed simulation. This may be because of the larger contact area during lower speeds that results in a larger contribution to the total frictional dissipation (Figure 6.22)

A number of animations related to this particular problem are provided on a Compact Disc along with this. The names of the animations are self exploratory and typically correspond to the still pictures in the body of the text.

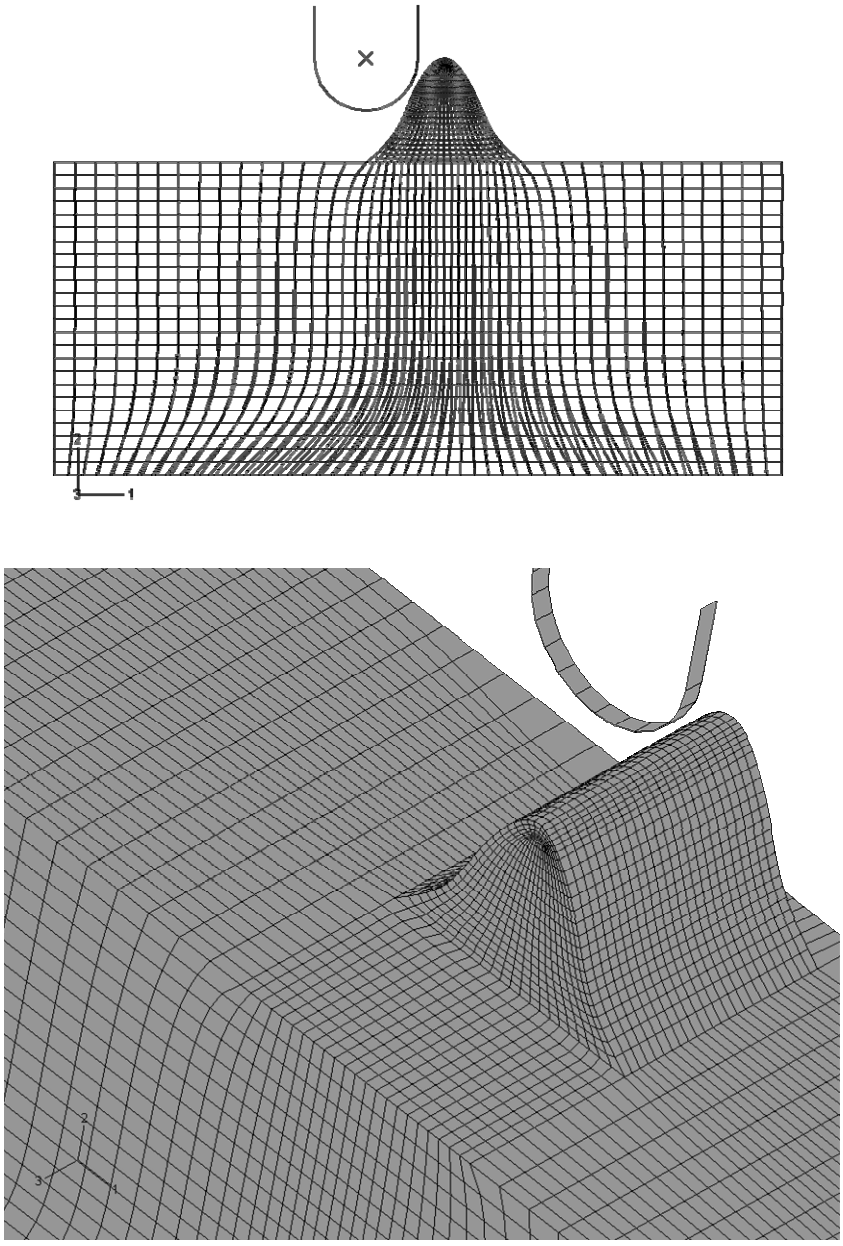

FIGURE 6.6: Mesh for the 3d- flap problem with an asperity of infinite radius
Top: Front view Bottom: Isometric view.

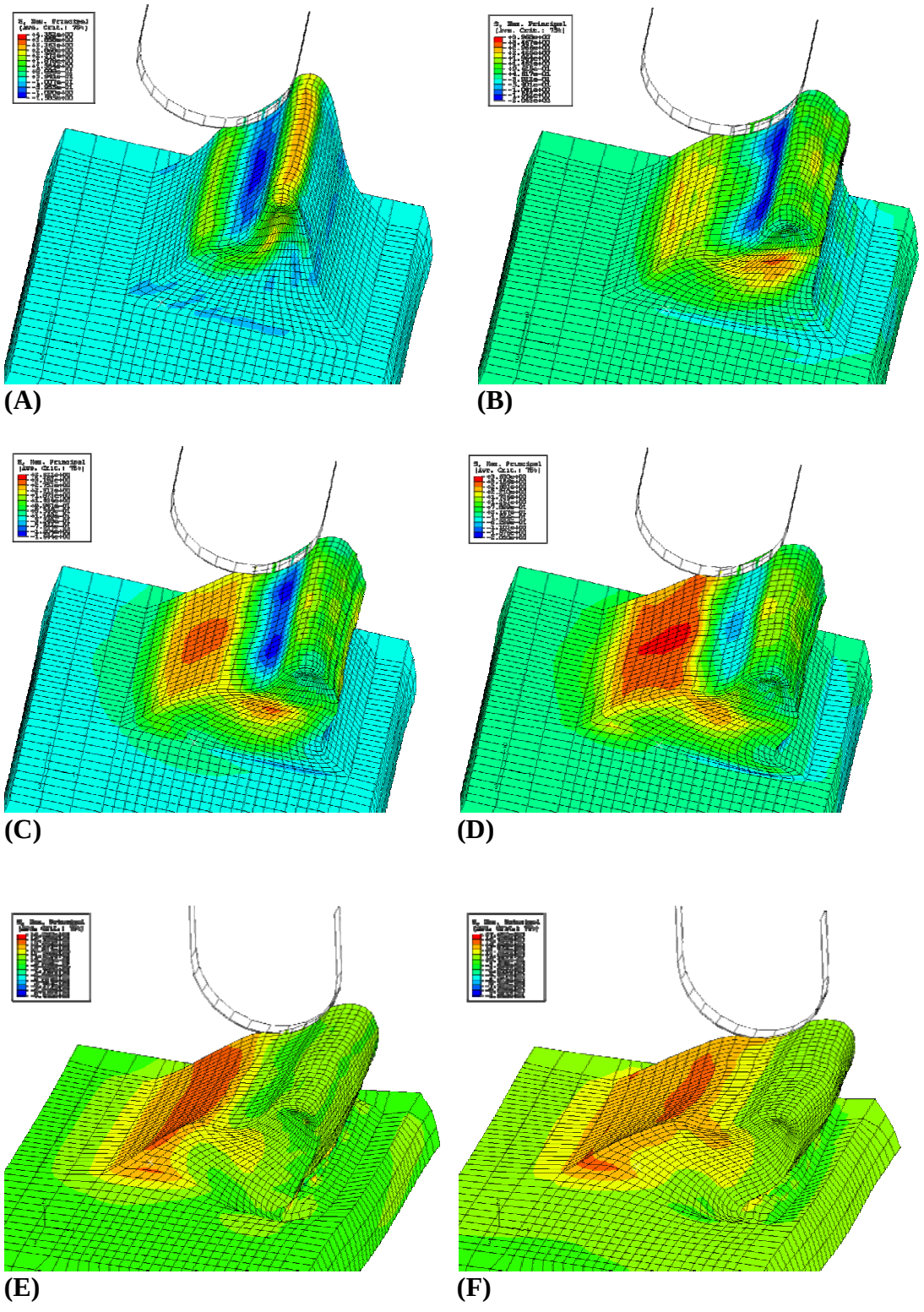

FIGURE 6.7: Principal Stress Contours for Flap deflection under a moving asperity (A-F) of an infinite radius with frictionless contact.

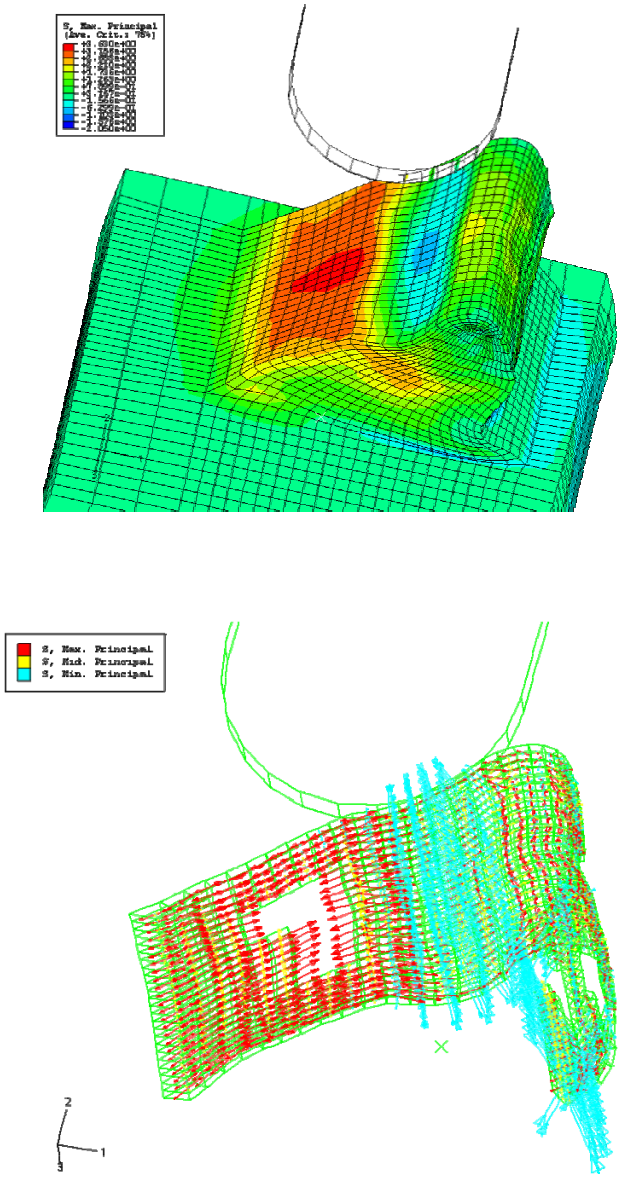

FIGURE 6.8: Top Principal Stress Contours for Flap deflection (Frame D, figure 6.7) Bottom Direction of Principal Stresses Color scheme: Red: Max Principal Blue: Min Principal Yellow: Mid Principal.

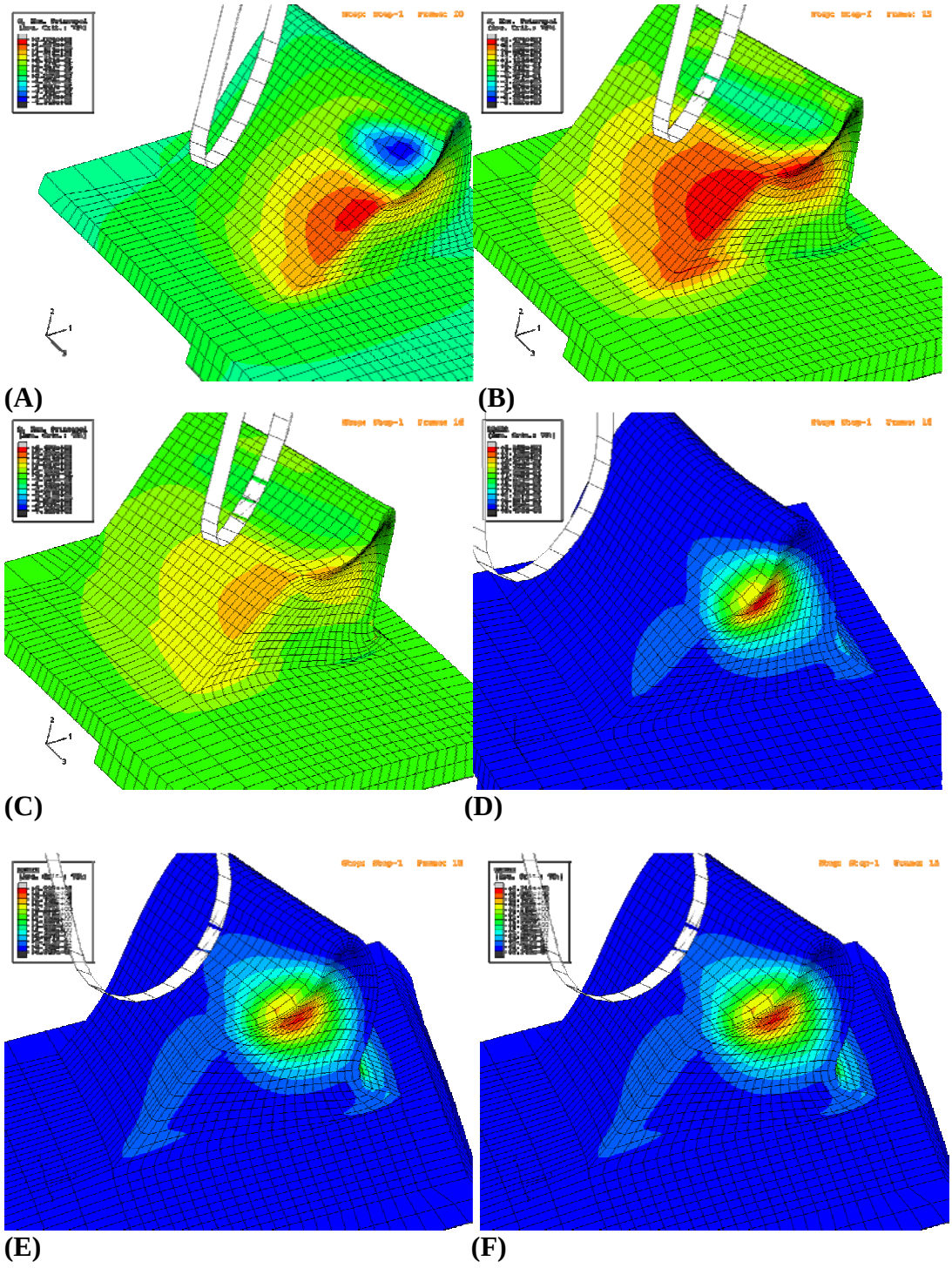

FIGURE 6.9: Principal Stress Contours for Flap deflection with an asperity contacting at an angle of 30 degrees (A-C) Maximum Principal Stress (D-F) Strain Energy Density

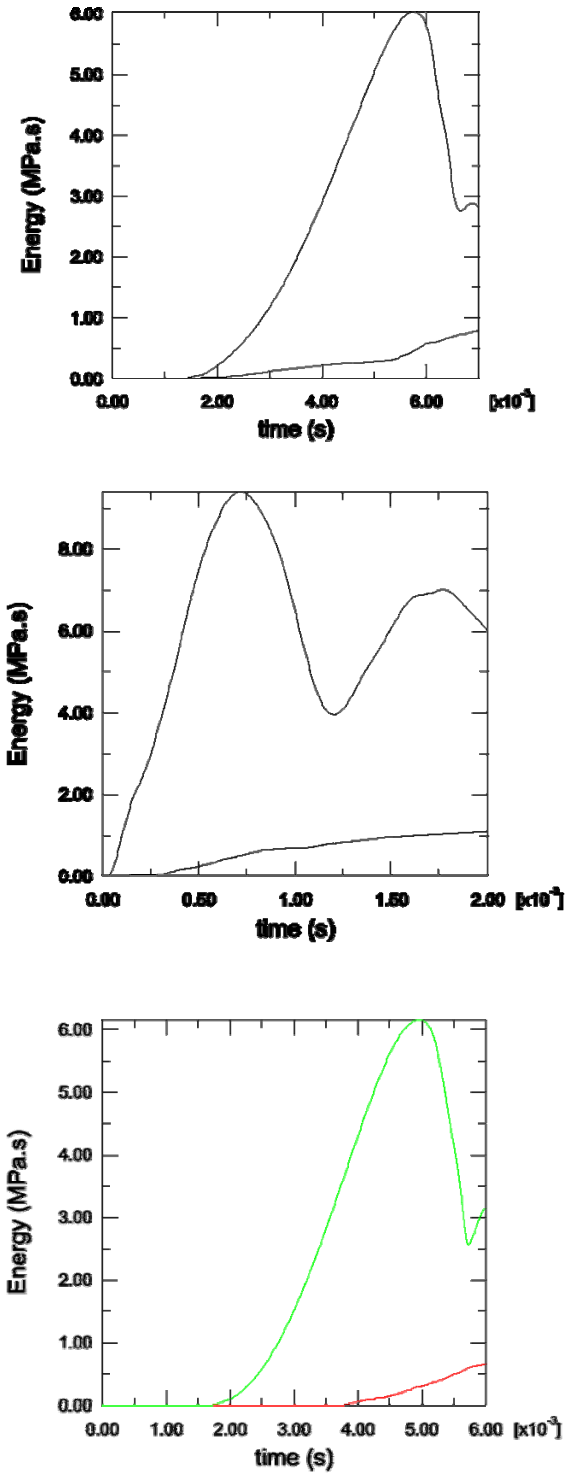

.

FIGURE 6.10: Total Strain Energy and Artificial Energy induced in the model during the simulation. Top: Straight approach Middle: Approach at 30 degrees. Bottom: Asperity Approach at 45 degrees.

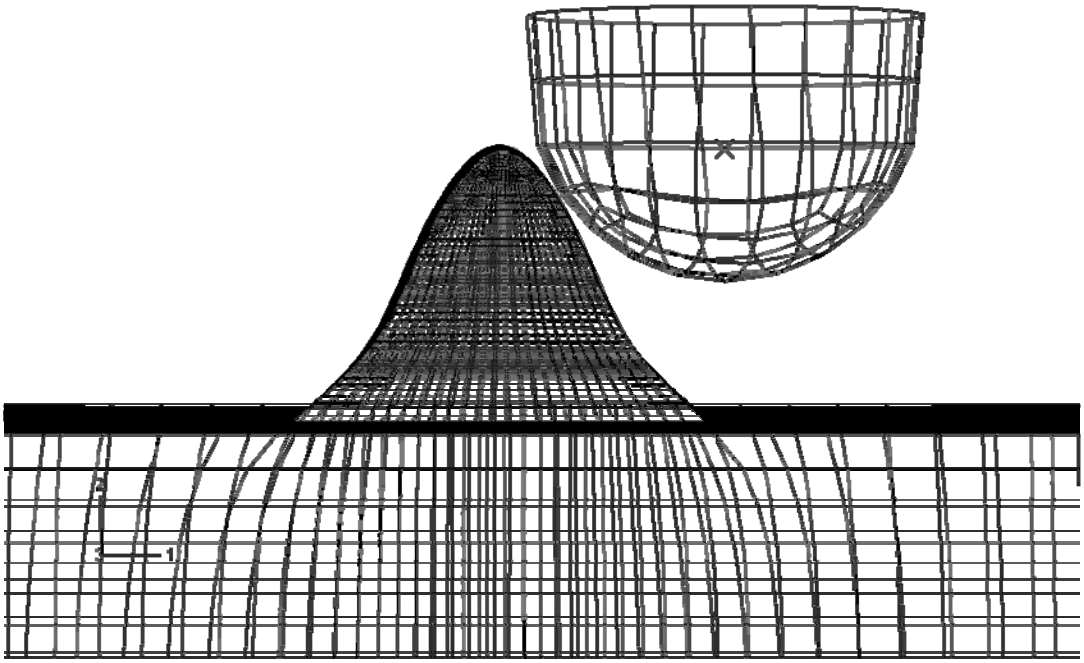

FIGURE 6.11: Mesh for the dynamic impact with a spherical asperity

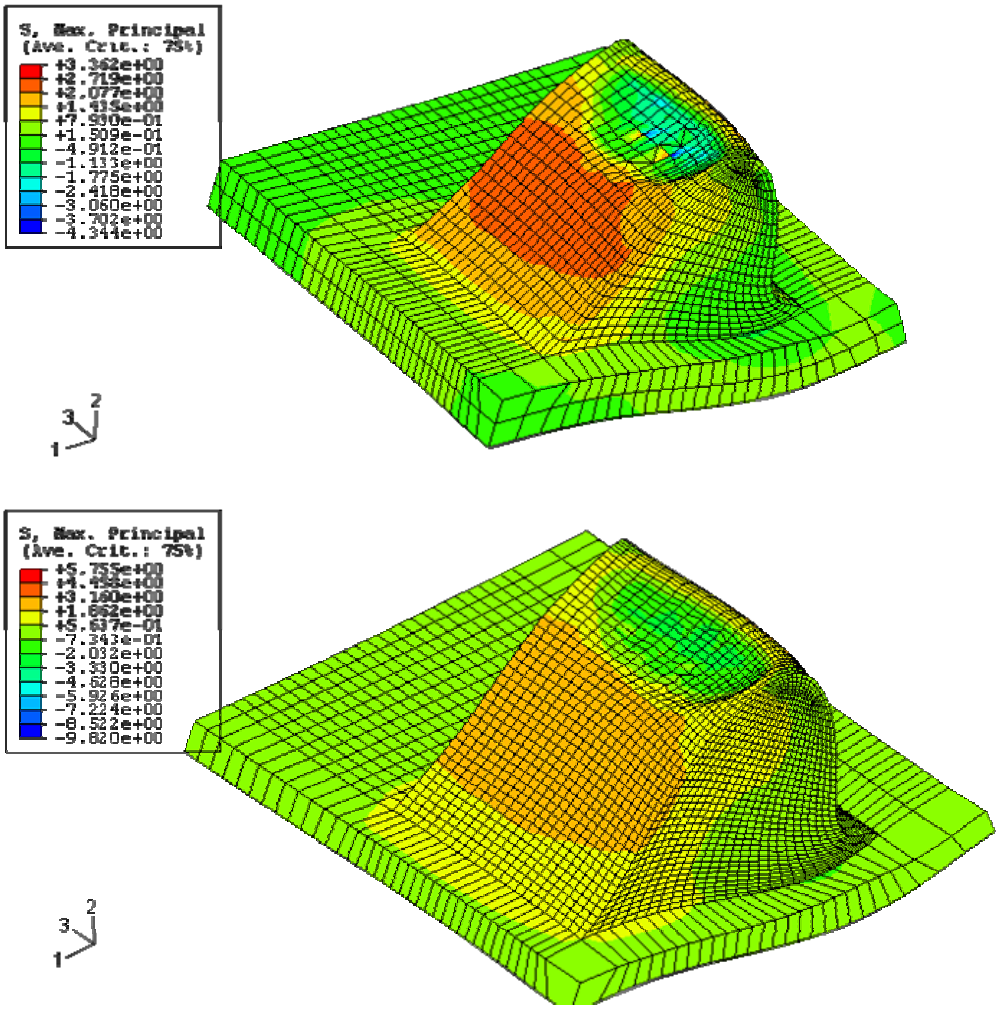

FIGURE 6.12: Max Principal Stress distribution for Top Sphere with R/h = 0.5, Bottom Sphere with R/h = 0.75 For frictionless dynamic interaction at speed = 36 km/s at t = 2 milliseconds

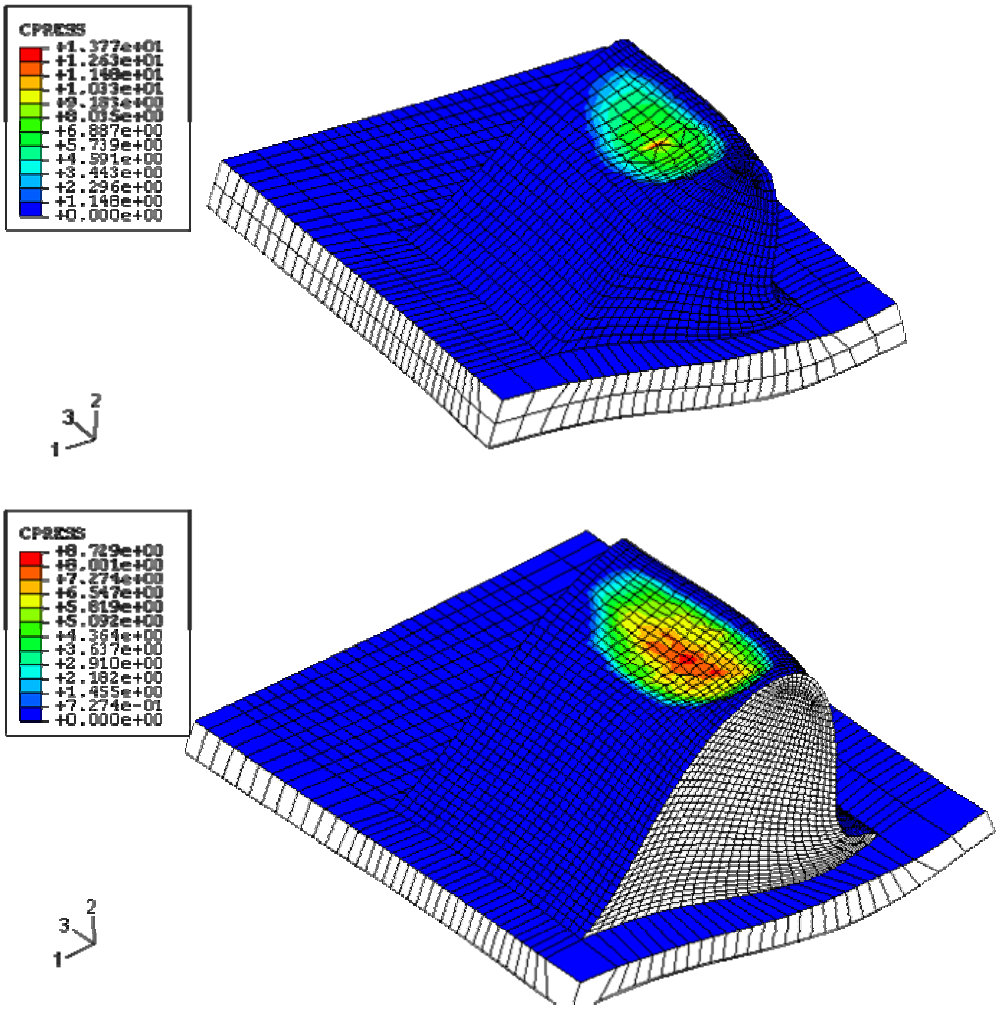

FIGURE 6.13: Contact pressure distribution for Top Sphere with R/h = 0.5, Bottom Sphere with R/h = 0.75. For frictionless dynamic interaction at speed = 36 km/s at t = 2 milliseconds

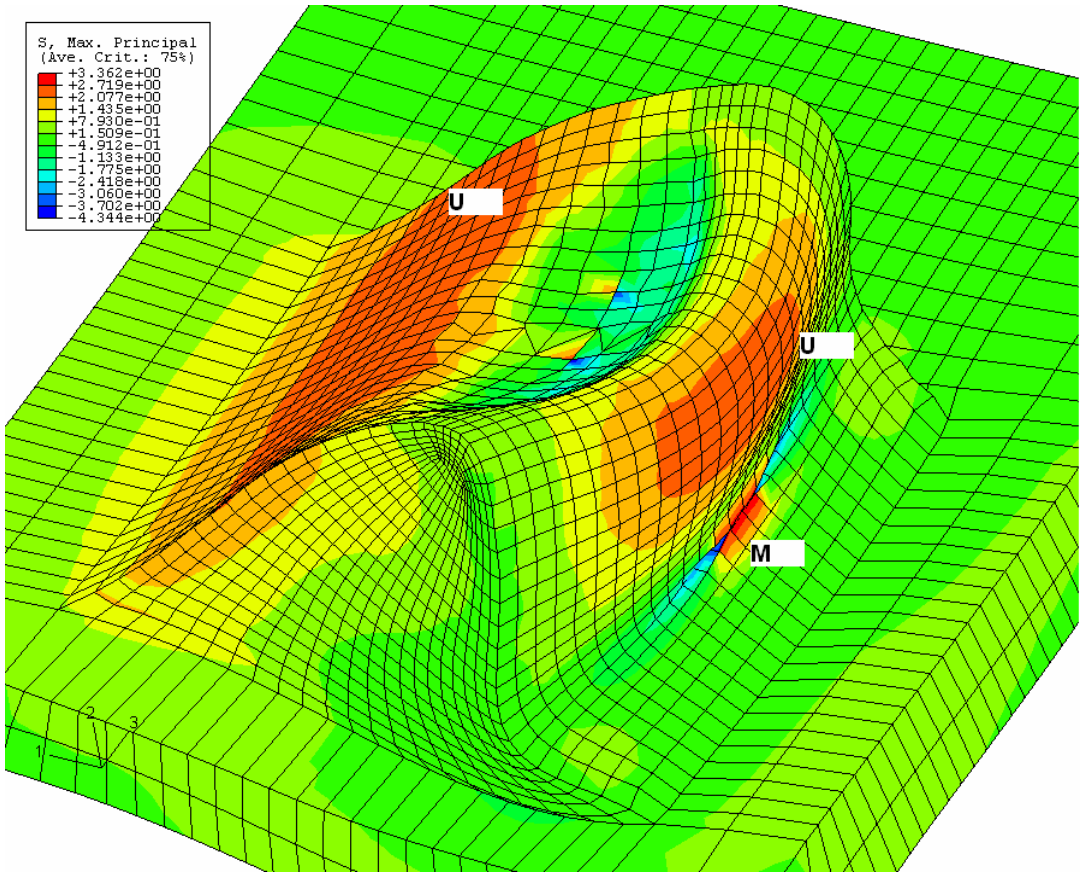

FIGURE 6.14: Maximum Principal Stress distribution for Sphere with R/h = 0.5. The label 'U' denotes high stress areas with predominantly biaxial tensile stress. The label M denotes high stress area with multi-axial stress state as shown in figure

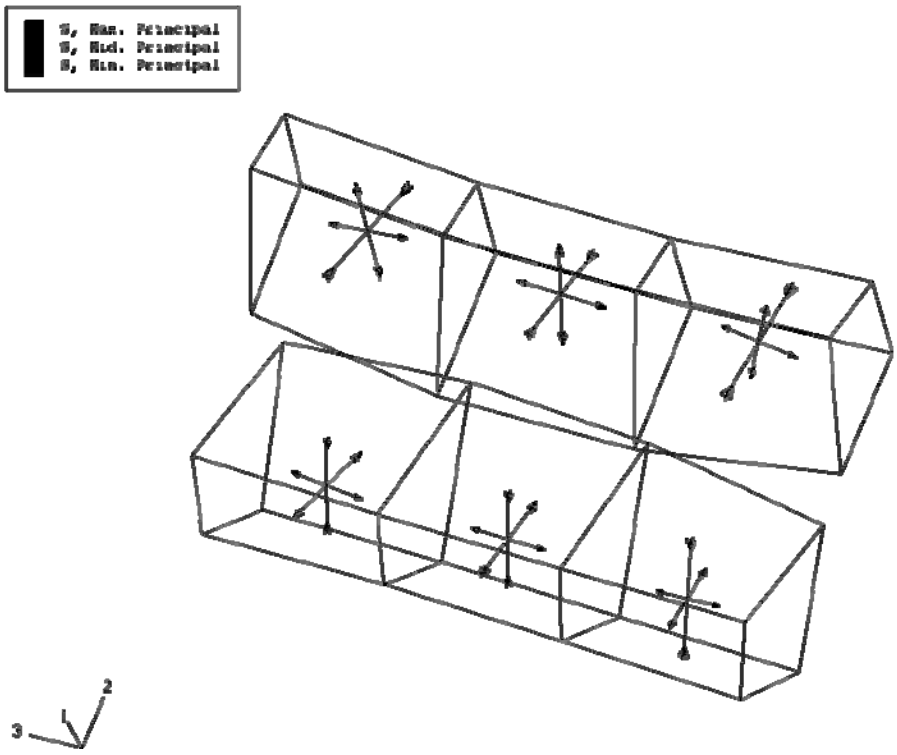

FIGURE 6.15: The Principal Stresses' direction for elements with label 'M in figure 6.14

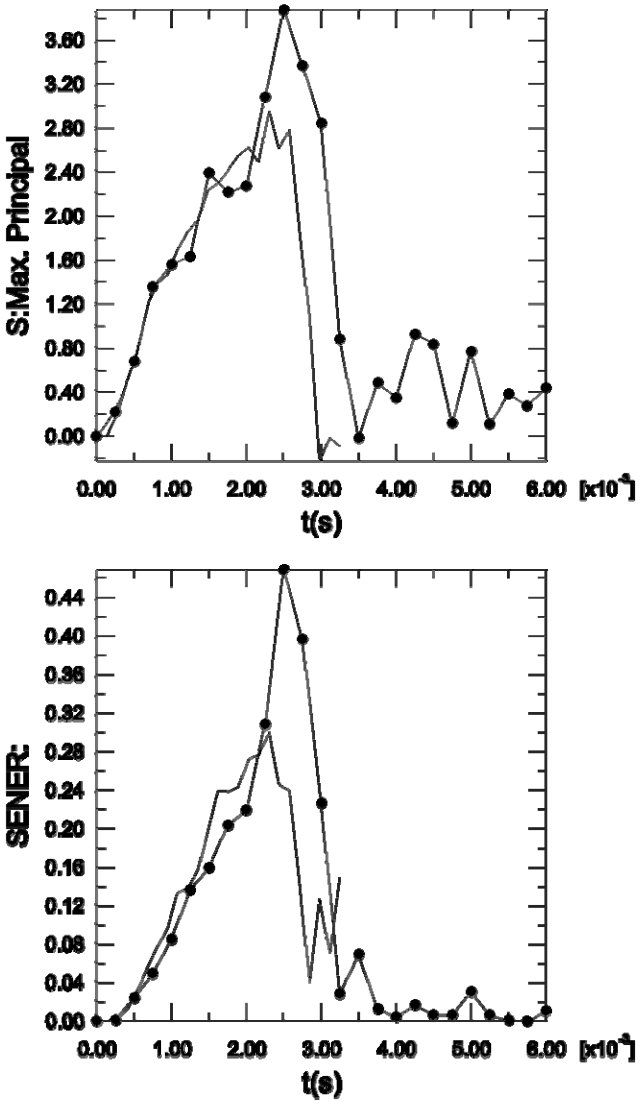

FIGURE 6.16: History of the Maximum Principal Stress and Strain Energy Density (SENER) at mid node of the surface in the wake of the asperity for R/h = 0.75 and R/h = 0.5

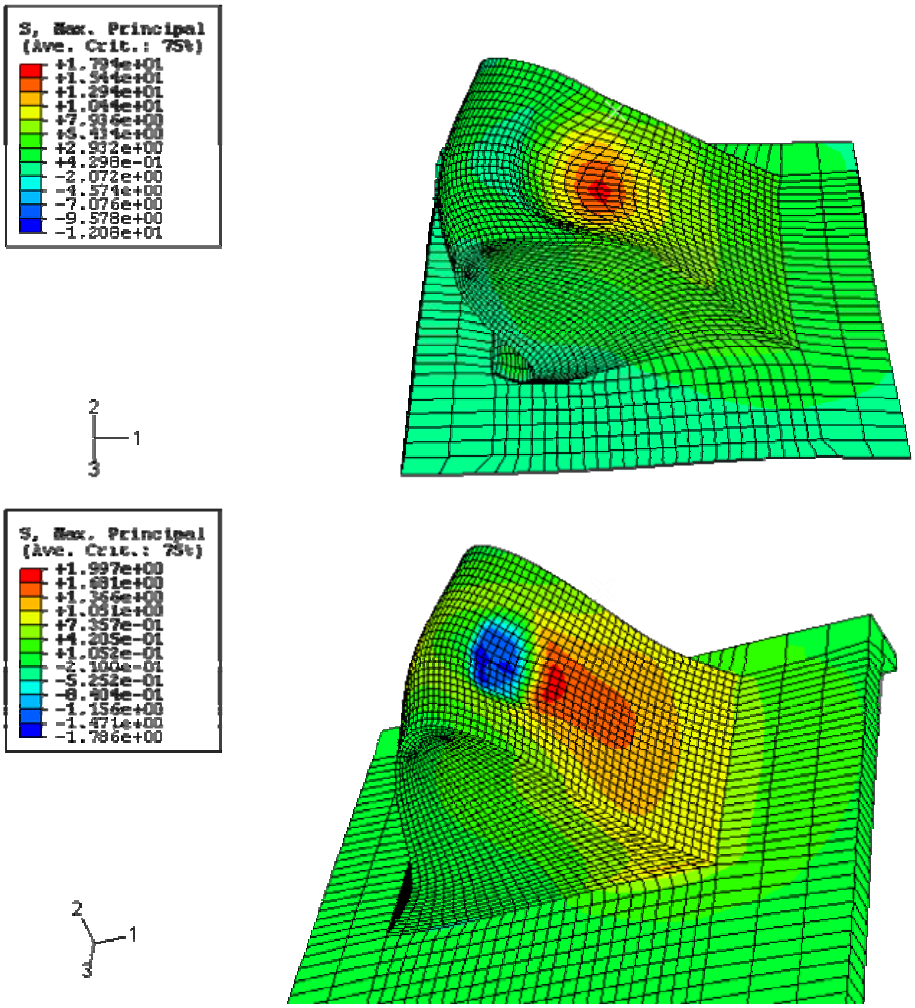

FIGURE 6.17: Maximum Principal Stress contour for dynamic asperity – flap interaction for R/h = 0.75 and velocity pressure dependent friction. Speed = 36 km/hr, Top and 10 km/hr, Bottom

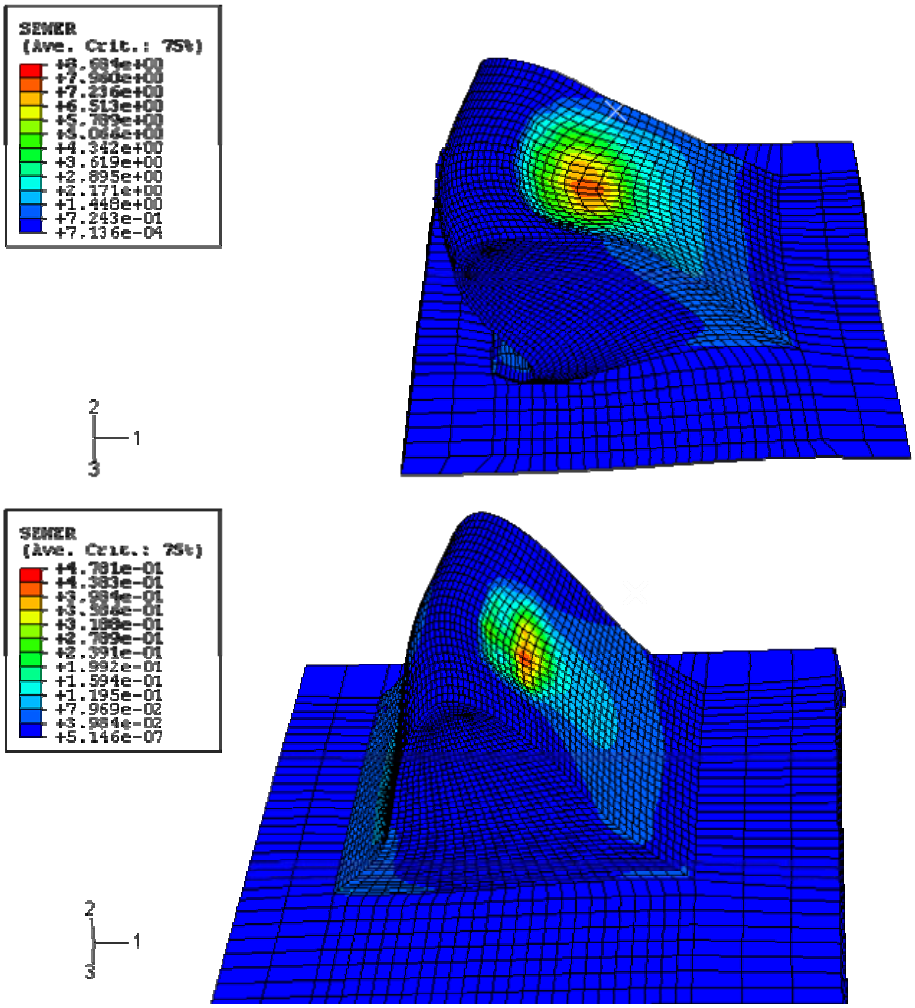

FIGURE 6.18: Strain Energy Density distribution for dynamic asperity – flap interaction for R/h = 0.75 and velocity pressure dependent friction. Speed = 36 km/hr, Top and 10 km/hr, Bottom

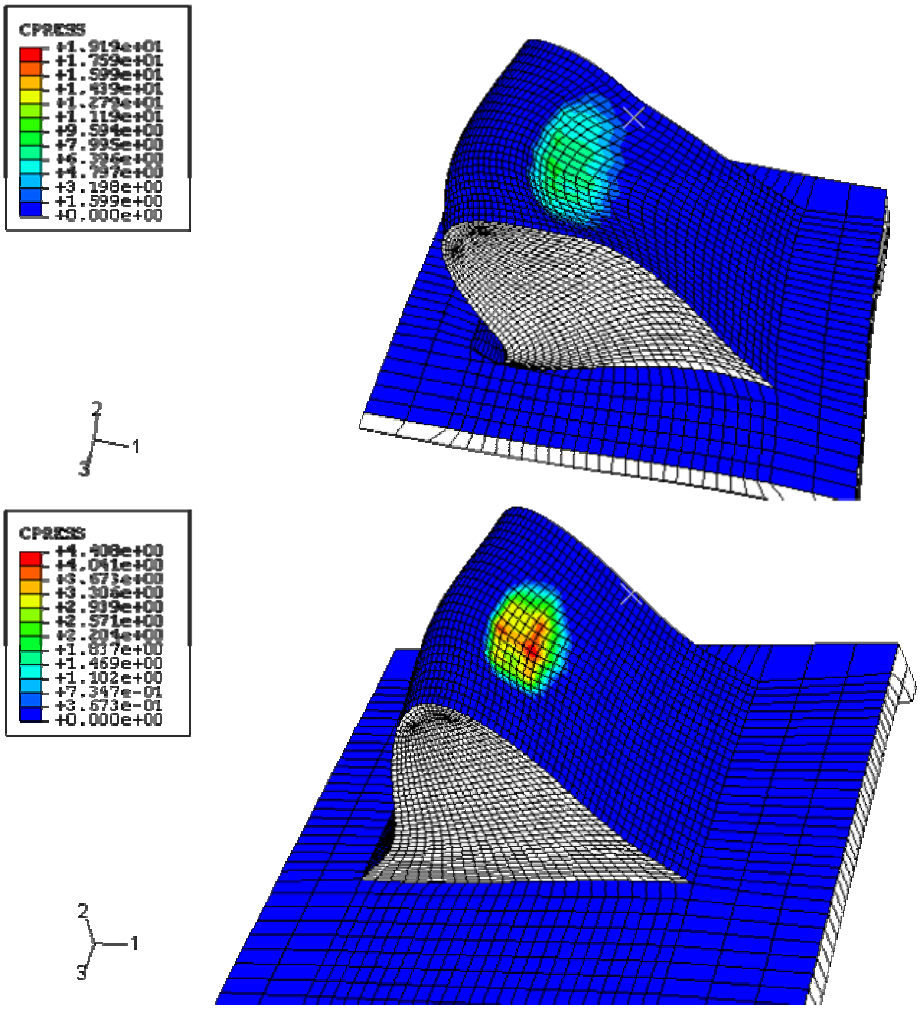

FIGURE 6.19: Contact Pressure distribution for dynamic asperity – flap interaction for R/h = 0.75 and velocity pressure dependent friction. Speed = 36 km/hr, Top and 10 km/hr, Bottom

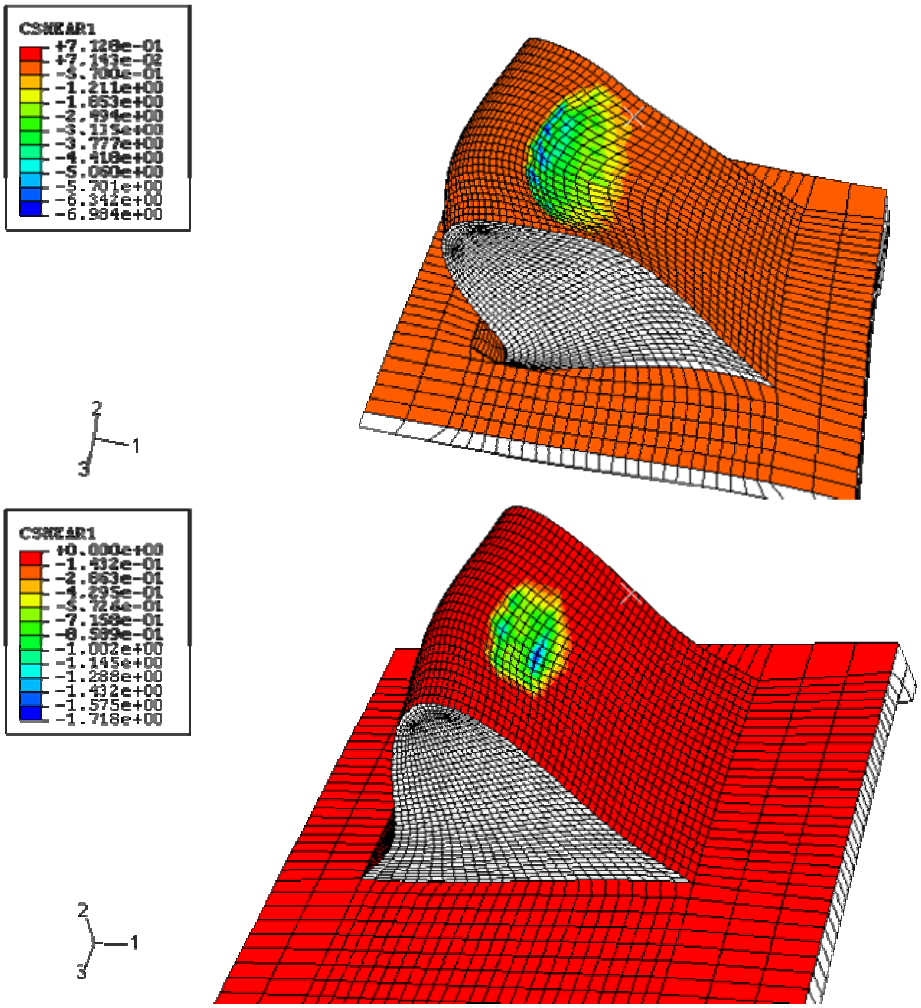

FIGURE 6.20: Shear force distribution in direction 1 on the surface for dynamic asperity – flap interaction for R/h = 0.75 and velocity pressure dependent friction. Speed = 36 km/hr, Top and 10 km/hr, Bottom

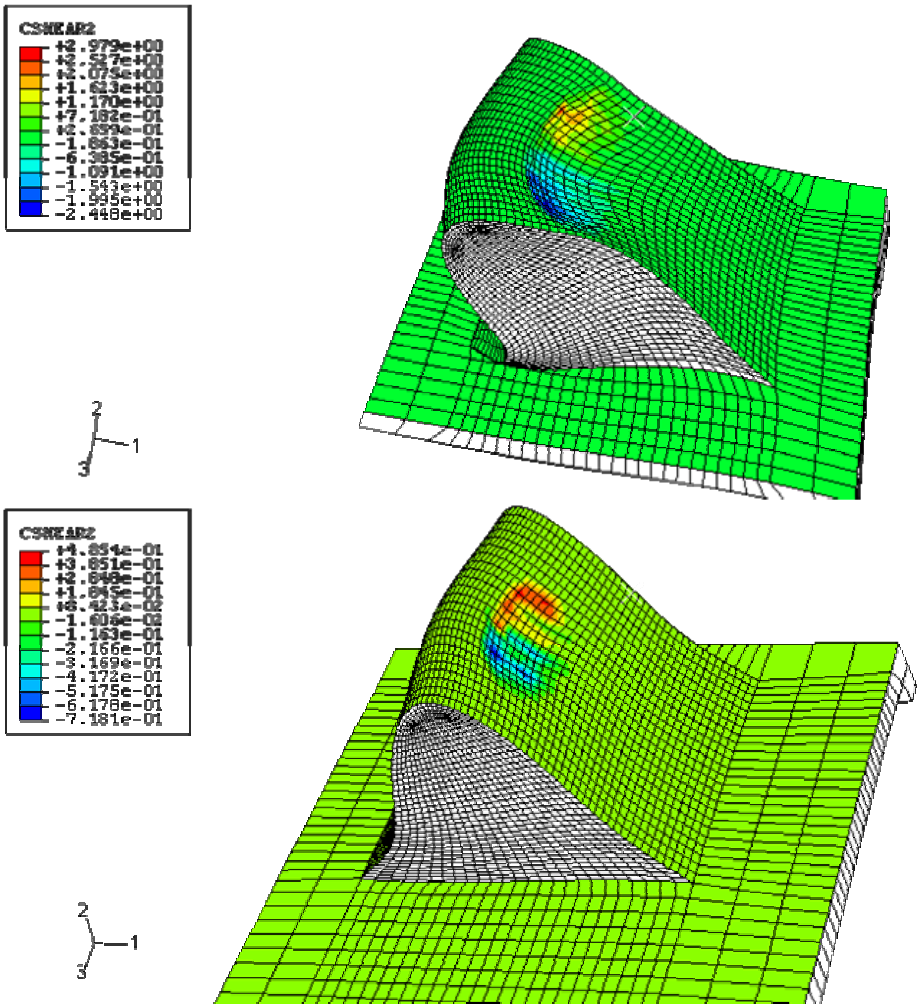

FIGURE 6.21: Shear force distribution in direction 1 on the surface for dynamic asperity – flap interaction for R/h = 0.75 and velocity pressure dependent friction. Speed = 36 km/hr, Top and 10 km/hr, Bottom

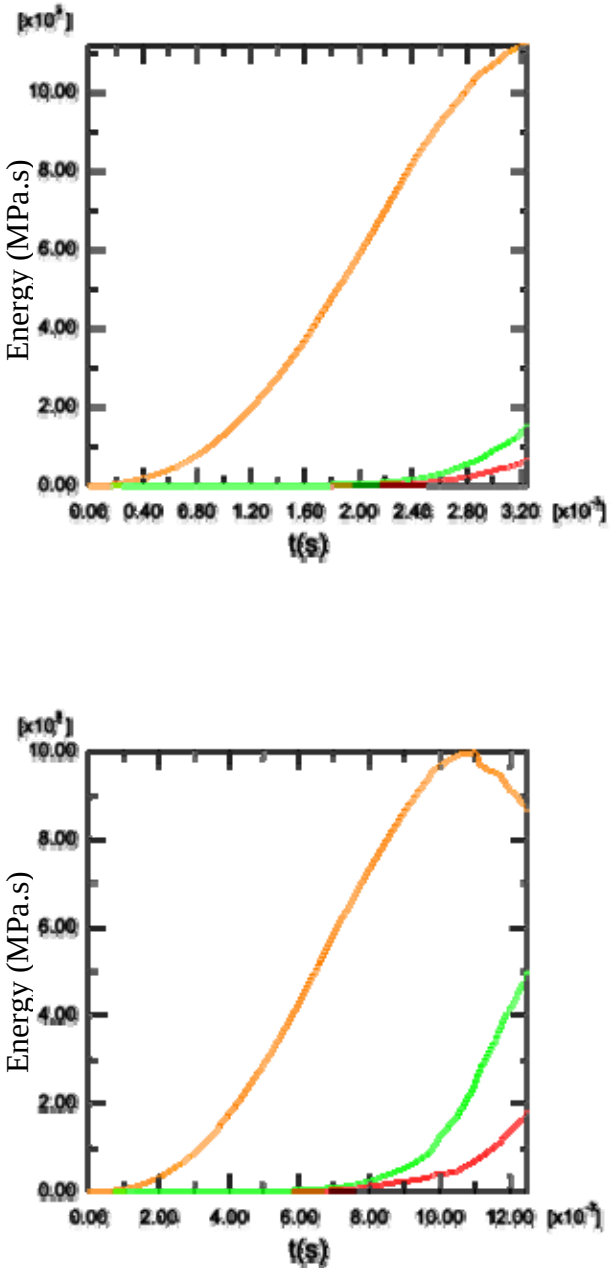

FIGURE 6.22: Global Strain Energy (Orange), Frictional dissipation (Green) and artificial energy (Red) for dynamic asperity – flap interaction for R/h = 0.75 and velocity-pressure dependent friction. Speed = 36 km/hr, Top and 10 km/hr, Bottom

CHAPTER VII

CONCLUSIONS

In the present work, principal features of asperity interaction with rubber were studied using numerical models. The report shows the complexity of such an interaction, even when a single asperity is considered. The motivation for the research comes from past work on rubber friction and wear. This work was largely focused on experimental measurements of gross wear rates of rubber under different influencing variables such as applied loads, kinematic conditions, material and frictional characteristics. More recently, there were a series of studies at the wear laboratory at University of Akron [64-66,125] that focused on evolution of wear morphology as well as the microstructure of the filled rubber. The experiments in understanding of wear provide a great deal of qualitative details regarding evolution of wear morphology and its relation to material microstructure as well as physical variables. Similarly, gross quantitative details of wear such as wear rate or statistical distribution of wear particle sizes are also available. But the exact mechanism of mechanical wear based on local deformation conditions is better suited for numerical and analytical studies. Although there is a large body of work associated with fracture mechanics of rubber, there has been a serious lack of effort in using numerical tools to understand the process of wear. Recently, Mehdi [64] applied some ideas from linear elastic fracture mechanics (LEFM) to explore crack propagation in rubber. The work was able to make some quantitative predictions of effect of material

properties, filler content and loading conditions on crack propagation in rubber. The present work improves upon the work by incorporating non linear material properties, realistic contact behavior involved in asperity rubber interaction, inertial dynamics and actual wear morphologies other than crack. The principle results concluded from this investigation are as follows.

7.1 Steady State Asperity Interaction with Rubber

A series of two dimensional FEA models were studied for asperity penetration and travel for an infinite hyperelastic rubber body with a crack. The main observations from this study are as follows:

(1) The stress distribution created by straight penetration of a rigid asperity into an elastomer creates a highly non-Hertzian contact condition. The state of deformation decays away from the site of penetration.

(2) The maximum principal stress along the surface of the rubber is almost tangential to the surface away from the contacting zone. At the same time, the maximum principal stress goes from being compressive in the contact zone to a tensile state away from the contact zone. The surface of the elastomer sees the peak compressive stress in the contact zone and the peak tensile stress just outside of the asperity contact zone. The two locations along the surface corresponding to peak compressive and tensile stresses also correspond to the locations where strain energy density is maximum.

(3) Keeping all the other variables constant, the peak compressive stress in the contact zone and the peak tensile stress outside the contact zone increase with increase in depth of penetration or coefficient of Coulomb friction. Also, the peak compressive and tensile stresses become sharper (narrower) with increased depth of penetration or friction.

Higher the peak surface stresses, the distance over which they 'decay' away from the asperity penetration, increases gradually. An increasing coefficient of friction also causes the orientation of the maximum principal surface stress to deviate from the local tangent to the surface geometry. This effect is more severe in the contact zone itself. The maximum principal stress remains tangential to local surface away from the contact.

(4) For a given depth of penetration, a material with higher elastic modulus produces larger magnitude of peak stresses at the surface. Thus an elastomer with higher carbon filler content will experience larger surface stresses at the same depth of asperity penetration compared to lower filler content materials or unfilled materials.

(5) The previous observations hold true for both plain strain and plain stress conditions. But given identical boundary conditions, the level of maximum principal stresses along the surface of an elastomeric body is higher in the case of plain strain than plain stress condition. This effect is self-evident and is particularly amplified due to incompressible or near incompressible behavior of rubber.

(6) When the rigid asperity penetration is in the vicinity of a pre-existing surface crack, the deformation field is altered. The change is equivalent to the change in deformation from altering the boundary conditions, as a surface crack effectively 'interrupts' the infinite elastomer body.

(7) The extent of change in deformation field around asperity penetration depends upon the relative dimension of the asperity with respect to crack length, depth of penetration and distance of the point of penetration from the crack location. The crack is most effective in altering the deformation field if its dimensions are comparable to the asperity

size or the depth of penetration. Also, a crack closer to the asperity contact zone is more effective in altering the deformation field.

(8) The presence of a crack with a length comparable to the asperity dimension, reduces the peak tensile and compressive surface stresses due to asperity penetration. The point on the surface where the crack face meets is free to rotate and stress-free. The presence of a crack causes the surface stresses to decay faster away from the contact zone. Closer the penetrating asperity to a crack location, sharper the decay of the principal surface stress and smaller the peak tensile stress near the contact zone.

(9) A crack that is perpendicular to the surface of the elastomer body is more effective in reducing the principal surface stresses. A crack with identical length but at an angle to the normal direction to the surface is less effective in reducing the peak tensile stress near the contact zone when compared to a crack perpendicular to the surface. Conversely, for small depth of penetrations or for an asperity with smaller dimensions compared to the crack length, a crack with large angle to the surface normal is more effective in reducing peak normal stress near the contact zone.

(10) The reduction in surface stresses and strain energy density under penetration caused by the presence of a surface crack is compensated by increase in crack tip stresses. Typically, penetration near a straight (perpendicular) crack results in tensile crack tip stress, as long as the asperity contact zone does not include the crack tip. This causes a Mode I type opening for the crack-tip. At depth of penetration or asperity size comparable to the crack length, the effect is more severe. On other hand, if the asperity is so near the crack location that the contact zone encompasses part of the crack geometry, the crack tip may see compressive stresses. Close and deep asperity penetration may also

load one crack face more severely than other, resulting in Mode II type behavior (Appendix C).

(11) Under the loading condition when an asperity moves along the crack surface at a fixed depth of penetration at slow speeds, the surface stresses in the contact zone show high degree of asymmetry when they are near a surface crack. As the spherical asperity moves away from the crack, the stress distribution in and around the contact zone may become nearly symmetric for a frictionless condition. However, when friction is included, the contact zone in the 'wake' of the asperity sees larger surface stresses, magnitude of which increase with the asperity progressively away from the crack. The effect is expected from the previous results related to simple asperity penetration.

(12) With an asperity moving away from the crack, the crack tip may see compression followed by tension. Also, depending on the depth of penetration and crack orientation, the crack tip may undergo complex folding, where the crack faces may come into contact at multiple sites. When the asperity has moved away sufficiently, there is gradual unfolding where the crack faces separate and are restored to original configuration. This is accompanied by crack tip undergoing tensile state of stress from the initial compression.

7.2 Determination of Crack Spacing

Numerous experimental studies [1,3,88] report the evolution of pattern wear on the surface of a rubber component under repeated loading. These studies have been able to establish relationship of the crack spacing, depth and orientation to the relative speed between the contacting bodies [1,88]. However, these experimentally derived observations fall short of explaining the actual process by which morphological evolution

happens in pattern wear. Gerrard [65] speculating based on experimental observations proposed the stress relief in the vicinity of a surface crack as a possible mechanism responsible for evolution of pattern wear. The observations in the previous section quantitatively describe the effect of a preexisting surface crack on the deformation field in its vicinity. In order to determine the effect of this crack induced stress relief on initiation and propagation of new surface cracks, a crack propagation criteria based on energy release rate, was proposed. The method uses experimental energy release rate data for fracture in thin sheets of rubber to determine if the deformation field will result in critical energy release rate required for mechanically induced crack propagation. The method also assumes that the crack propagation will proceed along the direction normal to maximum principal stress orientation. Based on the criteria following conclusions are derived for the asperity interaction models described in the previous section.

(1) The reduction in stress intensity because of an existing crack also reduces the potential energy release rates available for a defect of smaller length scales (1 order or more) than the existing crack. However, the available energy release rate available for surface crack propagation goes up steadily as the asperity moves away from the crack

(2) Depending on the depth of penetration, friction conditions and asperity dimension relative to the crack length, the deformation field induced by asperity loading may result in critical energy release rate allowing for crack propagation in a single pass.

(3) Since the energy release rates at the surface are reduced near an existing crack, critical stress energy release rate required for crack propagation may occur only at a certain distance from it. For asperities with dimensions comparable to the crack length, the typical crack spacing may vary from 1to 3 R based on frictional conditions (R,

asperity radius) for depth of penetrations of the order of the radius of the asperity. The effect of various important physical variables affecting this critical distance between the existing crack and a new crack propagation site is shown in table 7.1.

(4) Asperities much smaller or much larger than the existing crack may still create a smaller crack spacing at relatively low depth of penetrations.

(5) For low depth of penetration and friction coefficient(s), the surface energy release rates generated by a passing asperity may not be sufficient for crack propagation in a single asperity pass. Still, the resulting energy release rate may create other cracks under repeated asperity passes. The resulting crack spacing from fatigue loading is much smaller than the typical crack spacing from a single asperity pass. Since this mode of crack initiation takes several thousand cycles (for the materials studied here), they propagate at a relatively slow rates.

(6) At large distances (greater than crack length) from the existing crack, the potential energy release rate is nearly constant almost equal to the equivalent energy release rate in an elastomeric body without a crack. However, within the distance of one crack length from the crack, the energy release rates are a strong function of local deformed geometry, friction and material properties. The highly nonlinear nature of the stress field near the crack vicinity precludes more general observations regarding effects of specific physical variables on crack spacing from fatigue loading.

(7) It would be safe to assume that given identical force-loads from asperity, a higher filler content in the elastomer will result in larger spacing, assuming that in general, the critical energy release rate for crack propagation is higher for materials with higher filler content.

Table 7.1: Effect of principle physical variables on crack spacing.

Variable	**Effect on crack spacing**
Increasing Friction	Decreases
Increasing Depth of Penetration	Decreases
Increasing Radius	Increases
Increasing crack angle to the vertical	Decreases

(8) The existing crack itself may propagate under the loading from a similarly sized asperity, if the depth of penetration is high enough. For a blunt crack tip, smaller crack may result all along the crack tip due to fatigue loading. A straight orientation of crack is most susceptible to high magnitudes of crack tip stresses. However, a crack oriented at an angle greater than 90 degrees away from the direction of asperity travel sees similarly high tip stresses over a larger period of asperity travel. Thus crack orientation may determine the nature of crack branching through propagation of smaller cracks from a blunt crack.

(9) Crack faces and the tip are subjected to alternate compressive and tensile loads during an asperity pass. Due to high friction forces between crack faces under contact and the tensile loading due to crack tip opening, a number of smaller cracks may result all along the crack faces.

(10) Even though the crack tip may see extreme compressive stresses under asperity pass, the resulting stresses were found insufficient to create cavitation like damage even for high depth of penetrations. Damage mechanisms related to fatigue under compression loading may still create further material weakening and fatigue crack propagation for the existing crack.

(11) When an asperity is approaching an existing crack, it typically ends up closing the crack mechanically and may allow for crack propagation in its wake. The resulting crack spacing may be smaller than similar crack spacing created when the asperity is moving away from the crack.

(12) In case of an existing crack with faces of different heights, it is possible that the opposite crack face sees straight loading. This type of asperity loading may propagate the existing crack directly.

7.3 Asperity Loading at High Speeds

The prior conclusions related to crack spacing were based on numerical simulations where the loading speed was considered to be very slow (nearly zero). In practical applications such as tires coming in contact with asphalt roads, large loading speeds can be reached very easily. In such cases, strain rates up to a million per second may be achieved at sub millimeter length scales. Deformation behavior at such high rates is drastically different as the material behavior is a function of strain rates. At the same time , frictional behavior is nonlinear and shows slip rate dependence. A number of explicit dynamic simulations with strain rate dependant material behavior and nonlinear frictional behavior were carried out for asperity loading near a crack. The conclusions from this study were as follows.

(1) When an elastomeric medium experiences asperity loading at high speed, the deformation field is highly affected by the rate dependant properties of material. For an unfilled elastomers, significant stiffening happens at higher strain rates. Under asperity loading of same depth of penetration at a higher speed, such stiffening causes effective contact area to reduce in comparison to contact area under steady state conditions (slow speeds).

(2) Based on asperity speeds, the surface of the elastomer as well as crack tips of existing surface cracks see extremely high deformation rates. This results in local stiffening. This

behavior leads to higher tensile stresses even at low strains, along the crack faces and in the wake of a traveling asperity.

(3) Slip speed dependence of friction may create instabilities in the contact zone leading to loss of contact at high asperity speeds. A high value of Coulomb friction tends to dampen such behavior. Such instabilities due to dynamic friction models may create wavelike phenomena and confirm with experimental observations of Schallamach waves. However, contrary to unfilled rubber as modeled in this study, filled rubber with higher stiffness and dissipation characteristics within the range of asperity loadings relevant to practical applications such as tires.

(4) The energy release rate method applied to the steady state asperity loading problem is inapplicable to the dynamic methods as the material deformation history is highly dynamic with strain rates varying dynamically. However, the wave propagation at higher deformation rates may create instantaneous high stresses locally. Phenomena such as Schallmach waves will also affect crack spacing in materials with lower stiffness. Conversely, their effect will be reduced at higher stiffness or in the presence of other dissipative mechanisms related to fillers such as Carbon black.

7.4 Asperity Loading at Microscales

The conclusions related to asperity interaction with elastomeric body in previous sections were based on numerical models that assumed the body to be homogeneous material. Experimental evidence shows that at scales of the order of tens of microns, the elastomer is essentially inhomogeneous. The structure at this scale is characterized by large number of domains separated by weak boundaries of cohesion between elastomer particles and agglomerates containing filler particles. A simplistic numerical model

replicating the inhomogeneous structure qualitatively was analyzed with FEA methods under asperity loading. Following broad conclusions are arrived from these models.

(1) The inhomogeneous structure at micron scales affects the deformation field from asperity loading. The weak boundaries around the microscopic domain partially isolate the stress from asperity loading being transferred to the rest of the body. At the same time, the energy from deformation field may result in gross motions of the domain immediately in contact with the asperity. This may create large displacements and result in further weakening of the cohesive strength between the domains

(2) The mechanism described above may result in partial or complete separation of microscopic domain and contribute to wear debris. This is consistent with observations regarding the size of the domains [66] and size of the smaller particles in the wear debris [125].

(3) The asperity loading at micro-scales also creates high concentration of stresses around filler particle agglomerates with rubber. This is because of their high relative stiffness and strong adhesion with the surrounding rubber. Additionally, such stress concentration may happen away from the contact zone and even inside the bulk of the material. However at least for the conditions investigated in the study, the resulting strain energy density around the filler particles were lower than the required deformation energy to break the carbon –rubber bond as reported in the literature [131,132,136].

(4) The observations on the current numerical models are very approximate, as the material properties of the individual domains, the cohesion strength between domains are at best crudely approximated by macroscopic properties of rubber.

7.5 Asperity Interaction with a Rubber Flap Geometry

A large crack in the form of a rubber flap is another characteristic wear morphology, at large scales (millimeters or higher). The stress field induced in such geometry under asperity loading is of interest in studying wear with respect to slip angle direction. A three dimensional flap geometry idealized by a Gaussian distribution curve was studied for asperity loading under dynamic conditions. Following conclusions were drawn from the numerical simulations.

(1) In case of a three dimensional geometry such as the flap, an asperity loading creates a number of locations with large maximum principle stresses and resulting high strain energy densities. As the asperity passes a flap of finite height and width, the stretching of the flap in the direction of the asperity motion results in a large maximum principle stresses in the direction of stretching. These high stresses in the wake of the asperity on the surface of the crack create purely tensile biaxial stress state. Similarly, the flap results in a highly compressive state of stress on the face opposite of the face loaded with asperity. As the asperity leaves the contact with the rubber flap, it may create a highly tensile stress in the lateral orientation on the opposite face.

(2) An asperity with much larger dimensions than the flap creates a more uniform biaxial state of stress near the contact zone with no variation along the lateral direction. An asperity with dimensions comparable to the dimensions of the flap height creates a larger lateral variation in the regions where there are high tensile stresses on either side of the face. Given identical loading conditions, a slightly larger asperity has a larger contact area. This implies that the lateral dimensions of the zones with higher stresses are proportionately larger.

(4) In a three dimensional geometry stretching due to asperities results in frictional shear in the contact zone in two perpendicular directions tangent to the surface. This accentuates the stresses in the lateral direction.

(3) When an asperity approaches the flap at an angle, the effective geometric stiffness presented to the asperity is different than a straight approach to the flap face. In this case there maybe a substantial 'twisting' of the flap. This leads to significantly different deformation field.

(4) At slow speeds, experimental energy release rate data from biaxial stretching maybe applied in a manner similar to the two dimensional asperity models, in order to estimate probable crack propagation. The observations 1 through 3 imply that a large number of localized cracks may propagate in the regions of high maximum principle stress regions on either faces of the flap. Also, the dimensions of the crack in the lateral direction may also be substantial. Such localized cracks with different characteristics depending on their location along the flap are consistent with observations of wear debris along the length of a flap as observed by Gerrard [65] and Prasad [125].

(5) Calculations of probable crack propagation rates will also help us understand the effect of change in slip speed on gross wear rate of the material.

7.6 Suggested Future Work

The present study demonstrated the possibility of using critical energy release rate as a criterion in determination of the crack propagation rates and resulting crack spacing in a pattern wear. It would be valuable to verify these predictions in experiments of asperity loading on a rubber block with a preexisting crack.

The input from experimental verification of the numerical models may direct us towards improving upon the numerical model assumptions. In case of highly dynamic loading better constitutive models for material and frictional behavior would be important.

In practical applications of asperity modeling, contacting surface typically has multiple asperities with a distribution of shapes and sizes. Numerical models with multiple asperities would also be a logical extension of the present effort. Modeling of actual crack propagation based on the energy release rate criteria, would lead us closer to actual wear simulation. Such large scale simulations with appropriate numerical resources will eventually predict wear rates quantitatively. Other than large computer resources and constitutive modeling such simulations would also require better theoretical understanding of criterion for material failure especially under highly dynamic loading conditions.

Similar improvement in understanding and modeling efforts for micro-scale structure under asperity loading may help us better understand the relationship between microscopic structure and its influence on gross wear. This will be helpful in the choice of process conditions to obtain desired wear characteristics.

REFERENCES

1. A. Schallamach, Wear **1**, 384 (1958).

2. A.G. Veith, Rubber Chem. Technol. **46** (4), 801 and 821 (1973).

3. E. Southern, A.G. Thomas, Rubber Chem. Technol. **52**, 1008 (1979).

4. A.G. Veith Rubber Chem. Technol. **65**, 601 (1992).

5. G.J. Lake, and P.B. Lindley, J. Appl. Polym. Sci., **9**, 1233 (1965).

6. A.N. Gent, Rubber Chem. Technol. **62**, 750 (1989).

7. A.K. Bhowmick, Rubber Chem. Technol. **55**, 1055 (1982).

8. J. Padovan, N. Parasad, D. Gerrard N. Lindsley, Rubber Chem. Technol. **72**, 343 (1999).

9. A. Schallamach, Trans. Inst. Rubber Indust., 256 (1952).

10. A.N. Gent, and C. Pulford, J. Appl. Polym. Sci., **28**, 943 (1983).

11. F. P. Bowden and D. Tabor, Friction and Lubrication of Solids, Clarendon Press, Oxford, Part I, 90 –121, (1950).

12. F.P. Bowden, A.J.W. Moore, and D. Tabor, Journal of Applied Physics, **14**, 80-91, (1943).

13. E. Rabinowicz, Friction and Wear of Materials, Wiley, New York, pp. 51-108 (1965).

14. N.P. Suh, H. Sin Wear (added) Vol. **69**, pp. 91-114 (1981)

15. N.P. Suh, Wear, **25**, pp. 111-124 (1973).

16. K.L. Johnson, K. Kendall, and A.D. Roberts, Proc. R. Soc. London A, **324,** 301-312 (1971)

17. K.A. Grosch, Proc. R. Soc. London A, Vol. 274, pp. 21-39 (1963).

18. M. Barquins and R. Courtel, Wear, **32** 133-150 (1975)

19. K.C. Ludema, D. Tabor, Wear, **9** 329-348 (1966).

20. R.A. Rorrer, N.S. Eiss, and R.S. Togni, Wear and Friction of Elastomers, 50-64.

21. H.W. Greensmith, Journal of Applied Polymer Science, **III** , No. 8, 183-193, (1960).

22. A.G. Thomas, Journal of Applied Polymer Science, **III** , 8, 168-174, (1960).

23. Y.B. Chernyak and A.I. Leonov, Wear, **108**, 105-138, (1986).

24. A.I. Leonov, Wear, **141**, 137 (1990).

25. C.M. Ettles, Tire Science and Technology, **14**, No. 1, 44-72 (1986).

26. H. Hertz, J. Reine Angew, Math. **92**, 156 (1882).

27. J. Boussinesq, *Application des potentials à l'étude de l'équilibre et du mouvement des solides élastiques* ,Gauthier-Villars, Paris 1885, nouveau triage Blanchard, Paris, (1969).

28. R.S. Bradley, Philos. Mag. **13**, 853 (1932).

29. B.V. Deryagin, Kolloid Z. **69**, 163 (1934); cf also B.V. Deryagin, N.A. Krotova, V.P. Smilga: *Adhesion of solids* (Consultant Bureau, New York 1978).

30. K.L. Johnson, Brit. J. Appl. Phys. **9**, 199 (1958).

31. K.L. Johnson, K. Kendall, A.D. Roberts: Proc. Roy. Soc. Lond. A **324**, 301 (1971).

32. K. Kendall, J. Phys. D: Appl. Phys. **4**, 1186 (1971).

33. K. Kendall, J. Adhesion **5**, 77 (1973).

34. K.L. Johnson, *The mechanics of the contact between deformable bodies*, ed. by de Pater, Kalker (University Press, Deflt 1975) 26-40

35. K.N.G. Fuller, D. Tabor, Proc. Roy. Soc. Lond. A **345**, 327 (1875).

36. D. Maugis, M. Barquins, R. Courtel, “Métaux, Corrosion, Industrie”, **605**, 1 (1976).

37. B.V. Derjaguin, V.M. Muller, Yu. P. Toporov, J. Colloid Interface Sci. **53**, 314 (1975).

38. D. Tabor, J. Colloid Interface Sci., **58** 2 (1977).

39. V.M. Muller, V.S. Yushchenko, B.V. Derjaguin, J. Colloid Interface Sci. **77**, 91 (1980).

40. V.M. Muller, V.S. Yushchenko, B.V. Derjaguin, J. Colloid Interface Sci. **92**, 92 (1983)

41. M. Barquins, D. Maugis, J. Méc. Théor. Appl. **1**, 331 (1982).

42. I.N. Sneddon, Int. J. Eng. Sci. **3**, 47 (1965).

43. D. Maugis, J. Colloid Interface Sci,. **150**, 243 (1992).

44. A.N. Gent, “Constitutive models for rubber III”, Busfield and Muhr, eds, 95, Swets and Zeitlinger, (2003).

45. A.A. Griffith, Phil. Trans. Roy. Soc. (London). Ser. A 221, **163** (1921).

46. T.L. Smith, Strength and Extensibility of Elastomers, “Rheology: Theory and Applications”, (F.R. Eirich, ed), Vol. 5, Ch.10, Academic Press Inc. New York, (1969).

47. D. Ferry, “Viscoelastic Properties of Polymers” 3rd ed., Wiely, New York, (1980).

48. A. Kadir, A.G. Thomas, Rubber Chem. Technol. **54**, 15 (1981).

49. T.L. Smith, J. Polym. Sci., **32**, 99 (1958).

50. R.S. Rivlin, A. G. Thomas, J. Poly. Sci., **10**, 291 (1953)

51. J.C. Halpin, J. Appl. Phys. **36**, 2975 (1965).

52. T.L. Smith, J. Polym. Sci., Pt. A1, 3597 (1963).

53. E.H. Andrews, Proc. Phys. Soc., **77**, 483 (1961).

54. W. G. Knauss, Experimental mechanics, **8**, 177 (1968).

55. J. V. Kraghelsky and E. F. Nepomnyashchi, Wear, **7**, 303 (1964).

56. A. G. Thomas, J. Polymer Sci., **31**, 467 (1958).

57. G. J. Lake,and P. B. Lindley, J. Appl. Polym. Sci., **10**, 343 (1965).

58. G. J. Lake,and P. B. Lindley, J. Appl. Polym. Sci., **9**, 1233 (1965).

59. D. G. Young, Rubber Chem. Technol., **59**, 809 (1986).

60. G. J. Lake, Rubber Chem. Technol. **68**, 435 (1995).

61. A.N. Gent, and C. Pulford, J. Appl. Polym. Sci. **28**, 943 (1983).

62. N.P. Suh, "Tribophysics", Prentice-Hall, New Jersey 1986.

63. D. Maguis, "Contact, adhesion and rupture of elastic solids", Springer, 1999.

64. R.K. Mehdi, "A numerical approach to understanding the mechanism of fatigue wear in tread vulcaizates during rolling of tires", dissertation, University of Akron, 2000

65. D.P. Gerrrard, "Dynamic and kinetic effects in friction and wear of rubbers", Dissertation, University of Akron, 2002.

66. M.N. Quereshi, "Hierarchial microdomains in solutions and emulsion polymerized elastomers induced by synthesis and processing and potential effects of properties". Dissertation, University of Akron, 2002.

67. S.V. Parthasarathy, Masters Thesis, University of Akron, 2001.

68. M. Barquins, "Adherence, friction and wear of rubber like materials" in 'Wear and friction of elastomers', ASTM, Philadelphia, 1992.

69. R.Bond, G. Lee and A.R. Williams, "The physics of tire traction", D.F. Hayes and A.L. Browne, Eds., Plenum Press, Elmsford, New York, 1974.

70. M. Shiratori, T. Miyoshi, Y. Sakai and G.R. Zhang, Trans. Japan. Society of Mech. Eng., **53**, 779, (1987).

71. A. Schallamach, Wear, **35**, 375, (1975).

72. P.R. Nayak, Trans ASME, J. Lubr. Technol. **93**, 398 (1971).

73. J. Peklenik, Proc. Inst. Mech. Eng. **182**, 108 (1967-1968).

74. J.A. Greenwood, J.B.P. Williamson, Proc. Roy. Soc. A **295**, 300 (1966).

75. J.B.P. Williamson, Proc. Inst. Mech. Eng**. 182**, 21 (1967-1968).

76. J.A. Greenwood, Proc. Roy. Soc. **A 393**, 133 (1984).

77. J.A. Greenwood, 'Contact of rough surfaces', *Fundamentals of Friction: Macroscopic and Microscopic Processes*, ed. by I.L. Singer, H.M. Pollack (Kluwer Academic Publishers), pp. 37-56, (1986).

78. J.F. Archard, Tribology Int. 213-220 (1974).

79. D.J. Whitehouse, J.F. Archard, Proc. Roy. Soc. A **316**, 97 (1970).

80. S. Mukherjee, Boundary Element Methods in Creep and Fracture, Applied Science, (1982).

81. A.N. Gent, M. Razzaghi-Kashani, Rubber Chemistry and Technology 73 818-829, (2000).

82. G.J. Lake, C.C. Lawrence, A.G. Thomas, Rubber Chemistry and Technology 73 801-817, (2000).

83. D. Cummings, A.N. Gent, W. Kim, J. Padovan, Rubber Chemistry and Technology, **65**, 223-230 (1992).

84. O.H. Yeoh, Mechanics of Materials, **34** 459-474 (2002).

85. J. Knowles, SIAM-AMS Proceedings, **12** 81-96 (1979).

86. G. Marci, Fatique Fract. Engng Mater. Struct. **17-8** 891-907 (1994).

87. J. Padovan, Y.H. Guo, Engineering Fracture Mechanics **48-3** 405-425 (1994).

88. Y. Uchiyama, Y. Ishino, Wear, **158,** 141-155 (1992).

89. V.P.W. Shim, L.M. Yang, C.T. Lim, P.H. Law, Journal of Applied Engineering Science **92** 523-531 (2004).

90. S.L. Burtscher, A. Dorfmann, Constitutive Models for Rubber, Dorfmann & Muhr (eds) 201-209 (1999)

91. E. Klarreich, Science News **167** 106-108 (2005)

92. J. Knowles, International Journal of Fracture, **13** 611-639

93. K. Layouni, L. Laiarinandrasana, R. Piques, Constitutive Models for Rubber III, Dorfmann & Muhr (eds) 273-281 (2003).

94. P. Charrier, Ostoja-Kuczynski, E. Verron, G. Marckmann, L. Gornet, G. Chagnon, Constitutive Models for Rubber III, Dorfmann & Muhr (eds) 3-10 (2003).

95. A. Dorfmann, K.N.G. Fuller, R.W. Ogden, Constitutive Models for Rubber III, Dorfmann & Muhr (eds) 253-261 (2003).

96. N. Wada, Y. Uchiyama, Wear **162-164** 930-938 (1993).

97. N. Murphy, C. Spratt, S. Ronan, S. Jerrams, R. Johannknecht, Constitutive Models for Rubber III, Dorfmann & Muhr (eds) 21-27 (2003).

98. C. Timbrell, M. Wiehahn, G. Cook, A.H. Muhr, Constitutive Models for Rubber III, Dorfmann & Muhr (eds) (2003).

99. I.C. Papadopoulos, H. Liang, J.J.C. Busfield, A.G. Thomas, Constitutive Models for Rubber III, Dorfmann & Muhr (eds) 33-39 (2003).

100. A. Kadir, A.G. Thomas, Rubber Chemistry and Technology 54 15-23 (1981)

101. E. Ostoja-Kuczynski, P. Charrier, E. Verron, G. Marckmann, L. Gornet, G. Chagnon, Constitutive Models for Rubber III, Dorfmann & Muhr (eds) 3-10 (2003).

102. A.I. Leonov, A. Srinivasan, Int. J. Engng Sci **31** 453-473 (1993).

103. C. Timbrell, M. Wiehahn, G. Cook, A.H. Muhr, Constitutive Models for Rubber III, Dorfmann & Muhr (eds) 11-20 (2003).

104. U. Sellgren, S. Bjorklund, S. Andersson, Wear **254** 1180-1188 (2003).

105. J. Streator, Journal of Tribology **125** 25-32 (2003).

106. J.W. Ringsberg, B.L. Josefson, Proc Instn Mech Engrs **215** 243-259 (2001).

107. Q.V. Bui, J.P. Ponthot, Wear **252** 150-160 (2002).

108. I.A. Polonsky, L.M. Keer, Wear **231** 206-219 (1999)

109. W.W. Tworzydlo, W. Cecot, J.T. Oden, C.H. Yew, Wear **220** 113-140 (1998).

110. R. Buzio, C. Bragno, U. Valbusa, Wear **254** 917-923 (2003).

111. M. Kluppel, H. Gert, Rubber Chemistry and Technology **73** 581-606 (2000)

112. A.A. Hon, J.J.C. Busfield, A.G. Thomas, Constitutive Models for Rubber III, Dorfmann & Muhr (eds) 301-307 (2003)

113. P.B. Lindley, A. Stevenson, Rubber Chemistry and Technology **55** 337-351 (1982)

114. R.W. Ogden, J. Phys. D: Appl. Phys., **12** 465-479 (1979).

115. N. Viswanath, D.G. Bellow, Wear **181-183** 42-49 (1995).

116. B.N.J. Persson, Physical Review Letters **87** 1-4 (2001).

117. J.A.W. van Dommelen, W.A.M. Brekelmans, F.P.T. Baaijens, Computational Materials Science **27** 480-492 (2003).

118. K. Legorju-jago, C. Bathias, International Journal of Fatigue **24** 85-92 (2002).

119. M. Mareanukroh, R.K. Eby, R.J. Scavuzzo, G.R. Hamed, J. Preuschen, Rubber Chemistry and Technology **73** 912-925 (2000).

120. A.N. Gent, P. Marteny, Journal of Materials Science **17** 2955-2960 (1982).

121. J.F. Hwang, J.A. Manson, R.W. Hertzberg, G.A. Miller, L.H. Sperling, Polymer Engineering and Science **29** 1477-1487 (1989).

122. Zhao Xiaopeng, Int J Fatigue **13** 341-344 (1991).

123. B.N.J. Persson, O. Albohr, U. Tartaglino, A.I. Volokitin, E. Tosatti, Journal of Physics: Condensed Matter **17** R1-R62 (2005).

124. I. Bekar, MS Hoo Fatt and J. Padovan, Tire Science and Technology Journal, **30**, No. 1, pp. 45-58, 2002

125. N. Prasad, Topology of Wear Particles, Thesis, University of Akron, 1998.

126. K-J. Bathe, Finite Element Procedures, Prentice Hall, 1995.

127. Y. Kwon, , Dissertation, Dept. of Polymer Engineering, University of Akron, 1994.

128. ABAQUS User Manuals, v 6.2, ABAQUS Inc, Providence, RI, 2003.

129. A. Dorfmann and A. Muhr (eds), Proceedings of the First European Conference on Constitutive Models for Rubber, Balkema, Rotterdam 1999.

130. Z. N. Gerek, Dept. Of Chemical Engineering, University of Akron, Private Communication, 2005.

131. M. J. Wang, S. Wollf, and E. –H. Tan, Rubber Chem. Technol., **66**, 178 (1993).

132. S. Wolf, and J. –B. Donnet, Rubber Chem. Technol., **63**, 32 (1990).

133. F. Erdogan and G. C. Sih, J. Basic Eng., Trans. ASME 85, **519** (1963).

134. R. J. Nuismer, Int. J. Fract. 11 (2), **245** (1975).

135. G. C. Sih, Int. J. Fract. 10 (3), **305** (1974).

136. W. Zhang,, Inverse Gas Chromatographic Studies of the Filler-Filler and Filler-Rubber Interactions, Masters Thesis, University of Akron, May 2000.

APPENDICES

APPENDIX A

STATISTICAL DESCRIPTION OF ROUGH SURFACES

This is a summary of classical models of rough surfaces as excellently described by Maugis [63]. Consider a surface of a solid defined by contour lines (Figure A.1). Summits are the surface points higher than their immediate neighbors. Contact is typically initiated at these points. The profile of this surface can be obtained at different locations along a set of reference planes along parallel lines of length L. The profile results in a series of *peaks* and *valleys* (Figure A.2).

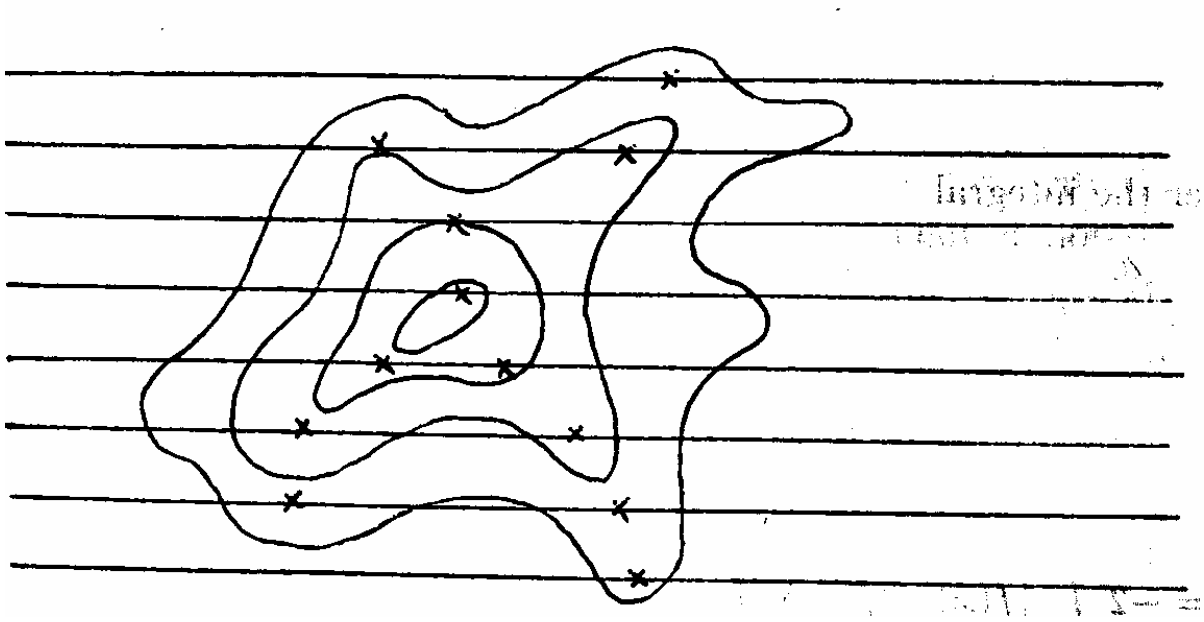

FIGURE A.1: Illustration of a surface with contours [63]

It should be noted that the 'peak' characterizes a two dimensional profile and its properties such as a height and radius of curvature may not match the corresponding

properties of a summit. This is because a section has little chance to pass through a summit as illustrated by 'x' marks in figure A.1. For convenience an index 'p' will denote peaks and index 's' a summit. [72]. One of the important difficulties in the characterization of a rough surface is the fractal nature of the surfaces.

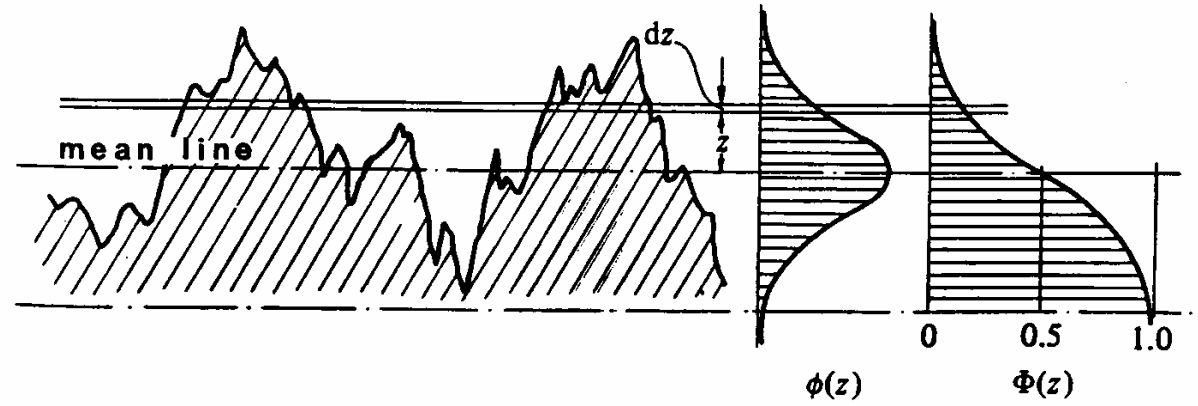

FIGURE A.2: Illustration of a profile with respect to a reference plane.[63]

Consider a given profile *f(x)*, with a datum line or mean line as $\bar{f}(x)$. Then the mean line is determined by the condition the deviation with respect to this line is a minimum. Mathematically, this means that equation A.1 is a minimum

$$\sigma^2 = \frac{1}{L}\int_0^L (f - \overline{f})^2 dx \qquad \text{A.1}$$

Implying that,

$$\int_0^L (f - \overline{f}) dx = 0 \qquad \text{A.2}$$

The heights measured with respect to this line and denoted *z(x).* The *average roughness* R_a, or the CLA (center line average), is:

$$R_a = \frac{1}{L}\int_0^L |z|\, dx \qquad \text{A.3}$$

and the *root mean square roughness* σ is defined by

$$\sigma^2 = \frac{1}{L}\int_0^L z^2 dx \qquad \text{A.4}$$

where σ^2 is the *variance* and σ the *standard deviation.*

If $\varphi(z)\,dz$ is the probability for a point of the surface to have a height between z and $z + dz$, the average roughness and the RMS roughness are given by:

$$R_a = \int_{-\infty}^{+\infty} |z| \varphi(z) dz = 2 \int_{0}^{+\infty} z \varphi(z) dz \qquad \text{A.5}$$

$$\sigma^2 = \int_{-\infty}^{+\infty} z^2 \varphi(z) dz \qquad \text{A.6}$$

In general a central moment of order r is defined as:

$$\overline{z^r} = \int_{-\infty}^{+\infty} z^r \varphi(z) dz \qquad \text{A.7}$$

and reduced (non-dimensional) central moments as ($\overline{z}^r / \sigma^r$). The first central moment is the mean and is zero, the second central moment is the variance, the third reduced central moment, denoted S_q (for skewness), describes the asymmetry and the fourth reduced central moment, denoted E_k, describes the shape (for kurtosis), either flattened or sharp. For a Gaussian distribution, the skewness is 0 and the kurtosis has the value 3 [73].

The probability for a point of the profile having a height larger than z is the *cumulative height distribution*.

$$\Phi(z) = \int_{z}^{\infty} \varphi(u) du \qquad \text{A.8}$$

This function varies from 0 to 1 when z varies from $+\infty$ *to* $-\infty$ and represents the S-shaped curve, seen in Figure A.2. This is also known as the *Abbott bearing area curve* (after Abbott and Firestone, 1933). A horizontal cut of a profile results in a plateau. The Abbot bearing area curve represents the length of this curve. Abbott proposed that the wear follows this pattern and as the area of the plateau increases, wear slows down. This requires a tacit assumption that and the variation of plateau areas on the surface follow the same relation as that of the profile.

Besides the cumulative height distribution, the cumulative peak height distribution $\phi_p\,(z_p)$, of density $\varphi_p\,(z_p)$ can also be studied. The mean peak height will be

$$\bar{z}_p = \int_{-\infty}^{+\infty} z_p \varphi_p(z_p) dz_p \qquad \text{A.9}$$

$$\sigma_p^2 = \int_{-\infty}^{+\infty} (z_p - \bar{z}_p)^2 \varphi_p(z_p) dz_p \qquad \text{A.10}$$

Greenwood and Williamson [74] showed experimental evidence that the height distribution of a number of technical surfaces was near to Gaussian. Additionally the peak height distribution was also Gaussian but with a different mean value and a different standard deviation.

One way of characterizing the longitudinal distribution of various profiles is to estimate the root mean square slope σ_m and the root mean square curvature σ_κ. However, these two measures are very sensitive to the resolution and may lead to an undefined derivative along a profile. Instead the autocorrelation or covariance is useful. This is defined as:

$$R_z(\lambda) = \frac{1}{L} \int_0^L z(x) z(x+\lambda) dx \qquad \text{(A.11)}$$

Or in a normalized sense:

$$\rho_z(\lambda) = \frac{R_z(\lambda)}{\sigma^2} \qquad \text{(A.12)}$$

Here λ is the distance between two points a profile and the functions described above assume that λ is small compared to the total distance L. Power spectral method may also be used for an alternate description as:

$$G_z(f) = \frac{2}{\pi} \int_0^\infty R_z(\lambda) \cos(2\pi f \lambda) d\lambda \qquad \text{(A.13)}$$

For isotropic random surfaces whose height distribution is Gaussian (with standard deviation σ) all the characteristics of the surface are contained in the power spectral density of the profile. The principal observations from this are [74,75]:

1. The density of peaks per unit length are related to the density of summits per unit area as:

$$\eta_s = \frac{2\pi}{3\sqrt{3}} \eta_p{}^2 = 1.209\eta_p^2 \qquad \text{(A.14)}$$

2. Mean heights for peak and summit are related as:

$$\bar{z}_s = \frac{4\sqrt{2}}{\pi} \bar{z}_p = 1.8\bar{z}_p \qquad \text{(A.15)}$$

3. The corresponding relationship for curvatures is:

$$\bar{\kappa}_s = \frac{8\sqrt{2}}{3\pi} \bar{\kappa}_p = 1.20\bar{\kappa}_p \qquad \text{(A.16)}$$

Based on the above terminology following is a summary of some of the roughness models:

Greenwood and Williamson Model.

Greenwood and Williamson [76,77] proposed a model, which assumes that the surface is uniformly covered by asperities (density η_s) whose summits have all the same radius of curvature *R*, but with a random heights. The distribution of the height z_s of the summits, *measured with respect to the mean plane of summits*, is found to be Gaussian, with a standard deviation σ_s, given by

$$\varphi_s(z_s) = \frac{1}{\sigma_s\sqrt{2\pi}} \exp\left(-\frac{z_s^2}{2\sigma_s{}^2}\right) \qquad \text{(A.17)}$$

The expression $\varphi_s(z_s)dz_s$ is thus the probability for a summit to have a height between z_s and $z_s + dz_s$ above the summits' mean plane and was found true for a number of technical surfaces. The parameters σ_s, R and η_s are shown to be related as [78]

$$0.03 < \sigma_s R\eta_s < 0.05$$

Whitehouse and Archard Model.

The above model was further extended by Whitehouse and Archard (79). They proposed a model of profile where the height distribution is Gaussian with a standard deviation σ and where the horizontal spread is defined by an exponential autocorrelation function

$$R_z(\lambda) = \sigma^2 e^{-\lambda/\lambda^*} \tag{A.18}$$

When the normalized autocorrelation function is less than 0.1, the two peaks are considered non-correlated. This happens when $\lambda > 2.3\lambda^*$. Thus a sampling interval of λ - $2.3\lambda^*$ is sufficient to reveal main structure of the profile. In this model the radii of curvature of peaks have a distribution which depends on their height: the higher the peaks, the lower their radius of curvature.

Whitehouse and Archard [79] showed that the number of summits per unit area η_s, their mean radius of curvature R, and the standard deviation of their height distribution σ^* are given by:

$$\eta_s = \frac{1}{5}\left(\frac{1}{2.3\lambda^*}\right)^2 \tag{A.19}$$

$$R\,\alpha\,\frac{\lambda^{*2}}{\sigma} \tag{A.20}$$

$$\sigma^*\,\alpha\,\sigma \tag{A.21}$$

Thus standard deviation of height σ and the correlation length λ^* together can define a surface. Also, the above three equations result in the relation $\sigma^* R \eta_s = \text{const}$ This is in accordance with the result by Greenwood and Williamson [77].

APPENDIX B

CONTACT MECHANICS

This is a review of some of the heuristic schemes used in the resolution of geometric contact between two interacting surfaces. The size of a "potential contact area" is a function of the problem involved, since it is dictated by the geometry and the load deformations involved in a problem. The contact and separation behavior of the surfaces is categorized into a variety of constraints named as contact modes. Contact modes thus act in conjunction with the boundary conditions of a numerical problem and are required to be prescribed in those regions where the surfaces have potential for coming into contact. Table B.1, describes the various contact modes that can occur for a contacting node pair from two surfaces. Here, t_t and t_n are the tangential and normal tractions, and u_t and u_n are the tangential and normal displacements respectively, expressed in local coordinates. Definitions for each contact mode are as shown in the table below

.**Separation**	**Slip**	**Stick**
$t_t^a - t_t^b = 0$	$t_t^a - t_t^b = 0$	$t_t^a - t_t^b = 0$
$t_n^a - t_n^b = 0$	$t_n^a - t_n^b = 0$	$t_n^a - t_n^b = 0$
$t_t^a = 0$	$t_t^a \pm \mu t_n^a = 0$	$u_t^a + u_t^b = 0$
$t_n^a = 0$	$u_n^a + u_n^b = gap^{ab}$	$u_n^a + u_n^b = gap^{ab}$

Table B.1 : Modes of Contact [80]

In addition to the above modes, a node-pair in contact situation may exhibit a partial Slip mode. This contact mode is useful in defining node pairs which become restrained in the tangential direction for the current load increment but may have undergone some slip during previous load increments. .

Contact Modeling Strategy:

A contact may be conforming or non-conforming as shown in Figure B.1. These contact situations warrant completely different modeling strategies in order to solve these problems accurately and efficiently.

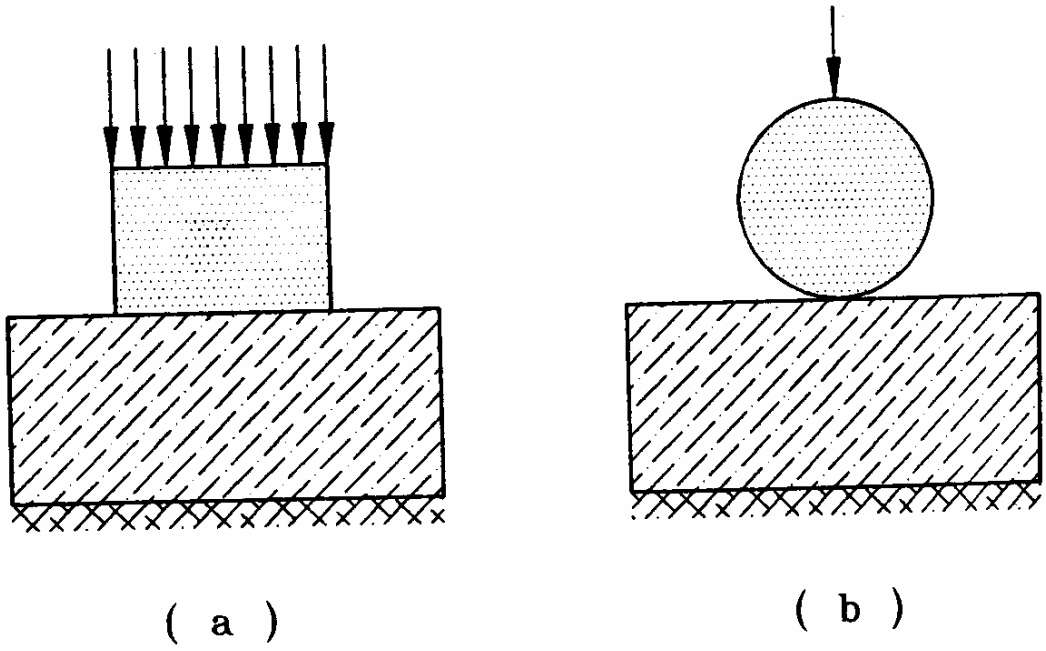

FIGURE B.1: (a) Confirming contact (b) nonconfirming contact [80]

Conforming contact problems :

In the absence of friction, these are the simplest contact examples. The problem is essentially reduced to a linear one with a known contact area and thus can be solved in one load step without iterations. With frictional conditions, iterations are needed in order

to determine the contact status along the contact interface. Since lateral displacement is restrained due to friction, the problem is solved with the total final load applied in one step and a "stick" initial contact mode prescribed for the entire contact interface; this solution is the first iteration. The resulting loads and displacements are then checked for violation of "stick" mode or "slip" mode. All "stick" node pairs that violate the friction law are then set to the "slip" mode and *vice versa*. These iterations are repeated until all the element pairs inside the contact region completely satisfy the contact conditions for "stick" or "slip".

Non Confirming Contact:

For a frictionless non-conforming contact problem iterations are required to obtain the correct contact area of the deformed bodies for the influence of the given total load. The problem thus involves application of the maximum load in one step followed by the iterations performed with contact area size increased or decreased until traction and displacement compatibility are satisfied simultaneously. A smooth and continuous normal traction over the entire contact zone is obtained for a final iteration. In particular, the edges of the contact region must be in traction-free state for a solution.

For frictional conditions, the solution of the contact state requires an iterative procedure; and since the size of the contact area is not known a priori, an incremental method must be employed to find the load step corresponding to each elemental increase or decrease in the area of contact. This is repeated till total external load or the final area of contact is reached.

APPENDIX C

CRACK PROPAGATION CRITERIA

In this section a review of existing crack propagation criteria are presented. All of the criteria were developed for the linear elastic fracture mechanics (LEFM) approach. This approach assumes small deformation (linear elastic) around the crack tip. The stress field around a crack tip is a function of three distinct classes of loading described as Mode I, II and III. For mode I and II loading, the crack tip stress and displacement field solution in polar coordinates are as follows:

$$\sigma_{rr} = \frac{1}{\sqrt{2\pi r}}\cos\frac{\theta}{2}[K_I(1+(\sin\frac{\theta}{2})^2) + \frac{3}{2}K_{II}\sin\theta - 2K_{II}\tan\frac{\theta}{2}] \quad \text{(C.1)}$$

$$\sigma_{\theta\theta} = \frac{1}{\sqrt{2\pi r}}\cos\frac{\theta}{2}[K_I(\cos\frac{\theta}{2})^2 - \frac{3}{2}K_{II}\sin\theta] \quad \text{(C.2)}$$

$$\sigma_{r\theta} = \frac{1}{\sqrt{2\pi r}}\cos\frac{\theta}{2}[K_I\sin\theta + K_{II}(3\cos\theta - 1)] \quad \text{(C.3)}$$

$$u = \frac{K_I}{4\mu}\sqrt{\frac{r}{2\pi}}\ [(2k-1)\cos\frac{\theta}{2} - \cos\frac{3\theta}{2}] + \frac{K_{II}}{4\mu}\sqrt{\frac{r}{2\pi}}\ [(2k+3)\sin\frac{\theta}{2} + \sin\frac{3\theta}{2}] \quad \text{(C.4)}$$

$$\upsilon = \frac{K_I}{4\mu}\sqrt{\frac{r}{2\pi}}\ [(2k+1)\sin\frac{\theta}{2} - \sin\frac{3\theta}{2}] - \frac{K_{II}}{4\mu}\sqrt{\frac{r}{2\pi}}\ [(2k-3)\cos\frac{\theta}{2} + \cos\frac{3\theta}{2}] \quad \text{(C.5)}$$

Here K_I and K_{II} are the stress intensity factors for Mode I and Mode II loading. Assuming above linear elastic solution to hold true, several crack propagation theories emerged in the literature. They are as follows.

(1) Maximum Tangential Stress Criterion:

In this approach, Erdogan and Sih [133] made the following assumptions

1- The crack extension starts at its tip in radial direction.

2- The crack extension starts in the plane perpendicular to the direction of greatest stress.

In general, the direction of maximum tangential stress or the principal stress is given by:

$$\cos(\theta/2)\,[K_I \sin\theta + K_{II}(3\cos\theta - 1)] = 0 \qquad \text{(C.6}$$

In which $\theta_0 = \pm\pi$ corresponds to the free surfaces, and for

$$K_I \sin\theta + K_{II}(3\cos\theta - 1) = 0 \qquad \text{(C.7)}$$

Symmetric loading: $K_{II} = 0$ $\theta_0 = 0$ deg.

Asymmetric loading: $K_I = 0$ $\theta_0 = -\text{arc}\cos 1/3 = -70.5$ deg.

Thus for mixed opening and sliding modes in a plane loading, the angle of crack propagation is a value between 0 and -70.5 deg.. An easy representation of a mixed mode I and II loading for experimental purposes is an angled crack in a plate under a uniform tension. Figure C.1(a) shows the geometry of crack, and figure C.1(b) represents the crack propagation angle (θ) as a function of the crack orientation (β).

With this theory, at failure:

$$\sigma_{\theta\theta}(2r)^{1/2} = \cos(\theta/2)\,[K_I \cos(2\theta/2) - (3/2)K_{II}\sin\theta] = constant \qquad \text{(C.8)}$$

For $\theta_0 = 0$ the above expression reduced to K_{Ic} for the mode I plane extension

(2) Minimum Strain Energy Density Criterion:

An alternate crack propagation criterion for the mixed mode fracture is based on the singularity strength of strain energy density field around the crack tip[135]. Based on

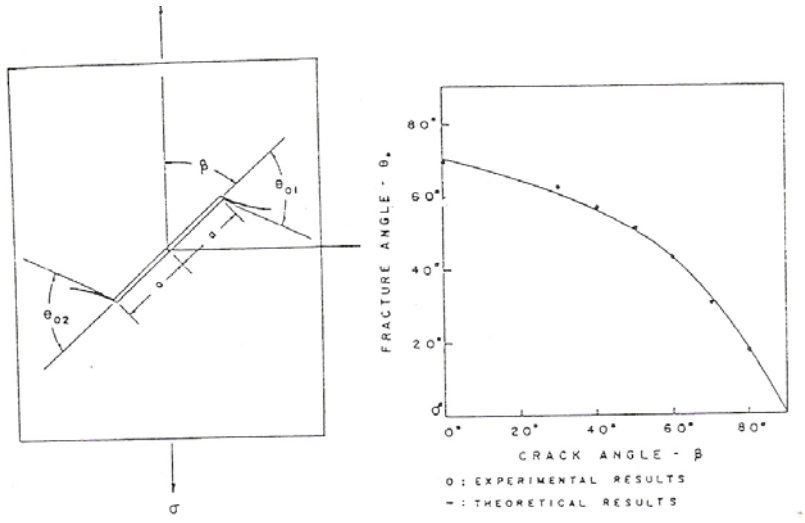

FIGURE C.1 a) Cracked plate under uniform tension b) Fracture angle versus crack angle in a cracked plate under uniform tension

the strain energy stored in an element dA=r dθ dr close to the crack tip, the energy density under a mixed mode loading condition is:

$$\frac{dW}{dA} = \frac{1}{r}(a_{11}K_I^2 + 2a_{12}K_I K_{II} + a_{22}K_{II}^2) = \frac{S}{r} \qquad \text{(C.9)}$$

The term *S* on the right hand side is called the strain energy density factor. According to the minimum strain energy density criteria, crack initiation takes place when *S* reaches a minimum value. It may be noted that this factor is a material property. This approach has limited applicability in stress cases where the loading is purely tensile. In a compression zone, the approach leads to erroneous results.

(3) Maximum Energy Release Rate Criterion:

Under the mixed mode loading condition described at the beginning of this appendix, a crack will propagate at an angle θ_0 which is not necessarily in its plane. The resulting stresses around the new crack tip may still be described with the equations C.1-

C-3 except with new values of r, θ, K_I and K_{II}. Energy release rate for the original crack is:

$$T_o = \frac{\mu(k+1)}{8\mu}\left(K_I^2 + K_{II}^2\right) \tag{C.10}$$

where μ is the sheer modulus of the material, and k=(3-υ)/(1+υ) for plane stress and k=3-4υ for plane strain cases, and K_I , K_{II} are intensity factors for the original crack. It should be mentioned that in this criteria fracture process is predicted based on *a priori* assumption regarding the crack propagation unlike the previous two approaches

In the geometry represented in figure C.2, when $a \to 0$, the stress field at the tip of the branch crack must approach the stress field at the tip of the original crack before propagation begins. In order to find the stress intensity factors for the branched crack, Nuimer [134] used a continuity assumption and concluded a quadratic form equivalent to (C.10) for an arbitrary propagation state, θ_o. Thus the energy release rate at this position is $T_{\theta 0}$ defined by the quadratic form:

$$T_{\theta o} = b_{11}K_I^2 + 2b_{12}K_I K_{II} + b_{22} + K^2{}_{II} \tag{C.11}$$

In this theory the direction of crack propagation corresponds to maximum energy release rate. The crack will begin to grow when energy release rate reaches a critical value $(G_{\theta 0})_c$. As with other criteria, this approach is limited to some special cases, and when a compound state of stress exists around the crack tip, this criterion might not determine the correct direction of crack propagation.

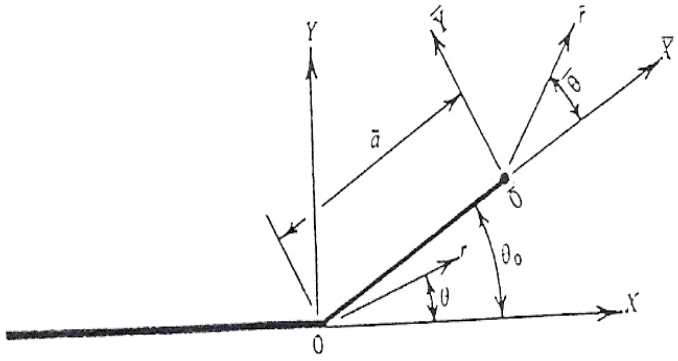

FIGURE C.2: Geometry and coordinate system for a branched crack.

APPENDIX D

VUMAT STRUCTURE

Chapter V discusses implementation of a strain rate dependent material law for unfilled elastomers for analyzing dynamic asperity loading. This is implemented using the ABAQUS/Explicit user subroutine VUMAT. Here we discuss the implementation within the ABAQUS framework [128]. This subroutine is called for blocks of elements integration points at each increment. When the subroutine is called, it is provided with the stress, solution-dependent state variables at the latest increment. It is also provided with the stretches and rotations at the beginning and the end of the increment. The variables provided by the solver for usage and update are described are listed on the following page. The ability of the VUMAT interface to pass block of integration point data to the subroutine on each call allows vectorization of the material subroutine.

According to ABAQUS convention all strain measures are calculated with respect to the midstep configuration. All tensor quantities are defined in the corotational coordinate system that rotates with the material or integration points. In the present implementation, the data at previous increments of stretches and strains is stored. Additional state variables are used for the purpose. For every increment, the strain rate is estimated (subroutine RATSTR) and used to calculate the new stress state (subroutine

Variables passed in for information:

Nblock : Number of material points to be processed in this call to **VUMAT**.
Ndir : Number of direct components in a symmetric tensor.
Nshr: Number of indirect components in a symmetric tensor.
Nstatev: Number of user-defined state variables that are associated with the material type
Nfieldv: Number of user-defined external field variables.
Nprops: Number of user-defined material properties
Lanneal: annealing process flag
stateNew: Corresponds to a new state of the stresses, stretches or zero initialization.
stepTime: Value of time since the step began.
totalTime: Value of total time.
dt : Time increment size.
cmname an upper case character string representing material name
coordMp(nblock,*): Integration point coordinates.
charLength(nblock) : Characteristic element length.
props(nprops): User-supplied material properties
density(nblock) : Current density at the integration points in the midstep configuration
strainInc (nblock, ndir+nshr): Strain increment tensor at each integration point.
relSpinInc (nblock, nshr): Incremental relative rotation vector at each integration point
tempOld(nblock): Temperatures at each integration point at the beginning of the increment.
stretchOld (nblock, ndir+nshr): Stretch tensor, U, at each material point
defgradOld (nblock,ndir+2*nshr) : Deformation gradient tensor at each integration point.
fieldOld (nblock, nfieldv) : Values of the user-defined field variables at integration point.
stressOld (nblock, ndir+nshr): Stress tensor at each integration point at tn
stateOld (nblock, nstatev): State variables at each integration point at the tn.
enerInternOld (nblock): Internal energy per unit mass at each integration point at the t_n
enerInelasOld (nblock): Dissipated energy per unit mass at each integration point at t_n.
tempNew(nblock): Temperatures at each integration point at the end of the increment.
stretchNew (nblock, ndir+nshr): Stretch tensor, U, at each integration point at t_{n+1}
defgradNew (nblock,ndir+2*nshr): Deformation gradient tensor at each t_{n+1}
fieldNew (nblock, nfieldv) Values of the user-defined field variables at each integration point at t_{n+1}

Variables required to be defined :

stressNew (nblock, ndir+nshr): Stress tensor at integration point at t_{n+1} .
stateNew (nblock, nstatev): State variables at each integration point at t_{n+1}.

Variables that may be updated :

enerInternNew (nblock) : Internal energy per unit mass at each integration point at t_{n+1}.
enerInelasNew (nblock): Dissipated energy per unit mass at each integration point at t_{n+1}.

RCUNFILL). The stresses are the Cauchy or True stresses. The user defined variables are then updated for the next increment (subroutine RUPSTATE). The call structure from the VUMAT is described as follows:

User Subroutine coding for the strain rate dependant unfilled rubber model.

```
subroutine VUMAT(
C Read only (unmodifiable)variables -
1 nblock, ndir, nshr, nstatev, nfieldv, nprops, lanneal,
2 stepTime, totalTime, dt, cmname, coordMp, charLength,
3 props, density, strainInc, relSpinInc,
4 tempOld, stretchOld, defgradOld, fieldOld,
5 stressOld, stateOld, enerInternOld, enerInelasOld,
6 tempNew, stretchNew, defgradNew, fieldNew,
C Write only (modifiable) variables -
7 stressNew, stateNew, enerInternNew, enerInelasNew )
C
include 'vaba_param.inc'
C
dimension props(nprops), density(nblock), coordMp(nblock,*),
1 charLength(nblock), strainInc(nblock,ndir+nshr),
2 relSpinInc(nblock,nshr), tempOld(nblock),
3 stretchOld(nblock,ndir+nshr),
4 defgradOld(nblock,ndir+nshr+nshr),
5 fieldOld(nblock,nfieldv), stressOld(nblock,ndir+nshr),
6 stateOld(nblock,nstatev), enerInternOld(nblock),
7 enerInelasOld(nblock), tempNew(nblock),
8 stretchNew(nblock,ndir+nshr),
8 defgradNew(nblock,ndir+nshr+nshr),
9 fieldNew(nblock,nfieldv),
1 stressNew(nblock,ndir+nshr), stateNew(nblock,nstatev),
2 enerInternNew(nblock), enerInelasNew(nblock),
C
character*80 cmname
C
do 100 km = 1,nblock
call RATSTR(defgradOld ,StateOld,,StretchOld, StrainInc)
call RCUNFILL(StressNew,StressOld,Stretch Old, StrainInc, defgradOld)
call RUPSTATE(StateOld,StateNew)
C
100 continue
return
end
```